8-18-2015 12:00 AM

Smart PV Inverter Control for Distribution Systems

Ehsan M. Siavashi
The University of Western Ontario

Supervisor
Prof. Rajiv K. Varma
The University of Western Ontario

Graduate Program in Electrical and Computer Engineering
A thesis submitted in partial fulfillment of the requirements for the degree in Doctor of Philosophy

SMART PV INVERTER CONTROL FOR DISTRIBUTION SYSTEMS

(Thesis format: Monograph)

by

Ehsan Mohammadi Siavashi

Graduate Program in Electrical and Computer Engineering

A thesis submitted in partial fulfillment
of the requirements for the degree of
Doctor of Philosophy

The School of Graduate and Postdoctoral Studies
The University of Western Ontario
London, Ontario, Canada

ABSTRACT

PV solar systems employ inverters to transform dc power from solar panels into ac power for injecting into the power grids. Inverters that perform multiple functions in addition to real power production are known as “smart inverters”.

This thesis presents a novel control of PV inverter as a dynamic reactive power compensator – STATCOM. This “smart PV inverter” control enables a PV solar inverter to operate in three modes – i) Full PV, ii) Partial STATCOM, and iii) Full STATCOM, depending upon system needs. The novel control is developed and demonstrated for the objectives of a) symmetrical voltage regulation, b) temporary overvoltage reduction, c) power factor correction, and d) reactive power control.

In Full PV mode, the inverter performs only real power production based on solar radiation. In Partial STATCOM mode, the controller uses the remaining capacity of the inverter for voltage control, power factor correction and reactive power control. The Full STATCOM mode is invoked in emergency scenarios, such as faults, or severe voltage fluctuations. In this mode, the real power production is shut down temporarily and the entire inverter capacity is utilized for voltage regulation or TOV curtailment for providing critical support to the power system.

This thesis presents a comprehensive design of the proposed smart inverter controller with all its associated system components. The performance of the smart inverter is simulated using the electromagnetic transients software PSCAD/EMTDC. It is further validated through Real Time Digital Simulation and Control Hardware in the Loop (CHIL) simulation. Finally the successful performance of the smart inverter controller is demonstrated on a 10 kW inverter in the laboratory on a simulated feeder of Bluewater Power, Sarnia, where this smart inverter is proposed to be installed.

The smart PV inverter control is further shown to enhance the connectivity of PV solar farms in a realistic 44 kV Hydro One distribution feeder. It is demonstrated that if such a

novel control is implemented on a 10 MW solar farm, the need for the actually installed STATCOM for voltage regulation and TOV control can be either minimized or altogether eliminated, bringing a significant savings for the utility.

Keywords

Photovoltaic Solar system, Distribution system, STATCOM, Voltage Source Inverter, PWM Control, Voltage Control, Reactive Power, Power Factor Correction, Real-time Digital Simulation, Hardware-in-the-Loop Simulation, Temporary Overvoltage, Fault studies, Flexible AC Transmission System (FACTS)

ACKNOLEDGEMENTS

I would like to express my sincere gratitude to my supervisor, Dr. Rajiv K. Varma for his valuable support, motivation, wisdom, enthusiasm and immense knowledge throughout of this research. His incredible support and guidance helped me to gain precious experiences during my PhD study. I am extremely thankful for his effort in providing me a unique opportunity to work in London Hydro Inc. No words are adequate to express my gratitude to him. I can only convey my warm regards to him.

I am also thankful to Dr. Vinay Sharma from London Hydro Inc. for the opportunity to work with London Hydro for my research work.

This research would have been impossible without the financial support of London Hydro Inc., Bluewater Power Distribution Corporation, Hydro One Network Inc, RTDS Technologies and Ontario Centres of Excellence. I would like to thank all these companies and organization for their valuable support.

I take this opportunity to express my gratitude to all of my friends Mansour, Omid, Byomakesh, Akshaya, Arif, Vishwajit, Sibin and Izad for their kind support during my research study at Western University.

Finally, I would like to dedicate my thesis to my dear parents and my family for their innumerable support throughout my life. Mother and Father, words cannot express my gratefulness when I think about what you have done for me. Father, you have encouraged me throughout my life to beat difficulties and now I want you to embrace the pain and get well soon.

I would like to express my affectionate appreciation to one and all, who directly or indirectly have helped me in this journey.

Ehsan M. Siavashi

TABLE OF CONTENTS

LIST OF FIGUERS

LIST OF SYMBOLS

P_{grid}	Active Power of Grid
Q_{grid}	Reactive Power of Grid
P_{Load} , P_L	Active Power of Load
Q_{Load} , Q_L	Reactive Power of Load
$P_{STATCOM}$	Active Power of STATCOM
$Q_{STATCOM}$	Reactive Power of STATCOM
P_{PV}	Active Power of Photovoltaic System
Q_{PV}	Reactive Power of Photovoltaic System
v_{PCC}	PCC Voltage
$v_{PCC,pu}$	Per-Unit Value of PCC Voltage
$v_{PCC,d}$	*d*-Component of PCC Voltage in *d*-*q* Frame
$v_{PCC,q}$	*q*-Component of PCC Voltage in *d*-*q* Frame
v_i	Inverter Voltage at AC Side
v_{id}	*d*-Component of Inverter Voltage in *d*-*q* Frame
v_{iq}	*q*-Component of Inverter Voltage in *d*-*q* Frame

V_{rms}	RMS Voltage
V_{L-L}	Line to Line Voltage
V_{dc}	Inverter Voltage at DC Side
$V_{dc,ref}$	Reference value of DC loop Controller
i_{grid}	Grid Current
$i_{STATCOM}$	STATCOM Current
i_{PV}	PV Current
i_{Load}	Load Current
i_{SPV}	Smart PV Inverter Current
$i_{Inverter}$, i_i	Inverter Current
i_{id}	*d*-Component of Inverter Current in *d*-*q* Frame
i_{iq}	*q*-Component of Inverter Current in *d*-*q* Frame
R_f	Filter Resistance
L_f	Filter Inductance
C_f	Filter Capacitor
R_d	Damping Resistance

L_t	Transformer Inductance
I_{SC}	Short Circuit Current of Solar Panel
n_P	Number of Parallel Solar Modules
n_S	Number of Series Solar Modules
f_{SW}	Switching Frequency
ω_0	Nominal Angular Frequency
ω_c	Cut-off Frequency
δ_m	Maximum Phase Margin
T_f	Filter Time Constant
σ_i	Time Constant of Inverter Current Controller
θ	Phase Angle

LIST OF ABBREVIATIONS

FACTS	Flexible AC Transmission System
STATCOM	Static Synchronous Compensator
PV	Photovoltaic
DG	Distributed Generation
PCC	Point of Common Coupling
VSC	Voltage Source Converter
VSI	Voltage Source Inverter
CSI	Current Source Inverter
PWM	Pulse Width Modulation
PLL	Phase Locked Loop
IGBT	Insulated-Gate Bipolar Transistor
RTDS	Real Time Digital Simulator
SLG	Single Line to Ground
LLG	Line to Line to Ground
TOV	Temporary Over Voltage
HIL	Hardware-In-Loop
GUI	Graphic User Interface

CHAPTER 1

1 INTRODUCTION

1.1 General

Environmental concerns such as pollution and limited resources of gas and fossil fuels have caused a surge of interest in renewable energy in recent years. One of the major renewable energy sources in the world is the photovoltaic system (PV) which converts solar power to electrical power. Historically, the first PV was used in space program as a cost efficient power supply in 1960s. In 1970s, governments started investing in solar power industry. For most of 1980s and 1990s, off-grid PV power plants were employed as an attractive cost effective power supply choice to electrify rural or inaccessible areas. In last two decades, due to significant developments in power electronics and solar panels, the solar energy industry has achieved a rapid growth in the world. This growth is expected to reduce PV electricity generation costs. Finally, with the drop of PV panel prices, the volume of PV installation has grown significantly. The world-wide installed capacity of PV systems reached 138.9 GW by end of 2013 compared to the installed capacity of 1.4 GW in 2000 [1]. By the end of 2013, the global outlook revealed that Germany was the world's largest overall producer of photovoltaic power with a total capacity of 35.7 GW while China had the fastest growth rate of 11.8 GW per year. In a short term outlook, it is expected by 2018, the worldwide capacity of PV power will reach almost 400 GW which implies a doubling of the capacity of year 2013 [2].

In 2009, the introduction of the Feed-In-Tariff (FIT) program has made Ontario a Canadian provincial leader in solar energy projects. In October 2010, the largest solar farm in the world was installed in Sarnia, Ontario with 80 MW which can supply more than 12,000 homes. The total installed PV power of Canada reached 1.2 GW by installing 444 MW in 2013 [3]. PV systems are classified as roof-top and ground-mounted systems with different capacities from few kilowatts to hundreds of megawatts. In roof-type photovoltaic system, solar panels are installed on rooftops of residential, commercial or institutional buildings whereas ground-mounted type photovoltaic systems are installed on the ground. Also, PV

systems can be installed either as a grid-connected system or stand-alone system (off-grid system). In case the system is grid-connected, when the power generation of PV system is more than the consumption by the load, the excess power can be fed to the grid [4].

Based on the power capacity, PV systems can be classified to utility-scale, medium-scale and small-scale. Utility scale PV sizes are between 1MW to 10 MW and connected to medium-voltage distribution feeder (e.g., 27.6 kV feeders) through one or more interconnection transformers. Medium-scale PV systems are defined to have a power range between 10kW to 1000kW, and installed on small and large buildings. A medium-size PV system is connected to medium or low voltage distribution feeders based on their capacity. Small-scale PV system is considered to be of capacity range up to 10kW. A small-scale PV is connected to low voltage feeder (120/208 V), either through three phase or single phase supply. In North America, many small-scale PV units are lumped and connected to a common PCC through a transformer [5].

The Ontario Power Authority (OPA) has rolled out the Feed-in Tariff (FIT) for the PV power fed to the grid, according to which the FIT price for the roof-type systems are higher than ground-mounted type PV systems for different range of power [3].

1.2 Distributed Generation (DG) System

The distribution system plays an important role in electric power system to provide a reliable supply to the end customers. Therefore, power quality issues in the distribution system reflect on other parts of power systems including loads. Most of distribution systems are based on radial structure, and therefore, the loss of any single component in the supply path disconnects the power supply to the end users [6-9]. Recently, several reasons such as increase in demand; technical and economic changes; and environmental concerns have encouraged industries to invest in Distributed Generation (DG) [10, 11]. Based on IEEE definition, DG is “the generation of electricity by facilities that are sufficiently smaller than central generating plants so as to allow interconnection at nearly any point in a power system” [12]. Renewable energy based DGs based on wind and solar energies have emerged as the most prominent ones [13, 14].

1.3 Challenges of Grid Integration of PV Distributed Generation (DG) Systems

Distributed Generators (DGs) reduce the cost of transmission network expansion. They also bring several benefits to existing network [10, 13]. However, these benefits come along with new challenges in the distribution systems. These include issues related to steady-state over voltage, temporary overvoltage (TOV), voltage flicker and harmonics [5, 15-18].

Due to varying sunlight availability and weather conditions (e.g. passage of clouds) the power of solar systems may fluctuate rapidly. This may impact the steady-state and dynamic behavior of the distribution system. PV integration impacts include voltage profile changes such as steady state overvoltage, temporary overvoltage (TOV), unbalanced voltage, power quality issues such as harmonics, frequent operation of conventional voltage regulators such as load tap changers and capacitor banks, changes in feeder power factor, etc. [5, 10]. On the other hand, connecting large solar systems to the grid causes power flow in the reverse direction resulting in over voltages at PCC which potentially limits any future DG installations [19-21].To avoid these problems, utility companies require PV systems to meet the IEC Standard 61727, IEEE Std. 1547 and Std. 929-2000 standards [22-25].

Hydro One, the largest transmission and distribution company in Ontario, has been connecting numerous solar farms in its distribution systems. To facilitate solar farm connection approval process, Hydro One performs several assessments in regards to the effect of PV systems on voltage performance [7, 26]. Conventionally, Hydro One has been using under load tap changers and capacitor switching to regulate voltage but these equipment have failed in presence of reverse power flow caused by PV solar farms and large load variations. When solar farm is connected to the grid, the surplus active power causes over voltage at PCC. This overvoltage can occur in the form of steady-state overvoltage or TOV. If these are higher than the interconnection rules of Hydro One, the solar farm is denied connection.

1.4 Static Synchronous Compensator (STATCOM)

Since DG resources such as PV solar farms may adversely impact the voltage levels, voltage regulation has become an important issue in their grid integration. Traditionally, shunt capacitor banks (SCs), on-load tap changers (OLTC) and step type voltage regulators (SVRs) are utilized for voltage control in the distribution systems. But the operating principle of these devices is based on unidirectional power flow and typical load variations. Since solar farms and wind farms may create reverse power flows, the traditional voltage regulators fail to operate satisfactorily. The voltage can however be controlled by dynamically exchanging reactive power at the feeder at which solar farms are connected, through Flexible AC Transmission Systems (FACTS) devices such as Static Var Compensator (SVC) [27-29] or STATic synchronous COMpensator (STATCOM) [30-33].

The STATCOM is a shunt-connected reactive power compensation device which essentially consists of a DC link capacitor, solid-state switches, filter elements and interfacing transformer. The STATCOM can enhance the distribution performance by controlling voltage flicker, temporary over voltage (TOV), steady-state over voltage as well as providing power factor correction.

The first STATCOM was installed in the Tennessee valley Authority (TVA) with 100MVA capacity in 1995. The objectives of this STATCOM were reduction of TVA's need for On Load Tap Changing (OLTC) transformers and resolving the overvoltage during off-peak conditions [31]. STATCOM can exchange reactive power by varying its terminal voltage. In other words, the difference in voltage between STATCOM terminals and PCC causes the reactive power to flow in a bidirectional manner. When the terminal voltage of the STATCOM is greater than PCC voltage, STATCOM generates reactive power and acts as a shunt capacitor. On the other hand, STATCOM absorbs reactive power like an inductor when its terminal voltage is lower than PCC voltage. In practice, the semiconductor switches of the STATCOM are not lossless, consequently the energy of the DC capacitor is dissipated due to internal loss of the converter. Hence, the STATCOM requires to absorb slight amount of active power from the grid to keep the capacitor charged to the required voltage level. It should be noted that if the STATCOM is equipped with an energy-storage device or a DC source like solar panel, active power generation can also be achieved.

In contrast with Static VAR compensator (SVC), the STATCOM is configured with power electronics converter instead of passive elements. Therefore, the interaction between STATCOM and the distribution system is smaller than in case of SVC. Also, as STATCOM controls the PCC voltage by injecting/absorbing current, the voltage control response is significantly faster than SVC response time [32, 34]. Figure 1-1 depicts the voltage-current characteristic of the STATCOM. It reveals that the STATCOM can operates in both inductive and capacitive regions by absorbing and injecting and reactive current, respectively. Also, in Figure 1-1, the maximum capacitive generation of the STATCOM is almost independent of the system voltage. This capability is needed to support the grid voltage during the voltage collapse or severe fault situation [35].

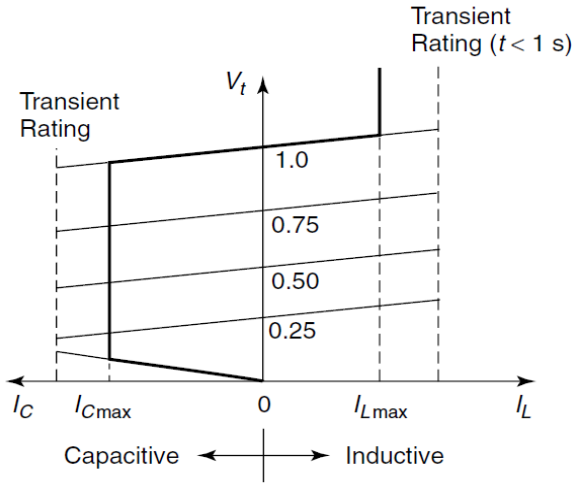

Figure 1-1: The voltage-current characteristic of STATCOM [29]

1.5 Smart Inverters

Inverters that can perform multiple functions in addition to their main task of converting DC power to AC power have been described as *smart inverters* [36, 37]. Such multifunctional smart inverters are being increasingly developed and implemented in power systems around the globe [38-40]. DG interconnection standards such as IEEE 1547 [25], and inverter testing standards such as UL 1741 [41], are being presently revised to facilitate the integration of smart inverters to exploit their benefits. Novel controls and applications of smart PV inverters; and the required standards for DG integration for smart PV inverter installations are discussed in this section.

1.5.1 Functions of Smart Inverters

Smart Inverters (also previously known as Advanced Inverters) represent a paradigm shift in the integration of Distributed energy resources [37, 42-44]. Under this concept, the inverters are being programmed with new functionalities that can support distribution system operations to help increase the penetration of the renewable energy based systems in electric power systems. Collectively, these programmable functions are called "smart inverter functionalities." [36, 45]. Several developments on smart inverters have already been reported in literature [13, 37, 42-44, 46-49].

A parallel development has also taken place in the development of smart inverters, by providing FACTS like capabilities in wind inverters [50, 51] to provide ancillary services.

PV systems use Voltage Source Converter for converting DC power to AC power, whereas STATCOMs provide reactive power exchange using a Voltage Source Converters. This common feature of PV system and STATCOM motivated the development of a patent pending technology for utilization of the PV inverter as STATCOM to provide reactive power control during nighttime and also during daytime together with production of real power [13, 44, 52].

This concept can bring reactive power support by installed PV systems without any high cost changes. A new control of PV inverter as a STATCOM was proposed for improving power transmission capacity [53]. New controls of PV solar farm as STATCOM (PV-STATCOM) were proposed for increasing transient stability and enhancing the connectivity of neighboring wind farms [54]. The voltage control functionality with PV system has also been proposed in [45, 55-57]. The application of PV inverter for supporting reactive power during night has been discussed in [13, 58]. Unbalanced voltage mitigation with PV system has been studied in [59, 60].

1.5.2 Modeling of Smart Inverters and Validation

The different methods of modeling the smart inverters and their validation through software simulation, Real Time Digital Simulation and Laboratory simulation, are presented in this section.

1.5.2.1 Modeling in Software

In [13] the authors utilized a conventional solar farm as a STATCOM during nighttime for supporting a wind farm. The study system and controller has been validated in MATLAB/SIMULINK software. The compensation of the unbalanced and non-linear load with solar farm has been presented in [61]. The application of the solar farm in the transmission system has been proposed in [53, 62]. In [62] the solar farm has been modeled in PSCAD/EMTDC software as STATCOM together with a damping controller for enhancement of the power transmission limit. The improvement of the transient stability of the transmission system has been discussed in [53]. In [63], an auxiliary controller has been added to the conventional PV controller to operate as a shunt active filter. The Reactive power compensation by PV solar system has been modeled in MATLAB/SIMULINK [56, 64].

1.5.2.2 Modeling in Real-Time Digital Simulator (RTDS)

The real-time digital simulation demonstrates better perspectives about controller performance than software study. In real-time study, actual sensor signals and PWM signals are involved in the control process. One of the commercial devices for real-time study and hardware-in-loop is Real Time Digital Simulator (RTDS). In [65] a novel MPPT control for a conventional PV solar has been implemented on the real-time digital simulator. The real-time simulation of the grid-connected wind farm has been presented in [66-68]. A combination of the wind farm and STATCOM for reactive power compensation has been modeled in RTDS hardware in [69, 70]. Also, in [71, 72] the effects of the STATCOM on the distribution networks have been discussed by means of real-time digital simulation.

1.5.2.3 Lab Validation

The final stage of the controller validation is the through an actual hardware simulation in the laboratory. In this stage, the small-scale model of the study system is implemented and the smart inverter controller with certain objectives is implemented in a lab setup. In [73] the authors used grid-connected PV system for harmonics and reactive power compensation and implemented a controller which was linked to actual lab setup. The lab

validation of a 20 kW solar system with reactive power compensation has been proposed in [74]. In [40] the power hardware-in-loop (PHIL) testing of a 500kW PV system is demonstrated for power factor correction and constant reactive power control. PHIL model consist of RTDS, PV array emulator, PV inverter and AC grid emulator. Southern California Edison (SCE) and National Renewable Energy Laboratory (NREL) are cooperating in this testing initiative. As a result of this testing, Volt/Var control will be added to PV inverter control and it will be installed on SCE distribution system [39]. In [75] the authors validated the dynamic model of the PV system with an actual hardware bench test in Southern California Edison Lab. In this paper, the lab results have been compared with PSCAD/EMTDC results.

1.5.3 Standards for Grid Integration of Distributed Systems

Distributed Generators (DGs) or Distributed energy resources (DRs) are widely used in the distribution system. One of the major technical challenges of distributed resources (DR) interconnection is the DR impact on electric power system (EPS). On the other hand, the DR interconnection location and the characteristics of EPSs vary rapidly and it leads to variation of the integration impacts. Some of the DR impacts on EPS are voltage unbalance, overvoltage, low voltage, improper regulation during reverse power flow. IEEE 1547 series of standards [22, 25] present the technical specifications and requirements for integration of distributed resources with the area electric power system. System operators can mitigate many undesirable system impacts by applying IEEE Std 1547-2003 appropriately. Based on IEEE Std 1547-2003 Sec. 4.1., “the DR shall not actively regulate the PCC voltage and cause the Area EPS service voltage at other Local EPSs to go outside of ANSI C84.1-1995, Range A.” [25]. In this standard it is indicated that the voltage regulation by DR can have conflict by other regulation equipment installed by area EPS operator. Numerous studies on voltage regulation by Distributed Resources motivated IEEE to modify its previous version of integration standard and release a new reversion known as IEEE Std 1547a-2014 [76]. IEEE Std 1547a-2014 indicates “Coordination with and approval of, the area EPS and DR operators, shall be required for the DR to actively participate to regulate the voltage by changes of real and reactive power. The DR shall not cause the Area EPS service voltage at other Local EPSs to go outside the requirements of ANSI C84.1-2011 1995, Range A”

[76]. Hence, Distributed resources such as photovoltaics, fuel cells, energy storage systems and wind systems can regulate the voltage even in presence of other regulation equipment. This revision in IEEE Standard 1547 and its further ongoing revisions have paved the path for connecting smart inverters with the distribution systems.

1.6 Concept of Smart PV Inverter Control as STATCOM (PV-STATCOM)

As described earlier, a STATCOM is a dynamic reactive power compensator based on voltage source converter (VSC), whereas a conventional PV system requires a VSC for converting DC power to AC power. On the other hand, a STATCOM is a device to exchange reactive power whereas a PV system generates active power. Therefore, the combination of these two concepts can support both active and reactive power. A new technology has been proposed for utilizing a PV solar system inverter as a STATCOM [13, 43]. The power output of a PV system during a typical sunny day is shown in Figure 1-2. It is clear that over 80% of the 24 hours, the PV system works below its rated power output and rest of the inverter capacity remains unused. Also, the entire PV inverter is idle during night time when sun is not available. The above novel concept of PV solar system as STATCOM is based on the utilization of the remaining inverter for exchanging reactive power with the grid for voltage control. This new technology can bring several benefits with little additional cost.

Voltage control and power factor correction are two control objectives that can be achieved through the remaining capacity of the PV inverter. In this thesis, exchanging (absorbing/injecting) reactive power with remaining capacity of the inverter is called smart PV inverter in "Partial STATCOM mode". In this mode, the priority of the smart PV is the generation of the active power and then exchanging the reactive power with remaining inverter capacity. However, a new patent-pending technology has been proposed [44] according to which during transients or faults, the PV solar system autonomously transforms into a full STATCOM. In this case, the smart PV system disconnects the solar panels and exchanges reactive power with its full inverter capacity as a STATCOM for the duration needed by the grid. This mode of the smart PV inverter operation is termed "Full STATCOM mode". In other words, the smart PV inverter autonomously determines its

operation mode and prioritizes between active power generation and reactive power exchange based on the system requirements, nature of transient/disturbance, time of the day and remaining inverter capacity.

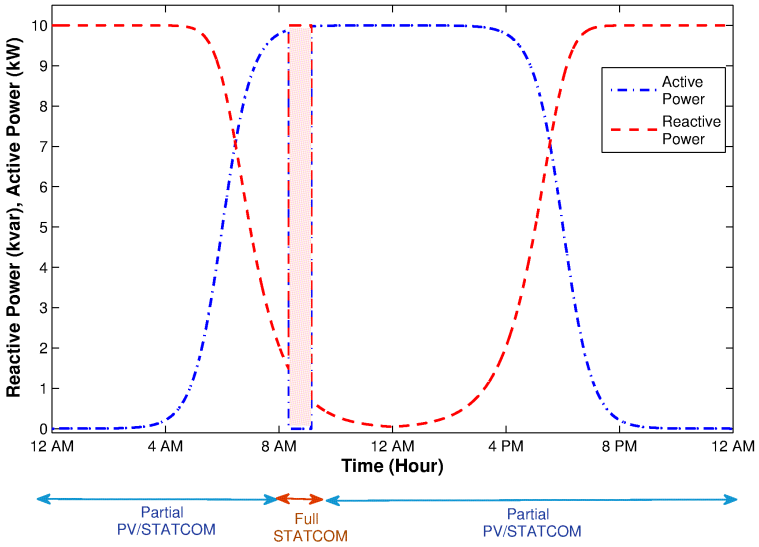

Figure 1-2: Power output of a 10kW PV system versus time on a sunny day

As described earlier, the adverse effects of DG systems on the voltage profile have led to utilities imposing limitations on the DG connectivity. As smart PV inverters can fully regulate voltage with reactive power support, it can be considered as a cost-effective solution for increasing the connectivity of DGs in distribution systems. It needs to be examined if PV solar farms equipped with this smart inverter control can indeed help in increasing the connectivity of PV solar farms.

1.7 Motivation and Scope of Thesis

The objective of this thesis is to model, test and validate the novel patent pending technology of the smart inverter control as PV-STATCOM [43, 44] which will lead to its *first-time* field implementation on a 10 kW PV solar farm in the feeder network of the distribution utility Bluewater Power, Sarnia.

This thesis will further examine the applicability of the proposed smart inverter control in a 30 MW PV solar farm in an actual Hydro One utility feeder (name withheld for confidentiality). Both partial STATCOM and full STATCOM modes will be implemented

to regulate the steady state overvoltage and to reduce the TOV to within acceptable limits, under a wide range of operating conditions. The objective will be to demonstrate that the need for an actual expensive STATCOM that has already been installed in the system for the same purpose, can either be reduced or totally eliminated

The objectives and scope of this thesis are therefore summarized as follows:

1) Development of a model of the novel smart PV inverter with the "Partial STATCOM" and "Full-STATCOM" mode of operation, for voltage control and power factor correction

2) Validation of the developed smart inverter model through industry grade electromagnetic transient simulation software EMTDC/PSCAD under different operating conditions.

3) Implementation of the developed smart inverter model and validation of its performance through Real Time Digital Simulation (RTDS) and Hardware in the Loop (HIL) simulation by modeling the smart inverter controller on a DSP-based control board dSPACE.

4) Validation of the developed smart inverter control on 10 kW inverter and demonstration of its performance on a laboratory scale model of the Bluewater Power Distribution Feeder System, prior to its field demonstration

5) Demonstration of the capability of the developed smart PV inverter control in an actual Hydro One distribution network for increasing the connectivity of PV solar farms without needing an actual STATCOM.

1.8 Outline of Thesis

A chapter-wise summary of this thesis is given below:

Chapter 2 demonstrates the modeling of smart PV inverter controller in the distribution system. This includes the modeling of the distribution system, PV solar system, harmonic filter, and smart PV inverter controller. The controller structure for general distribution

system is explained and then a realistic feeder in the Bluewater Inc. is chosen as a case study, and the procedure for design of smart inverter controller parameters is presented.

Chapter 3 demonstrates the software simulation studies of the study system for voltage control, power factor correction and reactive power control. The study system, passive load, harmonics filter, voltage source inverter (VSI) and solar panel are modeled in PSCAD/EMTDC software. Also, the controller is modeled for both Partial and Full STATCOM operation modes based on the designed parameters in Chapter 2. The smart inverter controller performance is demonstrated for voltage control, power factor correction mode and reactive power control in partial mode.

Chapter 4 presents the hardware-in-loop (HIL) simulation of the smart PV inverter controller. The hardware of the smart PV controller is implemented in dSPACE Controller board and the study network, passive loads, harmonics filter and PV solar system are modeled in Real Time Digital Simulator (RTDS). The required parameters for hardware controller operation such as PCC voltage, inverter current, load current and DC link voltage are received from the analog output card (GTAO) card of RTDS. The controller inside the dSPACE board generates the appropriate gates pulses for inverter model in the RTDS through the digital input card (GTDI) of the RTDS. These HIL studies validate the controller performance for both partial and full STATCOM operation modes for the study system.

Chapter 5 deals with the laboratory implementation of the smart PV controller for the study system. The Thevenin's equivalent of the Bluewater Power distribution network is represented by an appropriate inductor and resistor. 10 kVA/kW passive loads are applied for the different tests. A 10 kVA PV Simulator is used to model the characteristics of the solar panels. The PV Simulator generates active power based on irradiance and temperature profiles. A 10 kVA two-level IGBT module is used in the test plan to act as a voltage source inverter. The smart PV inverter is implemented on the dSPACE controller board. The gates of the inverter switches are activated by the PWM signals output of the dSPACE board. Also, an LCL filter is applied to remove the harmonics due to switching pulses. The performance of the smart inverter controller is evaluated for partial and full operation

modes for different control objectives. The experimental results are utilized to validate the performance of the designed smart inverter controller.

Chapter 6 presents the application of the proposed smart PV inverter controller for reduction of temporary overvoltage (TOV) and PV connectivity enhancement. For validation of the controller, a realistic 44 kV feeder of Hydro One network is chosen as a study system. The study system includes three 10 MW PV systems with total capacity 30 MW with interface and DG transformers. The entire systems including 44 kV feeder, passive loads and three 10 MW PV systems are modeled in PSCAD/EMTDC software. One out of three PV systems in the case study system is utilized with smart PV controller and other two PV systems operate as the conventional PV systems. The controller operates in partial and full STATCOM modes based on the network requirements. To enhance the PV connectivity of Hydro One network the partial mode of the controller is presented for voltage control. Also, the single-line-to-ground (SLG) fault is applied to create the temporary overvoltage with unacceptable level. The controller uses the entire capacity of the inverter to provide sufficient reactive power compensation for TOV reduction. The controller performance is validated for single-line-to- ground and line-to-line-ground faults for severe TOV. It is shown that if the proposed smart inverter control is implemented on one of the 10 MW PV solar farms, the need of the actually installed STATCOM is eliminated.

Chapter 7 presents the conclusions and the main contributions of this thesis. Future research work with this mart inverter controller is also proposed.

CHAPTER 2

2 MODELING OF DISTRIBUTION SYSTEM WITH SMART PV INVERTER

2.1 Introduction

This chapter presents the modeling of different components of a typical radial distribution system with a PV solar system utilizing a smart inverter. The principles of smart PV inverter in different operating modes of Full PV, Partial STATCOM and Full STATCOM are illustrated for voltage control and power factor correction. Since the objective of this thesis is to develop a 10 kW smart inverter that will be implemented in the distribution system of Bluewater Power Distribution Corporation, Sarnia, the procedure for design of various components of the smart inverter and its controllers are described in this chapter.

2.2 System Modeling

Figure 2-1 illustrates the single line diagram of a typical radial distribution system including substation, transformer, distribution line, load, and PV solar system as a Distributed Generator (DG).

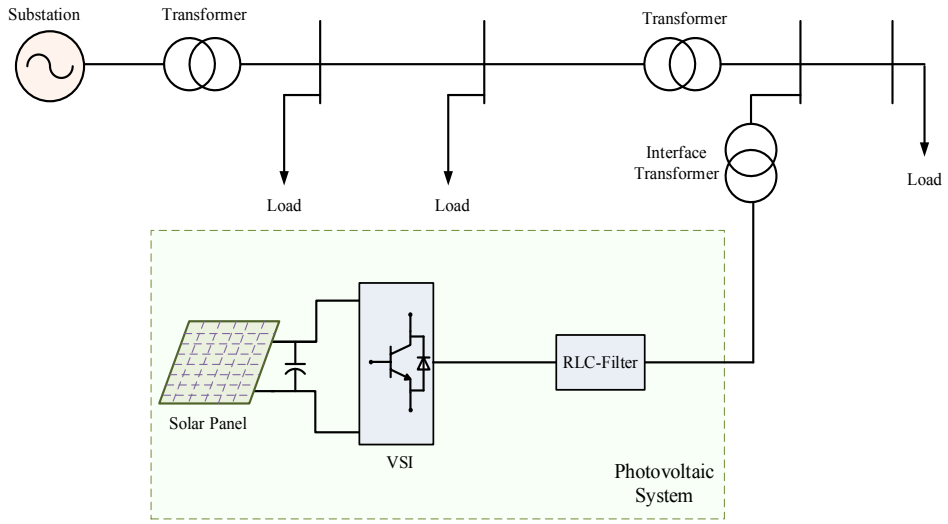

Figure 2-1: Single line diagram of the study distribution system

This section presents the general principles of modeling the different components of such a distribution system with a smart PV inverter.

2.3 Network Model

The main components of the network in the study distribution system are the substation system, transformer, power distribution line and electrical load. These are described below.

2.3.1 Substation System

The distribution substation comprises a group of transformers and switchgears located close to the users. The primary duty of the distribution subsystem is to receive power from the transmission system and disseminate to the distribution feeders. In addition to voltage level transformation, voltage regulation and switching are considered as other functions of the substation. Substation transformers are responsible to alter the voltage from transmission system level to distribution system level. In North America, the most common distribution feeders are 7.2 kV, 12.47 kV, 13.8 kV, 14.4 kV, 25 kV and 34.5 kV whereas the transmission voltage level are 765 kV, 500 kV, 230 kV, 115 kV and 69 kV [77-79]. It should be noted that in distribution systems, typically feeders emerge from the substation radially and feed the users [7, 80].

The substation is modeled as an equivalent voltage source with its short circuit impedance ($R+jX$).

2.3.2 Distribution Line Model

The distribution line is represented by the lumped- π model comprising the series components (resistance and reactance) and shunt components (conductance and susceptance) [81]. Based on Figure 2-2, the relationship between voltage and current of two ends of the line can be presented as below:

$$\begin{bmatrix} V_s \\ I_s \end{bmatrix} = \begin{bmatrix} 1+\frac{YZ}{2} & Z \\ Y\left(1+\frac{YZ}{2}\right) & 1+\frac{YZ}{2} \end{bmatrix} \begin{bmatrix} V_R \\ I_R \end{bmatrix} \tag{2.1}$$

where V_S and V_R are positive-sequence line to neutral voltages of each end of line, I_s and I_R are positive-sequence line currents of each end of the line. Also, $Z=(r+jx_L)l$ and Y are

series impedance and shunt impedance of the line where r and x_L are series resistance and series admittance, respectively, and l is the line length. Distribution feeders are considered as medium-length and short-length lines. In the π model of a short transmission line, the shunt admittance can be neglected. As a consequence, (2.1) is simplified to series impedance and $ABCD$ parameters in matrix format are obtained as below [82]:

$$\begin{bmatrix} V_s \\ I_s \end{bmatrix} = \begin{bmatrix} 1 & (R + jX_L)l \\ 0 & 1 \end{bmatrix} \begin{bmatrix} V_R \\ I_R \end{bmatrix} \tag{2.2}$$

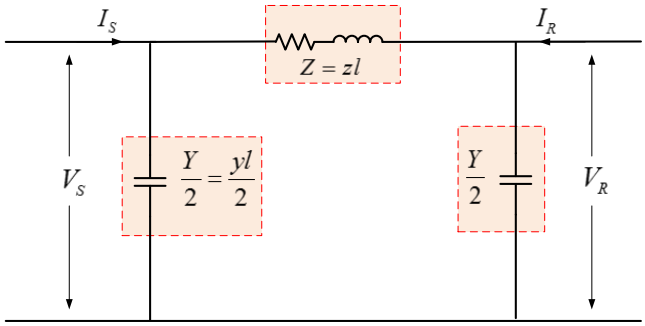

Figure 2-2: Equivalent lumped π-model of distribution line

2.3.3 Transformer

Transformers are used widely in the distribution system to operate several functions such as voltage transformation and isolation [83]. In distribution systems, the step-down transformer is used to provide power at lower voltage to the end users including DG systems. Also, the transformer is used to achieve the isolation between the DG system and the distribution line. A two winding transformer is modeled as shown in Figure 2-3. This transformer is represented by an ideal transformer with ratio k, a leakage impedance Z_L and a magnetizing impedance Z_M [84].

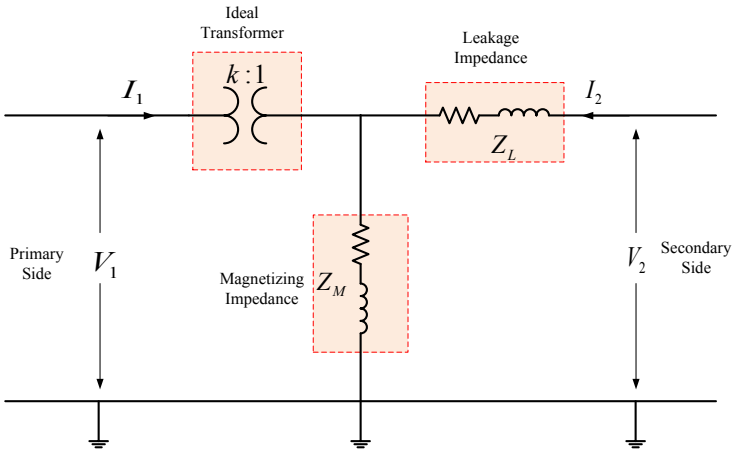

Figure 2-3: Two-winding transformer model

2.3.4 Load model

The power system loads, in general, can be classified as static loads, dynamic loads and power electronics based loads. A static load is time-independent and represented by active and reactive powers for certain voltage and frequency. On the other hand, a dynamic load is a time-variant load such as induction and synchronous motors [85]. In this thesis only static loads are considered.

2.3.4.1 Static Load

Based on the relationship of power to the voltage, the static loads can be classified into constant power, constant current and constant impedance loads. The polynomial form of the static load can be written as:

$$P_L = P_{L0}\left[a_1\left(\frac{V}{V_0}\right)^2 + a_2\left(\frac{V}{V_0}\right) + a_3\right]$$
$$Q_L = Q_{L0}\left[b_1\left(\frac{V}{V_0}\right)^2 + b_2\left(\frac{V}{V_0}\right) + b_3\right] \qquad (2.3)$$

where P_{L0} and Q_{L0} are active and reactive power at the initial conditions. For the resistive loads, the power is a quadratic function of voltage, and therefore, $a_2 = a_3 = b_2 = b_3 = 0$. A

constant current load follows the voltage changes linearly. Hence, $a_1 = a_3 = b_1 = b_3 = 0$ for the constant current load. Also, a constant power load is independent of the voltage changes $(a_1 = a_2 = b_1 = b_2 = 0)$ [86].

2.4 PV System Model

PV solar systems covert sunlight into electricity using PV arrays. As PV panels produce DC power, an inverter is used to convert the DC power to AC power. Depending on the system configuration, a PV system can operate in either stand-alone or grid-connected mode [87]. In comparison with stand-alone PV system, the grid-connected PV system is more reliable and efficient [88]. Figure 2-1 illustrates the structure of the grid-connected PV system in the distribution network. The PV system includes solar panels, DC/AC inverter, harmonics filter and an isolation transformer. In the following sections, each part of the PV system will be discussed.

2.4.1 Solar Panel

The solar cells generate electricity when exposed to light. The electrons inside the solar cell flow and produce current when the sun light is absorbed by the solar cell. The output of an individual cell is rather low. Hence, several cells are connected in a series-parallel configuration called a module to generate more output power. In general, a solar panel includes several arrays, while each array consists of many modules [89]. Two important factors, irradiance and temperature, affect the cell performance [90]. Figure 2-4 indicates the effect of solar radiation and temperature on the silicon cell. Figure 2-4 reveals that the current changes with the irradiance, whereas voltage is influenced by the temperature. Solar cells provide best performance under low temperatures and high irradiance.

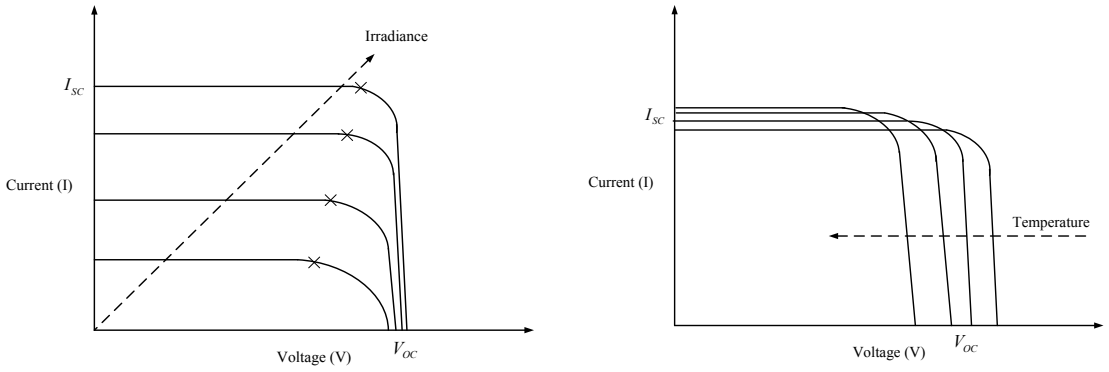

a) b)

Figure 2-4: Solar cell *i-v* characteristic based on the variations of a) Irradiance b) Temperature

Solar cells deliver highest power at the maximum value of the product of current and voltage. Hence, it is preferred both from technical and economic reasons that the solar cells operate at maximum power region. The power characteristic of solar cell versus voltage under temperature changes is shown in Figure 2-6.

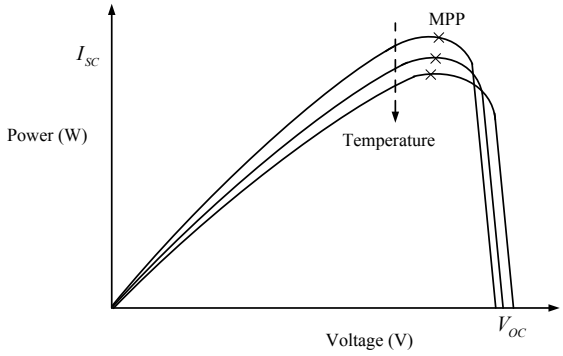

Figure 2-5: Power versus voltage characteristic of solar cell for different temperatures

As shown above, the maximum power point (MPP) of the solar cells is influenced by temperature and irradiance changes. Therefore, it is important to detect the MPP of the cell to provide maximum efficiency. Several maximum power point tracking (MPPT) methods

have been developed and implemented [91-95]. A simple equivalent circuit of a solar cell is shown in Figure 2-6.

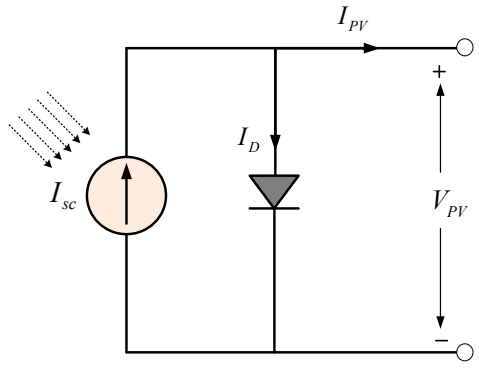

Figure 2-6: Equivalent circuit of a solar cell

This circuit is composed of an ideal current source and a parallel diode. In Figure 2-7, I_{SC} is the short circuit current of the cell, I_{PV} is the current output of the cell, I_D is the diode current and V_{PV} is the voltage output of the cell. The current and voltage of the output terminal can be written as below [91, 96]:

$$I_{PV} = n_p\left(I_{sc} - I_D\right) = n_p I_{sc} - n_p I_0\left[e^{\left(\frac{qV_{PV}}{kTn_s}\right)} - 1\right] \tag{2.4}$$

where, I_0 is the diode saturation current, electron charge $q = 1.6e^{-19}$ coulomb, T is the cell temperature, $k = 1.38e^{-23}$ is the Boltzmann's constant, while n_s and n_p are the number of series and parallel cells. By applying open circuit conditions $\left(I_{PV} = 0,\ V_{PV} = V_{OC}\right)$ into (2.4), the diode saturation current I_0 can be obtained as below:

$$I_0 = n_p I_{sc}\left[e^{\left(\frac{qV_{OC}}{kTn_s}\right)} - 1\right]^{-1} \tag{2.5}$$

Also, the terminal voltage of the solar cell can be found from (2.4).

$$V_{PV} = \frac{kTn_s}{q} \ln\left(1 - \frac{I_{PV} - n_p I_{sc}}{n_p I_0}\right) \tag{2.6}$$

2.4.2 PV Inverter

The PV inverter is the most fundamental part of the PV system, that converts DC power to AC power. Two types of inverters, voltage source inverters (VSI) and current source inverters (CSI), are used in PV applications [97-100]. The three-phase VSI is more commonly employed inverter for the grid-connected PV system for conversion of DC power to AC power [101]. A three-phase VSI is composed of IGBT switches and a capacitor at the DC side. There are several topologies of three-phase VSI such as two-level and multi-level which influence the performance of the inverter [102-108]. For this study, a two-level VSI is employed. The valves in each leg of VSI are switched by pulse width modulation (PWM) technique [109, 110]. The most common PWM modulation techniques are sinusoidal PWM (SPWM), space vector modulation (SVM), and random PWM. The different PWM techniques are compared in detail in [111] and [112]. Among the various PWM techniques, SPWM is a basic and most commonly used technique. It generates the switching signals for the converter by comparing a sinusoidal signal representing the phase voltage with the carrier signal [113]. In two-level VSI with SPWM technique, a higher switching frequency causes the output voltage and current to be more sinusoidal and clean with respect to harmonics. On the other hand, a higher switching frequency increases the losses. For higher voltage application, multi-level configuration has been proposed for VSI [102, 114-118]. For a two-level VSI with SPWM modulation, the relationship between DC voltage and AC side voltages is as follows [33]:

$$2\sqrt{\frac{2}{3}} V_{L-L} \leq V_{DC} \tag{2.7}$$

where V_{DC} and V_{L-L} are DC bus voltage and line-line voltage of AC side of the inverter, respectively.

The DC link capacitor provides a low impedance path for the ripple current caused by the inverter switching frequency. Several factors such as overall inverter cost and magnitude of current ripple determine the size of the DC capacitor. Two control modes, either voltage control or current control, can be implemented in the VSI. In voltage control mode, the AC terminal voltage of VSI follows the reference voltage in the controller whereas in current control mode, the inverter currents track the current reference values. Several advantages such as better dynamic characteristics and capability for limiting the inherent current in fault situation make the current control mode more efficient for grid-connected PV applications in comparison with voltage control.

2.4.3 Filter

Using the VSI for converting DC power of solar system to AC power causes harmonics due to switching frequency. Typically, VSI switching frequency is chosen between 2 kHz and 15 kHz. This high harmonic can disturb other equipment and affect the voltages and currents [119]. Hence, in order to improve the power quality, the VSI is connected to the PCC through a filter. It should be noted that the type of filter influences the control parameters in control plant. The filter parameters are determined as a tradeoff between the harmonics injection and operation range of the controller. Most common filters for grid-connected application of the VSI are LC and LCL filters [120, 121]. LC filter is a second order filter whereas LCL filter is a third order filter. In comparison with LC filter, LCL filter has better performance in removing the harmonics. However, due to more poles and zeroes, the use of LCL filter makes the control plant more complicated [122]. To mitigate the resonance problem of LC and LCL filters, a resistor is connected with filter capacitor in series. Figure 2.8 illustrates the LCL filter of a grid-connected VSI.

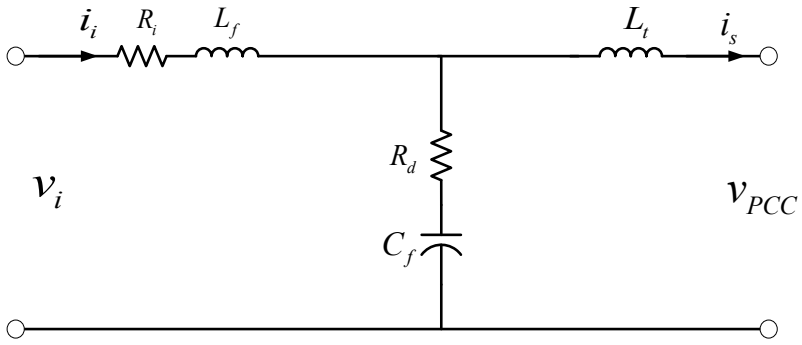

Figure 2-7: Model of LCL filter in a grid-connected VSI

In Figure 2-8, R_i represents the sum of IGBT resistor in ON-state and the internal resistance of the filter inductor. L_f represents the filter inductor which is connected to the inverter in series. C_f represents the filter capacitor which is connected in series with damping resistor (R_d). Both are connected in shunt between filter inductor and transformer (L_t). Filter parameters are determined based on several factors such as the harmonics of output current, the resonance frequency of LCL filter, voltage drop of filter inductance and reactive power compensation provided by the filter capacitor. Generally, to limit the VSI current ripple, the reactance of the filter inductor is selected between 0.1 to 0.25 pu [99]. The typical value of the current ripple is 10% of the inverter current peak [120, 123]. The voltage drop across the filter inductor can limit the voltage control by the VSI. Therefore, the voltage drop across the filter inductor should not exceed 0.3 pu. Otherwise a higher DC link voltage is needed to produce a specific AC voltage. Also, the amount of reactive power generated by the filter capacitor influences the reactive power compensation by the VSI. Hence, the filter capacitor value is designed to limit the reactive power exchange below 0.05 pu of the inverter power rate [123]. To avoid resonance between filter capacitor and inductor, a damping resistor is added to filter capacitor in series [124]. The inductance of the filter inductor is obtained by:

$$L_f = \frac{(V_{dc} - V_{grid,peak}) \times D}{2 \times i_{ripple} \times f_{sw}} \tag{2.8}$$

where V_{dc} is DC-link voltage, $V_{grid,peak}$ is peak value of the AC side voltage, D is modulation index, i_{ripple} is the acceptable value of ripple current and f_{sw} is switching frequency. It should be noted that the calculated admittance of the inductor should satisfy (2.9).

$$0.1 X_{base} < X_f < 0.25 X_{base} \tag{2.9}$$

As discussed above, the reactive power of filter capacitor should not exceed 5% of inverter capacity. Therefore, filter capacitor can be determined by:

$$X_c = \frac{1}{C_f \omega} \geq \frac{V_{ac,L-L}^2}{0.05 \times Q_n} \qquad \text{or} \qquad C_f \leq \frac{0.05 \times Q_n}{\omega \times V_{ac,L-L}^2} \tag{2.10}$$

In (2.10), C_f is the capacitance of the filter capacitor, ω is the nominal angular frequency, Q_n is nominal reactive power of the inverter and $V_{ac,L-L}$ is *rms* value of line-to-line voltage of the inverter. Based on components described in Figure 2-7, the resonance frequency can be obtained as below:

$$f_r = \frac{1}{2\pi} \sqrt{\frac{L_t + L_f}{L_f L_t C_f}} \tag{2.11}$$

The resonance frequency should be checked at the last stage of the design to satisfy the following condition [125]:

$$10 f_0 < f_r < 0.5 f_{sw} \tag{2.12}$$

To avoid resonance between the inductor and capacitor, a proper resistance should be added in series with capacitor. Based on [123, 126, 127], the resistor can be chosen as one third of the admittance of the capacitor at resonance frequency. Hence,

$$R_d = \frac{1}{3 \times \omega_r \times C_f} \tag{2.13}$$

2.4.4 Isolation Transformer

In North America, to connect PV system to any feeder above 208V, an isolation transformer is a necessity. An isolation transformer provides galvanic separation of the PV system from the utility network, in addition to transformation of voltage. On the other hand, to meet IEEE 1547 standard, some utility companies require PV inverters to have a ground at AC side of VSI [25]. The transformer and grounding configuration have an effect on the behavior of the system during the fault. One of the common faults in distribution system is single-to-line ground (SLG) fault. The SLG fault causes a temporary overvoltage (TOV) to appear on the distribution line which can be potentially dangerous for the connected power system equipment. One of the common methods to mitigate TOV is grounding of the transformer neutral terminal. As solid grounding in the distribution system leads to flow of large fault current through the neutral point, utilities traditionally mitigate TOV by means of "effective grounding" technique [128]. Based on this technique, the impedance ratio between zero sequence impedance and positive sequence reactance is as below:

$$0 \le \frac{X_0}{X_1} \le 3 \quad , \quad 0 \le \frac{R_0}{X_1} \le 1 \tag{2.14}$$

The most common configuration of transformer for PV system isolation is Delta-Wye. The Delta-Wye configuration provides full galvanic isolation between primary and secondary with ground fault protection. Also, by applying Delta at PV side, the zero order harmonic of PV currents such as 3rd and 9th harmonics circulate in the delta winding and do not percolate into the utility network [129].

2.5 Smart PV Inverter Control

In this section, the smart inverter control of a PV system is presented. Smart PV inverter control implies a multifunctional control of a PV inverter in addition to its prime purpose of real power generation. The smart PV inverter is a Voltage Source Converter (VSC) system with the capability of exchanging (injecting or absorbing) both active power and reactive power. Figure 2-8 illustrates the scheme of the smart PV inverter control in *d-q* frame. The structure of the controller is based on controlling active power and reactive

power through phase angle and voltage amplitude, respectively. In *d-q* reference frame, due to decoupled control, *d*- axis current loop controls active power and *q*-axis current control loop controls reactive power. The references value for the both current control loops are defined based on the smart inverter operation mode and control objectives.

This smart inverter control provides STATCOM functionality with reactive power exchange (both injection and absorption), besides real power generation. The smart inverter control utilizes the capacity of the inverter remaining after real power generation, for functioning as a STATCOM. This mode of operation is termed as "Partial STATCOM". However, if the reactive power requirement exceeds the remaining inverter capacity, the smart inverter control shuts down the real power generation temporarily, and transforms the PV inverter to operate as a STATCOM utilizing the entire inverter capacity. This mode of operation is termed as "Full STATCOM". Both the Partial and Full STATCOM modes of operation are utilized for providing voltage control (VC) and power factor correction (PFC). If the PV solar system is not operating as STATCOM (either in Partial or Full mode) during daytime, the operating mode is denoted as Full PV mode of operation.

It should be noted that the controller can follow any one of the objectives at a given time. Hence, the reference signal of *q*-axis control loop is defined by either PCC voltage controller or power factor correction unit. The reference of *d*-axis control loop varies based on PV solar system operating modes. When the smart inverter operates in full PV or partial STATCOM mode during daytime, the reference value of *d*-axis control loop has an appropriately high value to generate specific active power whereas during nighttime the reference value is small to only keep the DC capacitor charged. In the final stage, the PWM unit converts the modulation indices to six switching pulses and applies them to the IGBT gates of VSC. As the controller scheme is in the *d-q* frame reference, a PLL is used to generate the phase angle for transferring parameters from *abc* frame to *dq* frame and vice versa. Figure 2-8 depicts the smart inverter control which includes the PLL unit, *dq/abc* and *abc/dq* transformation units, current controllers, DC voltage controller, AC voltage controller, power factor correction unit and PWM unit.

2.5.1 *abc* to *dq* transform

In *abc*- frame and *αβ*-frame, the reference, feedback, and feed-forward signals are sinusoidal functions of time. In *dq*-frame sinusoidal signals are transformed to equivalent DC signals which are independent of time variation. Consequently, the compensator can be designed with better dynamics and is capable of having zero steady-state error by applying an integral term. The smart PV inverter controller is modeled in a synchronously rotating *d-q* reference frame to achieve better transient and steady-state performances. Figure 2-9 shows the phase diagram of a vector in *abc*- frame and *dq*-frame. In Figure 2-9, the vector *f(t)* rotates with time-variant frequency $\omega(t)$ in *abc*-frame. The phase difference between the rotating vector *f(t)* and stationary axes in *abc*-frame is defined by $\theta(t)$ whereas θ_0 indicates the initial phase angle. To achieve non-time-variant parameters, *dq*-frame needs to rotate with same frequency $\omega(t)$. In Figure 2-9, $\varphi(t)$ is phase difference between *abc*-frame and *dq*- frame whereas $\rho(t)$ is phase difference between rotating vector and rotating *dq*-frame.

The transformation between *abc*-frame and *dq*-frame can be written as [33]:

$$\begin{bmatrix} f_d(t) \\ f_q(t) \end{bmatrix} = \frac{2}{3} C\left[\varphi(t)\right] \begin{bmatrix} f_a(t) \\ f_b(t) \\ f_c(t) \end{bmatrix} \quad , \quad \begin{bmatrix} f_a(t) \\ f_b(t) \\ f_c(t) \end{bmatrix} = C\left[\varphi(t)\right]^T \begin{bmatrix} f_d(t) \\ f_q(t) \end{bmatrix}$$

$$C\left[\varphi(t)\right] = \begin{bmatrix} \cos\left[\varphi(t)\right] & \cos\left[\varphi(t) - \frac{2\pi}{3}\right] & \cos\left[\varphi(t) + \frac{2\pi}{3}\right] \\ -\sin\left[\varphi(t)\right] & -\sin\left[\varphi(t) - \frac{2\pi}{3}\right] & -\sin\left[\varphi(t) + \frac{2\pi}{3}\right] \end{bmatrix} \tag{2.15}$$

$$C\left[\varphi(t)\right]^T = \begin{pmatrix} \cos\left[\varphi(t)\right] & -\sin\left[\varphi(t)\right] \\ \cos\left[\varphi(t) - \frac{2\pi}{3}\right] & -\sin\left[\varphi(t) - \frac{2\pi}{3}\right] \\ \cos\left[\varphi(t) + \frac{2\pi}{3}\right] & -\sin\left[\varphi(t) + \frac{2\pi}{3}\right] \end{pmatrix}$$

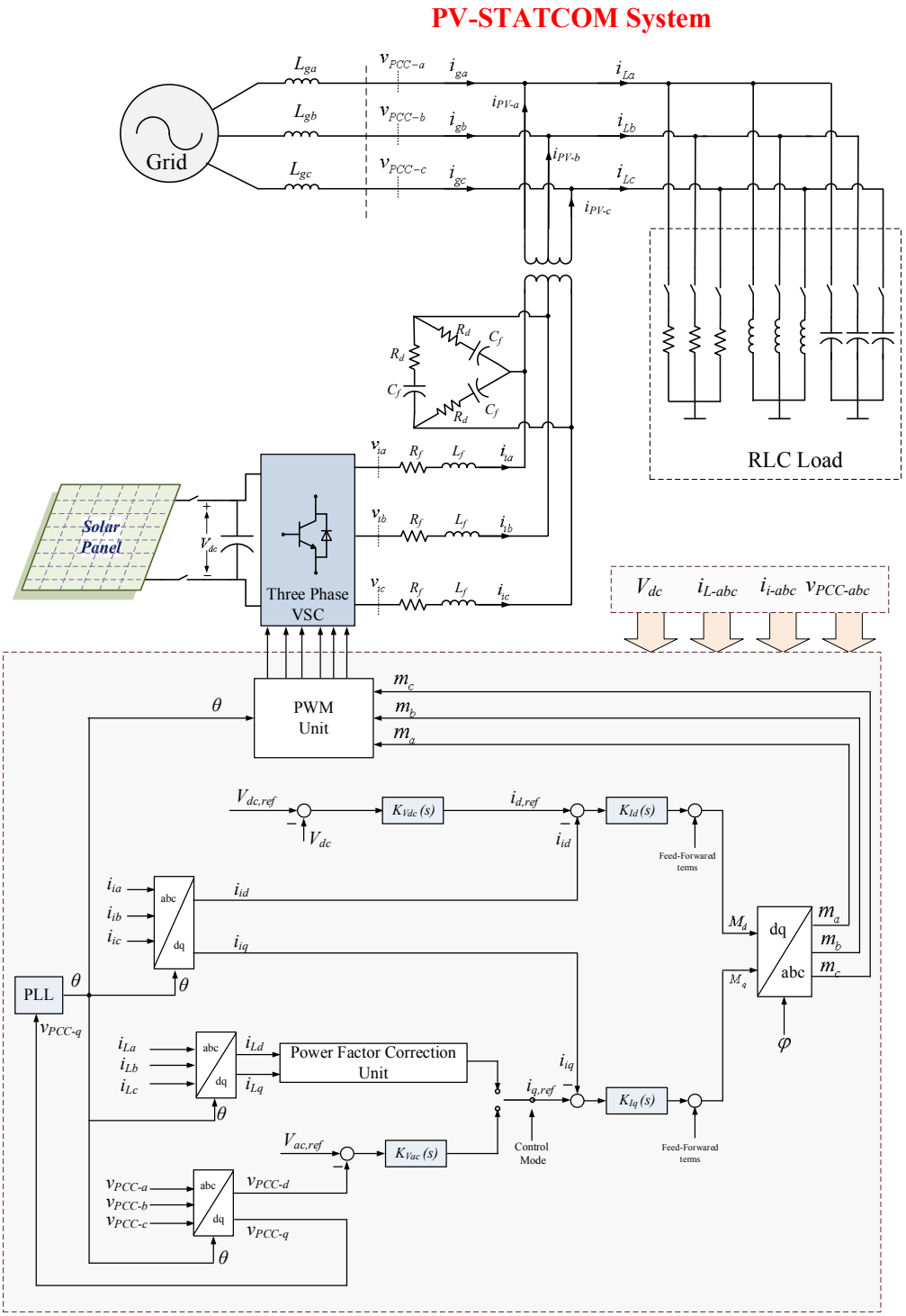

Figure 2-8: Control scheme of a Smart PV Inverter

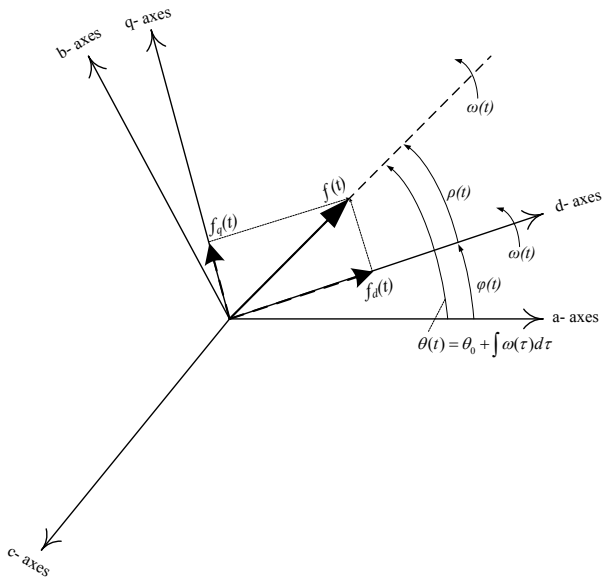

Figure 2-9: Phasor diagram of a parameter in *abc* and *dq* frames

where superscript *T* denotes matrix transposition. The smart PV control uses (2.15) to transform PCC voltage, inverter current and load current from *abc* to *dq* frame. Also, at the end stage of control plant, the modulation indices need to be transformed from *dq*-frame to *abc*-frame of reference.

2.5.2 Phase Locked Loop (PLL)

In Figure 2-9, consider the space phasor $f(t) = \hat{f}\, e^{j(\omega t+\theta_0)}$ which is changing with time in *abc*-frame. By choosing $\varphi(t) = \omega t$ the transformation in *dq*-frame can be written as:

$$f_d + j\, f_q = \hat{f}\, e^{j(\omega t+\theta_0)}\, e^{-j\omega t} = \hat{f}\, e^{j\theta_0} \tag{2.16}$$

The above equation confirms that both *d* and *q* components are DC quantities. In other words, by extracting the frequency of the signal and using in *abc* to *dq* transformation, the *d* and *q* components can be achieved as DC quantities. As per pervious discussion, the DC quantities bring the advantages of having simpler controllers with lower order dynamics. It should be noted that the error of frequency observation affects the response accuracy and stability of the control system. Hence, extracting the signal frequency can be considered an

important part of the control strategy. In power systems and FACTS Control, a Phase Locked Loop (PLL) is used as a common method of obtaining phase and frequency [130-134]. As synchronization process is a necessity for a grid-connected PV system, the smart PV inverter control uses PLL to synchronize the PV inverter system with grid in phase and frequency. Also, the PLL unit extracts the phase angle of PCC voltage for use in the control plant.

2.5.2.1 Open Loop PLL ($\alpha\beta$ PLL)

$\alpha\beta$ PLL is considered as an open-loop technique which uses the filtering method to obtain the phase angle of the grid bus voltage in $\alpha\beta$ - frame [135]. The $\alpha\beta$ - frame is a Cartesian coordinate system which is used to express three-phase system with two quadratic components. Transformation between *abc*-frame and $\alpha\beta$ -frame is given as:

$$\begin{pmatrix} f_\alpha(t) \\ f_\beta(t) \end{pmatrix} = \frac{2}{3} E \begin{pmatrix} f_a(t) \\ f_b(t) \\ f_c(t) \end{pmatrix} \quad , \quad \begin{pmatrix} f_a(t) \\ f_b(t) \\ f_c(t) \end{pmatrix} = E^T \begin{pmatrix} f_\alpha(t) \\ f_\beta(t) \end{pmatrix}$$

$$E = \begin{pmatrix} 1 & -\frac{1}{2} & -\frac{1}{2} \\ 0 & \frac{\sqrt{3}}{2} & -\frac{\sqrt{3}}{2} \end{pmatrix} \quad , \quad E^T = \begin{pmatrix} 1 & 0 \\ -\frac{1}{2} & \frac{\sqrt{3}}{2} \\ -\frac{1}{2} & -\frac{\sqrt{3}}{2} \end{pmatrix} \tag{2.17}$$

Figure 2-10 illustrates the phase angle detection through the open-loop $\alpha\beta$ method. In open-loop $\alpha\beta$ method, the PCC voltages are transformed from *abc*-frame to $\alpha\beta$ -frame by (2.17). In the next step, $\alpha\beta$ components are filtered through low pass filter to remove any distortion. Also, the phase compensator unit is used in order to compensate the phase lag of the low pass filter. The outputs of this method are applied to *abc-dq* transformation units. The performance of the low pass filter determines the efficiency of this method. If the cut-off frequency is chosen low, the filter causes a considerable delay although rejecting more distortion.

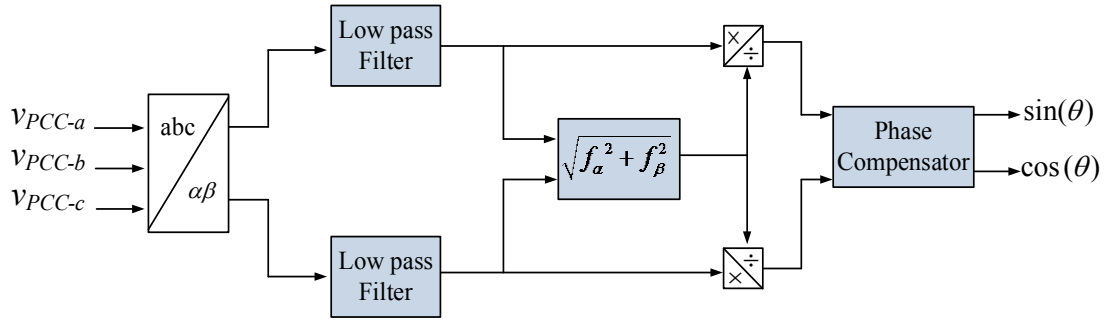

Figure 2-10: Open-loop PLL diagram

On the other hand, with a higher cut-off frequency, the open loop method will track the phase angle faster however, in presence of more distortion. Therefore, there is a trade-off between accuracy and speed of the method which defines the cut-off frequency. Also, this method is sensitive to base frequency. It means that if the base frequency (e.g. 60 Hz) gets changed during system operation, the open-loop method will not be able to track the phase angle.

2.5.2.2 SYNCHRONOUS REFERENCE FRAME (SRF)-PLL

By considering Figure 2-8, the PCC voltages can be expressed as:

$$\begin{aligned} V_{pcc-a} &= \hat{V}\cos(\omega_0 t + \theta_0) \\ V_{pcc-b} &= \hat{V}\cos(\omega_0 t + \theta_0 - \frac{2\pi}{3}) \\ V_{pcc-c} &= \hat{V}\cos(\omega_0 t + \theta_0 + \frac{2\pi}{3}) \end{aligned} \tag{2.18}$$

where $\hat{V}$ is the amplitude of PCC phase voltage, ω_0 is the system frequency and θ_0 is initial phase angle of the AC system. The PCC voltage components in *dq*-frame are as:

$$\begin{aligned} V_{pcc-d} &= \hat{V}\cos(\omega_0 t + \theta_0 - \varphi) \\ V_{pcc-q} &= \hat{V}\sin(\omega_0 t + \theta_0 - \varphi) \\ \frac{d\varphi}{dt} &= \omega(t) \end{aligned} \tag{2.19}$$

Based on the previous discussion, phase angle φ should be selected somehow to avoid any time- variant function in *dq* components. Let us assume $\varphi = \omega_0 t + \theta_0$ then $V_{pcc-d} = \hat{V}$ and $V_{pcc-q} = 0$. This results in *dq* components to be pure DC quantities based on (2.19). Therefore, regulating V_{pcc-q} to zero will be lead to DC components in *dq*-frame. This is the fundamental mechanism of three phase SRF-PLL. The basic structure of SRF-PLL is shown in Figure 2-11. The objective of PLL control schematic is to keep V_{pcc-q} at zero. A low pass filter with transfer function $G_{filter}(s)$ is used after *abc* to *dq* transformation block to extract the DC value of V_{pcc-q}. K_{pll} is the controller transfer function to regulate φ at $\omega_0 t + \theta_0$. The Voltage-Controlled Oscillator (VCO) block is a resettable integrator which converts frequency to phase angle based on (2.19). The VCO output φ is reset to zero whenever it reaches to 2π. It should be noted that if PLL tracks the phase angle properly V_{pcc-d} would be equal to the magnitude of PCC phase voltage base on (2.19).

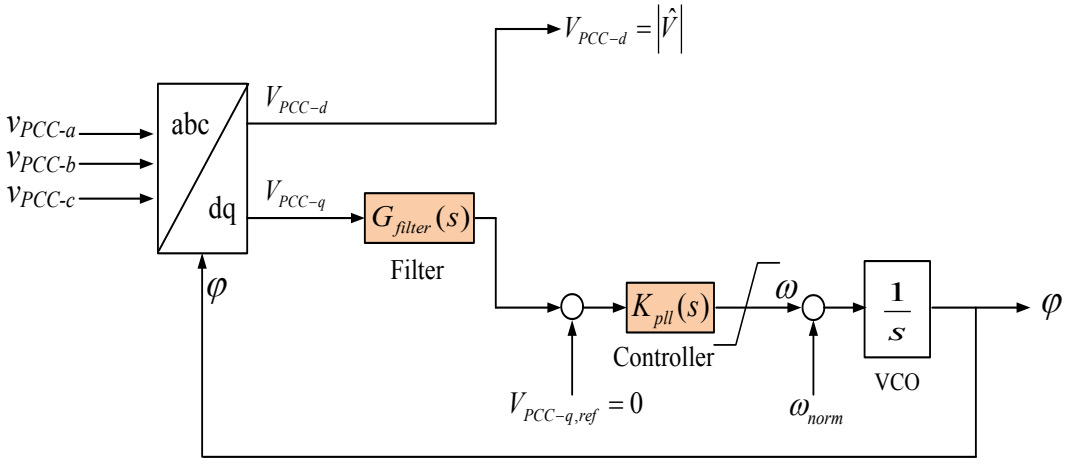

Figure 2-11: Structure of SRF-PLL

In Figure 2-11;

$$\omega(t) = K_{pll}\, G_{filter}\, V_{pcc-q}(t) \tag{2.20}$$

$$G_{filter}(s) = \frac{1}{1 + T_f s} \tag{2.21}$$

Substituting (2.19) in (2.20) gives:

$$\frac{d\varphi}{dt} = K_{pll}\,\mathcal{L}^{-1}\left(G_{filter}(s)\right)\hat{V}\sin\left(\omega_0 t + \theta_0 - \varphi\right) \tag{2.22}$$

In (2.22) to prevent improper response due to the nonlinear characteristics, the initial frequency is considered close to nominal frequency, and also, a limiter is applied to control loop after the controller. In SRF-PLL $\left(\omega_0 t + \theta_0 - \varphi\right)$ has a very small value. Consequently, $\sin\left(\omega_0 t + \theta_0 - \varphi\right) \simeq \left(\omega_0 t + \theta_0 - \varphi\right)$. Considering $\omega_0 t + \theta_0$ as a reference angle which is tracked by φ, (2.22) can be rewritten as:

$$\begin{aligned} &\frac{d\varphi}{dt} = \hat{V}\,K_{pll}\,\mathcal{L}^{-1}\left(G_{filter}(s)\right)\left(\varphi_{ref} - \varphi\right) \\ &\varphi_{ref} = \omega_0 t + \theta_0 \end{aligned} \tag{2.23}$$

Figure 2-12 illustrates the block diagram of PLL control based on (2.23).

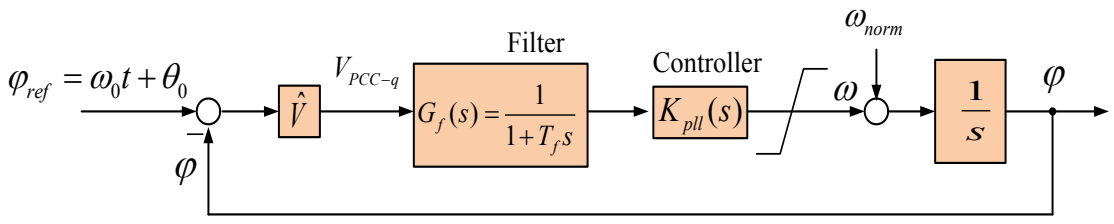

Figure 2-12: SRF-PLL structure with PI controller

2.5.3 Real and Reactive Current Control

In this section, the control structure of the inverter current for both real and reactive components is discussed. The active and reactive powers outputs of the inverter in *dq*-frame are calculated by [33]:

$$P_s(t) = \frac{3}{2}\left(V_{pcc-d}(t)\,I_{sd}(t) + V_{pcc-q}(t)\,I_{sq}(t)\right) \tag{2.24}$$

$$Q_s(t) = \frac{3}{2}\left(-V_{pcc-d}(t)\,I_{sq}(t) + V_{pcc-q}(t)\,I_{sd}(t)\right) \tag{2.25}$$

where $V_{pcc-d}(t)$ and $V_{pcc-q}(t)$ are PCC voltages in *dq*-frame, and $I_{sd}(t)$ and $I_{sq}(t)$ are inverter output currents in *dq*-frame. As PLL unit ensures that the phase angle is locked to the PCC voltages angle, therefore based on (2.19) $V_{pcc-d} = \hat{V}$ and $V_{pcc-q} = 0$. Consequently, (2.24) and (2.25) can be rewritten as:

$$P_s(t) = \frac{3}{2} V_{pcc-d}(t)\, I_{sd}(t) \tag{2.26}$$

$$Q_s(t) = -\frac{3}{2} V_{pcc-d}(t)\, I_{sq}(t) \tag{2.27}$$

Equations (2.26) and (2.27) reveal that at a certain PCC voltage, the active power and reactive power outputs of the inverter can be controlled by $I_{sd}(t)$ and $I_{sq}(t)$, respectively. Therefore, PLL plays a vital role in decoupling the control of active and reactive powers. From Figure 2-8, the dynamics of the AC side of the inverter are described as below:

$$\vec{V}_i = R\vec{i}_i + L\frac{d\vec{i}_i}{dt} + \vec{V}_{pcc} \tag{2.28}$$

Based on (2.18), (2.19) and (2.28), the equations in *dq*-frame can be written as:

$$L\frac{di_{id}}{dt} = L\omega(t)\, i_{iq} - Ri_{id} + V_{id} - V_{pcc-d} \tag{2.29}$$

$$L\frac{di_{iq}}{dt} = -L\omega(t)\, i_{id} - Ri_{iq} + V_{iq} - V_{pcc-q} \tag{2.30}$$

In steady-state, the PLL locks on the phase angle of PCC voltage leading to $V_{pcc-d} = \hat{V}$ and $V_{pcc-q} = 0$. Hence, $\omega(t) = \omega_0$ in (2.29) and (2.30). For the two-level VSC with SPWM the converter AC-side terminal voltage $V_{i,abc}$ is controlled as below:

$$v_{i,abc} = \frac{V_{DC}}{2}\, m_{abc} \tag{2.31}$$

where V_{DC} and m_{abc} are DC bus voltage and modulation waveforms in *abc*-frame respectively. Equation (2.31) in *dq*-frame can be written as:

$$V_{i,dq} = \frac{V_{DC}}{2} M_{dq} \tag{2.32}$$

Substituting (2.32) in (2.29),

$$L\frac{di_{id}}{dt} + Ri_{id} = L\omega_0 i_{iq} + \frac{V_{DC}}{2} M_d - V_{pcc-d} \tag{2.33}$$

$$L\frac{di_{iq}}{dt} + Ri_{iq} = -L\omega_0 i_{id} + \frac{V_{DC}}{2} M_q - V_{pcc-q} \tag{2.34}$$

Equations (2.33) and (2.34) reveal that due to the terms $L\omega_0 i_{id}$ and $L\omega_0 i_{iq}$, the dynamics of i_{id} and i_{iq} are coupled and also the system is nonlinear. This nonlinearity and coupling can be avoided in the control if two new control inputs, u_d and u_q, are defined as

$$L\frac{di_{id}}{dt} + Ri_{id} = u_d \tag{2.35}$$

$$L\frac{di_{iq}}{dt} + Ri_{iq} = u_q \tag{2.36}$$

Above equations show that i_{id} and i_{iq} are controlled by u_d and u_q signals. To obtain decoupled dynamics, feed-forward terms should be added to both u_d and u_q signals to achieve PWM modulation indices in *d-q* frame. Based on (2.33)-(2.38), the modulation indices can be obtained by:

$$M_d = \frac{2}{V_{DC}}\left(u_d - L_f\omega_0 i_{iq} + V_{pcc-d}\right) \tag{2.37}$$

$$M_q = \frac{2}{V_{DC}}\left(u_q + L_f \omega_0 i_{id} + V_{pcc-q}\right) \tag{2.38}$$

Figure 2-13 illustrates the current control of active-reactive power controller on the basis on (2.33)-(2.38). In Figure 2-13, $i_{d,ref}$ and $i_{q,ref}$ represents the active and reactive power references based on (2.26) and (2.27). On the other hand, P_{ref} and Q_{ref} are obtained from the outer loops of the controller based on control objectives (voltage control or power factor correction) and modes of operation. $K_{Id}(s)$ and $K_{Iq}(s)$ are current controllers in *d* and *q* axes, respectively.

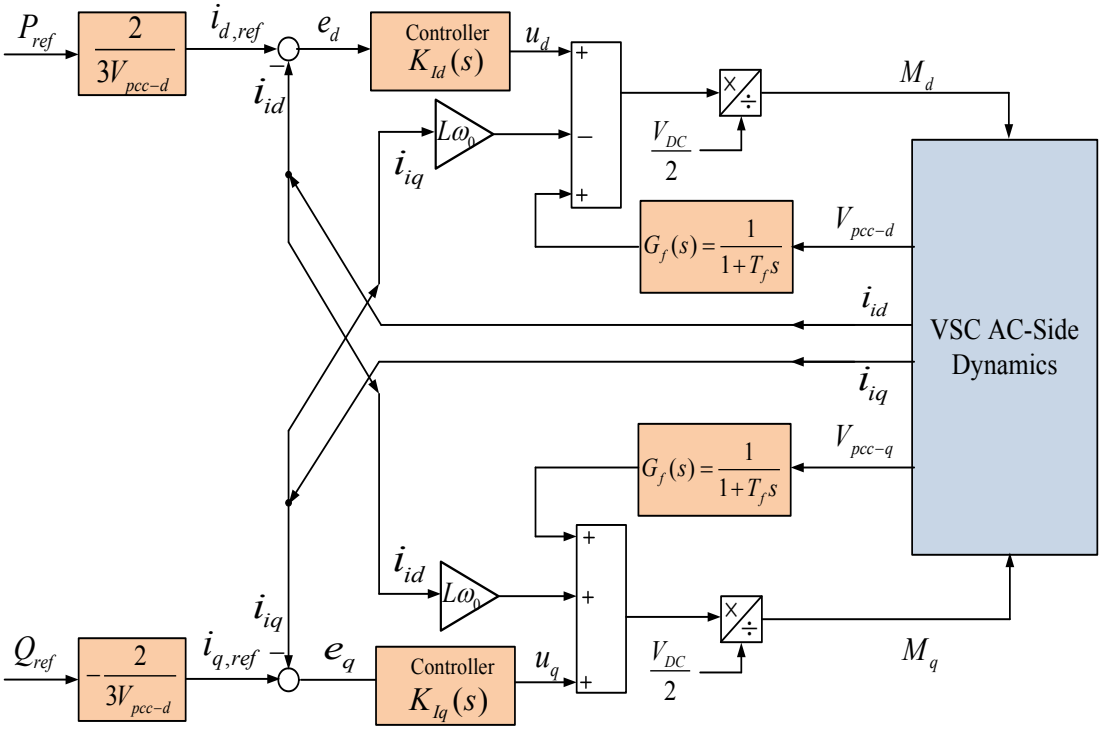

Figure 2-13: Control of active and reactive power in *dq*-frame

Low pass filters are used after feed-forward signals, V_{pcc-d} and V_{pcc-q}, to remove high frequency noise and provide clean DC quantities.

2.5.4 Operation Mode Selector of the Smart PV Inverter Control

During daytime, the smart inverter controller operates as a conventional PV system and generates active power. If control objectives require exchange of reactive power to either regulate the PCC voltage or provide power factor correction, the controller uses the remaining capacity of the inverter for exchanging reactive power. This mode of operation is called “Partial STATCOM Mode”. In this partial mode, the priority of the smart inverter is the generation of the active power and then exchange of reactive power with remaining inverter capacity. But during transients or faults the grid needs more reactive power support to maintain the voltage within an acceptable range. Consequently, the smart PV control disconnects the DC switches of solar panel and transforms the PV inverter to full STATCOM to exchange reactive power with the full capacity of the inverter. This mode of the smart PV control is termed “Full STATCOM Mode”. It should be noted that in full STATCOM mode, voltage regulation is considered as the sole control objective. In the proposed patent-pending control [43] in this thesis, the smart PV inverter autonomously determines its operating mode and prioritizes between active power generation and reactive power exchange based on the system requirements, nature of transient/disturbance, time of the day and remaining inverter capacity.

Figure 2-14 shows the flowchart of the smart PV inverter control to define the operation mode. During daytime, the inverter can act as a full PV, full STATCOM or partial STATCOM. Initially, the inverter operates as a PV inverter in conventional real power generation mode. Assume the PV panel is connected to the inverter and the PCC voltage suddenly violates the acceptable range. Based on the control algorithm, the controller immediately disconnects the switches at its DC side and converts the PV system to full STATCOM. During full STATCOM mode, the control objective is set to Voltage Regulation (VR) automatically and it cannot be changed to power factor correction (PFC). When fault is cleared, the reactive power output of the inverter is negligible. Hence, the controller realizes the fault status by checking DC switch status and reactive power output of the inverter. After fault has been cleared, the controller reconnects the solar panel to the inverter and operates again in full PV mode.

When the solar panel is connected to the inverter and utility needs to either regulate the voltage within acceptable range or correct the power factor, the remaining inverter capacity is used for exchanging reactive power. In other words, the reactive power requirement is limited by:

$$Q_{\max} = \sqrt{S^2 - P^2} \tag{2.39}$$

where S is apparent power of the inverter, P is actual power of the inverter. During night-time, the DC switch disconnects the solar panel from the inverter. Therefore, the control mode is full STATCOM. But the voltage changes can occur transiently or in steady-state. When PCC voltage is in acceptable range, the control objective can be either voltage regulation or power factor correction. But when the voltage violates the defined range due to transient events, e.g., Temporary Over Voltage TOV), the controller objective is set to voltage regulation and operates with its full capacity. Same as daytime, the controller realizes the fault has been cleared by reactive power output and previous state of its operation.

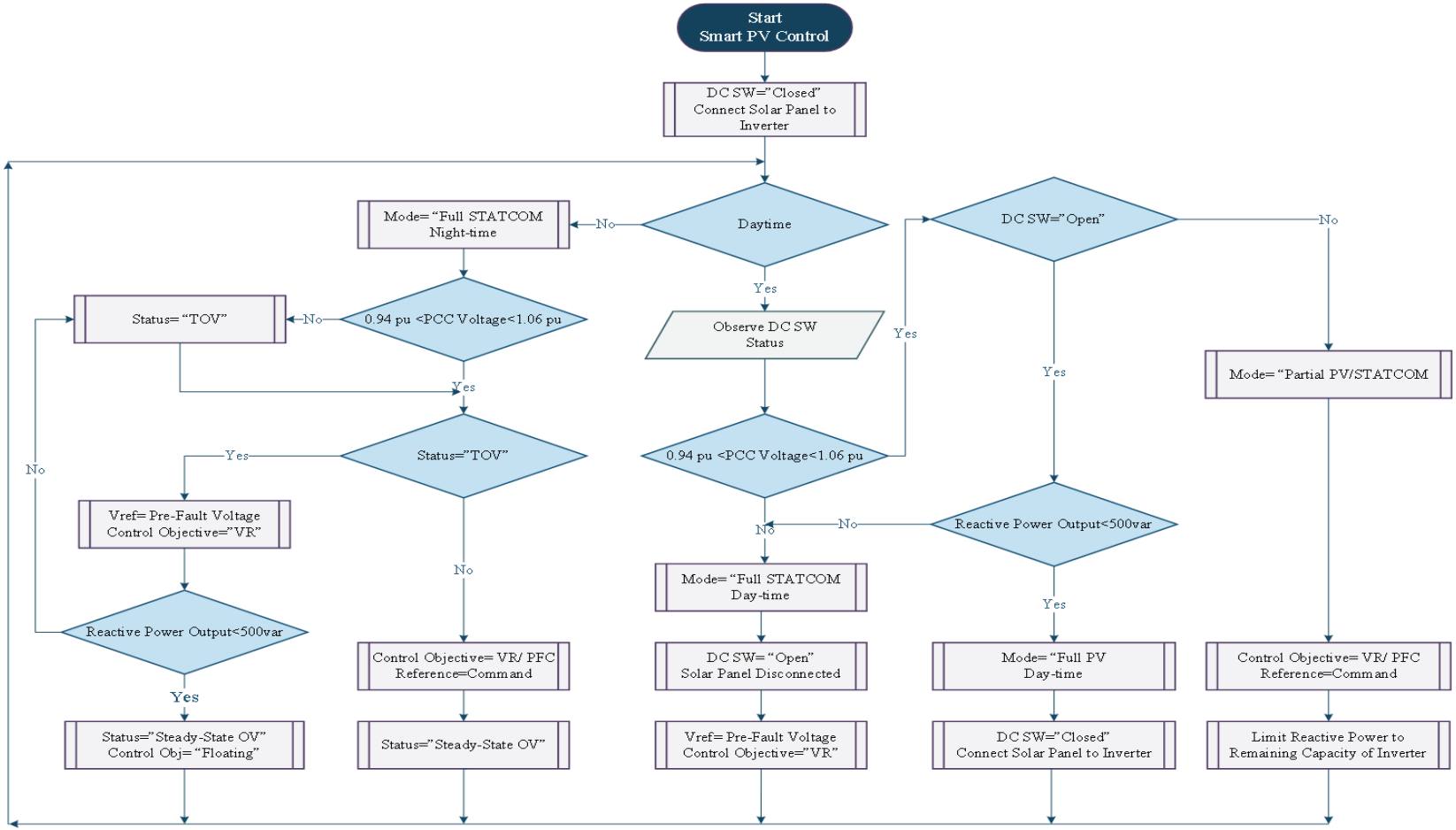

Figure 2-14: Flowchart of the smart PV inverter operating modes

2.5.5 DC Voltage Control Loop

As the inverter switches are not ideal, the DC link voltage provides real power to compensate the power loss of the switches. Consequently, the DC link capacitor is discharged, gradually. Hence, the inverter needs to absorb small amount of active power to keep DC link capacitor charged. When sun is available, the smart inverter control utilizes a small amount of solar power to keep the capacitor charged, while the rest of the solar power is injected into the grid. In absence of solar power (i.e. during night-time), the smart inverter control absorbs a small amount of real power from the grid and charges the capacitor through the inverter diodes. In Figure 2-8, the power balance at DC side can be shown as:

$$P_{PV} = P_{dc-cap} + P_{dc} \tag{2.40}$$

where P_{PV}, P_{dc-cap} and P_{dc} are PV panel power, DC-link capacitor power and DC side power of the VSC. PV panel power can be expressed in terms of PV current and voltage, as:

$$P_{PV} = I_{PV} V_{PV} \tag{2.41}$$

As in Figure 2-8, $V_{PV} = V_{dc}$ and also by substituting I_{PV} from (2.4), (2.41) can be rewritten as:

$$P_{PV} = n_p I_{sc} V_{dc} - n_p I_0 V_{dc} \left[e^{\left(\frac{qV_{dc}}{kTn_s}\right)} - 1 \right] \tag{2.42}$$

Equation (2.42) reveals that PV power varies as a non-linear function of V_{dc}. As described earlier, PV power depends on three main factors, irradiance, temperature and DC-link voltage. Hence PV power can be shown as a non-linear function of those factors.

$$P_{PV} = f(R, T, V_{dc}) \tag{2.43}$$

where *R* and *T* represent irradiance and temperature factors respectively.

Also, by ignoring the VSC loss, the DC side power of VSC can be considered equal to the power on the AC side. Thus,

$$P_{dc} \approx P_{ac} = P_R + P_L + P_i \tag{2.44}$$

In (2.44) P_R is the power loss in the resistor of the inductor circuit, P_L is the power loss of the inductor and P_i is the active power exchanged with the grid. Due to a small amount of loss in resistor and inductor, P_R and P_L can be neglected. Hence, it can be assumed $P_{ac} \approx P_i$. By considering (2.43) and (2.44), (2.40) can be rewritten as:

$$P_{dc-cap} = f(R,T,V_{dc}) - P_i \tag{2.45}$$

As $P_{dc-cap} = \frac{d}{dt}\left(\frac{1}{2}CV_{dc}^2\right)$ and based on (2.26), $P_i = \frac{3}{2}V_{pcc-d}I_{sd}$.

Hence (2.45) is converted as:

$$\frac{C}{2}\frac{d}{dt}\left(V_{dc}^2\right) = f(R,T,V_{dc}) - \frac{3}{2}V_{pcc-d}I_{sd} \tag{2.46}$$

In (2.46), V_{dc}^2 is the output, I_{sd} is control input and $f(R,T,V_{dc})$ is the disturbance input. Equivalently, as discussed it can be obtained:

$$I_{sd}(s) = G_{id}(s)I_{sd,ref}(s) \tag{2.47}$$

where $G_{id}(s)$ is the transfer function of closed-loop current loop. Thus,

$$\frac{d}{dt}\left(V_{dc}^2\right) = \frac{2}{C}\left(f(R,T,V_{dc}) - \frac{3}{2}V_{pcc-d}\mathcal{L}^{-1}\left(G_{id}(s)\right)I_{sd,ref}\right) \tag{2.48}$$

By ignoring the non-linear term $f(R,T,V_{dc})$, (2.48) becomes a linear system based on V_{dc}^2 and $I_{d,ref}$. However, the non-linear term is added as a feed-forward term to offset the solar power effect [136].

Therefore, the open-loop transfer function of DC voltage control can be written as:

$$G_{dc}(s)=\frac{V_{dc}^2}{I_{sd,ref}}=-\frac{3}{C}V_{pcc-d}\frac{1}{s(\sigma_{i,d}s+1)} \tag{2.49}$$

Figure 2-15 illustrates the block diagram of DC-bus voltage controller based on (2.48). It reveals that the non-linear term $f(R,T,V_{dc})$ can be added to the control plant as a feed-forward to implement (2.48).

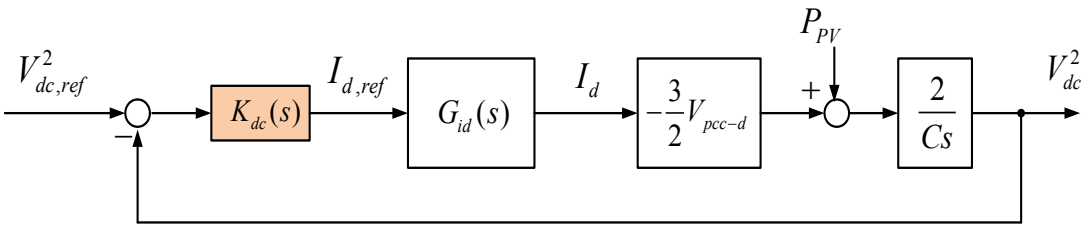

Figure 2-15: Block diagram of DC-bus voltage controller

It should be noted that in the STATCOM mode, the external active power source is zero. Therefore, P_{PV} is considered zero in Figure 2-15. In other words, the DC loop transfer function is converted to linear system when PV power is zero.

2.5.6 Reactive Power Control

In Figure 2-8, the reactive current reference, $i_{q,ref}$, is obtained based on the control objectives in both partial STATCOM and full STATCOM operation modes. The $i_{q,ref}$ represents a certain reactive power value to regulate the PCC voltage or correct the power factor. It should be noted that in PV operation mode the inverter is utilized to generate only active power. Hence, the reference of reactive power should be zero during the full PV operation mode.

2.5.6.1 Voltage Control

Depending on the loading conditions and line reactance, the PCC voltage can change beyond acceptable levels. Therefore, it is needed to regulate the voltage in present of load variations. In Figure 2-8, the PCC voltage and grid current can be written as:

$$V_{PCC,abc} = L_g \frac{di_{g,abc}}{dt} + V_{g,abc} \tag{2.50}$$

$$i_{g,abc} = i_{L,abc} - i_{PV,abc} \tag{2.51}$$

where $V_{PCC,abc}$ is PCC voltage in *abc*-frame, $i_{g,abc}$ is grid current, $V_{g,abc}$ is grid voltage, $i_{PV,abc}$ is current output of the PV system and $i_{L,abc}$ is load current.

$$\begin{aligned} V_{pcc-d} &= -L_g \omega i_{gq} + L_g \frac{di_{gd}}{dt} + \hat{V}\cos(\omega_0 t + \theta_0 - \varphi) \\ V_{pcc-q} &= L_g \omega i_{gd} + L_g \frac{di_{gq}}{dt} + \hat{V}\sin(\omega_0 t + \theta_0 - \varphi) \end{aligned} \tag{2.52}$$

By ignoring the transient variation of PLL, let us assume $\varphi = \omega_0 t + \theta_0$ and $\omega = \omega_0$. Subsequently (2.52) can be rewritten as:

$$\begin{aligned} V_{pcc-d} &= -L_g \omega_0 i_{gq} + L_g \frac{di_{gd}}{dt} + \hat{V} \\ V_{pcc-q} &= L_g \omega_0 i_{gd} + L_g \frac{di_{gq}}{dt} \end{aligned} \tag{2.53}$$

It should be noted V_{pcc-q} is controlled at zero level by PLL controller, and so, V_{pcc-d} represents the PCC voltage. By neglecting the current of the shunt filter capacitor,

$$i_{g,dq} = i_{L,dq} - i_{i,dq} \tag{2.54}$$

Therefore, the PCC voltage can be achieved by:

$$V_{pcc-d} = L_g \omega_0 i_{iq} - L_g \omega_0 i_{Lq} - L_g \frac{di_{id}}{dt} + L_g \frac{di_{Ld}}{dt} + \hat{V} \tag{2.55}$$

2.5.6.2 Reactive current reference unit for Power Factor Correction

The concept of power factor correction is to compensate some or all of the reactive power required by the load. In the other words, the smart inverter controller exchanges (generates/ absorbs) reactive power based on the reactive power consumption of the load. Consequently, the phase angle between PCC voltage and grid current is decreased and the grid power factor at PCC point is improved. Figure 2-16 illustrates the phasor diagram of the grid current and PCC voltage. Assume the grid current i_g has a leading phase angle corresponding to the PCC voltage V_{pcc}. As discussed before, the PLL locks the phase angle to place PCC voltage along *d*-axis thereby rendering $V_{pcc-d} = \hat{V}$ and $V_{pcc-q} = 0$. As $PF = \cos\delta$, the phase difference δ between voltage and current needs to be decreased to improve the power factor.

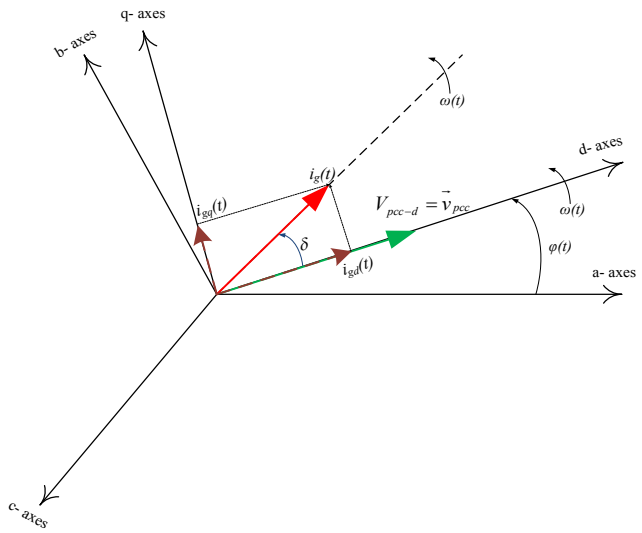

Figure 2-16: Phasor diagram of current and voltage of grid in *abc* and *dq*-frame

Figure 2-16 reveals that:

$$\tan\delta = \frac{i_{gq}}{i_{gd}} \tag{2.56}$$

By substituting $\delta = \cos(PF^{-1})$ in (2.56),

$$\tan(\cos^{-1} PF) = \frac{i_{gq}}{i_{gd}} \tag{2.57}$$

With reference to Figure 2-8, the relationship between grid, PV and load currents is given by:

$$i_{gdq} = i_{Ldq} - i_{PV,dq} \tag{2.58}$$

Also, the total reactive current of PV-STATCOM system is the sum of inverter current and the current of the filter capacitor.

$$i_{PV,q} = i_{iq} + i_{cq} \tag{2.59}$$

where i_{cq} is the reactive current (or total current) of filter capacitor. Substituting (2.58) and (2.59) in (2.57) results in,

$$\tan(\cos^{-1} PF) = \frac{i_{Lq} - i_{iq} - i_{cq}}{i_{Ld} - i_{PV,d}} \tag{2.60}$$

To achieve a specific power factor, the reference reactive current is obtained as below:

$$i_{iq} = i_{Lq} - \left(\tan(\cos^{-1} PF) \times (i_{Ld} - i_{PV,d})\right) - i_{cq} \tag{2.61}$$

Figure 2-17 illustrates the structure of power factor unit for generating reactive current reference when the objective of smart inverter control is power factor correction. The Power Factor Correction (PFC) unit generates the reactive current reference, $i_{q,ref}$, based on reference power factor PF_{ref}, real and reactive current drawn by the load ($i_{Ld,ref}$ and $i_{Lq,ref}$) and filter capacitor current (i_{cq}).

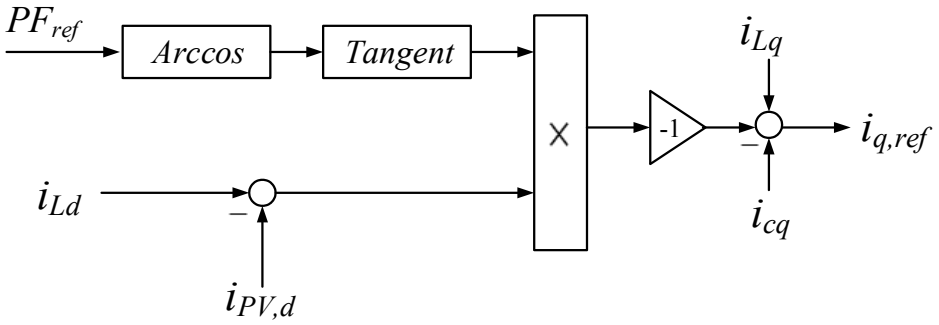

Figure 2-17: Structure of power factor unit

2.5.7 PWM unit

The pulse width modulation (PWM) unit generates six switching pulses by using PLL output, phase angle, and PWM reference signals in *dq*-frame. Two PWM reference signals, M_d and M_q, are converted to *abc*-frame by phase angle output of the PLL unit. Three PWM reference signals in *abc*-frame are compared with fixed frequency triangular carriers to generate the gate pulses of VSI switches. Figure 2-18 shows the PWM unit structure for obtaining gate pulses. The carrier frequency, which represents the switching frequency of the inverter, is chosen to be 10 kHz.

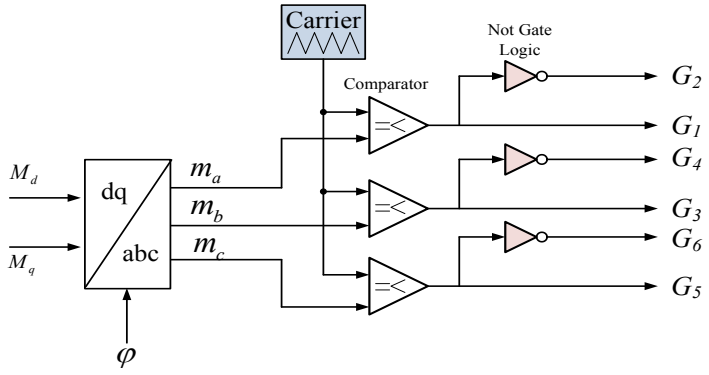

Figure 2-18: Structure of PWM unit

2.6 Modeling of Study System and Design of Smart Inverter Controller

The objective of this thesis is to design, develop and test a Smart PV Inverter control for a 10 kW PV solar system already installed in the network of the Bluewater Power, Sarnia, Ontario. This section describes the model of the study system in Bluewater Power, and the design of all the components of the smart inverter for the 10 kW PV solar system.

2.6.1 Bluewater Power Distribution Network

The Bluewater network is modeled as a Thevenin's equivalent voltage source behind its short circuit impedance. The Bluewater feeder as a study system is modeled with a 208V (L-L) voltage source with *X/R* ratio of 3. The Bluewater network parameters are given in Appendix A. 1.

2.6.2 Passive Load

In this thesis, the electrical load connected to the 10 kW PV solar system is considered as a 10 kVA constant-impedance static RLC load. Although the power consumption by the load varies as a function of the voltage, for a nominal voltage of 208/120 V, the total load remains 10 kVA: 10 kW if purely resistive, 10 kVar if purely inductive/capacitive or total 10kVA if resistive-inductive, etc.

2.6.3 PV Panels

In this case study, a 10 kW PV system is connected to the PCC. The PV array consists of several modules. PV panel parameters are given in Appendix A. 2. It should be noted that for MPPT control of this particular PV panel, it is assumed that the panel voltage is within the control range of the DC controller. Therefore, the need of DC/DC converter is neglected in all studies in this thesis.

2.6.4 PV Inverter

In this study, the PV system is equipped with a 10 kVA two-level six-pule IGBT-based VSI with SPWM technique. As a tradeoff between losses and harmonics generation, the switching frequency of the inverter is chosen 10 kHz for SPWM technique. It should be

noted that by considering turn-off and turn-on time of the IGBT gate, the dead-time delay has been chosen $1\mu s$ to avoid shoot-through of the IGBT switches in an inverter leg [137, 138]. The parameters of the IGBT switches, DC link capacitor and inverter are provided in Appendix A. 3.

2.6.5 Harmonics Filter

To mitigate the harmonics generated by switching frequency, an LCL filter is used to refine the current and voltage output of the inverter. Equations (2.8)-(2.13) are used to design the filter parameters. By considering 10% current ripple ($i_{ripple} = 0.1 \times I_{inverter,peak}$) and assuming ripple occurs at *D=0.5*, substituting system parameters in (2.8), the filter inductance is calculated as:

$$L_f = \frac{(400-200)\times 0.5}{2\times 0.1\times 40\times 10000} = 0.00125 \text{ mH} \tag{2.62}$$

The reactance value is chosen $L_f = 1.2$ mH and it is used to check the condition in (2.9).

$$\mathrm{X}_f = 2\pi f_0 L_f = 2\times\pi\times 60\times 0.00125 = 0.47\ \Omega \tag{2.63}$$

and

$$\mathrm{X}_b = \frac{V_{b,L-L}^2}{P_b} = \frac{(208)^2}{10000} = 4.326\ \ \Omega \tag{2.64}$$

By comparing (2.63) and (2.64), the admittance of calculated filter inductor is approximately 0.11 *pu* and thus the condition in (2.9) is satisfied.

Based on (2.10),

$$C_f \le \frac{0.05\times 10000}{377\times(208)^2} = 31\,\mu F \tag{2.65}$$

Hence, the filter capacitor is chosen $C_f = 30\,\mu F$.

Assuming the leakage impedance of the transformer to be about 0.1 *pu,* the resonance frequency would be:

$$f_r = \frac{1}{2\pi}\sqrt{\frac{2}{L_f C_f}} = \frac{1}{2\pi}\sqrt{\frac{2}{1.2\times10^{-3}\times30\times10^{-6}}} = 1186.3\,\text{Hz} \tag{2.66}$$

Equation (2.67) reveals that the calculated resonance frequency is in the valid range per (2.12).

$$600\,\text{Hz} < f_r = 1186.3\,\text{Hz} < 5000\,\text{Hz} \tag{2.67}$$

In the last stage of the filter design, the damping resistor is designed based on (2.13).

$$R_d = \frac{1}{3\times2\times\pi\times f_r\times C_f} = \frac{1}{6\times\pi\times1186.3\times30\times10^{-6}} = 1.49\ \Omega \tag{2.68}$$

Therefore, filter parameters are obtained as $L_f = 1.2$ mH, $C_f = 30\,\mu F$ and $R_d = 1.49\ \Omega$.

2.6.6 Transformer

In this study, a 10 kVA Delta-Wye grounded transformer is used for isolation of PV system from the distribution system. In other words, the inverter terminals are connected to Delta side and PCC connected to Wye side. The transformer has a unity ratio and it is used only for isolation purpose. The transformer parameters are provided in Appendix A. 4.

2.7 Design of Smart Inverter Controller for the Study System

This section presents the design of smart PV inverter controller for the study system in Bluewater network.

2.7.1 PLL Design

In the smart PV control plant, the three phase SRF-PLL is used. In this section, the design of the PLL is presented based on the principles in previous section. The Bluewater network

operates with 60 Hz and 208 V line-to-line voltage. Therefore peak AC voltage is obtained by:

$$\hat{V} = \sqrt{2}\left(\frac{V_{L-L}}{\sqrt{3}}\right) = \sqrt{\frac{2}{3}} \times 208 = 169.83 \tag{2.69}$$

Also, to remove higher harmonics of the measurement, the time constant of the filter in (2.21) is considered as $T_f = 1\ ms$. In Figure 2-12, the open loop transfer function without compensation is:

$$G_{PLL}(s) = \frac{\hat{V}}{s(1+T_f s)} \tag{2.70}$$

Equation (2.70) reveals that the transfer function has a pole at $s = 0$. Hence, the "symmetrical optimum" technique is used to design the PI controller [139]. The *PI* control is assumed as below:

$$K_{PLL}(s) = k_{PLL,gain}\frac{s + z_{PLL}}{s} \tag{2.71}$$

Then, by considering (2.70) and (2.71), the open loop transfer function is transformed in present of the controller as:

$$H_{PLL}(s) = K_{PLL}(s) \times G_{PLL}(s) = \frac{\hat{V} \times k_{PLL,gain}}{T_f}\left(\frac{s + z_{PLL}}{s + T_f^{-1}}\right)\frac{1}{s^2} \tag{2.72}$$

At low frequency $\angle H_{PLL}(j\omega) \approx 180^\circ$ due to the double pole at $s = 0$. By assuming $z_{PLL} < T_f^{-1}$, the angle of $\angle H(j\omega)$ is decreased by the Zero of the function when the frequency is increased. This decrement continues till it reaches to maximum angle δ_m at the certain frequency ω_m. Therefore, if the cross-over frequency ω_c is chosen at ω_m then δ_m will be the phase margin of the function in (2.72). The maximum phase margin δ_m and ω_m are obtained as:

$$\delta_m = \sin^{-1}\left(\frac{1 - T_f\, z_{PLL}}{1 + T_f\, z_{PLL}}\right) \tag{2.73}$$

$$\omega_c = \omega_m = \sqrt{T_f^{-1}\, z_{PLL}} \tag{2.74}$$

Technically, δ_m is chosen between 30° and 75° to achieve faster response and a reasonable phase margin. By using (2.73) and (2.74), the parameters of the *PI* controller can be obtained as below:

$$z_{PLL} = \frac{1 - \sin(\delta_m)}{\left[1 + \sin(\delta_m)\right] T_f} \tag{2.75}$$

$$\omega_c = \sqrt{T_f^{-1}\, z_{PLL}} \tag{2.76}$$

$$k_{PLL} = \frac{\omega_c}{\hat{V}} \tag{2.77}$$

Before obtaining the controller parameters, first the uncompensated open loop function needs to be analyzed. Figure 2-19 illustrates the Bode diagram of uncompensated system in (2.70).

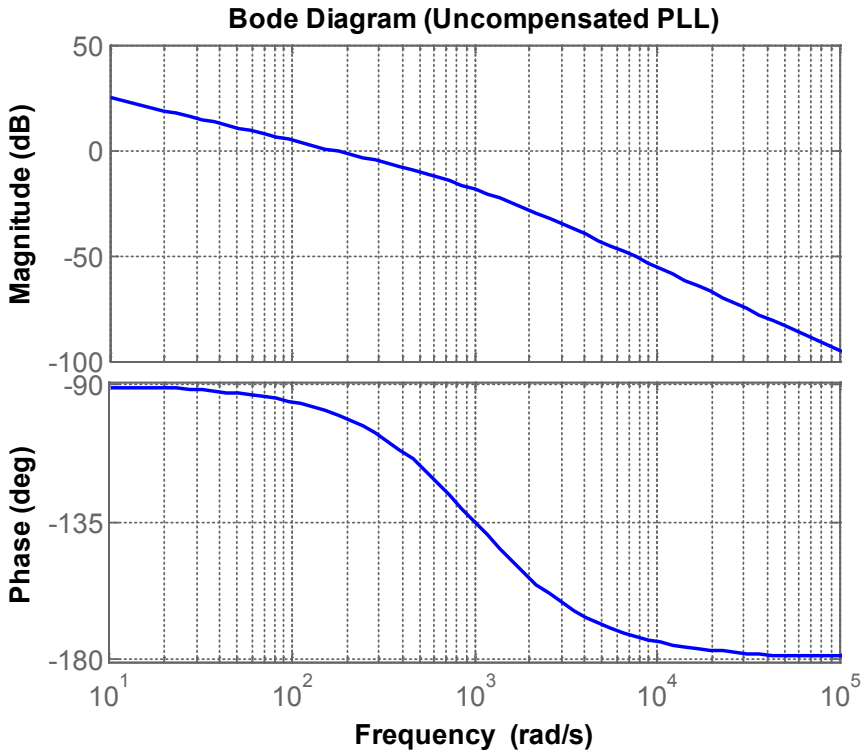

Figure 2-19: Bode diagram of uncompensated PLL transfer function

Figure 2-19 reveals that the uncompensated system is stable but the PI controller makes the control system faster and more reliable. Although PI controller reduces the steady-state error and response time, it affects the stability margin. Therefore, a trade-off has to be made. To achieve better control performance, the phase margin is chosen $\delta_m = 60^\circ$. For the chosen δ_m, T_f and $\hat{V}$ as well as using (2.75)-(2.77), the *PI* controller parameters for the PLL are obtained as below:

$$\begin{cases} \delta_m = 60^\circ \\ T_f = 0.001s \\ \hat{V} = 169.83V \end{cases} \Rightarrow \begin{cases} z_{PLL} = 71.8 \\ \omega_c = 268 \text{ rad/s} \\ k_{PLL} = 1.577 \end{cases} \tag{2.78}$$

Applying the control parameter values in (2.72), the transfer function of the compensated system can be written as:

$$H_{PLL}(s) = \ 2.68\times10^{5}\left(\frac{s+71.8}{s+1000}\right)\frac{1}{s^{2}} \tag{2.79}$$

The Bode diagram of the compensated PLL system represented by $K_{PLL}(s)$ shown in Figure 2-20. It demonstrates that the controller parameters are designed correctly and $\delta_m = 60^{\circ}$ is exactly achieved at $\omega_c = 268$ rad/s.

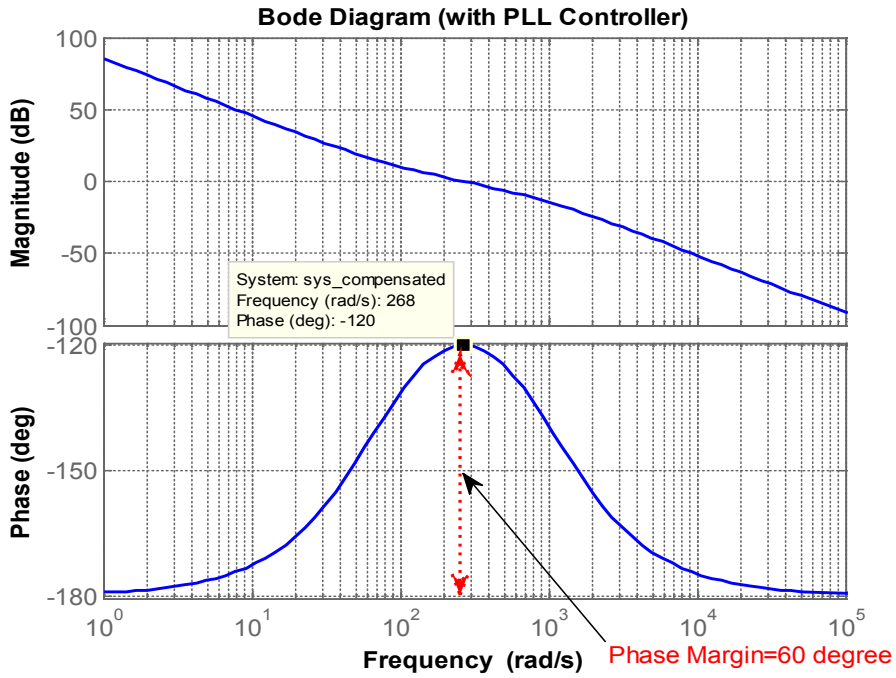

Figure 2-20: Bode diagram of the compensated PLL control loop

2.7.2 Design of Current Controller

In (2.33) and (2.34), the current components and control signals can be considered as the controller inputs and controller output, respectively. For achieving a proper modulating signal, the feed-forward terms are added to the controller signals based on (2.37) and (2.38). Hence, the uncompensated open-loop transfer functions of current control are:

$$\frac{u_d}{i_{id}} = \frac{1}{L_f s + R_f} \tag{2.80}$$

$$\frac{u_q}{i_{iq}} = \frac{1}{L_f s + R_f} \tag{2.81}$$

Figure 2-21 illustrates the *d-q* current control loop with a compensator. (2.80) and (2.81) reveal that the dynamic equations of current in *d-q* frame are stable. Thus, a *PI* controller can be used to make the steady-state error zero and decrease the response time. To reduce the response time, it needs to move the transfer function pole farther from origin of the real-imaginary coordinates.

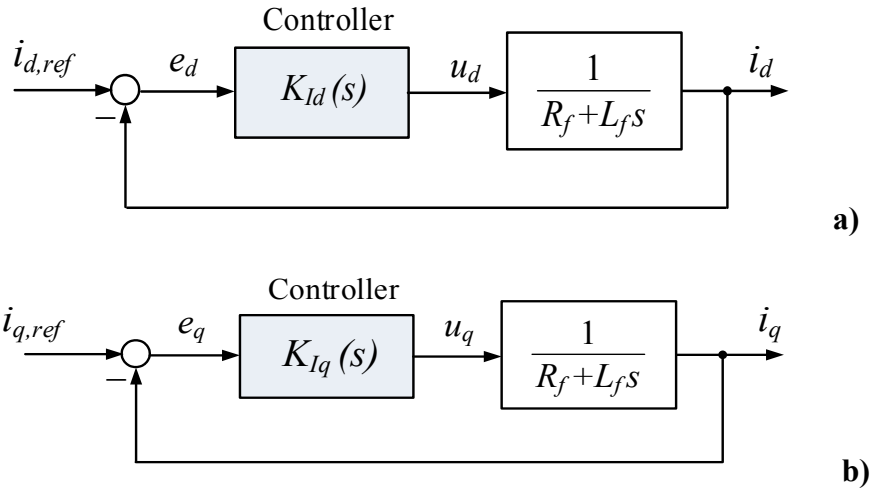

Figure 2-21: Current loop with PI controller

a) *d*-Component control loop b) *q*-component control loop

It can be achieved by choosing the control parameters as:

$$K_{Id}(s) = \frac{k_{p,d} s + k_{I,d}}{s} \tag{2.82}$$

$$K_{Iq}(s) = \frac{k_{p,q} s + k_{I,q}}{s} \tag{2.83}$$

where

$$k_{p,dq} = \frac{L}{\sigma_{i,dq}} \tag{2.84}$$

$$k_{I,dq} = \frac{R}{\sigma_{i,dq}} \tag{2.85}$$

In (2.84) and (2.85), $\sigma_{i,dq}$ is the time constant for *d*-control and *q*-control loops to shift the transfer function pole. It is practically between 0.5 *ms* to 5 *ms*. It should be noted that different time constants can be used for *d*-control and *q*-control loops to provide different response times for those two loops. Based on design parameters, $L = 1.2\,\text{mH}$ and $R = 1\ \text{m}\Omega.$. Also, the time constant for both loops is chosen *1 ms*. Therefore,

$$k_{p,dq} = \frac{1.2\times10^{-3}}{1\times10^{-3}} = 1.2 \ , \qquad k_{I,dq} = \frac{1\times10^{-3}}{1\times10^{-3}} = 1 \tag{2.86}$$

The closed-loop transfer function of the compensated control loop is thus given as:

$$G_{Id} = \frac{i_d}{i_{d,ref}} = \frac{1}{1+\sigma_{i,d}s} \tag{2.87}$$

$$G_{Iq} = \frac{i_q}{i_{q,ref}} = \frac{1}{1+\sigma_{i,q}s} \tag{2.88}$$

2.7.3 DC Voltage Controller Design

Equation (2.49) reveals that the uncompensated DC voltage loop is unstable due to the pole on the right hand side of the imaginary axis. For compensating the unstable transfer function, a *PI* controller is considered for the DC voltage controller as below:

$$K_{dc}(s) = k_{dc,gain}\frac{s + z_{dc}}{s} \tag{2.89}$$

Therefore, in presence of the controller, the open loop transfer function is transformed to:

$$H_{dc}(s) = K_{dc}(s) \times G_{dc}(s) = -\frac{3 \times V_{pcc-d} \times k_{dc,gain}}{2 \times \sigma_{i,d}} \left(\frac{s + z_{dc}}{s + \sigma_{i,d}^{-1}}\right)\frac{1}{s^2} \tag{2.90}$$

The DC voltage control loop is considered as an outer loop whereas the *d*-component control loop of the current is the inner loop. Technically, inner loop should be faster than outer loop to ensure stability of the both the control loops. As the compensated system includes two poles in its dynamic equation, the "*symmetrical optimum*" technique can be applied for the DC controller design. As discussed in Section 2.7.1 for PLL design, the control parameters can be obtained as below:

$$z_{dc} = \frac{1 - \sin(\delta_m)}{\left[1 + \sin(\delta_m)\right]\sigma_{i,d}} \tag{2.91}$$

$$\omega_c = \sqrt{\sigma_{i,d}^{-1}\, z_{dc}} \tag{2.92}$$

$$k_{dc,gain} = -\frac{C \times \omega_c}{3 \times V_{pcc-d}} \tag{2.93}$$

By choosing $\delta_m = 50^\circ$ the *PI* controller parameters are obtained as:

$$\begin{cases} \delta_m = 50^\circ \\ \sigma_{i,d} = 0.001s \\ V_{pcc-d} = \hat{V} = 169.83V \end{cases} \Rightarrow \begin{cases} z_{dc} = 132.5 \\ \omega_c = 364 \text{ rad/s} \\ k_{dc} = \text{-}0.0129 \end{cases} \tag{2.94}$$

By substituting the values of the control parameters value, the compensated transfer function is rewritten as:

$$H_{dc}(s) = 3.64\times10^5\left(\frac{s+132.5}{s+1000}\right)\frac{1}{s^2} \tag{2.95}$$

The Bode diagram of the DC voltage loop with the compensator $H_{dc}(s)$ is shown in Figure 2-22. It shows that the controller parameters are designed correctly and $\delta_m = 50^\circ$ is exactly achieved at $\omega_c = 364$ rad/s.

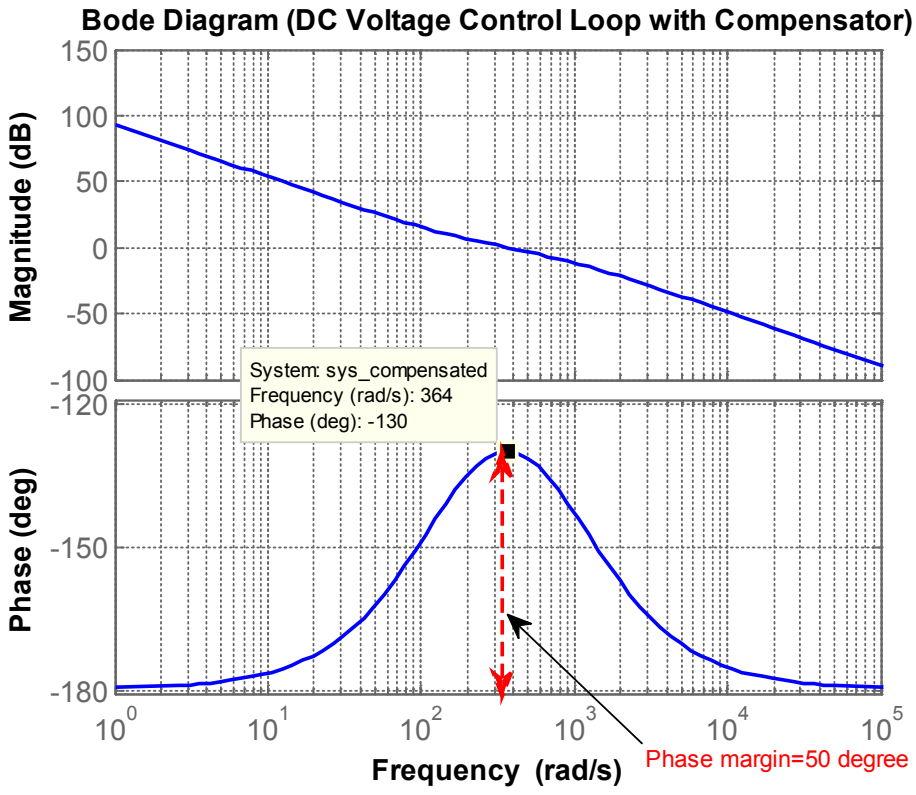

Figure 2-22: Bode diagram of the compensated PLL control loop

2.7.4 Design of AC Voltage Controller

The DC link voltage and active power are controlled by i_{id} whereas i_{iq} controls the PCC voltage and consequently the reactive power. Thus, active power and reactive power are controlled independently. Figure 2-23 illustrates the structure of PCC voltage control loop. The left hand side of (2.55) and the closed loop transfer function of current controller in *q*-axis are defined as the dynamic system for AC voltage controller. Hence, the uncompensated loop for ac voltage can be written as:

$$G_{ac}(s) = G_{iq}(s) \times \left(-L_g \omega_0\right) = \frac{-L_g \omega_0}{1 + \sigma_{i,q} s} \tag{2.96}$$

It should be noted that other terms of (2.55) can be added as feed-forward terms. Equation (2.96) reveals that the uncompensated loop of AC voltage loop is unstable due to negative gain. It should be noted that the AC voltage control loop includes the inner loop which is the current control loop. Therefore, the outer control loop needs to be slower than inner loop. This can be achieved by designing a proper controller to provide smaller bandwidth compared to current control loop. Also, the dynamics of *d*-axis as feed-forward term can be neglected when the current control loop is faster than AC voltage control loop [33].

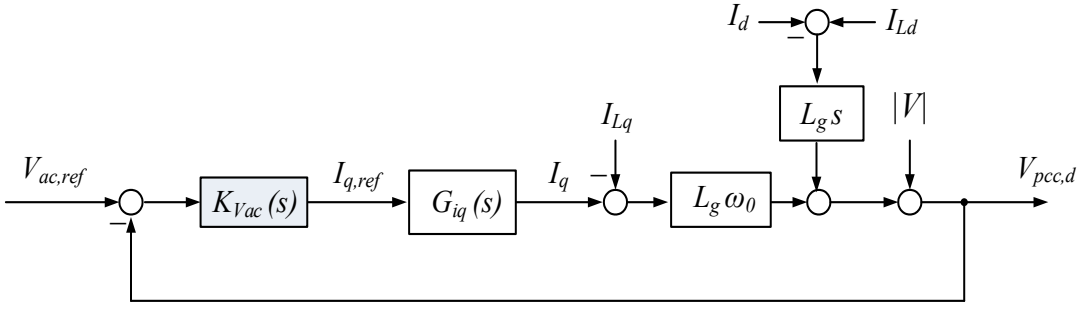

Figure 2-23: Block diagram of PCC voltage control loop

By considering $G_{iq}(s)$ in (2.88), the bandwidth of the inner control loop is given as $\omega_{c,iq} = 1000$ rad/s. The AC voltage controller is chosen as below:

$$K_{ac}(s) = \frac{k_{gain,ac}}{s} \tag{2.97}$$

By choosing $k_{gain,ac} = -222$ the closed-loop bandwidth of AC voltage loop would be $\omega_{c,AC} = 100$ rad/s which is 10 times smaller than current control loop. Figure 2-24 shows the Bode diagram of AC voltage control loop when the controller is applied to the control plant. It is demonstrated that the phase margin of $\delta_{AC} = 84^{\circ}$ will be achieved at the frequency $\omega_{c,AC} = 100$ rad/s .

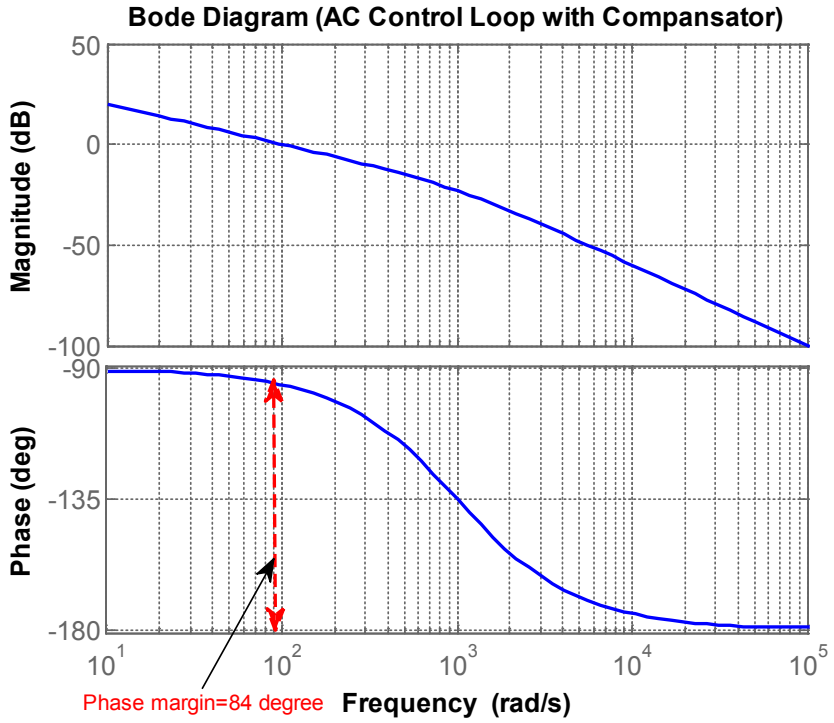

Figure 2-24: Bode diagram of the compensated AC voltage control loop

2.8 Conclusion

This chapter presents the modeling of different components of a typical radial distribution system with a PV solar system. The operating principles of the smart PV inverter are presented for both Partial and Full STATCOM modes, for the two control objectives of

voltage control and power factor correction. The different inverter components and controller parameters are designed for a 10kVA smart PV inverter system to be implemented in the distribution network of the Bluewater Power, Sarnia. The smart inverter controller includes PLL, *abc-dq* transformation block, *d-q* current controller, DC voltage controller, AC bus voltage controller, mode selector unit, power factor correction unit and PWM unit. The design procedure of each component is described for the study system. The controller parameters are designed utilizing classic control theory. The designed controllers are employed in simulation studies in the next chapters.

CHAPTER 3

3 SOFTWARE SIMULATION OF SMART PV INVERTER

3.1 Introduction

This chapter presents the simulation of a PV system with smart inverter controls in a distribution system utilizing the industry grade electromagnetic transients simulation software PSCAD/EMTDC. The study system corresponds to the distribution system of Bluewater Power Distribution Corporation, Sarnia, where a 10 kW PV system is installed on the site, as modeled in Chapter 2. The smart inverter controller follows two different control objectives, voltage control and power factor correction. The different modes of operation of the smart inverter: Full PV, Partial PV-STATCOM, and Full PV-STATCOM, are described. The performance of 10 kW PV solar system with the above smart inverter controls for different operating conditions, is illustrated.

3.2 Study System

Figure 3-1 depicts the study system for the smart inverter control simulation studies. The Bluewater power network is modeled by the short circuit impedance at the point of common coupling (PCC) of the 10 kW PV solar system, which is represented by equivalent resistance R_g and equivalent inductance L_g. Three subsystems are connected to the PCC in order to compare their individual performance. These subsystems are: 10 kVA PV system, 10 kVA STATCOM, and 10 kVA PV-STATCOM. The 10 kVA load comprises a parallel combination of Resistor, Inductor and Capacitor. The different system parameters are provided in Appendix A.

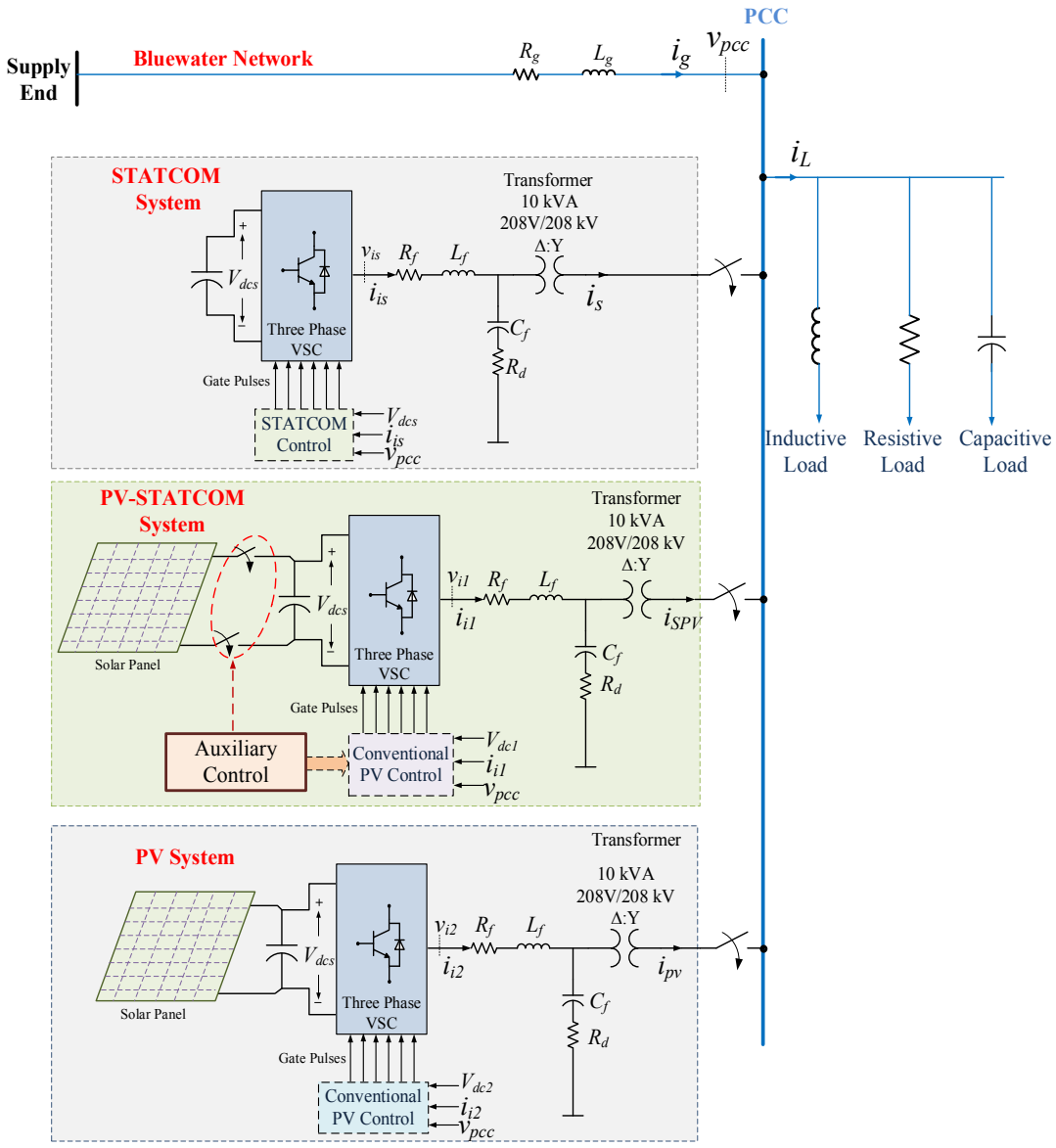

Figure 3-1: Study system

3.3 Simulation Results

The following system studies are conducted to evaluate the performance of the smart inverter in different modes of operation:

i) conventional PV operation during both forward and reverse power flow conditions,

ii) conventional STATCOM operation for reactive power control and voltage regulation,

iii) smart PV inverter operation in "Partial STATCOM" mode for power factor correction and voltage control, and

iv) smart PV inverter operation in "Full STATCOM" mode for voltage control during both forward and reverse power flow conditions.

In all simulation results, the PCC voltage is denoted with v_{pcc}. Grid current and load current are represented by i_{grid} and i_{Load} respectively. Also, the PV system current before and after harmonics filter are represented by $i_{inverter}$ and i_{PV} respectively.

3.3.1 Conventional PV System Operation

In this section, the performance of a conventional PV system (or, smart PV inverter in conventional PV operating mode) is analyzed for forward and reverse power flow. Hence, only the PV subsystem is considered to be connected to the PCC in Figure 3-1, while the other subsystems are disconnected. The forward and reverse power flow conditions are created by an appropriate choice of the PV power and load power. Three events are studied for both forward and reverse power flow scenarios. These are i) connection of PV system, ii) change of power output of PV system, and iii) disconnection of PV system.

3.3.1.1 Forward Power Flow

The active and reactive power loads in Figure 3-1 are considered as 6 kW and 6 kvar, respectively. Initially, the PV system is assumed to generate 3 kW active power. Therefore, a net forward power flow occurs from the grid towards the load. Figure 3-2 (a)-(e) illustrate the PCC voltage v_{pcc}, grid current i_{grid}, PV system current after filter i_{pv}, inverter current before filter $i_{inverter}$ and load current i_{load}, respectively.

At $t=1$ sec the PV system is connected to the grid when it generates 3 kW. The PV current i_{pv} transiently increases and takes about one cycle to stabilize. This transient is also reflected in grid current i_{grid}. Injection of 3 kW of PV power causes the PCC voltage v_{pcc} to rise, resulting in a steady state rise in current i_{load} through constant impedance load,

although after a transient. The inverter filter effectively removes the harmonics in the inverter current $i_{inverter}$.

At *t=1.04* sec, the PV system power changes from 3 kW to 6 kW. This causes PV current i_{pv} and PCC voltage v_{pcc} to rise. The load current i_{load} increases slightly due to rise in PCC voltage, but the grid current i_{grid} decreases since the load is now supplied more by the PV power output.

At *t=1.08* sec, the PV system is disconnected from the PCC. The inverter current $i_{inverter}$ and PV current i_{pv} go to zero instantaneously. The PCC voltage v_{pcc} decreases reducing the load current i_{load} correspondingly. The grid current increases, as it now has to supply the entire load

3.3.1.2 Reverse Power Flow

Figure 3-3 (a)-(c) illustrate the PCC voltage v_{pcc}, grid current i_{grid} and PV system current i_{pv} for PV test during reverse power flow. In this test, the active and reactive load are considered as 1 kW and 1 kvar, respectively.

At *t=1* sec, the PV system is connected to the grid with 3 kW power generation. Hence, the surplus power flows in the reverse direction towards the grid source. The PV current i_{pv} transiently increases and takes more than one cycle to stabilize. However, the sudden power reversal in the grid causes a bigger transient in grid current i_{grid}, as well as in the PCC voltage. The PCC voltage rises due to injection of real power from the PV system.

At *t=1.04* sec, the PV generation increased from 3 kW to 6 kW. This causes PV current i_{pv} and PCC voltage v_{pcc} to rise. The grid current i_{grid} increases in the reverse direction due to PV power generation becoming higher than the required load power.

At *t=1.08* sec, the PV system is disconnected from the PCC. The PV current i_{pv} goes to zero instantaneously. The PCC voltage v_{pcc} decreases slightly and the grid current goes to its initial value before PV system connection.

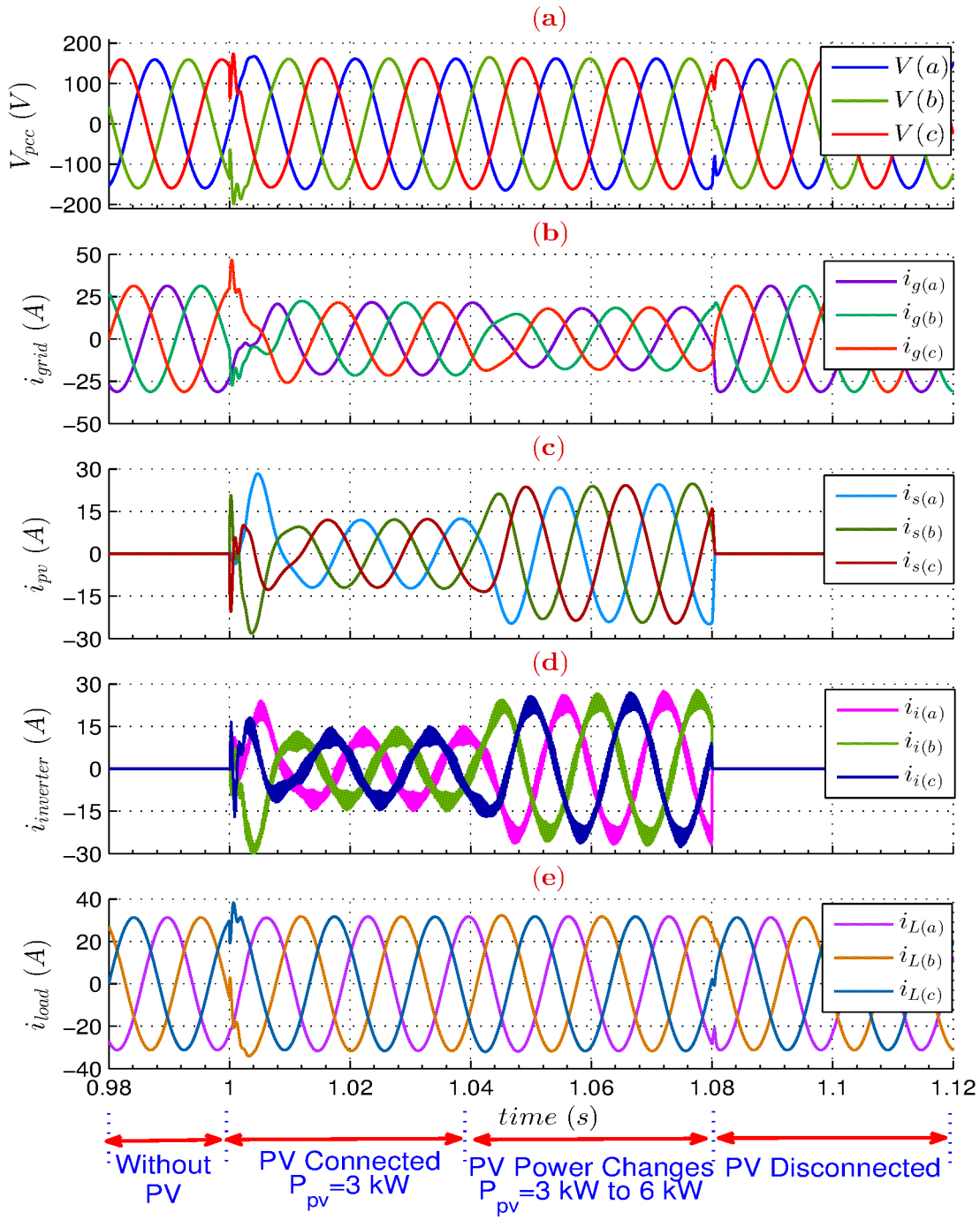

Figure 3-2: Voltage and currents waveforms for full PV operation during forward power flow

a) PCC voltage b) Grid current c) PV current d) Inverter current e) Load current

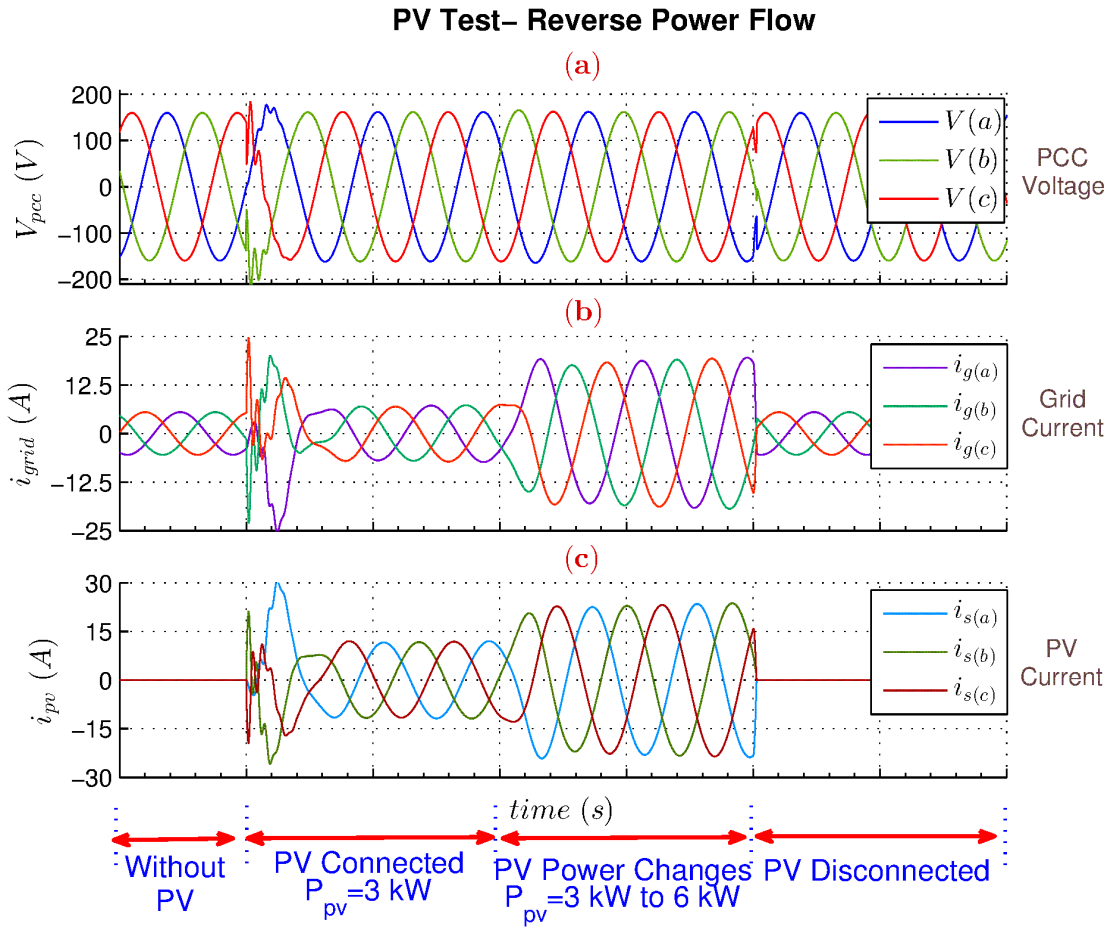

Figure 3-3: Voltage and currents waveforms for full PV operation during reverse power flow

a) PCC voltage b) Grid current c) PV current

3.3.2 STATCOM Operation

In this section, the performance of a conventional STATCOM system is analyzed for voltage control and reactive power control. Therefore, in Figure 3-1 the STATCOM system is connected to the grid whereas PV and PV-STATCOM systems are disconnected. Two tests, reactive power control and voltage control, are performed to show the effects of the STATCOM on the grid.

3.3.2.1 Reactive Power Control

The reactive power control of a STATCOM is presented in this section. For this study, the active and reactive power of the load are considered as 6 kW and 6 kvar, respectively. Figure 3-4 (a)-(c) demonstrate the PCC voltage (v_{pcc}), grid current (i_{grid}) and STATCOM current ($i_{STATCOM}$). Also, Figure 3-5 (a) and (b) illustrate the active and reactive power based on the following events.

At *t=1* sec, STATCOM is connected to the grid while the reactive power reference value is 10 kvar capacitive. Reactive power injection by STATCOM to the grid causes PCC voltage (v_{pcc}) to rise. As some portion of reactive power requirement of the load is supplied by STATCOM, the grid current (i_{grid}) reduces slightly. Active power of the STATCOM ($P_{STATCOM}$) is negligible due to losses of the IGBT switches. Hence, the active power of the load (P_{Load}) is supplied by the grid. Reactive power output of the STATCOM ($Q_{STATCOM}$) is exactly 10 kvar capacitive based on the reference value of the controller. As the reactive power (Q_{Load}) requirement of the load is about 6 kvar inductive, the surplus reactive power of the STATCOM injected to the grid as grid reactive power (Q_{grid}).

At *t=1.04* sec, the controller reference value for reactive power is changed from 10 kvar capacitive to 7.5 kvar inductive. The controller follows the reference value and absorbs 7.5 kvar. Subsequently, the PCC voltage (v_{pcc}) drops significantly after a transient. As both STATCOM and load consume inductive reactive power, the grid current (i_{grid}) is increased to support the load. Also, the phase angle of STATCOM current ($i_{STATCOM}$) changes 180^{o} due to shifting from capacitive to inductive operation mode. Active power of the STATCOM remains at zero level whereas the reactive power of STATCOM ($Q_{STATCOM}$) follows the reference value and changes from 10 kvar capacitive to 7.5 kvar inductive.

At *t=1.08* sec, the reference value of the reactive power changes from 7.5 kvar inductive to 10 kvar capacitive. The results reveal that the PCC voltage increases due to STATCOM reactive power injection. Also, the STATCOM accurately tracks the reference command to provide 10 kvar reactive power.

At *t=1.12* sec, the STATCOM is disconnected from the PCC. The STATCOM current ($i_{STATCOM}$) goes to zero instantaneously. Disconnection of the STATCOM reduces the PCC voltage (v_{pcc}) correspondingly. The grid current increases, as it now has to supply the entire load.

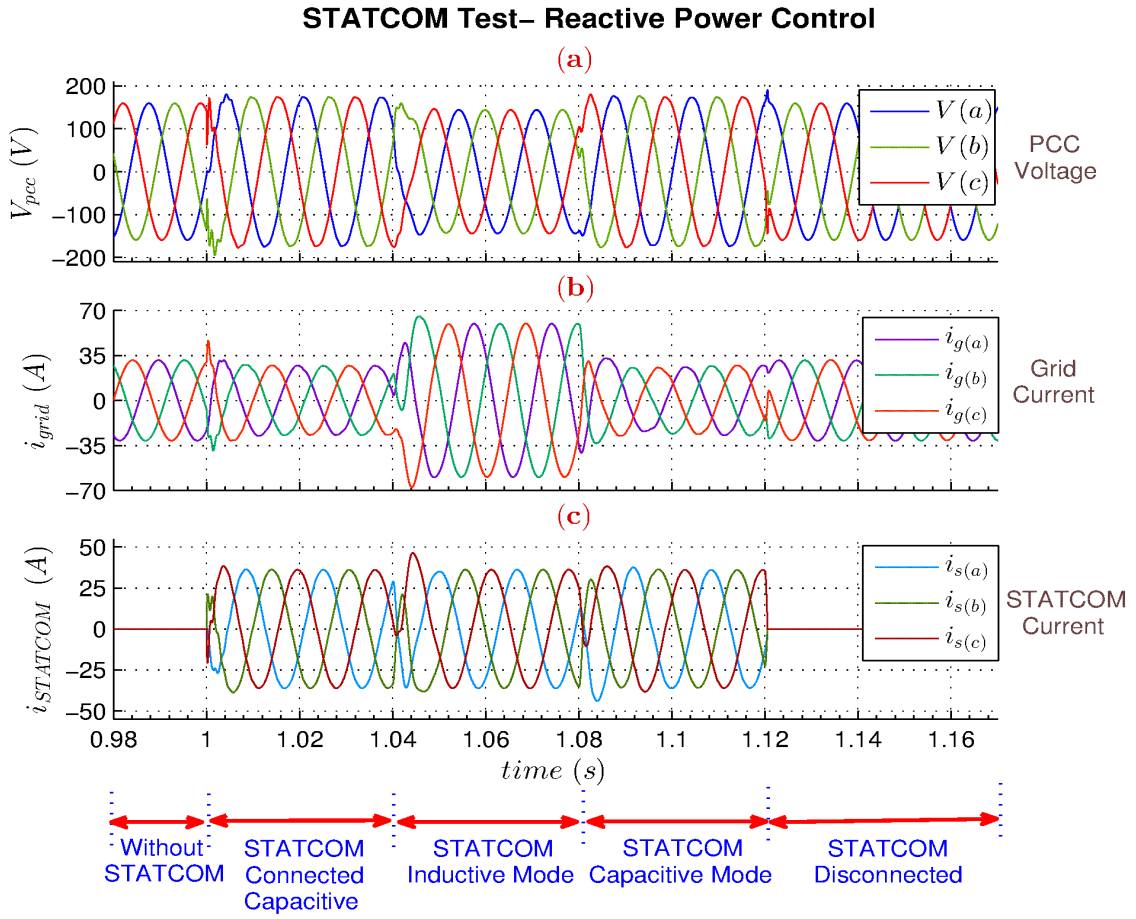

Figure 3-4: Voltage and currents waveforms for STATCOM operation with reactive power control

a) PCC voltage b) Grid current c) STATCOM current

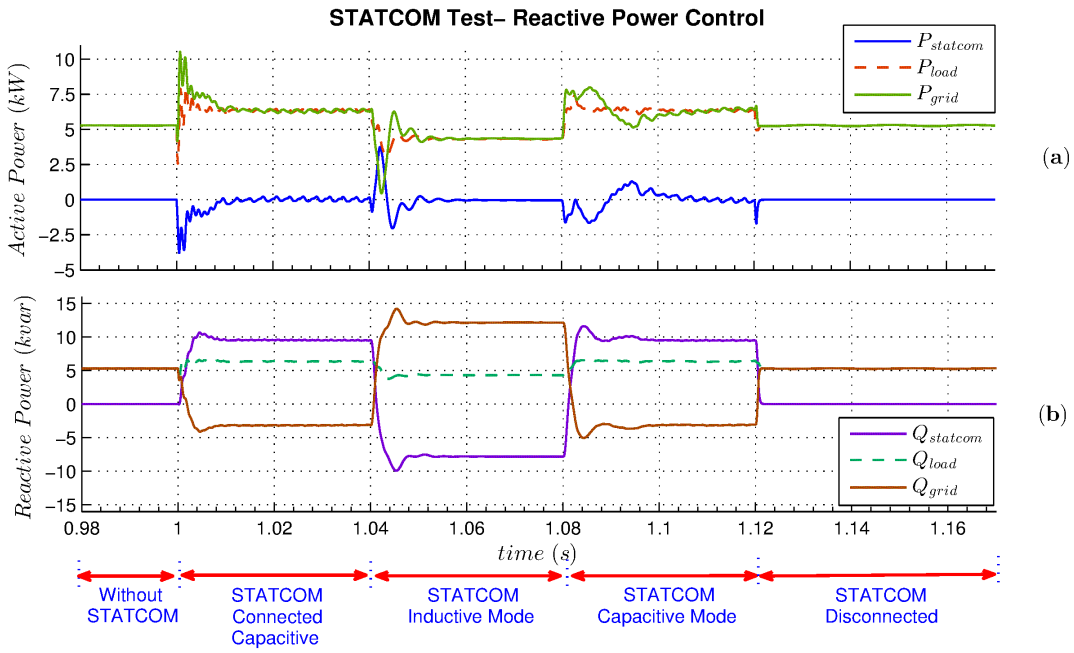

Figure 3-5: Active and reactive power waveforms for STATCOM operation with reactive power control

a) Active Power b) Reactive Power

3.3.2.2 Voltage Control

The STATCOM is now used to control or regulate the PCC voltage. The load power is kept 3 kW for this study of STATCOM with voltage control. Figure 3-6 (a)-(d) shows the per-unit voltage of the PCC ($v_{PCC,pu}$), PCC voltage waveforms (v_{pcc}) and grid current (i_{grid}) and STATCOM current ($i_{STATCOM}$).

At $t=1$ sec, the STATCOM is connected to the PCC while initially the reference voltage is 1.06 pu. The STATCOM follows the reference value and increases the PCC voltage ($v_{PCC,pu}$) from 1pu to 1.06 pu. The PCC voltage waveforms (v_{pcc}) shows the enhancement of the voltage due to the STATCOM operation. Due to surplus STATCOM current ($i_{STATCOM}$), grid current (i_{grid}) is increased. The PCC voltage tracks the reference value within one cycle.

At *t=1 .04* sec, the reference value of the voltage controller is changed from 1.06 pu to 0.94 pu. The per-unit value of PCC voltage as well as PCC voltage waveform show that the STATCOM reduces the bus voltage and controls it accurately to 0.94 pu. The STATCOM current ($i_{STATCOM}$) is shifted from 90^o leading to 90^o lagging to reduce the PCC voltage. The STATCOM current causes the grid current (i_{grid}) to increase.

At *t=1.08* sec, the reference value of the voltage is changed from 0.94 pu to 1.06 pu. In other words, the operation region of the STATCOM is changed from inductive to capacitive. The PCC voltage waveform (v_{pcc}) confirms that the controller follows the reference value and regulates the voltage to 1.06 pu. The results reveal that the STATCOM changes the PCC voltage within one cycle.

At *t=1.12* sec, the STATCOM is disconnected from the PCC. The STATCOM current ($i_{STATCOM}$) goes to zero instantaneously. As the last operation mode of the STATCOM is capacitive, disconnection of the STATCOM reduces the PCC voltage ($v_{PCC,pu}$) correspondingly. The grid current increases, as it now has to supply the entire load.

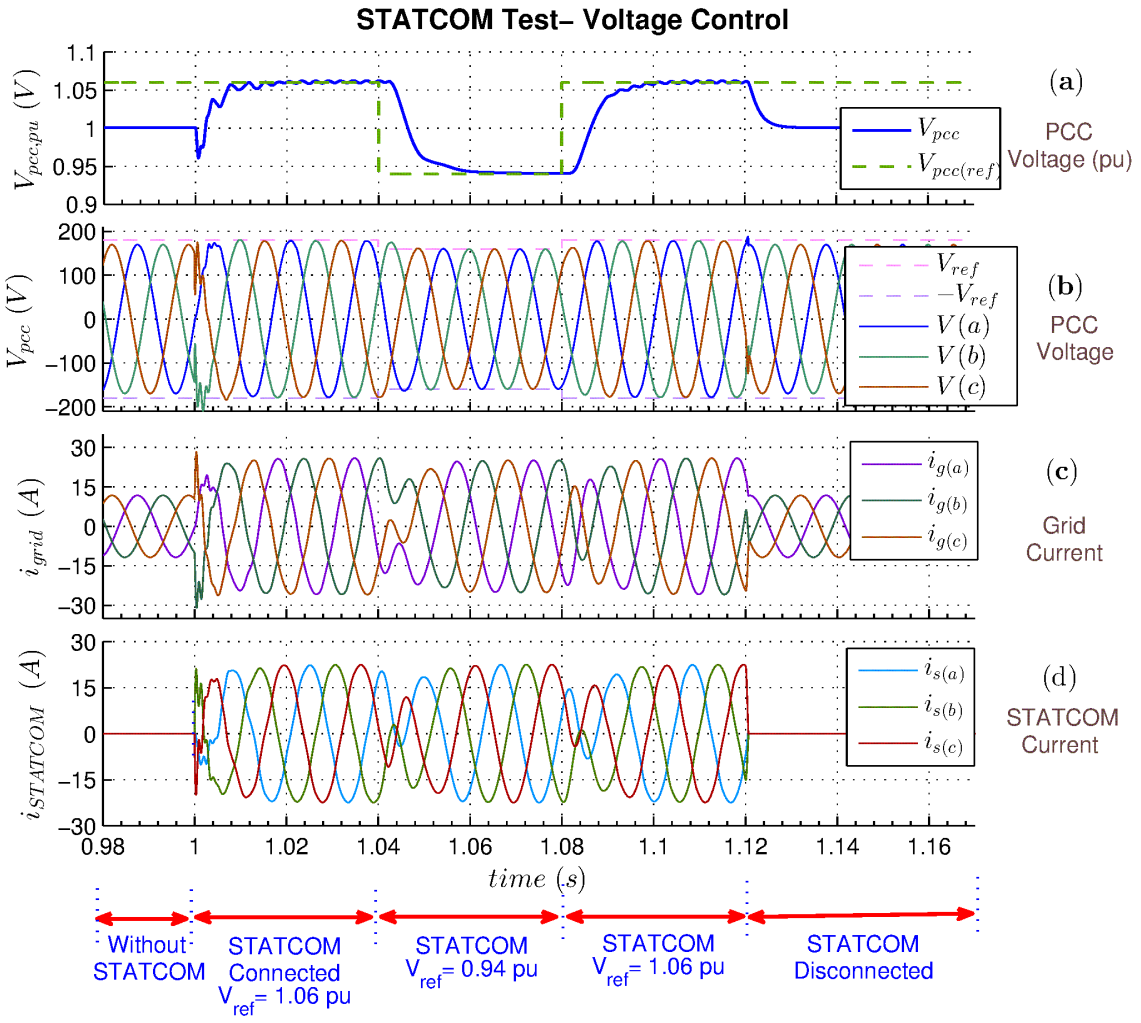

Figure 3-6: Voltage and currents waveforms for STATCOM operation with voltage control

a) PCC voltage (pu) b) PCC Voltage c) Grid current d) STATCOM current

3.3.3 Smart PV Inverter Operation in Partial STATCOM Mode

In this section, the remaining capacity of the inverter is used to exchange reactive power. Hence, this mode of the controller called "Partial STATCOM" mode. In other words, the conventional PV system operates as a STATCOM with the partial capacity of the inverter during daytime. In partial mode, the controller objectives are power factor correction and voltage control. For validating the proposed novel controller, the PV-STATCOM system

in Figure 3-1 is connected to the grid whereas the conventional PV system and STATCOM system are disconnected.

3.3.3.1 Power Factor Correction

Figure 3-7 (a)-(c) demonstrates grid power factor, PCC voltage (v_{pcc}) and grid current (i_{grid}) for phase "A" while the control objective of the smart PV inverter is power factor correction. In this study, the active load is 6 kW whereas reactive load is changed from inductive to capacitive. Initially the reactive load is 4 kvar inductive. Figure 3-8 (a) and (b) show the active and reactive power changes of the grid, load and PV system during load and PV power variations.

At *t=1* sec, the PV-STATCOM system is connected to the grid and control objective is set to PV mode. In this stage, the PV system output is 3 kW. The power factor of the grid is about 0.69 when PV-STATCOM only generates active power. Therefore, PCC voltage (v_{pcc}) and grid current (i_{grid}) are not in phase. Active power of the load (P_{load}) is supplied by both grid (P_{grid}) and PV-STATCOM system (P_{spv}) whereas most part of the reactive load (Q_{load}) is supplied by the grid (Q_{grid}). The reactive power of PV-STATCOM (Q_{spv}) is equal to reactive power of harmonics filter which is not considerable.

At *t=1.04* sec, the power factor correction mode is activated and the controller uses the remaining capacity of the inverter to improve power factor to unity. The grid power factor is enhanced from 0.69 to unity by the controller. As a consequence, the PCC voltage (v_{pcc}) and grid current (i_{grid}) become in phase after a transient. To improve power factor, the PV-STATCOM exchanges reactive power equal to the reactive power requirement of the load. Hence, the reactive power of PV-STATCOM (Q_{spv}) is equal to (Q_{load}), and so, the grid reactive power (Q_{grid}) falls to zero. Also, the results reveal that the power factor improvement by smart PV inverter does not influence the active power production. In other words, the active power output of PV-STATCOM (P_{spv}) remains at 3 kW during power factor correction. The decoupled operation of the real and reactive power controllers is thus demonstrated successfully.

At *t=1.08* sec, the reactive load changes from 4 kvar inductive to 3 kvar capacitive whereas the active load is remains constant at 6 kW. The power factor is kept unity by the controller in present of load variation. Therefore, PCC voltage and grid current remain in the same phase. In other words, the grid reactive power is zero and the load reactive power is supported by PV-STATCOM system.

At *t=1.12* sec, the active power output of the PV-STATCOM system changes from 3 kW to 4.5 kW. The load is kept constant at 6 kW and 3 kvar capacitive. The power factor remains at unity even during the active power changes of PV-STATCOM system. This demonstrates the effectiveness of decoupling between active and reactive power controllers. The entire reactive power of the load is supplied by the PV-STATCOM system while supplying 4.5 kW of the 6 kW active load.

At *t=1.16* sec, the PV-STATCOM system is disconnected from the grid, and so, the power factor drops down to 0.69 due to reactive load. Therefore, the grid current rises up to supply active and reactive loads.

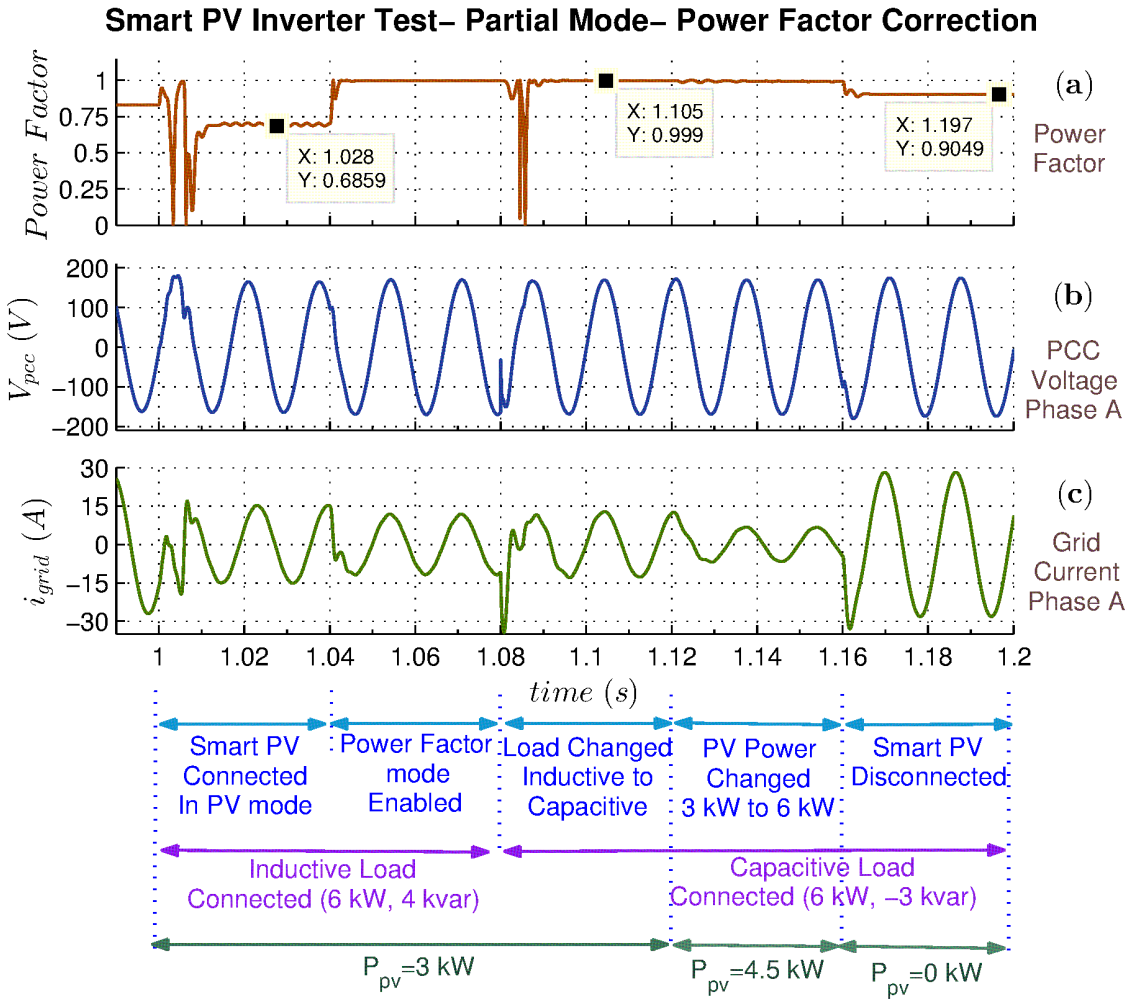

Figure 3-7: Simulation results for partial STATCOM mode with power factor correction

a) Power Factor b) PCC voltage (phase A) c) Grid current (phase A)

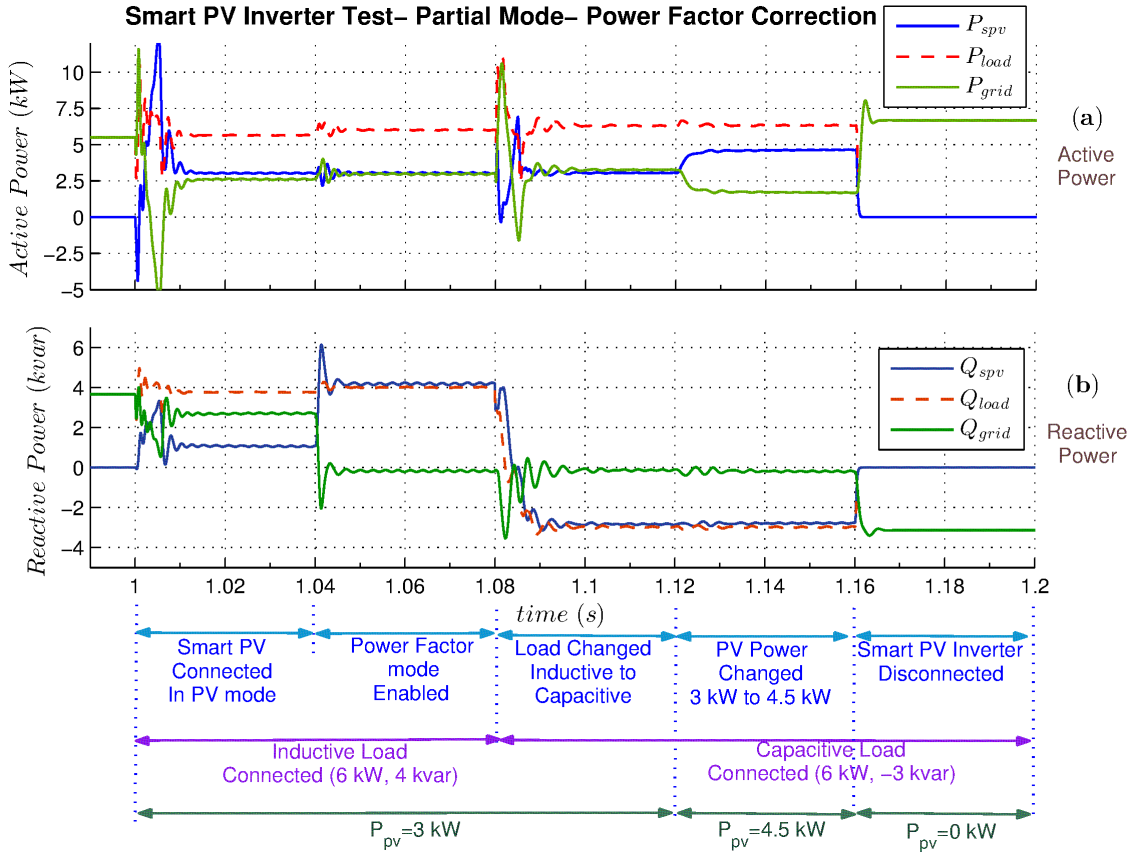

Figure 3-8: Active and reactive powers for partial STATCOM mode with power factor correction

a) Active power b) Reactive power

3.3.3.2 Voltage Control

In this test, the smart PV inverter controller uses the remaining capacity of the inverter in Partial STATCOM mode to control the PCC voltage. The active and reactive loads are presumed to be 6 kW and 3 kvar inductive in this study. Figure 3-9 (a)-(d) depicts the PCC voltage (v_{pcc}), grid current (i_{grid}), PV system current (i_{spv}), inverter current ($i_{inverter}$) waveforms, respectively. Figure 3-10 (a)-(f) demonstrate the control signals of the controller. Figure 3-10 (a), (b) and (c) show the PCC voltage in per-unit ($V_{pcc,pu}$) and voltage in *d-q* frame (V_d, V_q), respectively. Figure 3-10 (d) and (e) illustrate the d-component (i_d) and q-component (i_q) of the inverter current. Figure 3-10 (f) shows the DC link voltage (V_{dc}) for voltage control study in partial STATCOM operation mode.

Figure 3-9 and Figure 3-10 show the behavior of the system and controller parameters under following events:

At *t=1* sec, the smart PV inverter is connected to the grid in full PV mode while it generates 3 kW active power. After connectivity transient, the PV system provides a portion of the active load requirements and the rest of the power is absorbed from the grid by the load. Therefore, the power flows in the forward direction in the grid. The active power generation of the PV-STATCOM system increases the PCC voltage (v_{pcc}) slightly. Also, the PV-STATCOM current (i_{spv}) causes the grid current (i_{grid}) to reduce. The comparison between inverter current ($i_{inverter}$) before filter and PV-STATCOM current (i_{spv}) after filter validates the effectiveness of the filter harmonics. The *q*-component of the PCC voltage (V_q) reveals that the PLL unit of the controller keeps V_q at zero level properly. Subsequently, the *d*-component of the PCC voltage (V_d) represents the amplitude value. As at this stage, the voltage control is disabled (V_d) does not follow the reference value ($V_{d,ref}$). As the PV-STATCOM generates only active power at this period, d-component of the inverter current (i_d) follows the reference value ($i_{d,ref}$) to generate active power and keep the DC link voltage charged at a certain value. As the PV-STATCOM operates as the conventional PV system, the reactive power output of the inverter is equal to zero. Therefore, the reactive current (i_q) is controlled at zero level. Also, the DC link voltage (V_{dc}) follows the reference value ($V_{dc,ref}$) which is 400 V.

At *t=1.04* sec, the voltage control is enabled, and so, the smart PV inverter uses the remaining capacity of the inverter to regulate the PCC voltage. The active power output of the PV-STATCOM system is kept at 3 kW. The reference value of the voltage ($V_{pcc,ref}$) is set at 1.04 pu. The controller follows the reference value within one cycle and enhances the PCC voltage (v_{pcc} and $V_{pcc,pu}$) to 1.04 pu. The PV-STATCOM current (i_{spv}) is increased to control the voltage. The d-component of the PCC voltage (V_d) follows the reference value of the voltage control block whereas V_q is kept at zero by the PLL. As the active power of the PV-STATCOM is 3 kW, the reference value of the d-component of inverter current ($i_{d,ref}$) is not changed. The d-axis component of the inverter current (i_d) quickly follows the reference value after transient. The voltage controller changes the reference value of the *q*-component of the inverter current ($i_{q,ref}$) to regulate the voltage at 1.04 pu.

Hence, the *q*-component of the inverter current (i_q) tracks the reference value to control the voltage. The DC link voltage control is decoupled from the transients of AC voltage controller. Therefore, the DC link voltage (V_{dc}) follows the reference value ($V_{dc,ref}$) without any considerable transient.

At *t=1.08* sec, the voltage control is kept enabled while the reference value of the voltage controller ($V_{pcc,ref}$) is varied from 1.04 pu to 0.94 pu. The PCC voltage (v_{pcc} and $V_{pcc,pu}$) is reduced to the reference value accurately in a rapid manner. This part of the study confirms the performance of the controller in switching the operation between inductive and capacitive regions. The *d*-component of the PCC voltage (V_d) is reduced based on the reference value. The *q*-component of the PCC voltage (V_q) is stabilized at zero level after the transients of the controller. As the operation mode of the controller is changed from capacitive to inductive, the reference value of the *q*-component of the inverter current ($i_{q,ref}$) varies from negative value to positive value. The reference value of the active component of the inverter current is same as in previous case corresponding to 3 kW active power. The reactive component of the inverter current (i_q) tracks the reference value to reduce the PCC voltage. The DC link voltage of the inverter shows that the PCC voltage control has no effect on DC voltage controller, once again demonstrating the effective decoupling between the real and reactive current controllers.

At *t=1.12* sec, the active power output of the PV-STATCOM changes from 3 kW to 6 kW while the controller regulates the PCC voltage at 0.94 pu. This study presents the effect of the active power changes on the AC bus voltage controller. The PCC voltage (v_{pcc} and $V_{pcc,pu}$) is controlled at 0.94 pu after the transient. The PCC voltage reveals that the influence of the DC link voltage control on AC voltage controller is negligible. More solar power increases the PV-STATCOM current (i_{spv}), and so, the grid current (i_{grid}) is reduced. The *d*-component of the PCC voltage (V_d) is regulated at reference value. Also, the *q*-component of the PCC voltage (V_q) is kept at zero level. As in this period of the test, only active power changes therefore, the reference value of the active current ($i_{d,ref}$) varies whereas the reference value of the reactive current ($i_{q,ref}$) is preserved at the previous level. The active current (i_d) follows the reference value to enhance the active power output of the PV-STATCOM. Also, the reactive component of the inverter current (i_q) tracks the

reference value to regulate the PCC voltage at 0.94 pu. The DC link voltage shows that the active power changes of the PV-STATCOM influences the DC link voltage transient slightly.

At *t=1.16* sec, the PV-STATCOM system is disconnected from the grid. Subsequently, the inverter and PV system currents fall to zero and the grid solely supplies the load power.

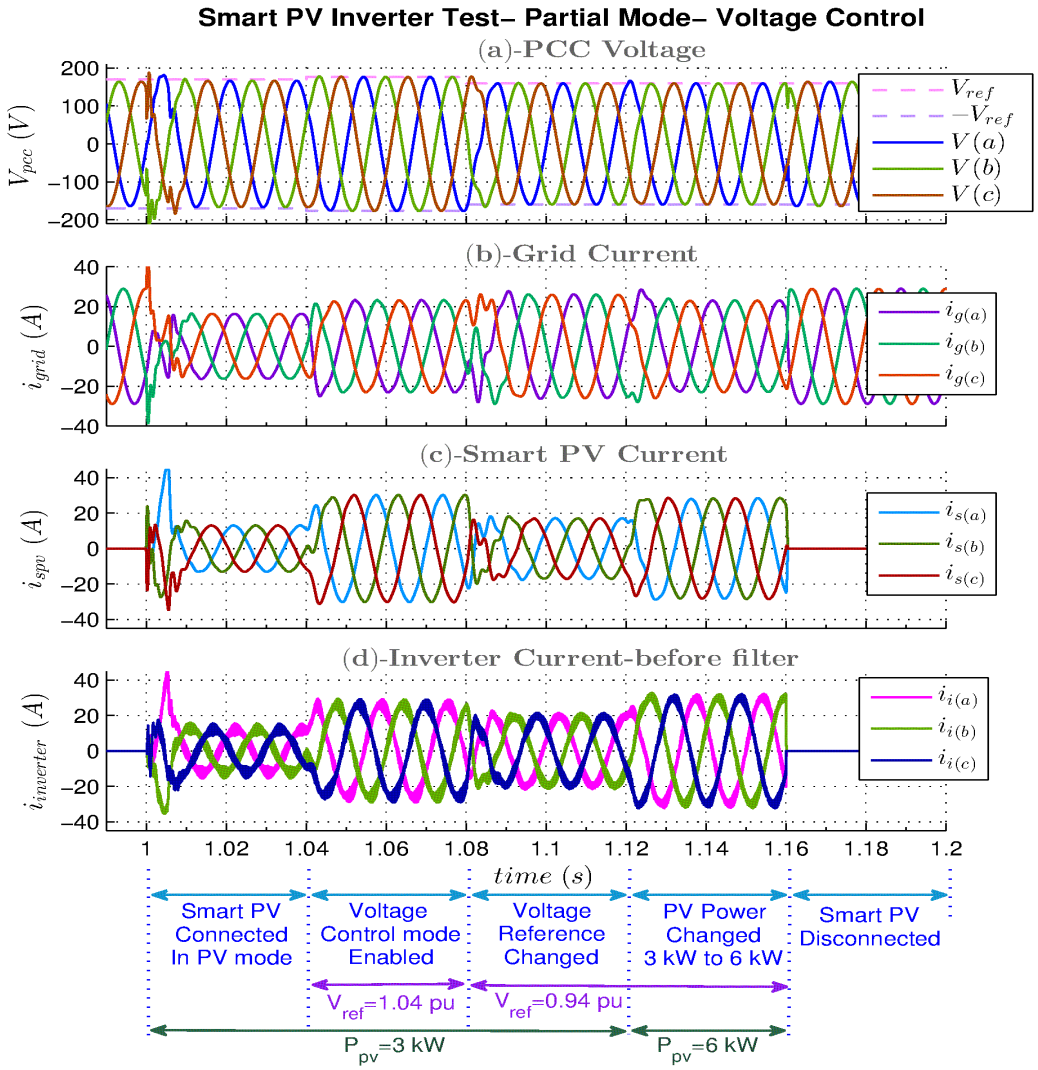

Figure 3-9: Simulation results for partial STATCOM operation with voltage control

a) PCC voltage b) Grid current c) Smart PV current d) Inverter Current

It should be noted the voltage control with partial capacity of the inverter is applied for forward power flow condition. Next section shows the smart PV controller operation with

full capacity of the inverter while the surplus power from PV system flows in the reverse direction in the grid.

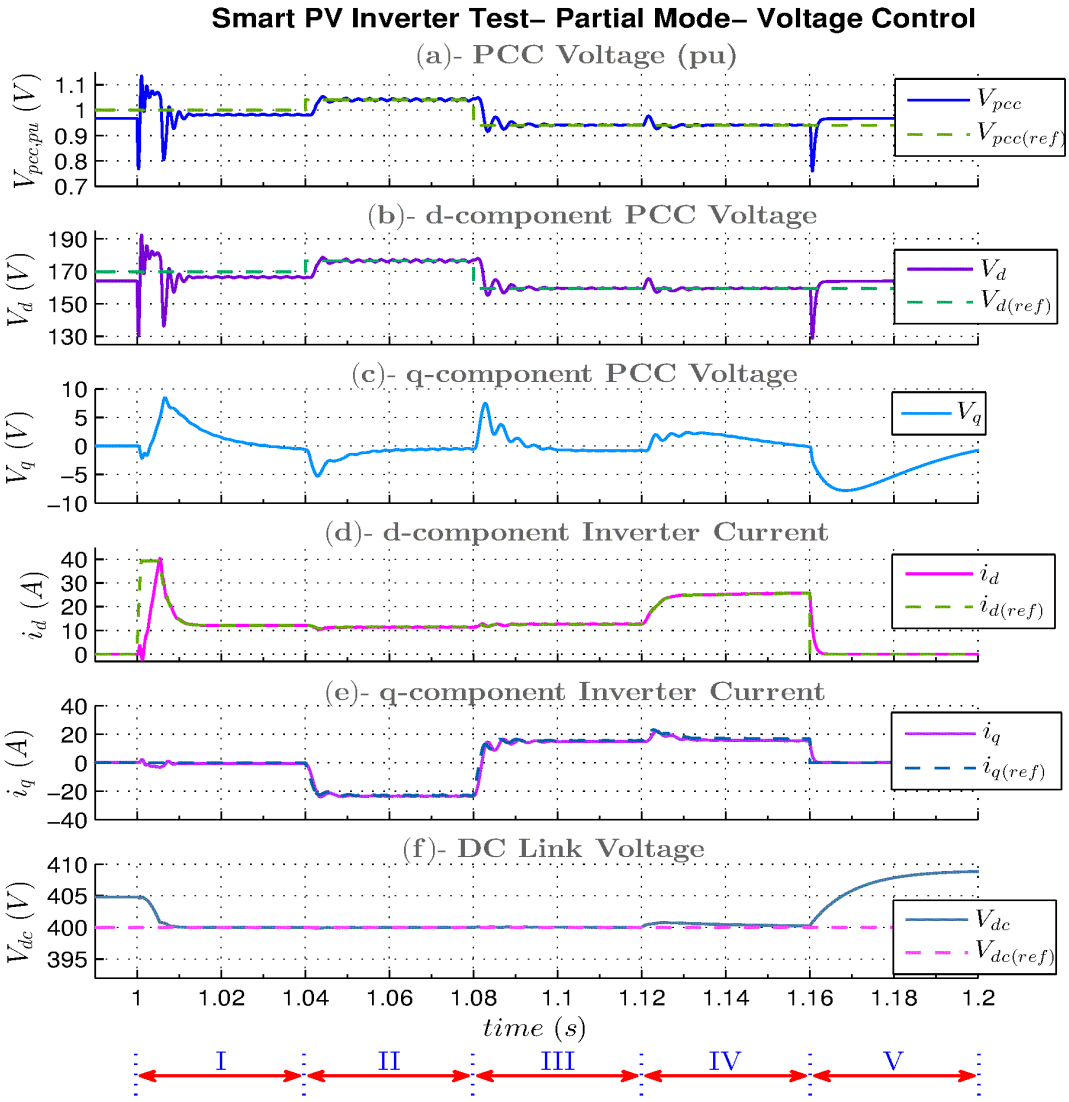

Figure 3-10: Control signals for partial STATCOM operation with voltage control

a) PCC voltage (pu) b) d-component voltage c) q-component voltage
d) d-component current e) q-component current f) DC link voltage

3.3.4 Smart PV Inverter Operation in Full STATCOM Mode

In this section, the smart PV inverter operation in full STATCOM mode is presented. To demonstrate the controller performance, it is assumed that PV system generation is more than load consumption. Therefore, the surplus power of the PV flows in the grid in reverse

direction. To assess the controller performance in Full STATCOM mode, the active and reactive power load are considered 2 kW and 2 kvar whereas the PV system generates 6 kW active power. Figure 3-11 (a) and (b) show the PCC voltage as per-unit and *abc* waveforms when the conventional PV system is subjected to a large load, suddenly.

At *t=1* sec, the PV system with conventional control is connected to the grid. The PCC voltage is increased due to active power generation of the PV system.

At *t=1.04* sec, a large reactive load is connected to the grid. Subsequently, the PCC voltage reduces significantly. The results show that the large load reduces the voltage to 0.91 pu which is outside the acceptable range of the utility.

At *t=1.10* sec, the network returns to the normal condition, and so, the voltage is recovers to about 0.99 pu.

At *t=1.14* sec, the PV system is disconnected from the PCC and in consequence the PCC voltage is reduced slightly.

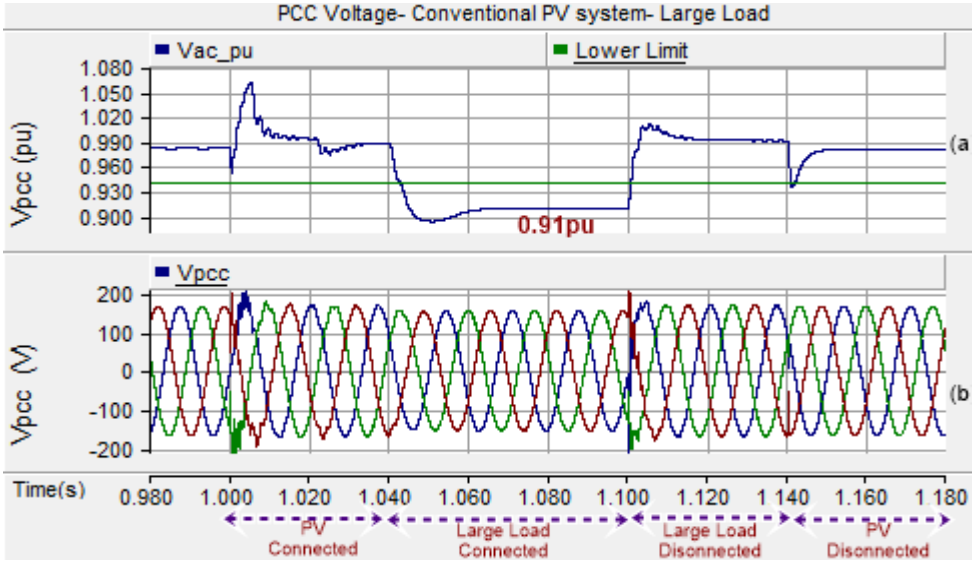

Figure 3-11: PCC Voltage of PV system without smart inverter controller
a) *rms* voltage in per-unit b) instantaneous voltage waveforms

Figure 3-11 reveals that the conventional PV system fails to provide any voltage support during the connection of a large load, and the voltage drops substantially. Hence, the

conventional controller is replaced by the novel smart inverter controller to control the voltage in this circumstance. Figure 3-12 (a)-(e) demonstrate the PCC voltage (v_{pcc}), grid current (i_{grid}), smart PV system current (i_{spv}), inverter current ($i_{inverter}$) and load current (i_{load}), respectively.

Control signals are shown in Figure 3-13 (a)-(e) for smart PV inverter operation in Full STATCOM mode. Figure 3-13 (a) represents the per-unit value of the PCC voltage ($V_{pcc,pu}$) in control plant . The *q*-component of the PCC voltages (V_q) is shown in Figure 3-13 (b). Figure 3-13 (c) and (d) illustrate the *d*-component (i_d) and *q*-component (i_q) of the inverter current. DC link voltage (V_{dc}) is shown in Figure 3-13 (e). The active and reactive power flows of the study system are shown in Figure 3-14 (a) and (b), respectively.

At *t=1* sec, the PV-STATCOM system is connected to the grid when it generates 6 kW active power as a conventional PV system. Initially, 2 kW and 2 kvar active and reactive loads are connected to the grid. The PV system connection creates a transient on the grid voltage (v_{pcc}) and grid current (i_{grid}). Active power of the PV-STATCOM system increases the PCC voltage (v_{pcc}) slightly. The grid current (i_{grid}) is decreased due to PV-STATCOM current (i_{spv}). By comparing inverter current ($i_{inverter}$) and PV-STATCOM current (i_{spv}) which is after filter harmonics, it is revealed that the harmonics filter is designed properly. The per-unit value of the PCC voltage shows that the PCC voltage ($V_{pcc,pu}$) reaches 0.97 pu after activation of the PV-STATCOM system. The PLL controller controls the q-component of the PCC voltage (V_q) at zero. Due to 6 kW solar power generation, the active component of the inverter current (i_d) follows the reference value ($i_{d,ref}$). As the PV-STATCOM system operates in the full PV mode, the reference value of the reactive component of the inverter current ($i_{q,ref}$) is zero. Therefore, the reactive current (i_q) is kept at zero level by the controller. The DC link voltage (V_{dc}) follows the reference value ($V_{dc,ref}$) which is 400 V. The PV-STATCOM system supplies active power consumption of the load (P_{load}) and surplus power flows into grid in the reverse direction. Therefore, active power of the grid (P_{grid}) becomes negative. The 2 kvar reactive load (Q_{load}) is supplied by the grid (Q_{grid}) and the harmonics filter of the PV-STATCOM (Q_{spv}). However, the reactive power output of the inverter is kept zero by controlling i_q at zero.

At *t=1.04* sec, a large amount of the load is connected to the grid suddenly. The total load becomes 4 kW active and 8 kvar reactive. The novel smart inverter controller controller disconnects the solar panel in this situation and controls the PCC voltage at pre-fault value with full inverter capacity in Full STATCOM mode. The PCC voltage (v_{pcc}) is successfully maintained at pre-fault value of 0.97 pu despite the sudden load connectivity. The PV-STATCOM current (i_{spv}) is increased due to the reactive current of the inverter for voltage control. Hence, the surplus reactive current increases the grid current (i_{grid}). The load current (i_{load}) rises significantly when the sudden load is connected. After a transient the PLL regulates the q-component of the PCC voltage tozero. As the solar panel is disconnected from the inverter, the active power output of the inverter reduces to zero. Correspondingly, the reference value of the active current ($i_{d,ref}$) is set to zero. The active current of the inverter (i_q) follows the reference value and is controlled at zero. Therefore, the controller is able to use the entire current rating for exchanging reactive current. The reactive current of the inverter (i_q) tracks the reference value ($i_{q,ref}$) to prevent the severe voltage drop. The DC link voltage (V_{dc}) follows the reference value ($V_{dc,ref}$) which is 400 V. Since the solar panel is disconnected by the controller, the active power output of the PV-STATCOM (P_{spv}) becomes zero, and the entire active load (P_{load}) is supplied by the grid power (P_{grid}). Due to the large load connectivity, the reactive power of the load (Q_{load}) increases suddenly. To control PCC voltage, the PV-STATCOM generates reactive power (Q_{spv}) during the transient.

At *t=1.10* sec, the large load is removed and the controller returns to full PV operation mode. In other words, the controller connects the solar panel to the inverter and generates only active power. The voltage control mode is deactivated as the PCC voltage (v_{pcc}) is within acceptable range. Due to a small amount of PV-STATCOM current (i_{spv}) to the grid, the grid current (i_{grid}) is reduced. As the large load is removed the load current (i_{load}) is decreased significantly. Due to PLL operation, the d-component of the PCC voltage ($V_{pcc,pu}$) becomes equal to the voltage magnitude whereas the q-component of the voltage (V_q) is zero. The active component of the inverter current (i_d) follows the reference value ($i_{d,ref}$) to generate 6 kW solar power. As the PV-STATCOM system operates as the full PV system, the reference value of the reactive component of the inverter current ($i_{q,ref}$) is made zero. Hence, the current controller regulates the reactive current (i_q) to zero. The DC link

voltage (V_{dc}) follows the reference value ($V_{dc,ref}$) after it is stabilized. As active power generation of the PV-STATCOM system (P_{spv}) is more than the active load consumption (P_{load}), the surplus power flows in the reverse direction in the grid. The reactive power output of the inverter is zero during the full PV mode of operation. However, the PV-STATCOM system exchanges reactive power (Q_{spv}) by the harmonics filter and the interface transformer. Hence, the 2 kvar reactive load (Q_{load}) is supplied by the grid (Q_{grid}) and the harmonics filter of the PV-STATCOM (Q_{spv}).

At *t=1.14* sec, the PV-STATCOM system is disconnected from the grid. In consequence, the PCC voltage (v_{pcc}) drops slightly. The PV-STATCOM current (i_{spv}) and inverter current ($i_{inverter}$) fall to zero. The grid current (i_{grid}) is increased to supply active and reactive loads. As the PV-STATCOM current is zero both d-component (i_d) and q-component (i_q) of the inverter current become zero. Also, the DC link voltage (V_{dc}) becomes equal to open source voltage of the solar panel. As both active power and reactive power of the PV-STATCOM are zero, the active power and reactive power of the load are equal to grid power.

.

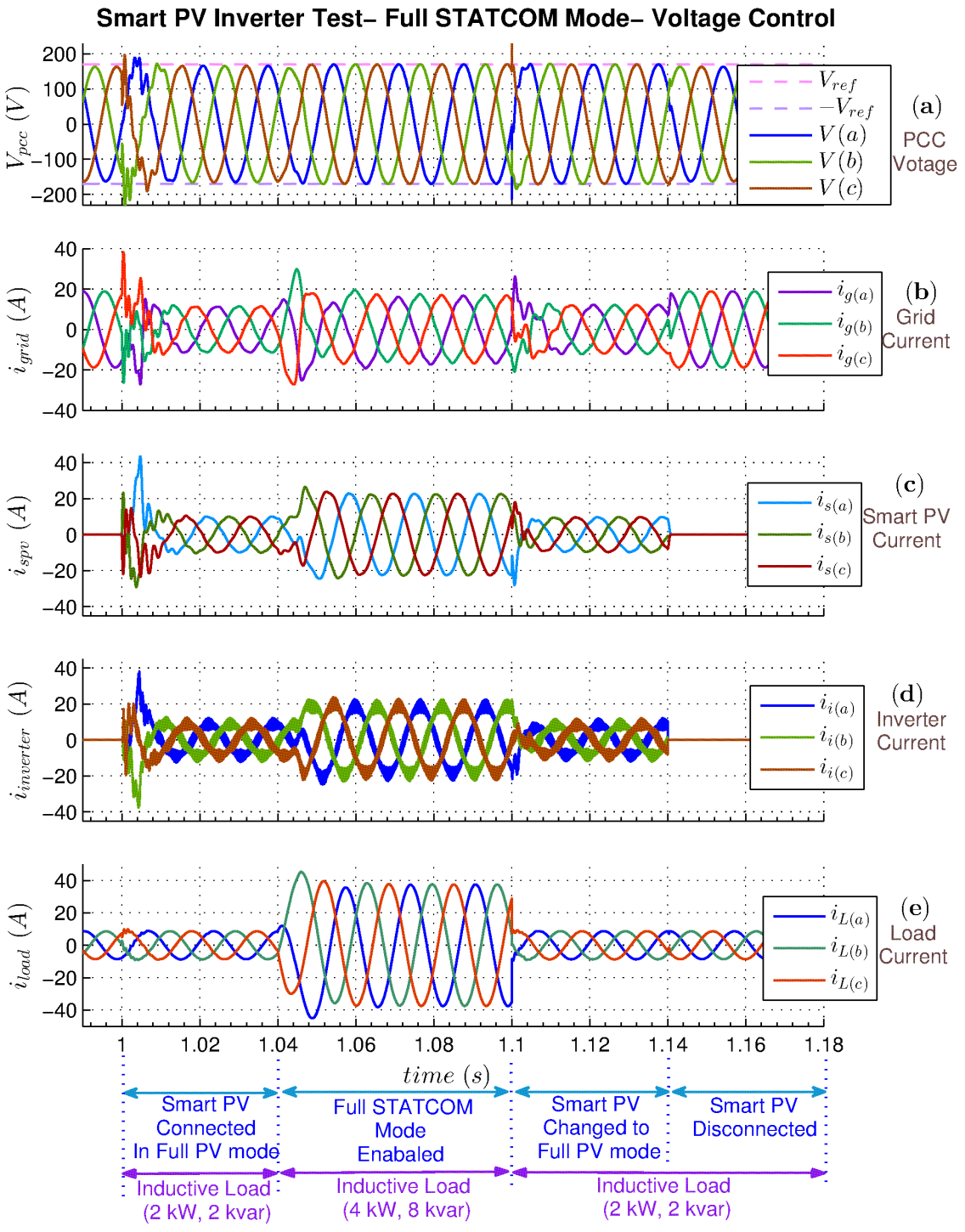

Figure 3-12: Simulation results for full STATCOM mode with voltage control

a) PCC voltage b) Grid current c) Smart PV current
d) Inverter current e) Load current

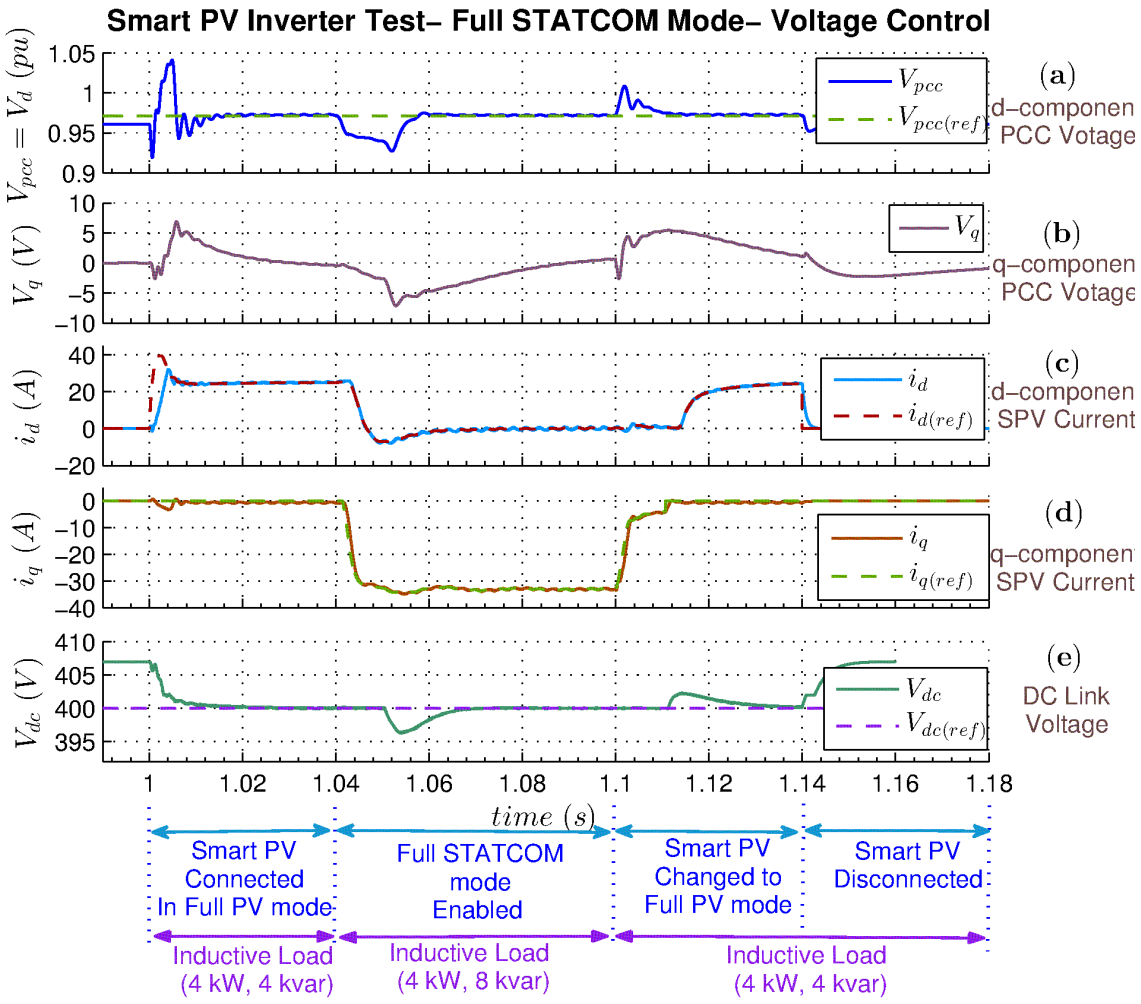

Figure 3-13: Control signals for full STATCOM mode with voltage control

a) PCC voltage (pu) b) q-component voltage c) d-component current
d) q-component current e) DC link voltage

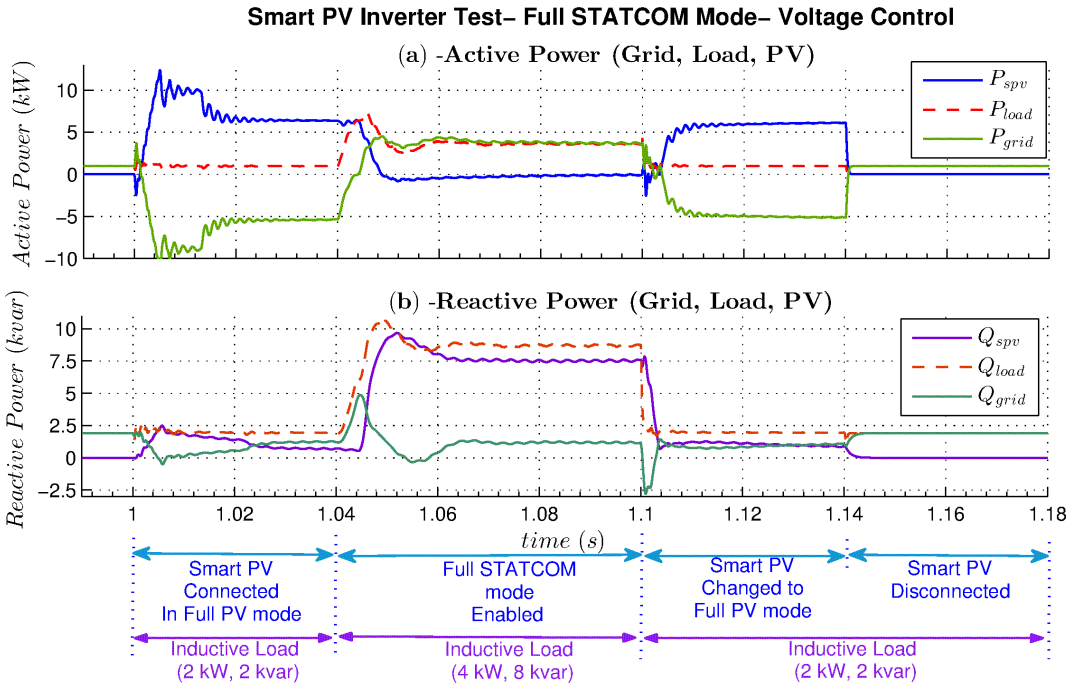

Figure 3-14: Active and reactive powers for full STATCOM mode with voltage control

a) Active power b) Reactive power

3.4 Conclusion

In this chapter, a system model of a realistic feeder of Bluewater Inc. network is developed in PSCAD/EMTDC software. A 10 kVA PV system is connected to the grid in presence of different loads. The controller of the conventional PV system is replaced by a smart inverter controller to operate in Partial STATCOM mode and Full STATCOM mode depending upon the system requirements. The control objectives for partial STATCOM operation mode are power factor correction, voltage regulation and reactive power control. However, voltage control is the sole control objective in full STATCOM operation mode. The software simulation studies validate the controller performance for both modes of operation for achieving the control objectives.

In partial STATCOM mode, the controller keeps the grid power factor at unity by providing the required reactive power of the load. Also, the controller is evaluated for voltage control

in both capacitive and inductive regions. During voltage control, the active power output of PV system is changed to demonstrate the successful decoupling of the active and reactive power controllers.

In full STATCOM operation mode, the sudden connection of load causes the controller to disconnect the solar panels from the inverter and control the voltage with full capacity of the inverter.

The smart inverter controller regulates the PCC voltage in both capacitive and inductive regions in one cycle.

CHAPTER 4

4 REAL TIME DIGITAL SIMULATION (RTDS) AND HARDWARE-IN-LOOP (HIL) SIMULATION OF SMART PV INVERTER

4.1 Introduction

This chapter presents the simulation of the proposed novel smart PV inverter control on the Real Time Digital Simulator (RTDS) utilizing Hardware-in-Loop (HIL) technique. The study system corresponds to the 10kVA Bluewater Power distribution network with the 10 kVA PV solar system. The equivalent study system including the grid, PV system and load are modeled in the Real Time Digital Simulator (RTDS) and the controller is implemented on dSPACE controller board. The RTDS is connected to the dSPACE through a hardware-in -loop configuration and the entire system is simulated in real-time. The results of this study are expected to better validate the smart inverter controller performance as compared to the PSCAD/EMTDC software simulation which was not in real-time.

4.2 Concept of Real Time Digital Simulation and HIL

The design of a prototype model and its controller such as for inverters and FACTS devices has to go through different stages of testing and validation before installation in the field. The first phase of performance testing is performed through industry grade electromagnetic transient software simulation studies. These simulation studies presents a perspective to the designer about power systems and the controller behavior during steady-state and transient conditions, such as faults [140, 141]. Correspondingly the novel smart PV inverter controller is modeled in PSCAD/EMTDC software for testing and validation.

Although, different types of extensive studies can be performed by these simulation software but these software model the power systems in non-real time. The simulation software needs substantially more time to evaluate the performance of simulated system than the time taken by the real phenomena, as several complex differential equations may need to be solved. For example, the simulation of a few millisecond transient occurring in a power system having an inverter may take few minutes of simulation time.

For this reason, the second phase of performance validation of the controller prototype is typically performed through real-time digital simulation studies. Such real time studies provide a more accurate and reliable perspective of the controller performance than non-real-time software studies. Recent improvements in computing hardware and processors have made real-time simulation of power systems, possible. The prominent real-time digital simulation hardware for the power system studies are RTDS and OPAL-RT [142, 143]. The RTDS Technologies have developed the Real Time Digital Simulator (RTDS) which is a specialized parallel-processing hardware to simulate the power systems models in real-time. The RTDS provides the real-time studies for power systems and power electronics models by employing high speed processors. The power system models such as generators, passive and dynamics load, inverter and converters, transmission line are implemented on the RTDS processors through the user interface software. However, it should be noted that in RTDS studies, all components including power systems, power electronics and controller are modeled on the RTDS hardware [144, 145]. Accordingly, the novel smart PV inverter controller as well as entire study system are implemented on the RTDS to verify the controller performance in real-time.

Although the RTDS is an effective tool, the effects of input/output (I/O) signals, environment disturbances on the controller signals and controller delays are neglected since all the component are implemented in software on the RTDS. A Hardware-In-the Loop (HIL) study is therefore considered as a next stage for more accurate testing and verification of the controller performance in real-time. In a HIL study, the controller is implemented on a separate hardware and linked with the RTDS hardware through actual input/output signals. While the RTDS simulates the mathematical models of power systems and power electronics components in software resident in the RTDS, the actual controller is implemented in hardware on a microcontroller or DSP-based board. The controller board and RTDS communicate through analog and digital input/output [146-148]. For HIL study of the novel smart PV inverter controller, the controller is implemented on the dSPACE board whereas the study system is modeled on the RTDS. The required signal for control functions are sent through the output cards of the RTDS to input channels of the dSPACE board. Moreover, the PWM signals for inverter model inside the RTDS are forwarded by means of PWM unit of the dSPACE to input card of the RTDS.

4.3 Overview of Real Time Digital Simulator (RTDS)

The Real Time Digital Simulator (RTDS) is a custom parallel-processing hardware architecture to model the study power system in real-time. The RTDS is utilized with real-time simulation software, RSCAD, which has a graphical user interface (GUI) and mathematical solution algorithms for network equations and component models. The processor cards of RTDS are classified as 3PC, GPC and PB5 cards, each one containing two RISC processors. The PB5 card operates with 1.5 MHz clock whereas the GPC clock is 1 GHz. It should be noted that both PB5 and GPC cards are considered as high speed cards. Therefore, for modeling small time step components such as voltage source inverter with high switching frequency, only these high speed cards are appropriate. The 3PC card has low speed and only can be used for simulation of large time scale component such as power systems components.

Also, the RTDS has various I/O cards such as Giga Transceiver Digital Input (GTDI) and Giga Transceiver Analog output (GTAO) to exchange data with external devices such as microprocessor or DSP boards which makes the RTDS capable of running simulation in real time with hardware-in-loop (HIL) feature [142, 149-151]. The study system can be modeled in RSCAD-Draft and the compiled file is uploaded on the RTDS processor cards through RSCAD-Runtime feature. Also, RSCAD-Runtime is used for monitoring the voltages and currents ae well as applying the commands like connect/disconnect switches. The RTDS is used for this research includes two GPC cards and two PB5 cards as well as one GTDI card and one GTAO card. Hence, both large time step and small time step components are modeled on high speed cards.

4.4 Overview of dSPACE Controller Board

The dSPACE controller board which is used in this research includes a DS1103 controller card and an I/O expansion box (CLP1103). The designed controller is implemented on DS1103 controller card. The DS1103 controller card includes a main processor with 333 MHz clock rate and a DSP microcontroller (TMS320F240) with 20 MHz clock rate. The analog and digital inputs/outputs of master and slave processors are available on CLP1103 expansion box. The detailed hardware architecture is provided in the dSPACE hardware

manual [152]. The MATLAB/Simulink software is used for programming of dSPACE board. In other words, the controller is designed in MATLAB/Simulink environment. Then, the designed controller is compiled and uploaded on DS1103 controller card as a binary code. The dSPACE board is utilized with GUI software which is called Control Desk. The Control Desk software is used to monitor and apply changes on the control variables.

4.5 HIL Structure

In this chapter, the entire study system with the PV inverter is implemented on the RTDS processor cards, GPC and PB5. The inverter model inside the RTDS receives six pulses signals for the IGBT gates through Giga Transceiver Digital Input (GTDI) card. Also, the required signals for the controller board are sent by Giga Transceiver Analog output (GTAO) card. On the other hand, the smart PV controller is implemented externally to the RTDS using the dSPACE controller board. The implemented controller inside dSPACE board generates the gates pulses for the inverter model residing in the RTDS.

The switching pulses are produced by the control algorithm and the pulses are sent to the GTDI card. Figure 4-1 illustrates the HIL structure of smart PV inverter system. As shown, the Bluewater network is modeled by an equivalent voltage source and the short circuit impedance. Also, a short power distribution line is modeled as an inductance and resistance. The passive loads are shown as resistive, inductive and capacitive loads. The PV system includes the solar panels, two-level three-phase voltage source inverter, harmonics filter and interface transformer. The implemented controller in dSPACE observes the PCC voltage, inverter current, load current and DC link voltage from the GTAO card. Based on the control objective and the operation mode, the controller produces appropriate switching pulses. The switching pulses through the PWM unit of the controller board are applied to GTDI card. Consequently, the smart PV inverter controller is simulated in real-time with hardware-in-loop structure. The hardware-wise view of the HIL structure is shown in Appendix B. 1.

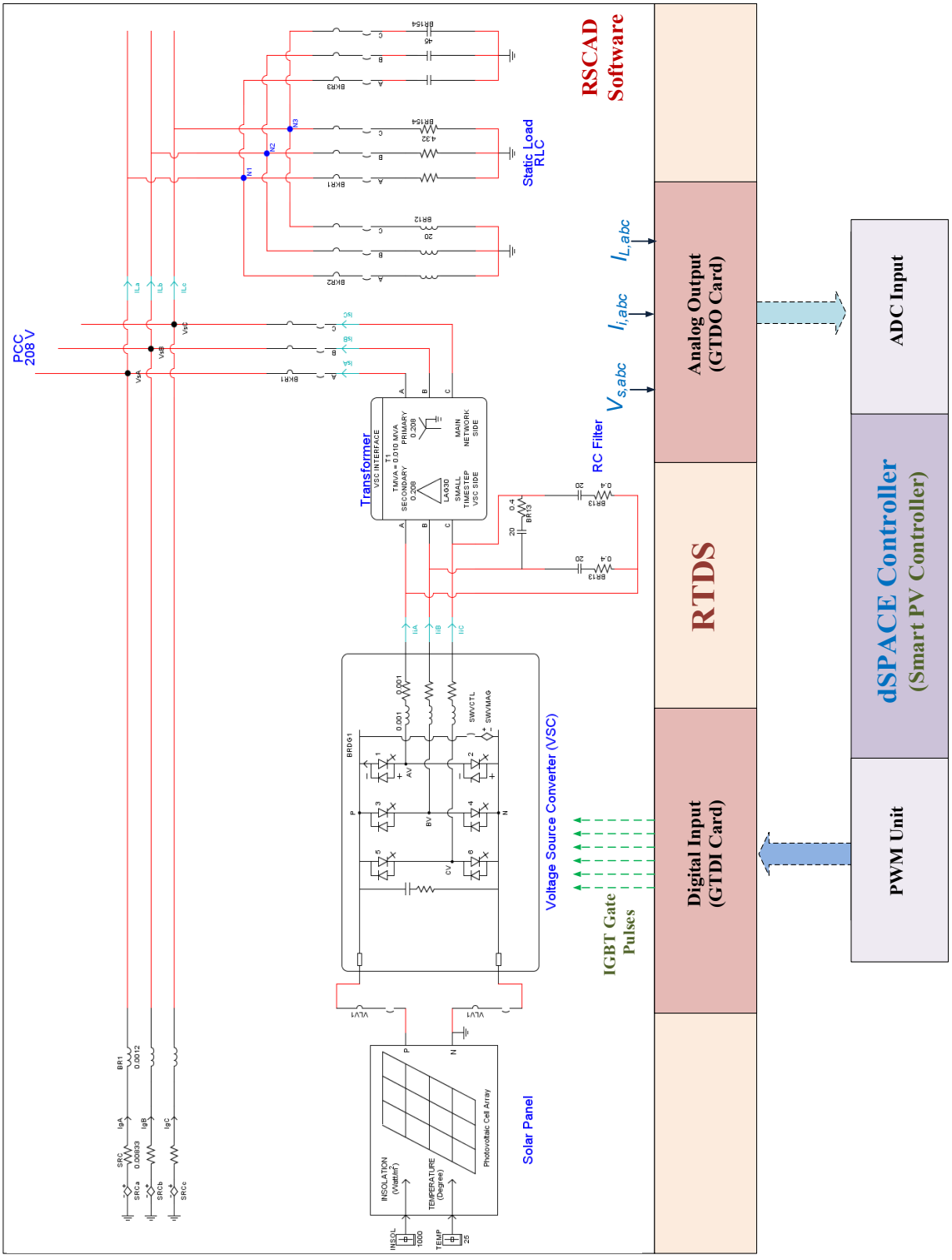

Figure 4-1: HIL structure of the smart PV inverter with RTDS and dSPACE

4.6 Modeling of Smart PV Controller in MATLAB/Simulink

To implement the smart PV inverter controller algorithm on the dSPACE controller board, MATLAB/Simulink software is used. In Simulink model, the input signals are assigned to specific analog-to-digital (ADC) channels. In other words, the PCC voltage, inverter current, load current and DC link voltage are received by ADC channels from RTDS output card. The controller is modeled based on the design description in Sec. 2.7. The simplified model of the smart PV controller in Simulink shown in Appendix B. 2.

4.7 Graphic User Interface Design

To monitor the network parameters such as voltages, currents and powers, a graphic user interface (GUI) is designed in RSCAD-Runtime software. Also, the designed GUI can provide an environment to apply certain changes to the network such as connecting or disconnecting loads. A view of the designed GUI in RSCAD shown in Appendix B. 3.

Another GUI software is designed in ControlDesk software to apply different operating modes and control objectives on the controller implemented on the dSPACE board. Also, all voltages, currents and powers can be monitored through the designed GUI. This GUI is the main interface to define the controller objectives. Appendix B. 4 illustrates the designed GUI in ControlDesk software.

4.8 HIL Study Results

In this section, the results of HIL study are demonstrated for Partial and Full STATCOM operating modes of smart PV inverter. The control objectives are power factor correction, voltage control and reactive power control for partial STATCOM mode whereas the objective is voltage control for full STATCOM mode. Appendix B. 5 shows the HIL setup for this study.

4.8.1 Smart PV Inverter Operation in Partial STATCOM Mode

In partial STATCOM mode, the controller uses the remaining capacity of the inverter to perform the different control functions. In other words, the remaining capacity of the

inverter is used in order to perform power factor correction, voltage control and reactive power control.

4.8.1.1 Power Factor Correction

For the power factor correction test, the active and reactive loads are considered 6 kW and 4.5 kvar whereas the active power generation of PV is 3 kW. Figure 4-2 (a)-(c) illustrate the power factor, phase "A" of PCC voltage (V_{sa}) and phase "A" of grid current (I_{ga}). As shown in Figure 4-2 (a), the power factor is about 0.5 when the PV system generates only active power. After the smart PV inverter controller is activated at t=0.020 sec, the power factor improves to unity in half a cycle. Also, Figure 4-2 (b) and (c) reveal that the current and voltage come in phase after the controller is activated. The PCC voltage (V_{sa}) is boosted based on the reactive power injection of smart PV inverter. Also, the grid current (I_{ga}) is reduced due to the reactive power compensation by PV-STATCOM system.

Figure 4-3 (a) and (b) show the reactive power and active power, respectively. Before power factor control activation, the load reactive power (Q_{load}) is about 4.5 kvar whereas reactive power of the PV-STATCOM ($Q_{STATCOM}$) is only due to the harmonics filter. Hence, most portion of the load reactive power is supplied from the grid (Q_{grid}). When the power factor correction mode is activated through the dSPACE GUI, the PV-STATCOM system exchanges same amount of load reactive power to obtain unity power factor. It should be noted that due to reactive power injection of the PV-STATCOM, the PCC voltage is enhanced. As a consequence, the active load (P_{load}) and reactive load (Q_{load}) are increased as the load type is constant impedance. The 6 kW active load (P_{load}) is now supplied by both PV-STATCOM system and grid. The active power of the PV-STATCOM ($P_{STATCOM}$) is stabilized after reactive power transient.

Figure 3-7 and Figure 4-2 reveal that the HIL results and software study results are similar in transient and steady-state.

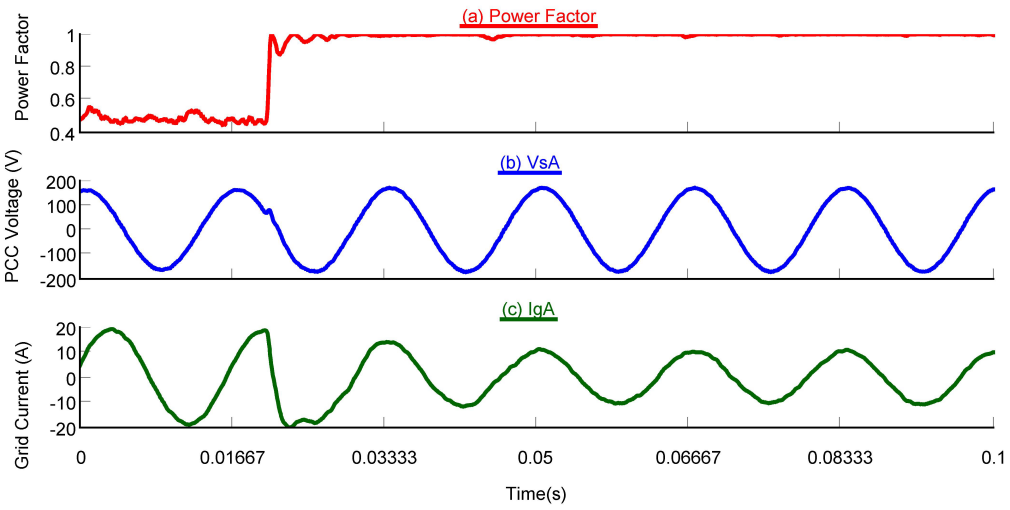

Figure 4-2: HIL results for smart PV inverter performance in partial STATCOM mode for power factor correction

a) Power Factor b) PCC voltage (phase A) c) Grid current (phase A)

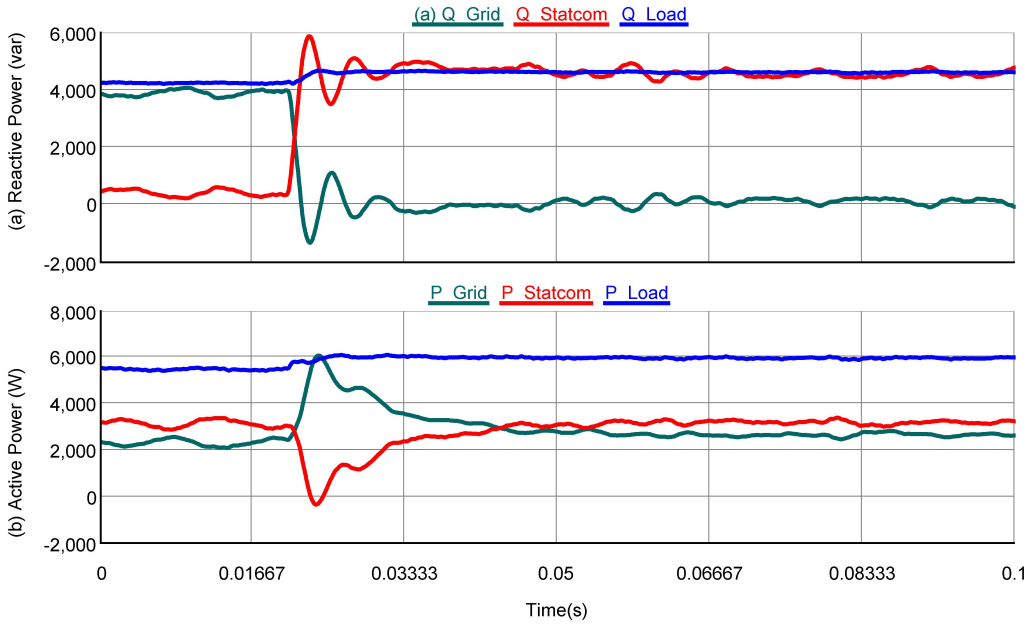

Figure 4-3: Active and reactive powers for smart PV inverter performance in partial STATCOM mode for power factor correction

a) Reactive power b) Active power

4.8.1.2 Voltage Control

This section presents the voltage control performance of the smart inverter controller operation in partial STATCOM mode. The controller performance is assessed for both capacitive and inductive operation regions. The voltage control study is performed while the PV system generates 3 kW active power.

4.8.1.2.1 Capacitive Mode of Operation

In this test, the active and reactive loads are 7 kW and 3 kvar, respectively. The reference value of the PCC voltage is changed in a step to 1.05 pu in the designed Control Panel of GUI. Figure 4-4 (a) and (b) depict the per-unit (*V_PCC(pu)*) and *abc* forms (*VsA, VsB* and *VsC*) of the PCC voltage. The PCC voltage rises up after the command is applied through the Control Panel. The controller precisely tracks the reference command (1.05 pu) in less than one cycle.

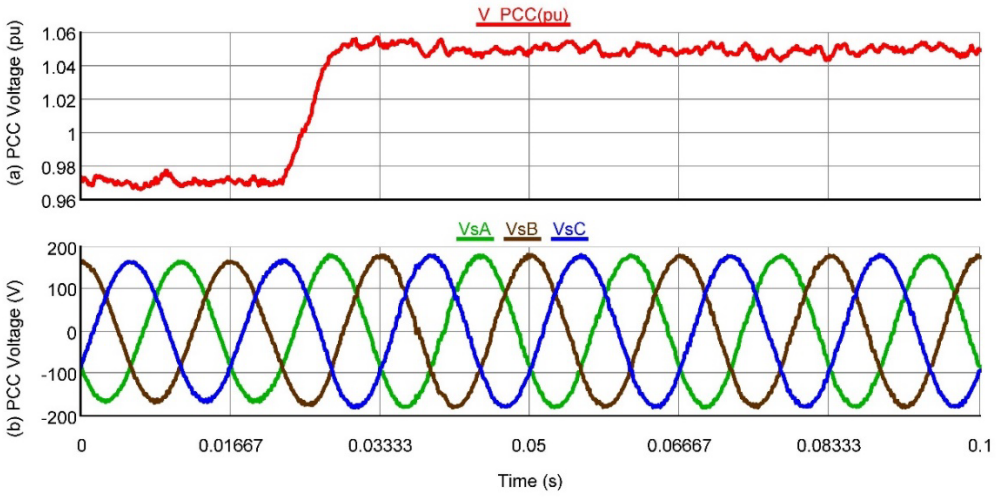

Figure 4-4: PCC voltage for smart PV inverter operation in Partial STATCOM mode for voltage control in capacitive mode

a) *rms* voltage in per-unit b) instantaneous voltage waveforms

Also, the grid current (I_g), smart PV system current (I_s), inverter current (I_i), load current (I_L) and DC link voltage (V_{dc}) are shown in Figure 4-5 (a)-(e). Figure 4-5 (a) shows the grid current changes due to change in PV current. Also, Figure 4-5 (b) and Figure 4-5 (c) validate the harmonic filter performance. The controller exchanges more reactive current

to track the reference voltage. Figure 4-5 (e) reveals that the DC voltage controller regulates the DC link voltage at reference value (400 V) accurately.

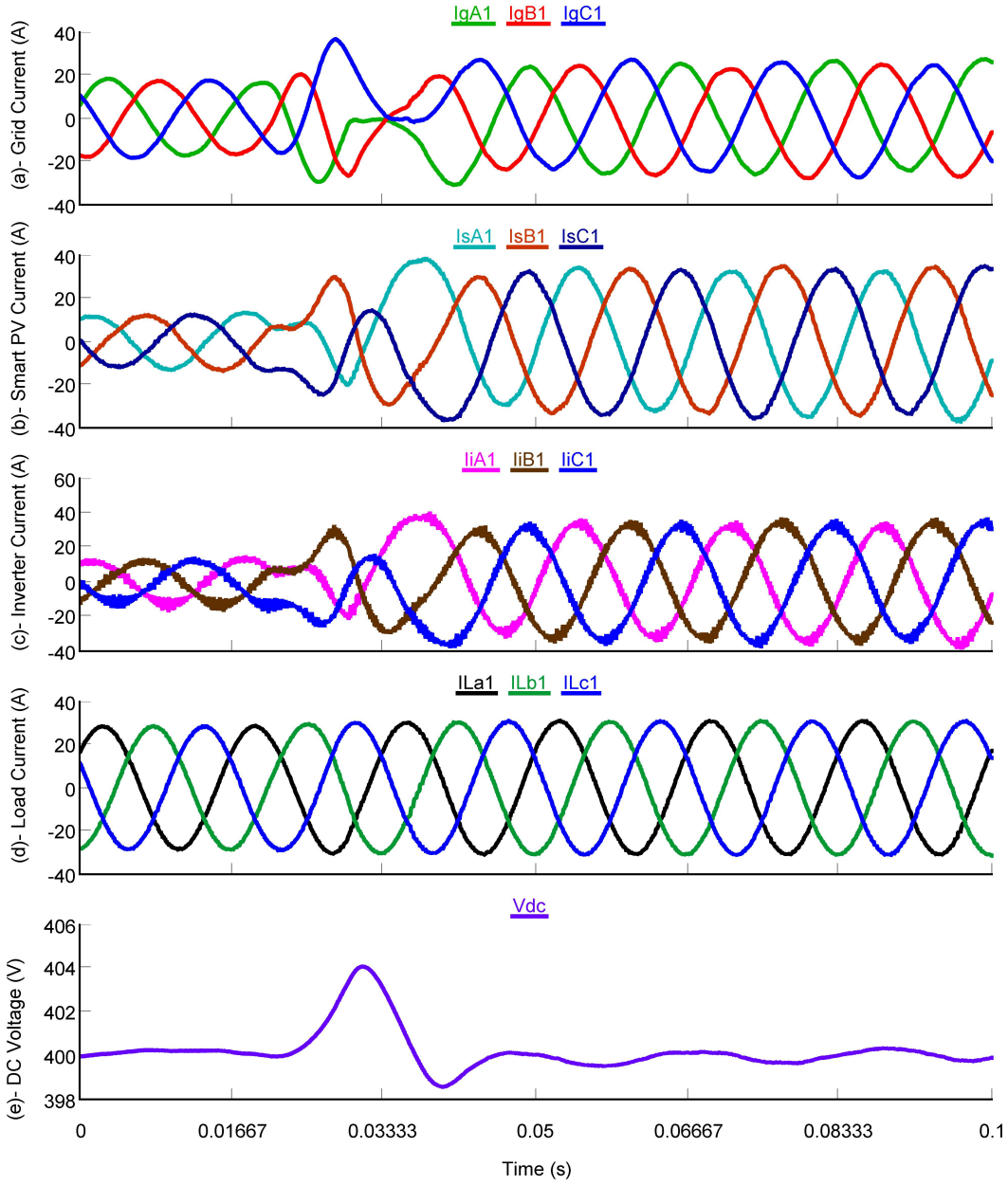

Figure 4-5: HIL results for smart PV inverter operation in Partial STATCOM mode for voltage control in capacitive mode

a) Grid current **b) Smart PV current** **c) Inverter PV current**
d) Load Current **e) DC link voltage**

4.8.1.2.2 Inductive Mode of Operation

In inductive mode of voltage control, the smart PV inverter controller reduces the PCC voltage by absorbing reactive power. However, the required reactive power is absorbed utilizing the remaining capacity of the inverter. In this mode, the generation of active power is at higher priority than voltage control. Figure 4-6 (a) and (b) show the PCC voltage ($V_{\_PCC(pu)}$) in per-unit and in *abc* frame (V_{sA}, V_{sB} and V_{sC}), respectively. To validate the controller performance for the inductive operation, the reference value of the voltage is changed in a step from 1.05 pu to 0.94 pu through the Control Panel of the designed GUI. As shown in Figure 4-6 (a) and (b), the voltage tracks the reference value in about one cycle. Therefore, the smart PV inverter controller effectively controls the PCC voltage in inductive region with the partial capacity of the inverter.

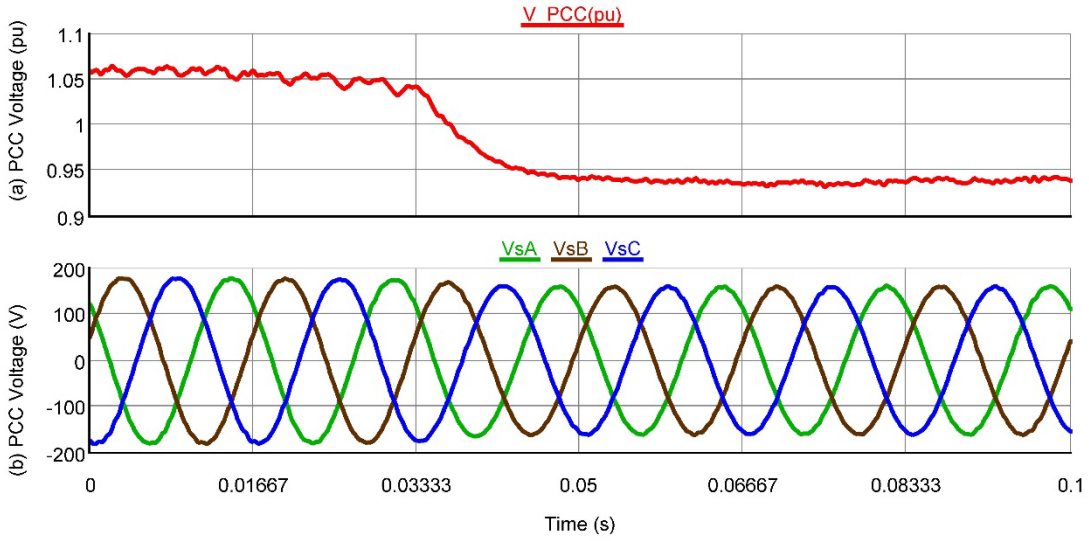

Figure 4-6: PCC voltage for smart PV inverter operation in Partial STATCOM mode for voltage control in inductive mode

a) *rms* voltage in per-unit **b) instantaneous voltage waveforms**

4.8.1.3 Reactive Power Control

Another control objective that can be achieved utilizing the partial capacity of the inverter is the reactive power control. Figure 4-7 (a) and (b) illustrate the reactive and active powers of the grid, load and PV system, respectively. As shown, the reactive power of the PV system ($Q_{STATCOM}$) changes from -5 kvar inductive to +8 kvar capacitive by means of the

designed GUI. It should be noted, as the constant impedance loads are considered for this test, the active load (P_{Load}) and reactive load (Q_{Load}) change due to voltage variations. The active load is supplied by 3 kW power of the PV-STATCOM system ($P_{STATCOM}$) and rest of the power requirement of the load is delivered by the grid (P_{grid}).

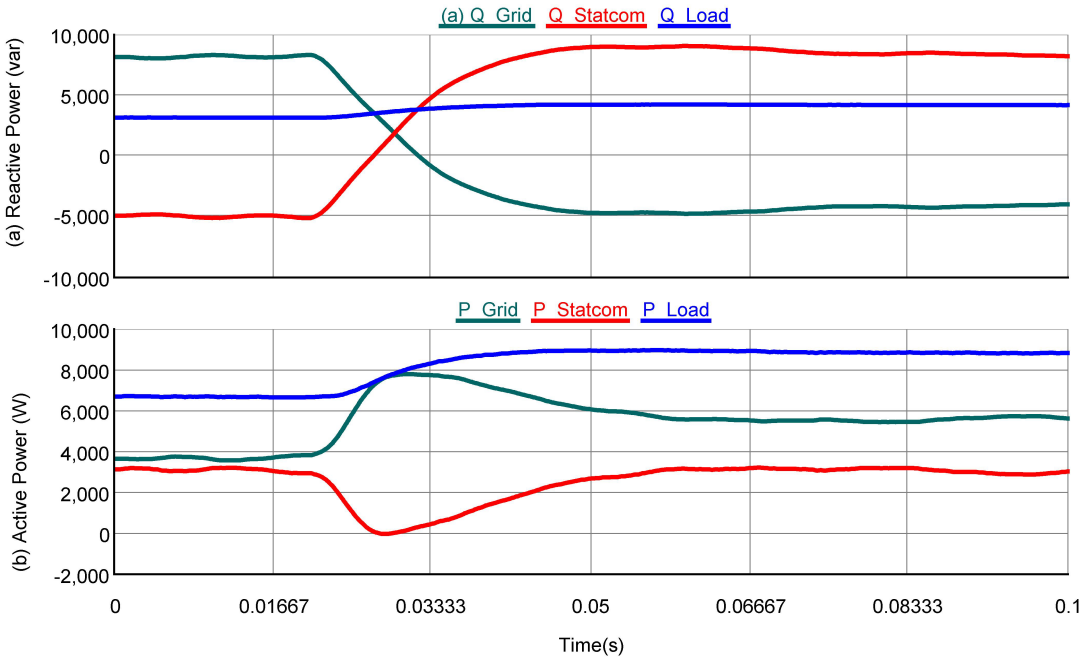

Figure 4-7: Variations in Power for smart PV inverter operation in Partial STATCOM mode for reactive power control

a) Reactive power b) Active power

The PCC voltage (V_s), grid current (I_g) and PV-STATCOM current (I_s) are shown in Figure 4-8 (a)-(c) for reactive power control in partial STATCOM mode. It is shown that the PCC voltage increases due to capacitive reactive power. Also, the PV-STATCOM system exchanges more current (I_s) to meet the control objective.

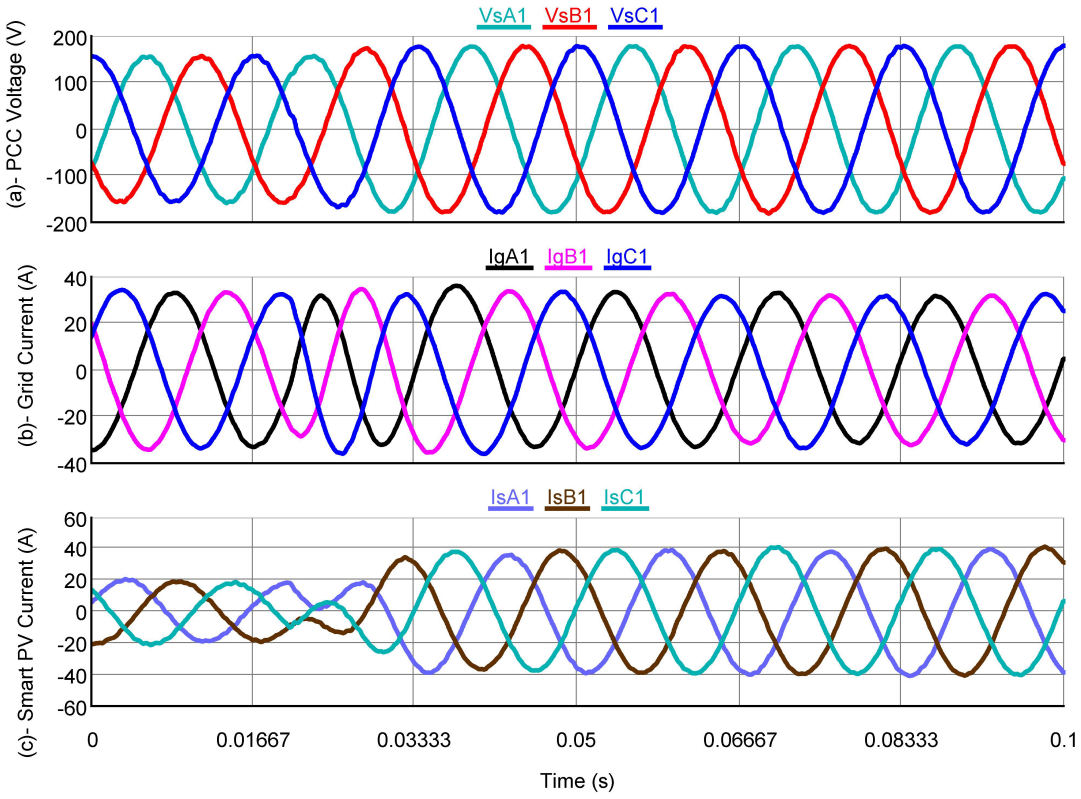

Figure 4-8: Simulation results for smart PV inverter operation in Partial STATCOM mode for reactive power control

a) PCC voltage b) Grid current c) Smart PV current

4.8.2 Smart PV Inverter Operation in Full STATCOM Mode

For validating the controller performance during full STATCOM mode of operation, a large load is connected in the designed network model inside the RTDS. This load is connected through the designed GUI in RSCAD-Runtime. For this study, the power generation of the conventional PV system is set to 3 kW. Figure 4-9 (a) and (b) show the changes of PCC voltage while the large load (8 kvar) is connected to the grid suddenly. The PCC voltage ($V_{\_PCC}$) reduces from 0.96 pu to 0.85 pu. According to the utility requirements, the voltage cannot be below 0.94 pu. In other words, the large load causes the voltage to decrease below the acceptable range. By replacing the conventional controller with the novel smart inverter controller, the smart PV controller transitions from the conventional Full PV mode to Full STATCOM mode to control voltage and mitigate

the voltage drop. Figure 4-10 (a) and (b) demonstrate the PCC voltage as per- unit ($V_{\_PCC}$) and *abc* waveforms (V_s) respectively.

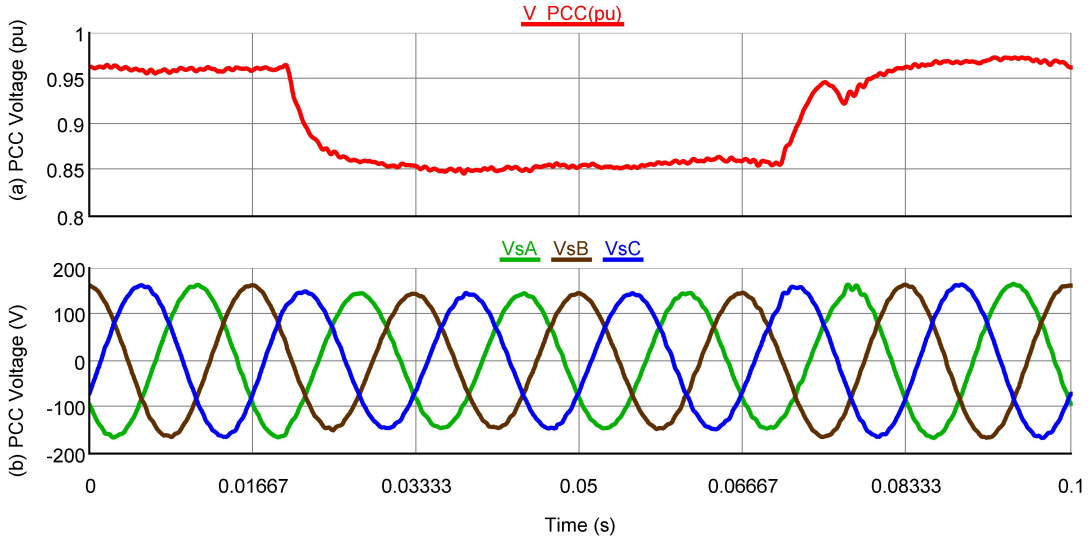

Figure 4-9: PCC Voltage in presence of large load, without the smart inverter controller

a) *rms* voltage in per-unit **b) instantaneous voltage waveforms**

Before the large load connection, the PCC voltage is about 0.96 pu. The large amount of load is connected suddenly at *t=0.02* sec. The smart inverter controller disconnects the solar panel from the inverter and uses the entire capacity of the inverter to maintain the voltage at the same value as in the pre-fault condition. Figure 4-10 (b) reveals that the controller regulates the voltage at the desired value in one cycle, approximately.

By considering Figure 4-10 (a) and Figure 3-12 (a), the PSCAD software study and HIL results are compared for full STATCOM mode operation mode. In both the studies, the PCC voltage is increased after the transient dip in the voltage. The software and HIL studies confirm that the response time of the controller is about one cycle for voltage regulation.

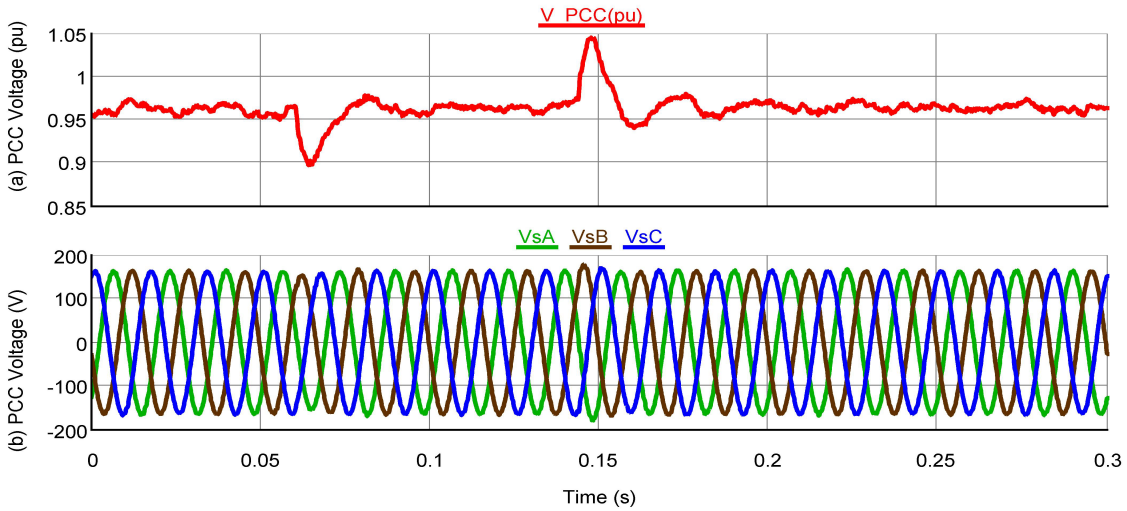

Figure 4-10: PCC voltage control with full STATCOM operation

a) *rms* voltage in per-unit b) instantaneous voltage waveforms

Figure 4-11 depicts the active power ($P_{\_PVSTATCOM}$) and reactive power ($Q_{\_PVSTATCOM}$) of the PV-STATCOM system in full STATCOM operation mode. After connection of the large load, the controller disconnects the solar panel, and consequently, the active power ($P_{\_PVSTATCOM}$) falls to zero. The full capacity of the inverter is used for voltage control. Figure 4-11 clearly shows that during large load connection, the active power of the PV-STATCOM ($P_{\_PVSTATCOM}$) system is almost zero whereas the reactive power ($Q_{\_PVSTATCOM}$) is 8.5 kvar. When the network returns to normal condition, the smart inverter controller returns to full PV mode of operation. The controller connects the solar panels and the active power returns to pre-fault value (3 kW) whereas the reactive power output of the PV system is reduced to zero.

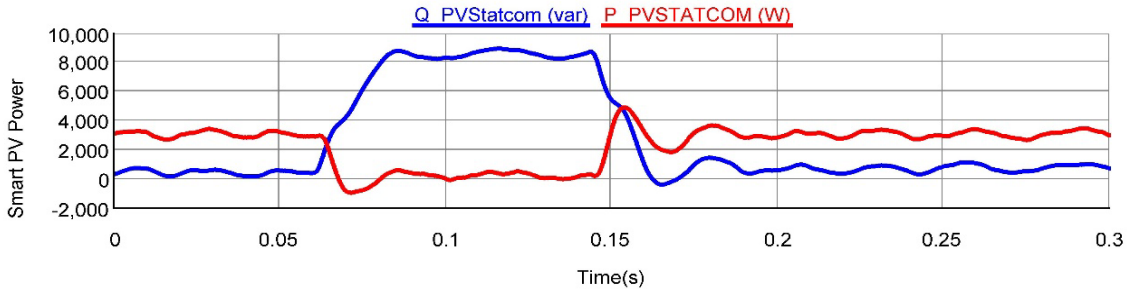

Figure 4-11: Active and reactive powers of smart PV inverter operation in Full STATCOM mode for voltage control

4.9 Conclusion

This chapter presents the Hardware-In-Loop (HIL) studies of the novel smart PV inverter controller with the Real-Time Digital Simulator (RTDS) and dSPACE Controller board. The study network is developed in RSCAD software and implemented on RTDS. The smart PV inverter controller is designed in MATLAB/Simulink and uploaded on the dSPACE controller. To control and monitor the RTDS and dSPACE models, two different graphic user interfaces (GUI) are designed in RSCAD-Runtime software and ControlDesk software, respectively. The operation mode, control objective, reference value of DC and AC voltages are set by the GUI in ControlDesk. The network changes such as load switching, etc. are applied by GUI in RSCAD. The output of the RTDS such as PCC voltage, inverter current, load current and DC link voltage are sent to ADC channel of the dSPACE controller board through GTAO card whereas the switching pulses outputted by the dSPACE controller are sent to the RTDS through GTDI card.

The HIL study is performed on the smart inverter controller for both partial STATCOM and full STATCOM modes of operation. This HIL study validates the real-time performance of the controller for different control objectives. During partial STATCOM mode, the controller uses the remaining capacity of the inverter to control voltage or correct power factor. In full STATCOM operation mode, the controller disconnects the solar panel to provide voltage support to the network utilizing the full capacity of the inverter. The controller disconnects the solar panel by sending a command to RTDS through DAC channel of the dSPACE board. The HIL study presented in this chapter verifies the effectiveness of the proposed novel smart PV inverter controller in real-time for both transient and steady-state conditions.

CHAPTER 5

5 LAB VALIDATION OF SMART PV INVERTER PERFORMANCE

5.1 Introduction

One of the main objectives of this thesis is to develop a laboratory-validated model of the novel smart inverter control in both Partial and Full STATCOM modes. This chapter presents the lab implementation and validation of the smart PV inverter for both the two STATCOM modes of operation. The design of the different controller parameters in the smart inverter has been described in Sec.2.7. The study system is modeled in the Power Systems Lab at Western University. This lab validation is the final stage of testing before its proposed installation in the utility network feeder.

5.2 Lab Modelling of Study System

Figure 5-1 depicts the single-line diagram of the lab setup for the study system. The short circuit impedance of the network and line impedance are represented by R_g and L_g. A 10kVA interface transformer is used for interconnection of the PV system to the PCC. The transformer configuration is Delta/Wye whereas the Delta winding connection is located on the inverter side. A 10 kVA IGBT-based full bridge is utilized to operate as a voltage source inverter. To remove the ripples due to the switching frequency, an LCL filter is installed after the inverter. The filter inductor is in series with the inverter and the filter capacitor is in shunt with Delta connected transformer winding. A 10 kVA PV Simulator is employed to simulate the behavior of the PV solar panels. The PV Simulator can generate variable real power based on the pre-settable temperature and irradiance profiles. Three types of loads, resistive, inductive and capacitive, having a total 10 kVA rating are used in the lab setup. Voltage and current sensors are designed to measure PCC voltage, inverter current, load current and DC link voltage. The sensor signals are delivered to dSPACE controller board through ADC channels. The smart PV inverter controller is implemented on dSPACE controller board, which generates appropriate firing pulses for the IGBT gates of the inverter based on control objectives and operation modes.

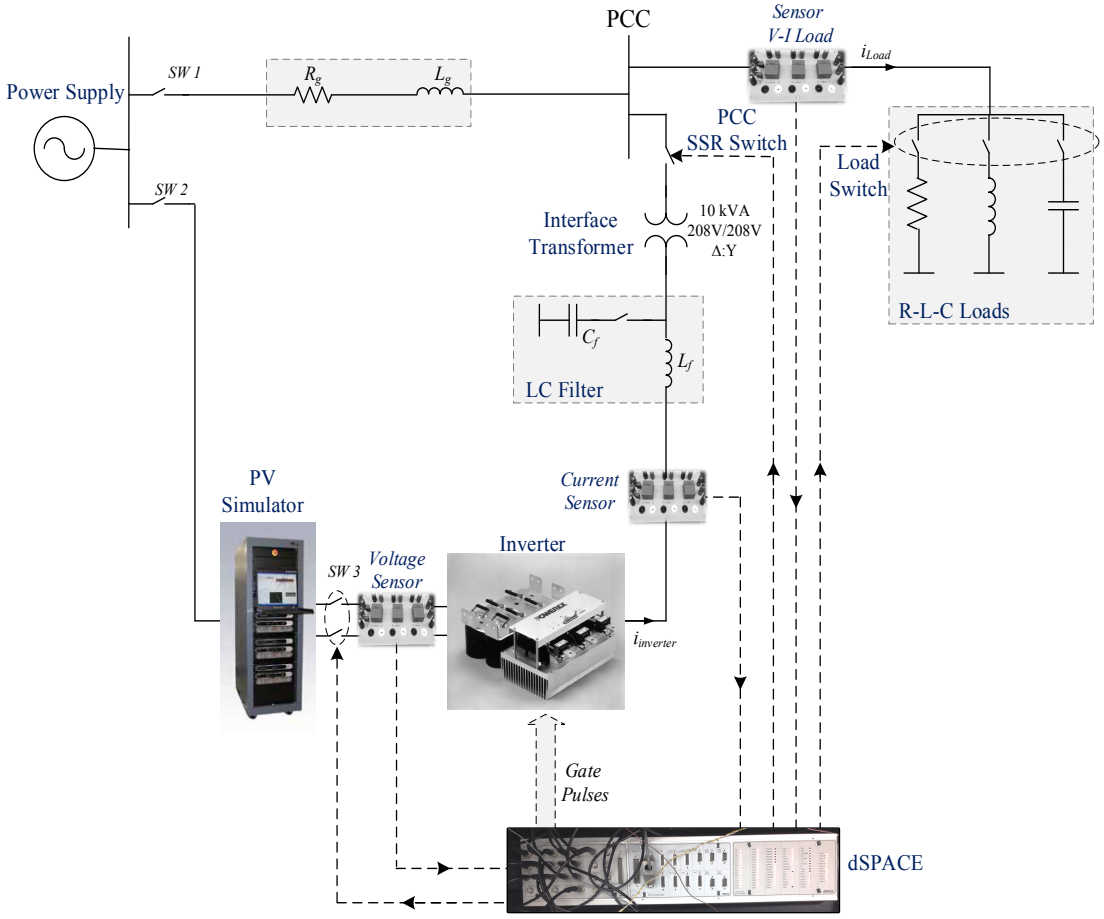

Figure 5-1: Lab setup of the study system with smart PV inverter

Figure 5-2 depicts the actual lab setup in Power Systems Laboratory of Western University. However, the inductive load and the interface transformer are not shown in this picture.

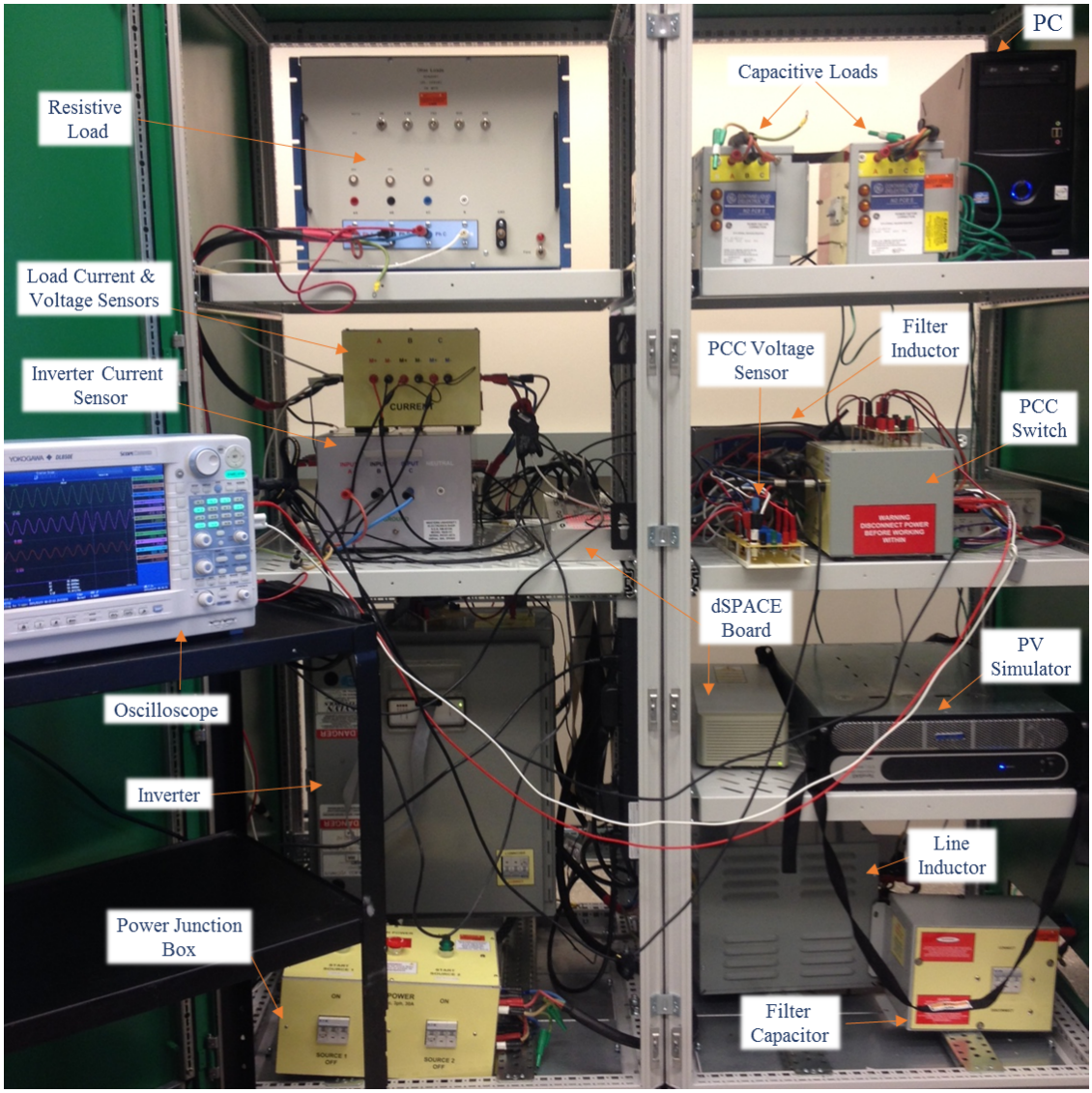

Figure 5-2: Actual lab setup of the study system with smart PV inverter

5.2.1 Overview of PV Simulator

The PV solar simulator is an integrated specialized computer system with a PV simulation engine. The Elgar TerraSAS PV solar simulator from AMETEK Programmable Power Inc., consists of a rack mounted controller, control system software, keyboard and GUI interface with a unique PV simulation engine that controls the output DC power supply. It has the capability to simulate different solar array *V-I* characteristics along with the flexibility to simulate different series/parallel combination of modules needed to meet the

operating voltage and power levels for grid tied photovoltaic inverters [153, 154]. The power rating of the PV Simulator is 10 kW. Appendix C. 1 shows the 10 kW PV Simulator. Figure 5-3 (a) and (b) show the characteristics of the PV Simulator. Figure 5-3 (a) shows the irradiance change with a fast ramp function for an ambient temperature of 25ºC. The maximum irradiance is chosen to be 1000 W/m^2. Also, Figure 5-3 (b) illustrates the current-voltage curve of the solar panels. The open-source voltage and short circuit current of the solar panels are 440 V and 17 A, respectively. The *V-I* curve of the solar panel also changes as a function of irradiance.

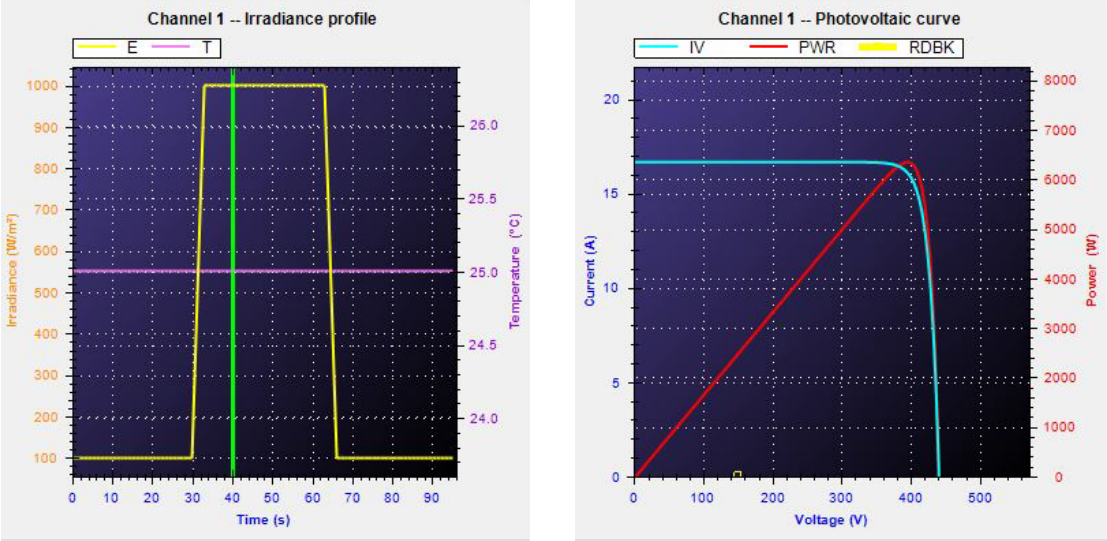

(a) (b)

Figure 5-3: Specified profiles of solar panel in PV Simulator

a) Temperature and irradiance profiles
b) Current- voltage and power-voltage curves

5.2.2 Voltage and Current Sensors

The voltage and current sensors observe the value of PCC voltage, inverter current, load current and DC link voltage, instantaneously. A current transducer with capability of 50 A (*rms*) is chosen as the current sensor. The frequency bandwidth and response time of the sensor are the two vital factors that effect on the controller performance. Hence, a specific current transducer is used with 200 kHz bandwidth and 1 µs response time. A voltage transducer with maximum capability 500 V and 40 µs response time is used for sensing

PCC voltage and DC link voltage. The output of the both current and voltage sensor boards are designed to be ±10V to be compatible with the voltage level of analog-to-digital (ADC) channels of the dSPACE.

5.2.3 Inverter

A two-level three phase IGBT power module supplied by Powerex with a rating 600 V and 100 A is chosen as the PV system inverter. The pulses for the IGBT gates are provided by dSPACE controller based on the control objectives. It should be noted that the voltage level of the PWM unit of the dSPACE controller is ±5V whereas the gate driver operates with ±15V. Hence, an interface voltage level shifter is designed to provide suitable voltage for gate driver of the IGBT. Similar to simulation studies and HIL study, the switching frequency is chosen 10 kHz for the actual inverter. Since, the IGBT switches are not ideal switches, the turn-off time and turn-on time of the switch are not equal. Hence, it is recommended to add dead-band time to avoid bridge shoot through. The dead-band time ensures that one IGBT switch will be off before another one turns on. Typically, the dead-band time is calculated based on time difference of turn-on time and turn-off time [155]. The actual inverter turn-on time is 100 ns and turn-off time is 300 ns [156, 157]. Two times of the difference time ensures the safety margin for the IGBT switches. Therefore, the dead-band time is chosen 400ns for the PWM signals. Appendix C. 2 presents a description of the three-phase IGBT module used in this research.

5.2.4 Harmonics Filter

To remove the switching harmonics from the waveforms, an LCL filter is used between inverter and PCC. A three-phase inductor with 1.2 mH inductance and 30 A rating is connected in series with the inverter. The turn-on resistance of the IGBT switch is considered as the series filter resistor. The filter capacitor is connected in shunt with Delta configuration of the transformer. The leakage inductance of the interface transformer is considered as the second inductor for the filter unit.

5.2.5 Interface Transformer

A 10 kVA transformer with Delta/Wye-grounded configuration is connected between the PCC and entire PV solar system. The main purpose of the transformer is to provide isolation between the PV system and grid. The leakage impedance of the transformer is 0.05 pu, as given by the manufacturer.

5.2.6 PCC Switch

The PCC connection switch is a three-phase solid state relay (SSR) with capability of 50 A [158]. The PCC switch turns to "Connected" state via the user command from the designed GUI in dSPACE software. When the PLL controller detects the phase angle of the PCC voltage properly, the GUI software will indicate that the PV system is able to connect to the grid. The SSR switch controls with a command signal having 0-15 V DC voltage level. As the output of the digital-to-analog (DAC) channels of the dSPACE are up to 10 V, an interface level shifter with capability of high current injection is designed with an optocoupler IC [159]. Optocoupler IC isolates the dSPACE controller from the SSR switch and it reduces the risk of controller damage due to high current injection.

5.2.7 Passive Load

Similar to previous studies, passive loads are considered in the lab implementation study. Three 10 kVA resistive, inductive and capacitive loads are connected to the PCC in parallel. The resistive and inductive load are connected with Wye-grounded configuration whereas the capacitive load is with Delta configuration.

5.3 Controller Design in MATLAB/Simulink

Similar to HIL study, the controller is designed in MATLAB/Simulink software and implemented on dSPACE controller board. The simplified controller design in MATLAB/Simulink is explained in Appendix B. 2. The outputs of current and voltage sensors are assigned to specific ADC. Also, the PWM pulses out of the dSPACE board are applied to the inverter interface panel through the level shifter circuit. To apply connect/disconnect command to PCC switch and load switch, DAC of the dSPACE are

used. The designed GUI in ControlDesk software provides the environment to supervise the PV system operation. Appendix B. 4 shows the designed GUI in ControlDesk software.

The control objectives and operation modes are defined in Control Panel of the GUI model. The controller can be set to operate as PV, STATCOM or PV-STATCOM. Also, control objectives such as voltage control and power factor correction can be specified by the Control Panel of GUI. The PCC voltage, inverter current, load current, active and reactive power and DC link voltage can be monitored in the GUI. The reference value for the DC link voltage and PCC voltage can be set to desired magnitudes. Also, the GUI is designed to monitor control variables in *d-q* frame. Therefore, the PLL performance can be validated by monitoring the PCC voltage in *d-q* frame. While the controller operation is set to PV system, the *q*-current loop keeps the reactive current at zero level. Therefore, the PV system only generates active power alike conventional PV system. Voltage control and power factor correction are activated when the PV-STATCOM operation mode is chosen. The controller either controls PCC voltage or performs power factor correction based on the control objectives. Also, the full STATCOM mode operation can be activated in Control Panel of GUI. If voltage suddenly drops and the reactive power requirement is more than the remaining capacity of the inverter, the controller limits the active current and operates as STATCOM. In full STATCOM operation, controller automatically defines voltage control as the control objective.

5.4 Startup Procedure for the Lab Test

Before connecting the PV system to the grid, the PLL controller needs to extract the phase angle of PCC voltage to synchronize the PV system parameters with grid parameters. Besides PLL performance, another vital factor for grid connectivity of the PV system is the in-rush current. When PCC switch connects the PV system to the grid, DC link capacitor charging starts with an inrush current. As the magnitude of inrush current is very large compared to the rating of other components, it can damage those components. Therefore, before connecting the PCC switch, the DC link capacitor is charged by PV Simulator to a level below the level which is defined by rectifier operation of full bridge module. When the IGBT gates of full bridge module are off and the full bridge is connected

to the grid, the DC capacitor of the full bridge charges to a level given by the following equation:

$$V_{dc} = \frac{3\sqrt{3}}{\pi} V_{ac,peak} \tag{5.1}$$

With 208 V line-to-line voltage the peak voltage of phase voltage is about 169.8 V. By substituting peak voltage in (5.1), the DC link capacitor is charged through inverter diodes to 280 V when IGBTs are off. Finally, the DC link capacitor charges up to 280 V by PV Simulator and then PCC switch is connected. After PV system connectivity to the grid is established, the PWM signals can be enabled to follow the control objectives. It should be noted that it is a necessity to control the DC link voltage at a certain level to control PCC voltage based on equation (2.7) .

5.5 Lab Implementation Results

This section demonstrates lab test results of the study system for partial and full STATCOM operation modes of the PV system. For partial mode, power factor correction and voltage control are considered as control objectives whereas voltage control with full inverter capacity is the sole control objective in full STATCOM mode. For all lab experiments, the oscilloscope channel #1 (*CH1*) is grid current (phase "A"), channel #2 (*CH2*) is PCC voltage (phase "A"), channel #3 (*CH3*) is PV system current (phase "A") and channel #5 (*CH5*) is load current (phase "A"). Also, for demonstrating the power flows, the active and reactive powers of the grid, PV system and load are shown before and after enabling the controller. In all following experiments, *P1* represents active power of grid for phase "A", *P2* is active power of PV system for phase "A" and *P3* is active power of load for phase "A". Also, *Q1*, *Q2* and *Q3* represent reactive power of grid, PV system and load for phase "A", respectively. Therefore, the total active power flow and reactive power flow are three times of phase "A". The time scale of the oscilloscope is set to 20 *ms/div*.

5.5.1 Partial STATCOM mode

The partial STATCOM tests assess the controller performance while both active and reactive power flows in the PV system. The controller performance is validated for power

factor correction, voltage control for both inductive and capacitive regions, and the effects of changes in active power.

5.5.1.1 Power Factor Correction

For the power factor correction test, the PV output is set at 3 kW by controlling the DC link voltage at 425 V based on Figure 5-3 (b). The active and reactive loads are considered to be 6 kW and 3 kvar, approximately. Figure 5-4 illustrates the PCC voltage, grid current and PV system current.

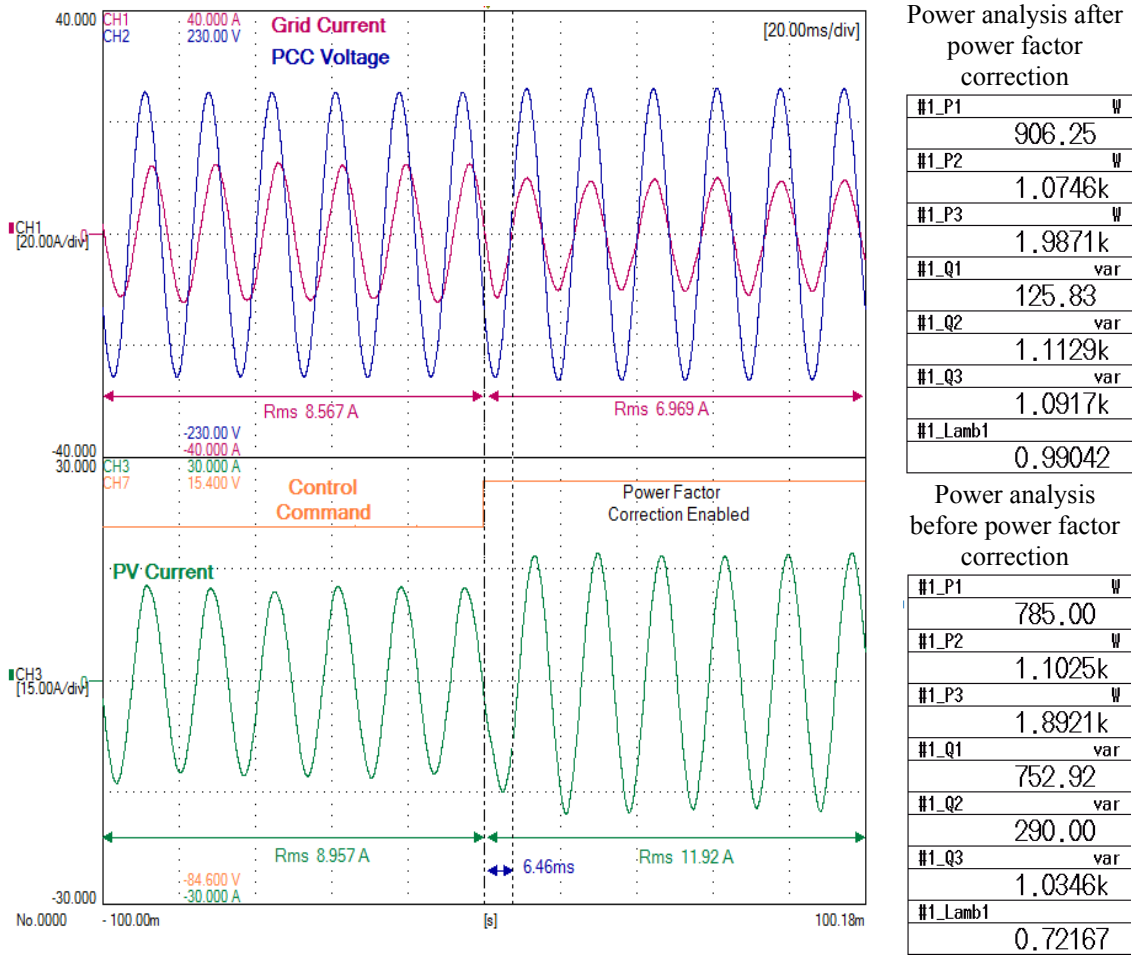

Figure 5-4: Lab results for smart PV inverter operation in Partial STATCOM mode for power factor correction

In Figure 5-4, Lamb1 represents power factor of the grid. It is shown that while the PV system operates as the conventional PV system with 3 kW PV active power, the power factor of the grid is about 0.72 lagging due to 6 kW and 3 kvar loads. In other words, the

entire reactive power of the load is supported by the grid. Channel #7 (*CH7*) represents the control command by the user. The control command is applied by the user through the designed GUI to enable power factor correction mode. After the controller is enabled, the PCC voltage and grid voltage come in phase due to reactive power exchange from the PV system. Consequently, the PV system provides the required reactive power of the load and the grid reactive power (*Q1*) becomes almost zero. Figure 5-4 reveals that unity power factor achieved by the controller in less than half a cycle. Due to reactive power exchange, the PV system current (*CH3*) increased.

5.5.1.2 Voltage Control - Capacitive Mode

This test shows the operation of the PV system to control the PCC voltage with partial capacity of the inverter. The PV system power output is set to 3kW whereas the load power is 6 kW. Figure 5-5 demonstrates the experimental results of the voltage regulation by the smart PV controller. When PV system generates active power in the conventional mode of operation, the PCC voltage is about 0.94 pu (113 V_{rms}). The voltage drop is due to grid inductance and the 6 kW load. In the designed GUI the reference voltage is set to 1.025 pu (123 V_{rms}) to demonstrate the controller performance in capacitive region. The power analysis shows that the PV system reactive power is almost insignificant before voltage control. Channel #7 (*CH7*) represents the user command to enable voltage control mode via GUI. In Figure 5-5, the controller enhances the PCC voltage (*CH2*) to the reference value in about one cycle. The power analysis after enabling voltage control shows that the PV system generates approximately 9 kvar capacitive reactive power (*Q2*) to increase the grid voltage whereas the reactive power of the PV system is about 3 kW. It means that full inverter capacity is used for active and reactive power generation.

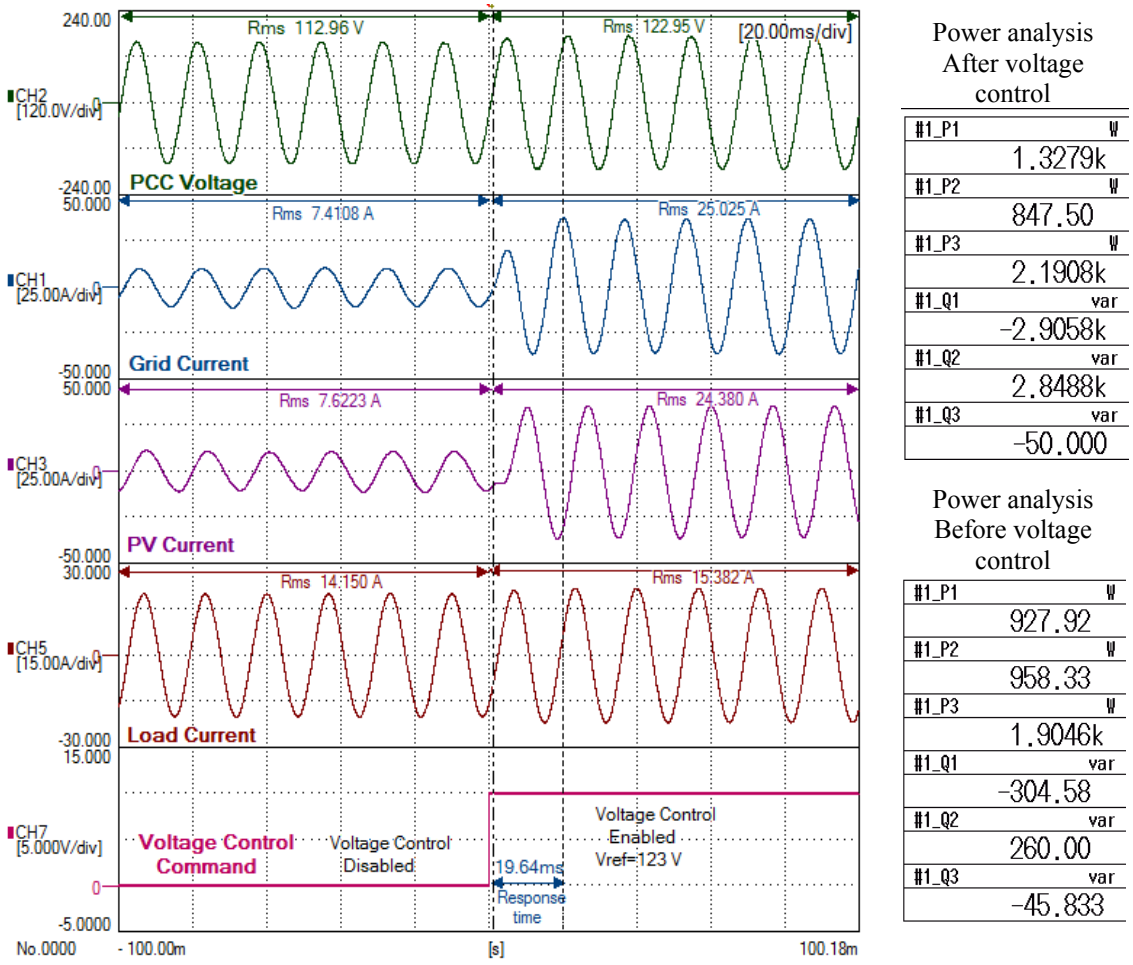

Power analysis
After voltage
control

#1_P1	W
	1.3279k
#1_P2	W
	847.50
#1_P3	W
	2.1908k
#1_Q1	var
	-2.9058k
#1_Q2	var
	2.8488k
#1_Q3	var
	-50.000

Power analysis
Before voltage
control

#1_P1	W
	927.92
#1_P2	W
	958.33
#1_P3	W
	1.9046k
#1_Q1	var
	-304.58
#1_Q2	var
	260.00
#1_Q3	var
	-45.833

Figure 5-5: Lab results for smart PV inverter operation in Partial STATCOM mode for voltage control in capacitive mode

5.5.1.3 Voltage Control – Inductive Mode

To show the controller performance for reducing an overvoltage, PV system active power (P2) is set to 6 kW by controlling DC link voltage at 400 V based on Figure 5-3 (b). The total active and reactive loads are considered 3 kW and 6 kvar capacitive. The experiment results of the partial PV system for voltage reduction are shown in Figure 5-6. The capacitive load and surplus PV generation causes the PCC voltage to increase up to 1.06 pu (127 V_{rms}). The power flow analysis before applying the voltage control shows that reverse power flows through the grid due to PV system generation and small active load consumption. The Controller starts to reduce the PCC voltage to 0.96 pu (116 V_{rms}).

Channel #7 (*CH7*) is triggered via GUI to change the controller objective to voltage control. It is shown that the PV system absorbs around 7 kvar inductive (*Q2*) to decrease the bus voltage. Subsequently, the PCC voltage (*CH2*) is reduced by controller from 1.06 pu to 0.96 pu (127 V_{rms} to 116 V_{rms}). The response time of the controller to track the reference voltage is about one cycle. Also, *CH3* shows that the PV system current is enhanced due to reactive current whereas the grid current is decreased.

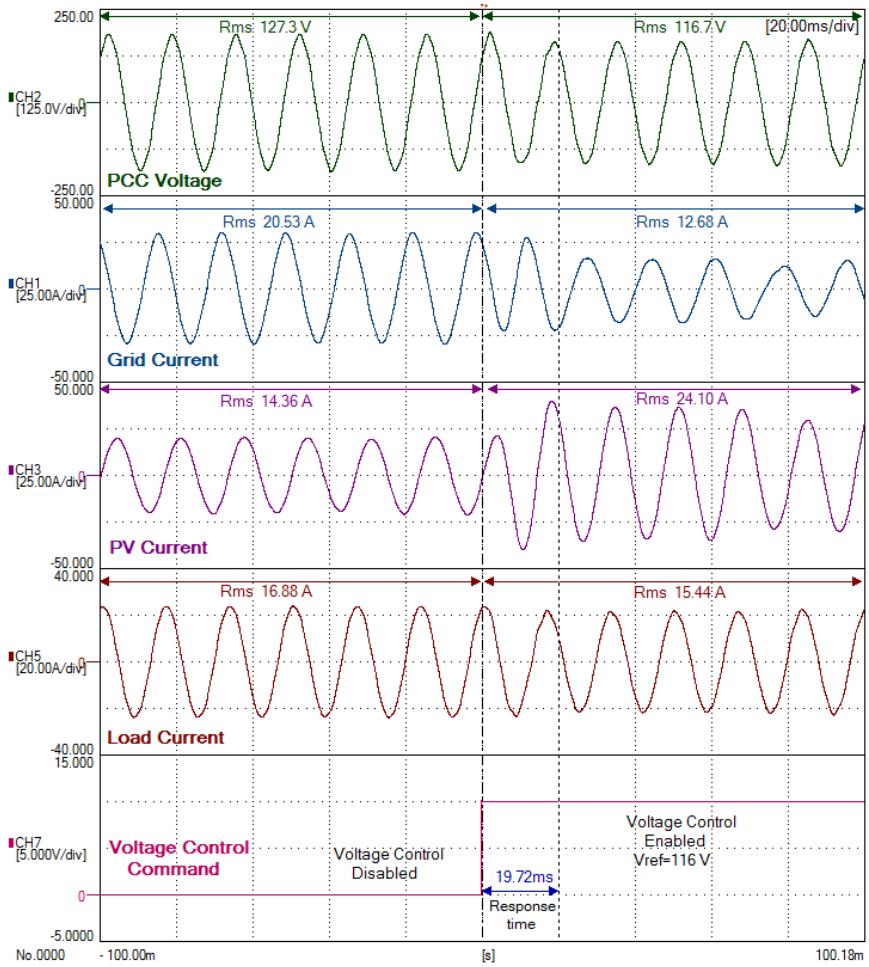

Power analysis
After voltage control

#1_P1	W
-1.4475k	
#1_P2	W
1.8958k	
#1_P3	W
443.75	
#1_Q1	var
450.42	
#1_Q2	var
-2.3833k	
#1_Q3	var
-2.0021k	

Power analysis
Before voltage control

#1_P1	W
-1.4746k	
#1_P2	W
1.9954k	
#1_P3	W
525.83	
#1_Q1	var
-2.5571k	
#1_Q2	var
288.33	
#1_Q3	var
-2.3375k	

Figure 5-6: Lab results for smart PV inverter operation in Partial STATCOM mode for voltage control in inductive mode

5.5.1.4 PV System Power Changes during Voltage Control

In the previous tests, the active power of the PV system is kept constant during voltage control. This test assesses the voltage control performance of the smart PV controller during active power changes of PV system. To change the active power of PV system the DC link voltage needs to be varied. By considering Figure 5-3 (b), the *I-V* curve and *P-V* curve reveal that the PV system power changes inversely with voltage between maximum power point voltage (V_{MPP}) and open circuit voltage (V_{OC}). In other words, within that specific region, solar panel produces more power at lower voltage. In this experiment, the active load and reactive load are set at 4.5 kW and 1.5 kvar, respectively. In this experiment, voltage control at 1 pu (120 V_{rms}) is considered as the control objective. While the PV system controls PCC voltage, the active power of the PV system changes from 6 kW to 3 kW. To generate 6 kW active power, the DC link voltage is controlled at 400 V whereas 3 kW active power needs 425 V.

Figure 5-7 depicts the experiment results of voltage control under PV power changes. Before changing the PV active power, the DC voltage set point is kept at 400 V to provide 6 kW active power. Simultaneously, the PV system uses remaining capacity of the inverter to maintain the PCC voltage at 120 V_{rms}. Power flow analysis shows that with 6 kW active power generation, 1.5 kW surplus power flows inversely in the grid due to 4.5 kW active load. To change the active power of the PV system, the reference value of the DC link voltage is set to 425 V. The command for the power changes is applied by GUI through channel #7 (*CH7*). The DC link voltage is shown in Channel #10 (*CH10*). It is seen that that the DC link voltage tracks the new reference value in less than two cycles. The active power of the PV system (*P2*) thus changes from 6 kW to 3 kW. Hence, the PV system current (*CH3*) gets reduced, and the grid provides more current to supply the load. Channel #2 (*CH2*) reveals that during active power changes of the PV system, the controller maintains the PCC voltage at 1 pu (120 V_{rms}). In other words, this test shows that the control of active and reactive powers are properly decoupled.

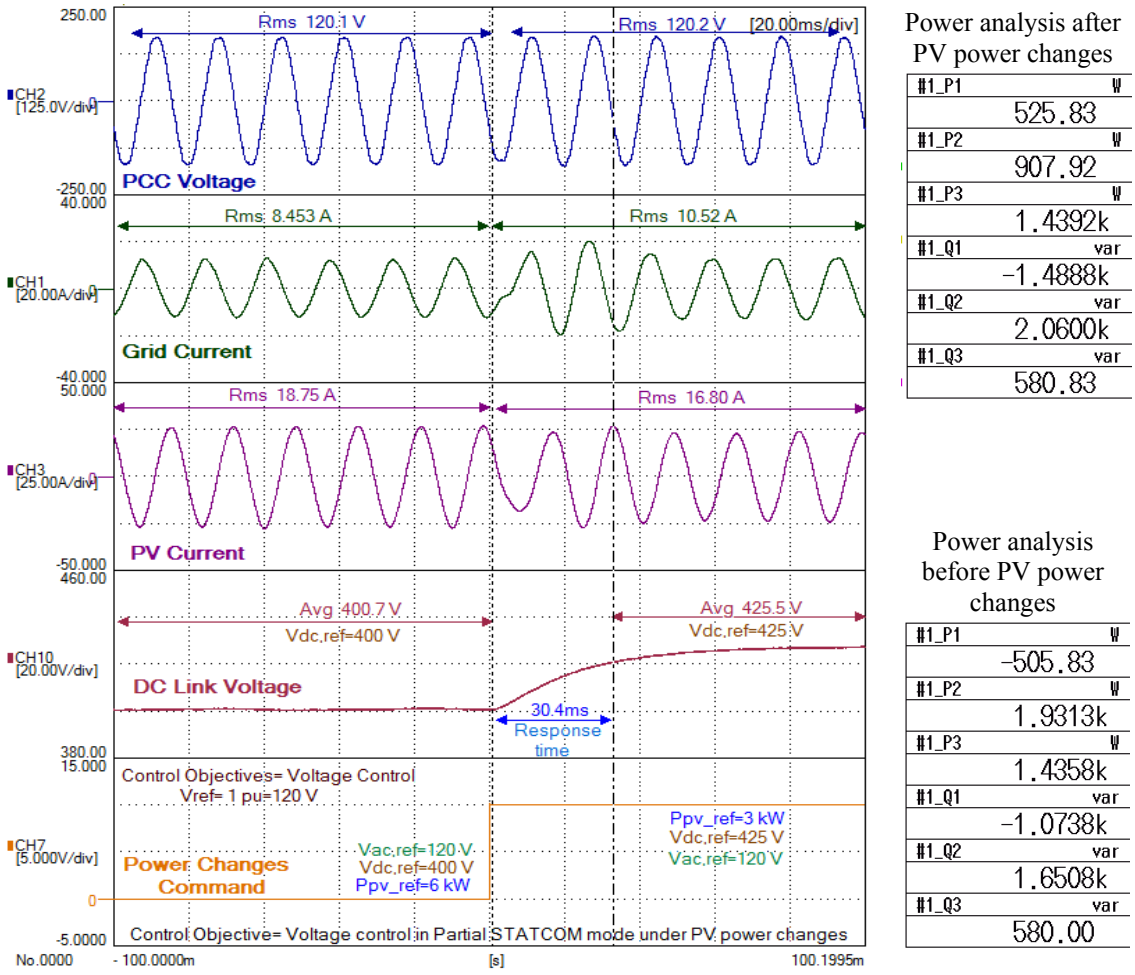

Figure 5-7: Lab results for smart PV inverter operation in Partial STATCOM mode for voltage control during active power variation

5.5.2 Full STATCOM mode

This section presents the lab implementation results of full STATCOM operation mode of the controller for voltage control. Demonstration of this patent-pending mode of control is the most important novel contribution of this thesis. In this test, the controller operates as a conventional PV system and suddenly a large amount of load is connected. Subsequently, PCC voltage changes and the controller shuts down real power production temporarily and uses the entire capacity of the inverter to regulate the voltage in the acceptable range. The full STATCOM tests are performed for voltage reduction and voltage rise by applying inductive and capacitive loads, respectively.

5.5.2.1 Voltage Reduction

In this test, the PV system generates 6 kW active power as a conventional PV system. Initially, a 1.5 kW resistive load is connected to the PCC. Figure 5-8 shows the PCC voltage, PV system current and load current when a large amount of load is connected to the PCC, while the PV system operates in a conventional manner. Channel #8 (*CH8*) represents the status of the large load switch, which is initially disconnected. As shown the PCC voltage (*CH2*) drops from 1.02 pu to 0.96 pu (122 V_{rms} to 115 V_{rms}) after the large load is connected to the PCC with total 6.5 kW and 3 kvar active and reactive power. After about six cycles, the load returns to initial value by disconnecting the load switch. Hence, the voltage returns to its initial value of 1.02 pu (122 V_{rms}).

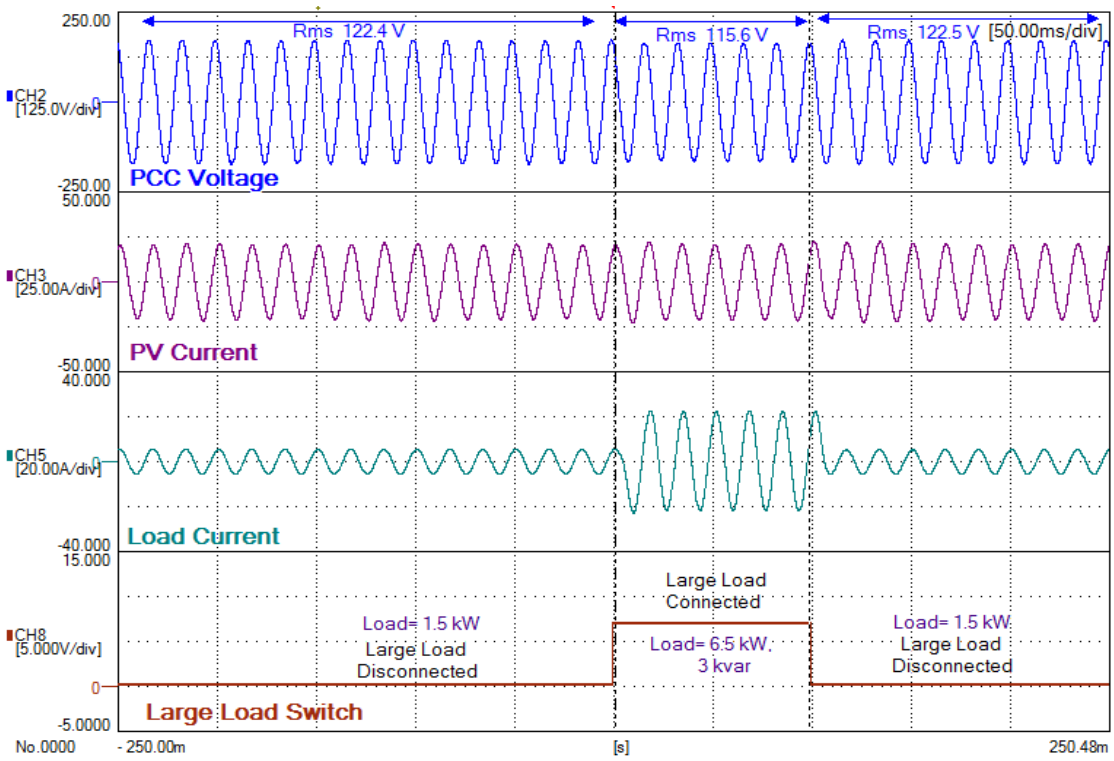

Figure 5-8: Voltage drop due to sudden connection of a large load during conventional Full PV mode of operation

Figure 5-8 reveals that the conventional PV system controller has no beneficial effect on the voltage, i.e. it is unable to control the voltage drop. Now the conventional PV system is replaced by the smart PV inverter controller. In this mode, the PV system initially operates in the Full PV mode and then converts the PV system to Full STATCOM mode

during the transient voltage reduction. Figure 5-9 illustrates the voltage control during a large load connection when the PV system is utilized with the smart PV controller. Channel #2 (*CH2*) and Channel #5 (*CH5*) present the PCC voltage and load current, respectively. Channel #4 (*CH4*) shows the reactive power output of the PV system. The large load with total 6.5 kW and 3 kvar power is connected to the PCC as shown in Channel #8 (*CH8*). As depicted in *CH2*, the controller regulates the PCC voltage during large load connection by injecting substantial amount of reactive power. Subsequently, the voltage recovers to the same value as in the pre-fault condition of about 1.02 pu (122 V_{rms}) within almost one cycle. This test validates the controller performance for full STATCOM operation mode when bus voltage drops by a sudden connection of a large load.

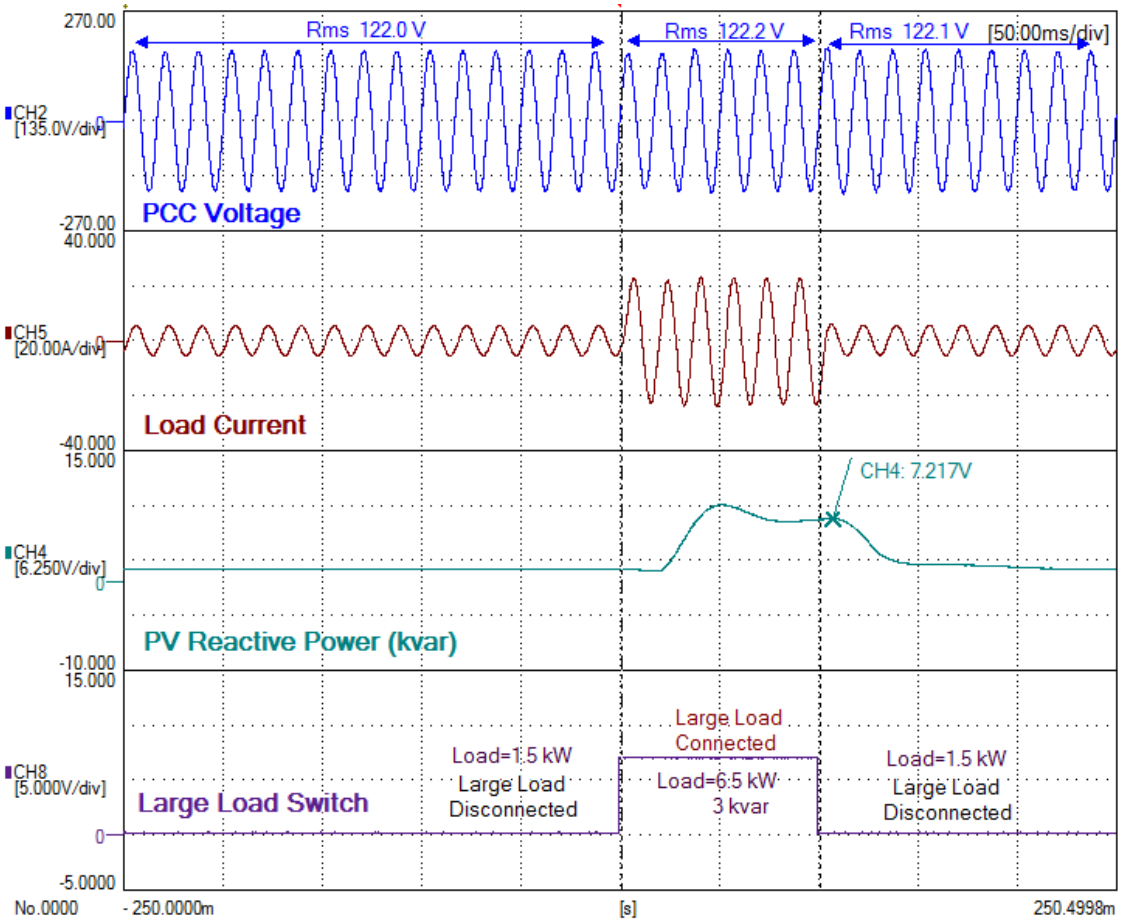

Figure 5-9: Lab Results of smart PV inverter operation in Full STATCOM mode for voltage control during sudden connection of a large load

5.5.2.2 Voltage Rise

This test assesses the controller performance against voltage rise due to capacitive load. Capacitive load simulates a typical fault condition which causes a rise in the voltage of the bus. In this test, PV system generates 6 kW active power in normal condition. Initially, a 1.5 kW resistive load is connected at PCC. Figure 5-10 presents PCC voltage, PV system current and load current of the conventional PV system during transient voltage rise. Channel #2 (*CH2*) reveals that without smart controller, the PCC voltage rises from 1.02 pu to 1.09 pu (122 V_{rms} to 131 V_{rms}) when a large amount of capacitive load with 7 kvar power is connected to the PCC. However, the voltage returns to pre-fault condition after the large load is disconnected.

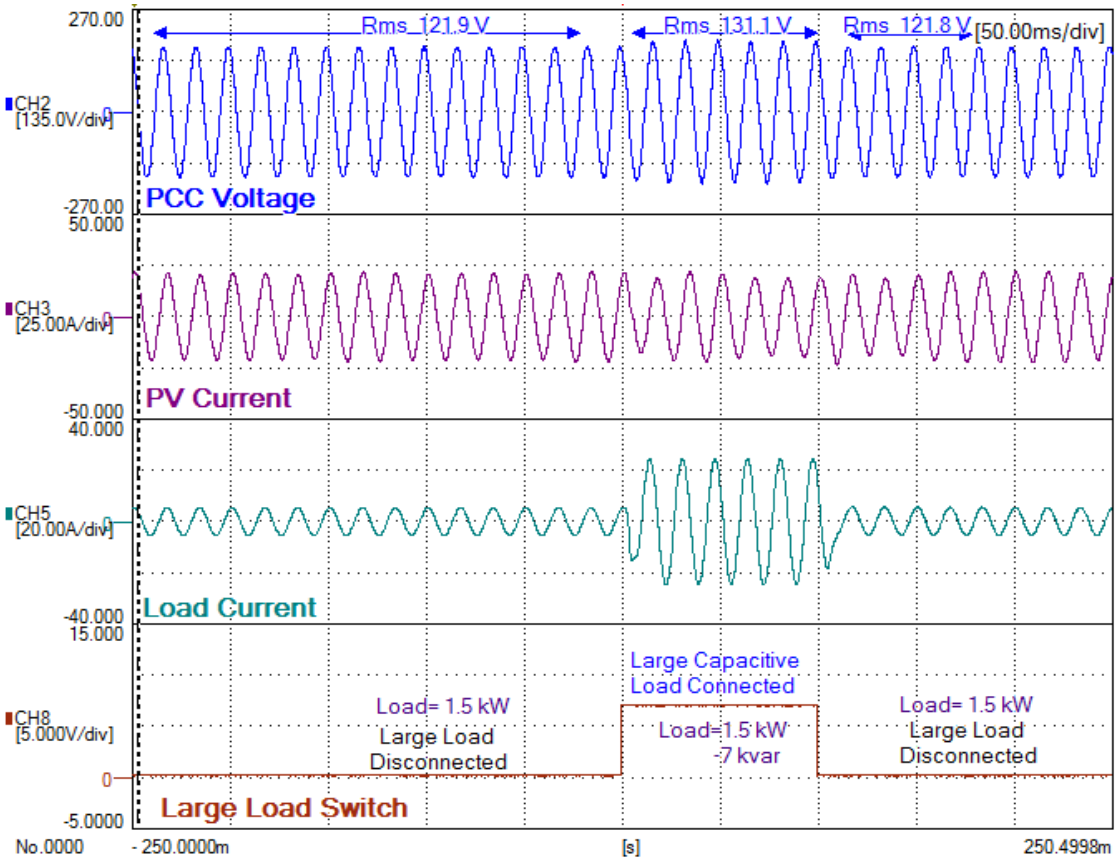

Figure 5-10: Voltage rise due to sudden connection of a capacitive load during conventional Full PV mode of operation

However, by replacing the conventional PV controller with a smart PV inverter controller, the PCC voltage can be effectively controlled during transient voltage rise conditions.

Figure 5-11 demonstrates the PCC voltage, load current and reactive output of the PV system when utilized as a smart PV inverter controller in Full STATCOM mode of operation. As shown, the controller attempts to maintain PCC voltage at pre-fault value within one cycle by absorbing reactive power. Channel #2 (*CH2*) confirms that the PCC voltage is not affected by transient capacitive load. However, the PCC voltage was 1.09 pu (131 V_{rms}) without control whereas it is 1.02 pu (122 V_{rms}) with the novel controller during capacitive load connection. This test validates the controller operation in full STATCOM mode in presence of voltage rise.

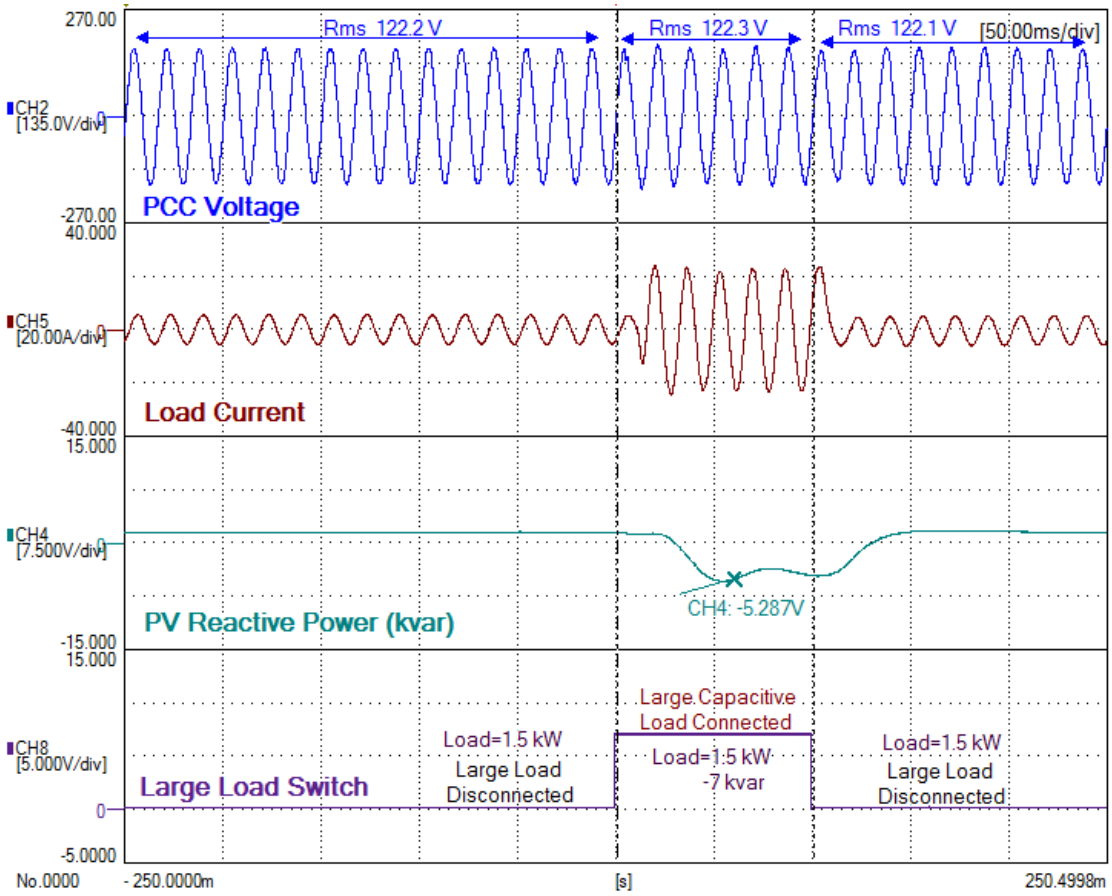

Figure 5-11: Lab Results of smart PV inverter operation in Full STATCOM mode for voltage control during connection of a capacitive load

5.6 Validation of Software Simulation Results and Hardware in Loop Testing Results with Laboratory Results of Smart PV Inverter Performance

This section presents the validation of PSCAD/EMTDC software simulation results and Hardware in Loop (HIL) testing results with the full scale laboratory results of the proposed smart PV inverter controller in different modes of operation.

5.6.1 Validation of PSCAD/EMTDC Software Simulation Results

The results of PSCAD/EMTDC software studies are compared with the results of the lab experiments in this section. The results relate to power factor correction and voltage control with partial STATCOM operation mode and voltage control with full STATCOM operation mode of the smart PV inverter.

5.6.1.1 Power Factor Correction with Partial STATCOM Mode of Operation

Figure 5-4 and Figure 3-7 depict the results of power factor correction of the smart PV inverter for lab experiment and PSCAD study, respectively. In PSCAD study the PV systems generates 3 kW; and the active load and reactive load are considered to be 6 kW and 4 kvar, respectively. In lab experiment, the PV simulator generates 3 kW, whereas the active load is 6 kW and reactive load is 3 kvar, respectively. Therefore, the initial conditions for two different studies are quite similar. The transients of the PCC voltage and grid current are very similar. Also, the steady-state results reveal that the PCC voltage and grid current come in phase, and in consequence, the power factor become unity. The response time for power factor correction obtained from the PSCAD study is about half a cycle, which is the same as obtained through lab experimental results in the laboratory.

This validates the performance of the smart PV inverter for power factor control as obtained from PSCAD simulation studies.

5.6.1.2 Voltage Control with Partial STATCOM Mode of Operation

Figure 5-5 and Figure 5-6 demonstrate the results of the lab experiments for voltage control for capacitive mode and inductive mode utilizing the Partial STATCOM mode of operation

of the smart PV inverter, respectively. Meanwhile, Figure 3-9 illustrates the results of the voltage control with the Partial STATCOM mode of operation of the smart inverter as obtained through PSCAD software simulation. In both software study and lab experiment, the PV-STATCOM system generates 3 kW whereas the active load is 6 kW. By considering Figure 5-5 and Figure 3-9 for the time interval of *t=1.04* sec to *t=1.08* sec, the PCC voltage as obtained through both software studies and laboratory experiment has identical transient response. The transient response in both studies has no overshoot and one cycle settling time. Further, the steady-state response of PCC voltage in both studies is also identical. Besides the PCC voltage, the grid current and PV-STATCOM current have similar behavior.

Figure 5-6 and Figure 3-9 are considered for the time interval *t=1.08* sec to *t=1.12* sec for comparing lab experiment results and software study results for voltage control in inductive operation mode with Partial STATCOM mode of operation of the smart inverter. The transient performance of the PCC voltage for both studies reveals that the controller tracks the reference value within one cycle for inductive mode. Similar to capacitive mode, the PV-STATCOM current and grid current present similar behavior for inductive operation mode in lab study and software study.

This validates the performance of the smart PV inverter for voltage control in Partial STATCOM mode as obtained from PSCAD simulation studies.

5.6.1.3 Voltage Control with Full STATCOM Mode of Operation

Figure 5-9 and Figure 3-12 illustrate the performance of full STATCOM operation mode of the smart PV inverter for voltage control as obtained from the lab experiments and PSCAD software simulation, respectively. In both studies, the PV system generates 6 kW active power in normal condition. The same response time of about one cycle is obtained from both the studies. However, in Figure 3-12, the transient response of the PCC voltage includes a high frequency spike whereas the PCC voltage in lab experiment does not exhibit any spike. Also, the grid current and PV-STATCOM current exhibit an overshoot during the transient in the PSCAD software simulations, which is not observed in actual

laboratory experiments. This is attributed to damping provided by circuit resistances in the hardware implementation.

A greater trust is placed in Lab experiments and since the same nature of response is obtained in PSCAD simulations as the lab experiments, the performance of the smart PV inverter for voltage control in Full STATCOM mode as obtained from PSCAD simulation studies is considered to be validated.

5.6.2 Validation of Hardware In Loop (HIL) Simulation Results

The results of the full scale lab experiment and HIL simulation studies are compared in this section for partial and full STATCOM modes of operation.

5.6.2.1 Power Factor Correction with Partial STATCOM Mode of Operation

Figure 5-4 shows the lab experiment result for power factor correction with partial STATCOM operation mode of the smart inverter, whereas Figure 4-2 demonstrates the HIL study results for the same objective. In both studies, the power factor of the grid is corrected to unity in half a cycle. Also, the transient response including overshoot and rise time of the PCC voltage and grid current are identical in both studies.

This validates the performance of the smart PV inverter for power factor control as obtained from HIL simulation studies.

5.6.2.2 Voltage Control with Partial STATCOM Mode of Operation

Figure 4-4 and Figure 4-5 demonstrate the HIL results for the voltage control of the smart PV inverter in Partial STATCOM mode in capacitive domain. On the other hand, Figure 5-5 depicts the lab experiment results for the same objective. A comparison of the two results demonstrates that in both studies the controller follows the reference value in one cycle. Also, PCC voltage in both studies does not exhibit any overshoot during the transient period. However, the grid and inverter currents present different transient responses in these two different studies. The transient of the grid current is smoother in lab study than in HIL study. The difference in transient response is related to applying the

control objective at different time instants in both the studies. However, the key factors such as overshoot and rise time are similar in two studies.

Figure 4-6 and Figure 5-6 demonstrate the voltage control of the smart PV inverter in Partial STATCOM mode in inductive domain in HIL study and lab study, respectively. The response time of the controller in both studies is one cycle. The PCC voltage waveforms of HIL study and lab study reveal that the transient behavior of the voltage is very much similar in both studies.

This validates the performance of the smart PV inverter for voltage control in both capacitive and inductive domain, as obtained from HIL simulation studies.

5.6.2.3 Voltage Control with Full STATCOM Mode of Operation

Figure 4-10 and Figure 5-9 demonstrate the voltage control of the smart PV inverter in Full STATCOM mode in HIL study and Lab study, respectively. Both studies show an identical behavior in terms of response time. However, the HIL study shows significant overshoot for the PCC voltage whereas in the lab experiments the PCC voltage is controlled with a minor overshoot.

Once again, the Lab experiments are considered to be more realistic, and since the same overall nature of response is obtained in HIL simulations as the lab experiments, the performance of the smart PV inverter for voltage control in Full STATCOM mode as obtained from HIL simulation studies is considered to be validated.

5.7 Conclusion

This chapter presents the laboratory testing and validation of the novel smart PV inverter controller. A similar model of the study system as in the utility network is implemented in the lab. A 10 kVA PV Simulator is used to generate active power based on temperature and irradiance profiles to simulate real solar panels. A 10 kVA three-phase IGBT module is used as the inverter. Also, sensor boards are designed to observe required signals for the controller inside dSPACE board such as PCC voltage, inverter current, load current and DC link voltage. A GUI in ControlDesk software is designed to apply different control

objectives and operation modes, as well as different reference values for PCC voltage and DC link voltage.

The smart PV inverter controller operates in either Partial STATCOM mode or Full STATCOM mode depending on the system requirement.

The partial STATCOM mode is utilized to demonstrate that the load power factor can be corrected to unity within half a cycle. Further, in partial STATCOM mode, the performance of the controller is evaluated for voltage control in both capacitive and inductive regions by applying inductive and capacitive loads, respectively. In partial STATCOM mode, the efficacy of the voltage controller is also demonstrated during active power output changes of the PV system.

In Full STATCOM operation mode, the controller is tested for both abrupt and large voltage rise and voltage reduction. By suddenly applying resistive-inductive loads the voltage declines substantially. The controller detects the sudden reduction of the voltage, disconnects the solar panel and utilizes the entire inverter capacity for regulating the PCC voltage at its pre-fault value within two cycles. Further, a sudden capacitive load is applied to provide a voltage rise condition. In a similar manner as above the smart inverter control use the full capacity of the inverter for reactive power exchange and regulates the PCC voltage to its pre-existing value within one cycles.

The experimental results obtained for both partial STATCOM and full STATCOM operation modes are utilized to validate the results obtained from PSCAD software simulation studies as well as the Hardware In Loop (HIL) studies for different control objectives.

This chapter thus demonstrates the successful testing and validation of the novel patent-pending smart PV inverter control both for power factor correction and voltage control, in both Partial STATCOM and Full STATCOM modes of operation.

CHAPTER 6

6 TEMPORARY OVERVOLTAGE REDUCTION AND PV CONENECTIVITY ENHANCEMENT WITH SMART PV INVERTER

6.1 Introduction

The province of Ontario, in Canada, launched a Renewable Energy Standard Offer Program (RESOP) in 2006 [160] followed by the Feed-In-Tariff program [161] in 2009, for facilitating the integration of renewable energy systems. Since then, Hydro-One which is the largest transmission and distribution company in Ontario, has been receiving large number of applications for connecting PV systems in its distribution systems [26]. One of the major challenges encountered in connecting PV systems is the high Temporary Over Voltage (TOV) caused by unsymmetrical faults in the network.

Hydro One has installed a physical STATCOM to control steady state voltage and TOV on one of its 44 kV distribution feeder caused by the connection of a 10 MW PV solar farm at a bus where two 10 MW PV solar farms are already connected.

In this chapter, a novel smart PV inverter control for the above incoming third 10 MW PV solar farm is presented, which can not only regulate steady state voltage but limit TOV to within acceptable limits without the installation of the additional STATCOM, thereby saving an enormous expense for Hydro One. The effectiveness of the performance of the proposed smart inverter control under different operating conditions is demonstrated through PSCAD/EMTDC software simulation studies.

6.2 System Description

Figure 6-1 depicts a 44 kV feeder of Hydro One distribution network (name and location withheld for confidentiality reasons). The study feeder system includes three 10 MW PV systems with a total capacity of 30 MW connected about 35 km away from the utility transformer station (TS). The 30 MW PV plant is connected to the distribution system through a 30 MVA interface transformer, although each 10 MW PV system uses an

intermediate transformer prior the interface transformer. The Hydro One network parameters are given in Appendix B. In Figure 6-1, two solar systems with 10 MW generation are already connected to the PCC. Connection of the additional 10 MW PV system causes increased reverse power flow during light load conditions. This causes steady state over voltages. Further, the TOV is also observed to exceed the permissible limits during single line to ground faults (SLGF) or line to line ground (L-L-G) fault scenarios. According to Hydro One interconnection requirements [162], the TOV caused by a DG facility should not exceed 1.25 p.u. on the distribution system and under no circumstances should exceed 1.30 p.u. Hydro One performs Connection Impact Assessment (CIA) studies to ensure that the interconnection of the PV system shall not cause TOV to exceed the allowable levels [162].

Hence, to allow the connection of the above 10 MW PV solar farm an actual STATCOM of 3.5 Mvar inductive rating is connected at the PCC to curtail temporary overvoltage (TOV).

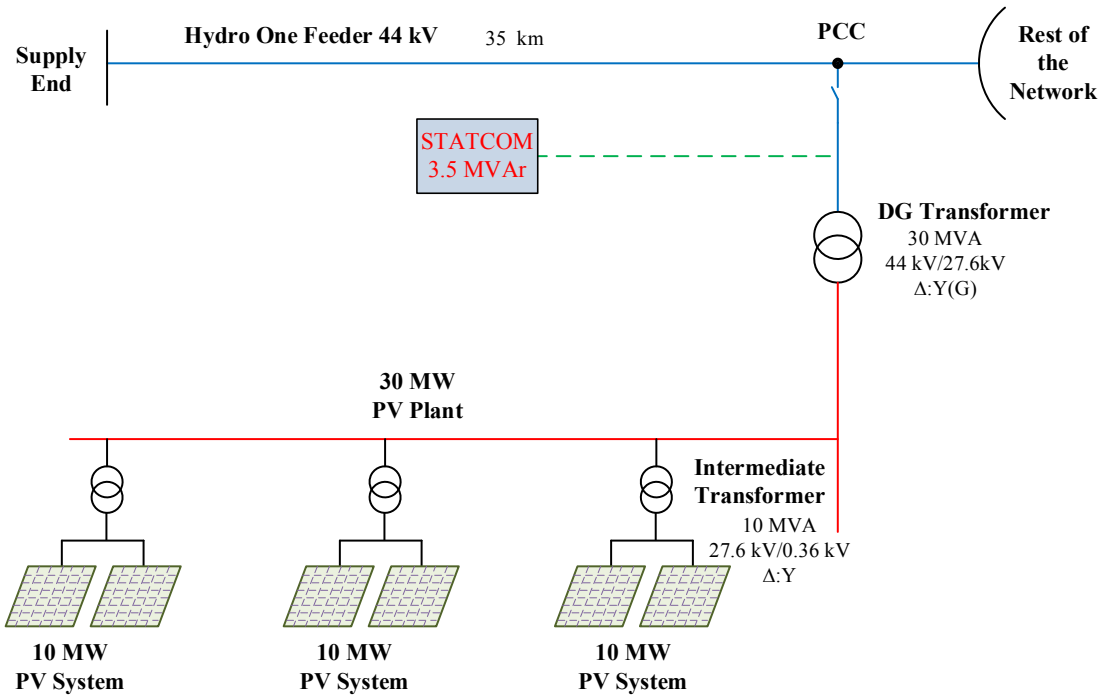

Figure 6-1: Single line diagram of the study system

6.3 Modelling of the Study System

This section presents the modeling of different components of the study system in EMTDC/PSCAD software. The model of the study system is depicted in Figure 6-2. In this figure, v_{pcc} represents PCC voltage; i_g and i_L are grid and load currents respectively, and i_i and i_{pv} are PV currents before and after the filter, respectively. The i_{is} and i_s represent STATCOM currents before and after the filter. This research proposes that the additional (third) 10 MW PV system be equipped with the proposed patent-pending smart PV inverter control, which will allows the PV system to operate in the Partial STATCOM mode or Full STATCOM mode based on the network requirements. The other two PV systems use only conventional controller to generate active power. To compare the study results with the proposed smart inverter control as PV-STATCOM, an actual STATCOM is considered to be connected at the same bus.

6.3.1 Feeder Network

The substation system is modeled as an equivalent voltage source with 1.05 p.u. voltage to supply the 44kV feeder. The 35 km line from substation to PCC is represented by a π model in which the shunt admittance (e.g. line charging) is neglected. In Figure 6-2, R_g and L_g represent the line resistance and inductance, respectively. The network data is given in Appendix D. 1.

6.3.2 Passive Load

The electrical load is considered to be a constant-power static RL load. At nominal voltage (44 $kV_{L\text{-}L}$), the total load is 30 MVA. The peak-time active and reactive loads are considered to be 27 MW and 6 Mvar, respectively, whereas during off-peak hours, these loads are 6 MW and 1.5 Mvar, respectively.

6.3.3 PV Solar Panel

Three solar panels of 10 MW each, are considered to be connected to the PV inverters to generate up to 30 MW in total. The solar panel consists of several modules in series and parallel. The solar panel specifications are provided in Appendix D. 2.

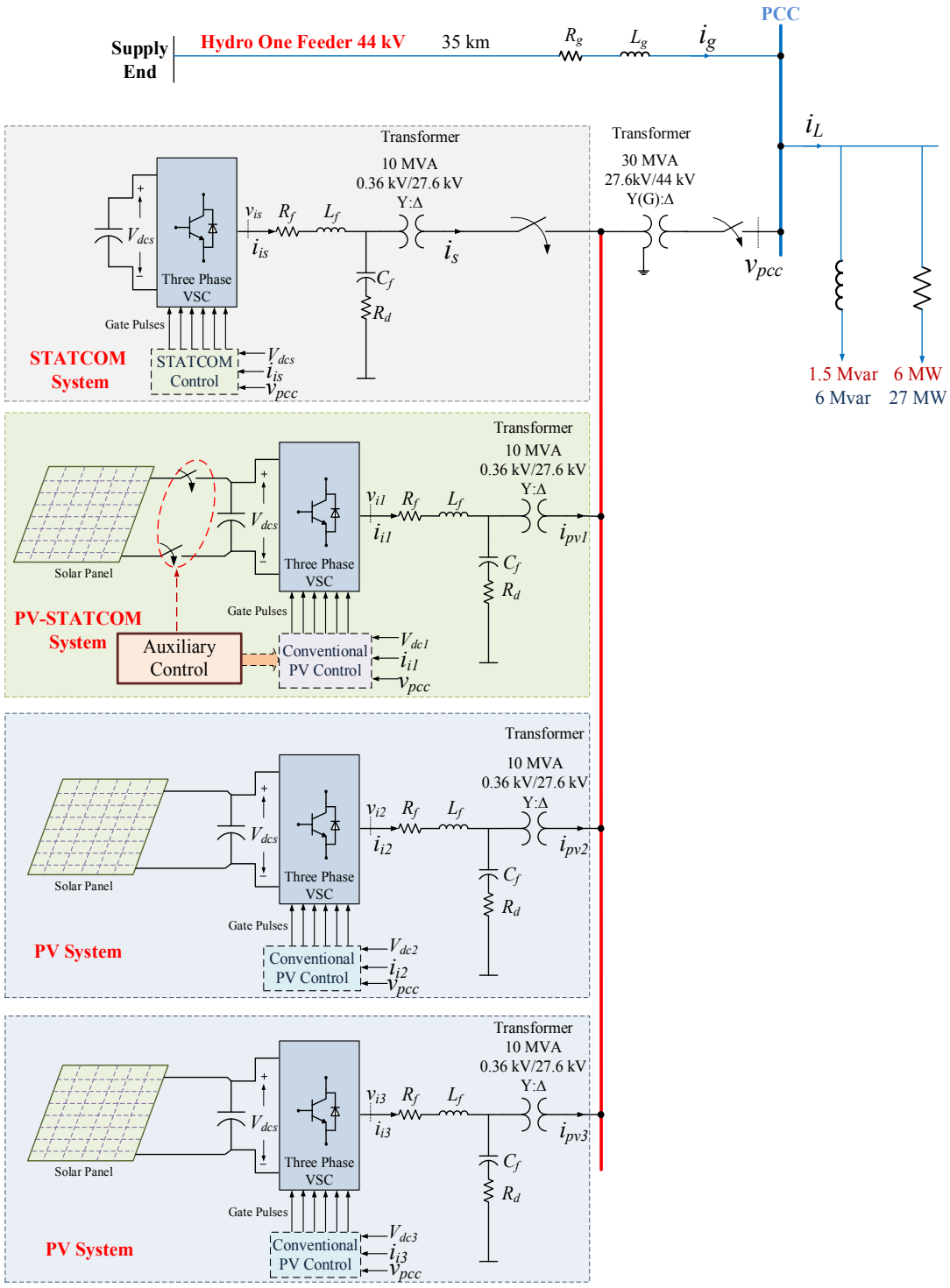

Figure 6-2: Study system model

6.3.4 Voltage Source Inverter

All three PV systems and STATCOM are utilized with 10 MVA two-level six-pulse IGBT-based voltage source inverters (VSI). The switching frequency is chosen to be 4 kHz to minimize the switching losses and obtain better harmonic performance. The data relating to IGBT switches, DC link capacitor and inverter are provided in Appendix D. 3.

6.3.5 Harmonics Filter

For each PV system as well as the STATCOM, an LCL filter is utilized to mitigate the harmonics caused by the switching frequency. The LCL filter consists of a series inductor (L_f), shunt capacitor (C_f) with series damping resistor (R_d) and another series inductor (L_t) corresponding to the transformer inductance. The combination of shunt capacitor in series with damping resistor is connected in delta configuration. Equations (2.8)-(2.13) are used to design the filter parameters. Considering 9% current ripple ($i_{ripple} = 0.09 \times I_{inverter,peak}$) at $D = 0.5$, and substituting system parameters in (2.8), the filter inductance is obtained as:

$$L_f = \frac{(925 - 293) \times 0.5}{2 \times 0.09 \times 22000 \times 4000} = 20 \ \mu\text{H} \tag{6.1}$$

Therefore, the inductance of the series inductor is chosen to be $L_f = 20 \ \mu\text{H}$.

Based on (2.10),

$$C_f \leq \frac{0.05 \times 10^{+7}}{377 \times (360)^2} = 100\, mF \tag{6.2}$$

Since the capacitor can cause a rise in both steady state voltage and TOV, it is decided to use a filter capacitor of a smaller value. Hence, the filter capacitor is chosen to be $C_f = 1 mF$. The resonance frequency resulting from the above filter components is:

$$f_r = \frac{1}{2\pi}\sqrt{\frac{L_t + L_f}{L_t L_f C_f}} = \frac{1}{2\pi}\sqrt{\frac{2}{20\times10^{-6}\times1\times10^{-3}}} = 1591.5\,\text{Hz} \tag{6.3}$$

In (6.3), the leakage impedance of the transformer (L_t) is considered to be 0.1 pu which is the same as filter inductor (L_f). As discussed in Sec. 2.4.3, the resonance frequency should be in an acceptable range as indicated in (2.12). Equation (6.3) reveals that the calculated frequency is indeed in the valid range.

$$10 f_0 < f_r < 0.5 f_{sw} \tag{6.4}$$

$$600\,\text{Hz} < f_r = 1591.5\,\text{Hz} < 2000\,\text{Hz} \tag{6.5}$$

By obtaining the resonance frequency in (6.3), the damping resistor can be calculated as:

$$R_d = \frac{1}{3\times2\times\pi\times f_r\times C_f} = \frac{1}{6\times\pi\times1591.5\times1\times10^{-3}} = 0.033\ \Omega \tag{6.6}$$

Therefore, the final filter parameters are $L_f = 20\ \mu\text{H}$, $C_f = 1mF$ and $R_d = 0.033\ \Omega$.

6.3.6 Transformer

Each PV system and the STATCOM are individually connected to a 10 MVA intermediate transformer having Wye-Delta configuration. Consequently, each PV system can be isolated from the other DGs. The intermediate transformer boosts the voltage from 360 V to 27.6 kV. The outputs of all PV systems and STATCOM after their intermediate transformers, are connected to a step up interface transformer having Delta-Wye grounded configuration, which connects to the PCC. The parameters of the interface and intermediate transformers are provided in Appendix D. 4 and D. 5, respectively.

6.4 Smart PV Inverter Control

As stated earlier, the third 10 MW PV system causes TOV which exceeds the Hydro One specified limits. Hence a STATCOM is connected to the PCC to absorb reactive power and reduce the voltage. However, as the STATCOM is designed for symmetrical voltage control, it actually failed in the field to control the Temporary Overvoltage (TOV) which is an unsymmetrical phenomenon.

The objective of this study is to demonstrate that if the third PV system is equipped with the proposed smart PV inverter control, the TOV can be restricted to be within acceptable limits and that the need for an additional highly expensive STATCOM can be avoided.

The proposed smart PV inverter control as PV-STATCOM operates as follows. During situations of steady-state overvoltage, the smart PV inverter operates in Partial STATCOM mode and uses the *remaining capacity* of the inverter to *control the voltage*. However, during scenarios of TOV, the smart PV inverter control operates in Full STATCOM mode to disconnect the solar panels from the VSC (inverter) and utilizes the *entire capacity* of the inverter to *absorb reactive power* (and thereby reduce the voltage). In other words, during a TOV event, the control mode changes from voltage control to reactive power control.

Figure 6-3 illustrates the schematic of the smart PV inverter controller. The controller is designed in *d-q* frame and includes *abc/dq* transformation block, PLL, DC controller, current controllers, AC voltage controller, TOV detector unit and PWM unit. The PLL unit extracts the phase angle of PCC voltage for transforming currents and voltages from *abc*-frame to *dq*-frame or vice versa. The DC controller, in order to regulate DC link voltage at the reference value, generates the reference current for *d*-component of inverter current which represents the active current component. Consequently, the current controller in *d*-axis regulates the active current component to its reference value.

The PCC voltage is controlled by the AC voltage controller when an overvoltage occurs. However, during TOV the solar panels are disconnected and the entire capacity of the inverter is used to absorb reactive power.

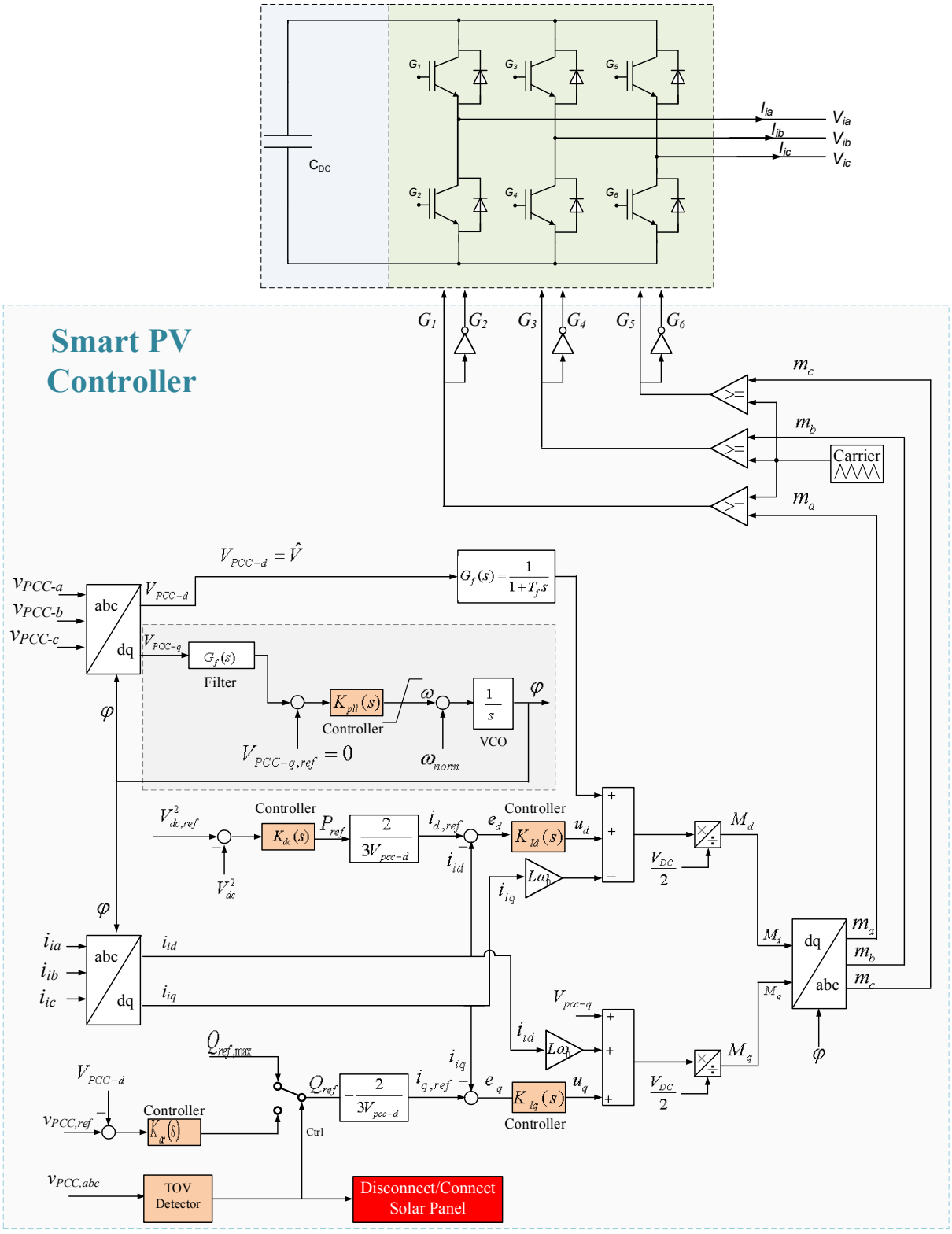

Figure 6-3: Structure of smart PV control for TOV control and voltage control

Therefore, either maximum reactive current or output of the AC voltage controller defines the reference value of reactive current control loop. The current controller in *q*-axis regulates the reactive current to its reference value. It should be noted that the TOV Detector unit switches between voltage control mode and TOV mitigation mode. Also, this unit generates the command to connect or disconnect the solar panels from the VSC. The outputs of the controller are modulation index in *d-q* frame, which are eventually converted to *abc*-frame using the phase angle of PCC voltage. At the final stage, the modulation indices in *abc*-frame are compared with carrier signal to generate gate pulses for the VSC switches.

6.4.1 PLL

As discussed in Sec. 2.5.2.2, to extract the phase angle of PCC voltage, the *q*-component of PCC voltage needs to be controlled at zero level. In other words, by controlling $V_{pcc-d} = \hat{V}$ and $V_{pcc-q} = 0$ the phase angle $\varphi = \omega_0 t + \theta_0$ can be obtained. The extracted phase angle is used to transform parameters from *abc*-frame to *dq*-frame or vice versa. Figure 6-4 illustrates the PLL control loop which consists of PCC voltage amplitude as a gain, low pass filter, controller and resettable integrator for converting frequency to phase angle.

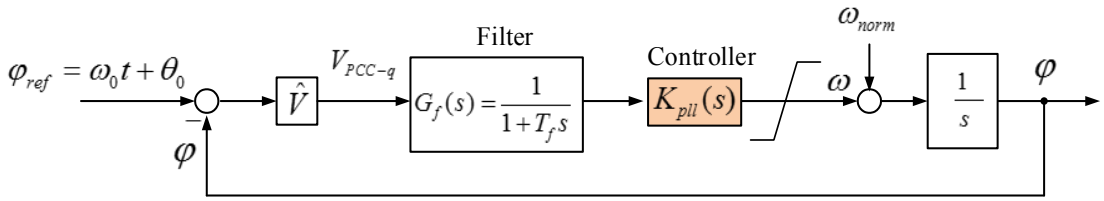

Figure 6-4: SRF-PLL structure with PI controller

The nominal frequency and voltage of the study system are 60 Hz and 44 kV line-to-line. Hence, maximum voltage is obtained as:

$$\hat{V} = \sqrt{2}\left(\frac{V_{L-L}}{\sqrt{3}}\right) = \sqrt{\frac{2}{3}} \times 44000 = 35925.85 \tag{6.7}$$

To clean q-component of PCC voltage from higher harmonics, the time constant of the low pass filter is chosen $T_f = 1\ ms$. By considering Figure 6-4, the open loop transfer function without the controller is:

$$G_{PLL}(s) = \frac{\hat{V}}{s(1+T_f s)} = \frac{35925.85}{s(1+0.001s)} \tag{6.8}$$

Figure 6-5 shows the Bode diagram of the uncompensated system in (6.8). The uncompensated system is stable but the phase margin is $\delta = 9.5^{\circ}$ which is very low in order to ensure stability.

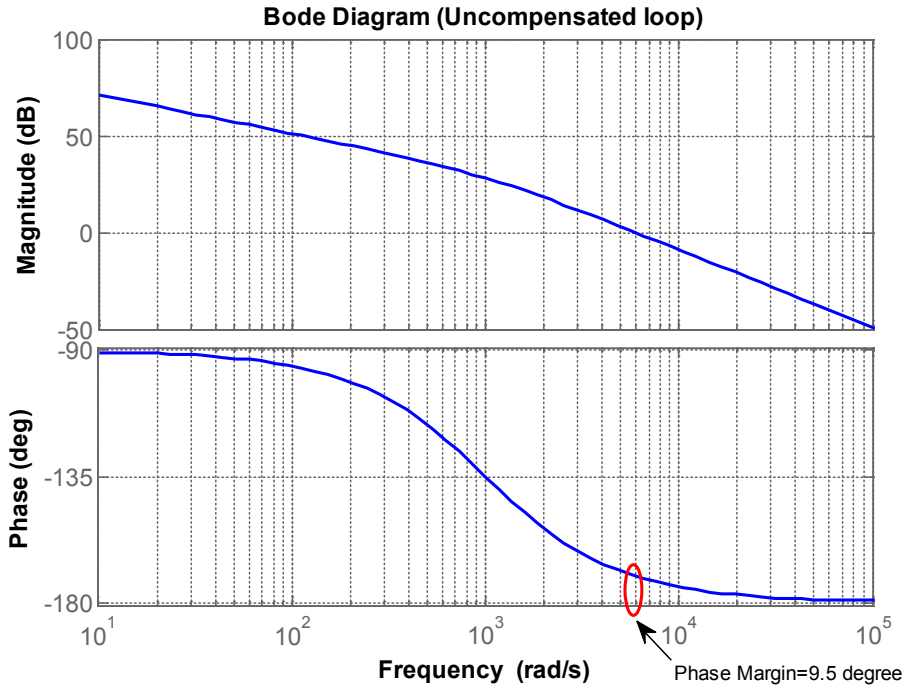

Figure 6-5: Bode diagram of uncompensated PLL transfer function

Hence, a PI controller is employed to increase the phase margin. The open loop transfer function with the controller is written as below:

$$H_{PLL}(s) = K_{PLL}(s) \times G_{PLL}(s) = \frac{\hat{V} \times k_{PLL,gain}}{T_f} \left(\frac{s + z_{PLL}}{s + T_f^{-1}} \right) \frac{1}{s^2} \tag{6.9}$$

where,

$$K_{PLL}(s) = k_{PLL,gain}\frac{s + z_{PLL}}{s} \tag{6.10}$$

Due to a pole at $s = 0$ in (6.8), the "symmetrical optimum" technique is used to design the PI controller which is discussed in detail in Sec. 2.7.1. By choosing the phase margin $\delta_m = 60^\circ$, $T_f = 1\ ms$ and $\hat{V} = 35925.85$ V, the controller parameters are obtained as:

$$z_{PLL} = \frac{1 - \sin(\delta_m)}{\left[1 + \sin(\delta_m)\right]T_f} = 71.8 \tag{6.11}$$

$$\omega_c = \sqrt{T_f^{-1}\, z_{PLL}} = 268 \text{ rad/s} \tag{6.12}$$

$$k_{PLL} = \frac{\omega_c}{\hat{V}} = 7.46\times10^{-3} \tag{6.13}$$

Therefore, the designed PI controller for the PLL loop is given as:

$$K_{PLL}(s) = 7.46\times10^{-3} \times \frac{s + 71.8}{s} \tag{6.14}$$

By substituting control parameters in (6.9) the transfer function of the compensated system is written as:

$$H_{PLL}(s) = \ 2.68\times10^{5}\left(\frac{s + 71.8}{s + 1000}\right)\frac{1}{s^2} \tag{6.15}$$

The Bode diagram of the PLL system compensated by $K_{PLL}(s)$ is shown in Figure 6-6. It demonstrates that the controller parameters are designed correctly and the desired phase margin of $\delta_m = 60^\circ$ exactly achieved at $\omega_c = 268$ rad/s.

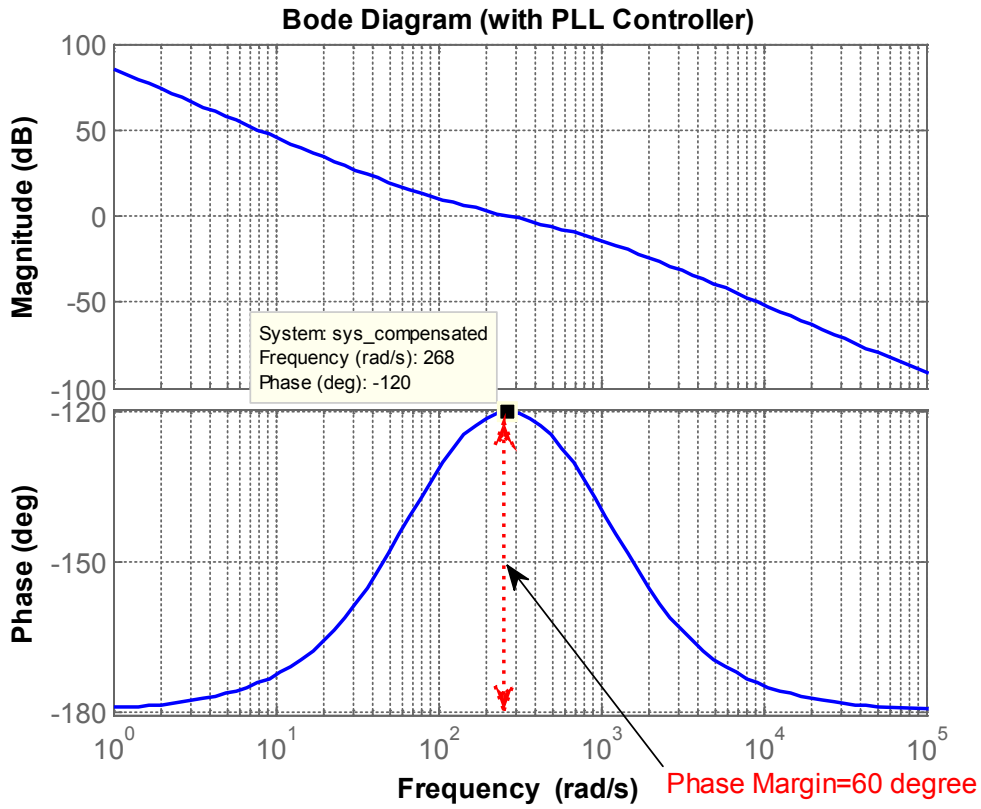

Figure 6-6: Bode diagram of the compensated PLL control loop

6.4.2 Real and Reactive Current Control

As described in Sec. 2.5.3, the inverter current components in *d-q* frame are written as:

$$L_f \frac{di_{id}}{dt} + R_f i_{id} = L_f \omega_0 i_{iq} + \frac{V_{DC}}{2} M_d - V_{pcc-d} \tag{6.16}$$

$$L_f \frac{di_{iq}}{dt} + R_f i_{iq} = -L_f \omega_0 i_{id} + \frac{V_{DC}}{2} M_q - V_{pcc-q} \tag{6.17}$$

To eliminate the coupling between i_{id} and i_{iq}, as well as for linearization, control inputs u_d and u_q are defined as:

$$L_f \frac{di_{id}}{dt} + R_f i_{id} = u_d \tag{6.18}$$

$$L_f \frac{di_{iq}}{dt} + R_f i_{iq} = u_q \tag{6.19}$$

Remaining terms of (6.16) and (6.17) are added as feed-forward terms to achieve PWM modulation indexes in *d-q* frame. Therefore,

$$M_d = \frac{2}{V_{DC}} \left(u_d - L_f \omega_0 \, i_{iq} + V_{pcc-d} \right) \tag{6.20}$$

$$M_q = \frac{2}{V_{DC}} \left(u_q + L_f \omega_0 \, i_{id} + V_{pcc-q} \right) \tag{6.21}$$

By considering (6.18) and (6.19), the uncompensated open-loop transfer functions of current control are obtained as below:

$$\frac{u_d}{i_{id}} = \frac{1}{L_f s + R_f} \tag{6.22}$$

$$\frac{u_q}{i_{iq}} = \frac{1}{L_f s + R_f} \tag{6.23}$$

The above transfer function is stable but there is a steady-state error as it is a zero-degree transfer function.

A PI controller can make the steady-state error zero due to a pole at $s = 0$. Also, a PI controller can reduce the response time by moving the pole of the closed loop farther from origin on the left side of the real-imaginary coordinates. Hence, the control parameters are obtained as below:

$$K_{Id}(s) = \frac{k_{p,d} s + k_{I,d}}{s} \tag{6.24}$$

$$K_{Iq}(s) = \frac{k_{p,q}s + k_{I,q}}{s} \tag{6.25}$$

where,

$$k_{p,dq} = \frac{L_f}{\sigma_{i,dq}} \tag{6.26}$$

$$k_{I,dq} = \frac{R_f}{\sigma_{i,dq}} \tag{6.27}$$

In (6.26) and (6.27), $\sigma_{i,dq}$ is the time constant for *d*-control and *q*-control loops to shift the transfer function pole, and is chosen to be 1 *ms*. As $L_f = 20\,\mu\text{H}$ and $R_f = 0.1\ \text{m}\Omega$, the controller parameters are calculated as:

$$k_{p,dq} = \frac{20\times10^{-6}}{1\times10^{-3}} = 0.02\ , \qquad k_{I,dq} = \frac{1\times10^{-4}}{1\times10^{-3}} = 0.1 \tag{6.28}$$

Consequently, the closed-loop transfer function of the compensated control loop is:

$$G_{Id} = \frac{i_d}{i_{d,ref}} = \frac{1}{1+\sigma_{i,d}s} = \frac{1}{1+0.001s} \tag{6.29}$$

$$G_{Iq} = \frac{i_q}{i_{q,ref}} = \frac{1}{1+\sigma_{i,q}s} = \frac{1}{1+0.001s} \tag{6.30}$$

6.4.3 DC Voltage Control Loop

Due to losses in the switches of the inverter, the DC link of the inverter needs to absorb a slight amount of active power to maintain the DC voltage at the specific level. The required level of the DC voltage is determined by AC side voltage of the inverter. When the smart inverter control operates in Full STATCOM mode, the grid supplies the required active power. However, in the PV mode, this active power is provided by the solar panels. The

design steps of the DC voltage controller are discussed in Sec. 2.5.5 in details. Active power balance between PV side, DC link and AC side is written as:

$$\frac{C}{2}\frac{d}{dt}\left(V_{dc}^2\right) = f(R,T,V_{dc}) - \frac{3}{2}V_{pcc-d}I_{sd} \tag{6.31}$$

where,

$$f(R,T,V_{dc}) = P_{PV} = n_p I_{sc} V_{dc} - n_p I_0 V_{dc}\left[e^{\left(\frac{qV_{dc}}{kTn_s}\right)} - 1\right] \tag{6.32}$$

$f(R,T,V_{dc})$ represents the solar power, which is a non-linear function of irradiance (R), temperature (T) and DC link voltage. As the closed loop transfer function of active current loop is:

$$G_{Id} = \frac{i_d}{i_{d,ref}} = \frac{1}{1+\sigma_{i,d}s} = \frac{1}{1+0.001s} \tag{6.33}$$

Equation (6.32) can be rewritten as:

$$\frac{d}{dt}\left(V_{dc}^2\right) = \frac{2}{C}\left(f(R,T,V_{dc}) - \frac{3}{2}V_{pcc-d}\mathcal{L}^{-1}\left(G_{id}(s)\right)I_{sd,ref}\right) \tag{6.34}$$

In (6.34), V_{dc}^2 is the output, $I_{sd,ref}$ is control input and $f(R,T,V_{dc})$ is the disturbance input which can be added as a feed-forward term to eliminate the solar power effect from the dynamic equation [100]. Hence, the open-loop transfer function of DC voltage control without compensation can be written as:

$$G_{dc}(s) = \frac{V_{dc}^2}{I_{sd,ref}} = -\frac{3}{C}V_{pcc-d}\frac{1}{s(\sigma_{i,d}s+1)} \tag{6.35}$$

In (6.35) $C = 150\,mF$, $V_{pcc-d} = 35925.85$ and $\sigma_{i,d} = 0.001$. Due to a negative gain the closed-loop transfer function of DC loop control is unstable. A PI controller is used to

move the pole from right side of the real-imaginary coordinates to the left side as well as to increase the phase margin of the control loop. By assuming PI control as below:

$$K_{dc}(s) = k_{dc,gain}\frac{s+z_{dc}}{s} \tag{6.36}$$

the open-loop transfer function with the compensation is rewritten as:

$$H_{dc}(s) = K_{dc}(s)\times G_{dc}(s) = -\frac{3\times V_{pcc-d}\times k_{dc,gain}}{C\times\sigma_{i,d}}\left(\frac{s+z_{dc}}{s+\sigma_{i,d}^{-1}}\right)\frac{1}{s^2} \tag{6.37}$$

As the compensated system includes two poles in its dynamic equation, the "symmetrical optimum" technique can be applied for the DC controller design. By choosing $\delta_m = 70^\circ$ the PI controller parameters are achieved as:

$$z_{dc} = \frac{1-\sin(\delta_m)}{\left[1+\sin(\delta_m)\right]\sigma_{i,d}} = 31.09 \tag{6.38}$$

$$\omega_c = \sqrt{\sigma_{i,d}^{-1}\, z_{dc}} = 176.3 \quad \text{rad/sec} \tag{6.39}$$

$$k_{dc,gain} = -\frac{C\times\omega_c}{3\times V_{pcc-d}} = \text{-}2.45\times10^{-4} \tag{6.40}$$

By substituting the values of control parameters, the compensated transfer function is rewritten as:

$$H_{dc}(s) = \ 1.763\times10^{5}\left(\frac{s+31.09}{s+1000}\right)\frac{1}{s^2} \tag{6.41}$$

The Bode diagram of the DC voltage loop with the compensator $H_{dc}(s)$ is shown in Figure 6-7. It reveals that the controller parameters are designed correctly and a desired phase margin $\delta_m = 70^\circ$ is exactly achieved at $\omega_c = 176$ rad/s .

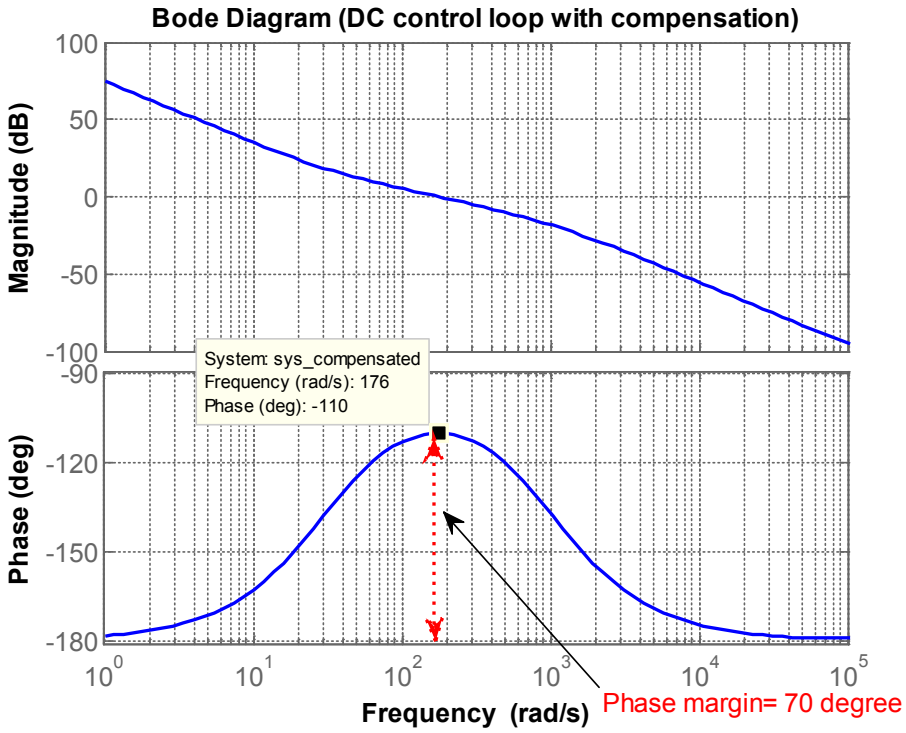

Figure 6-7: Bode diagram of the compensated DC voltage control loop

6.4.4 Selection of Mode of Operation of the Smart Inverter

In this study, two control objectives, i) steady state voltage control and ii) TOV mitigation due to faults, are considered for the 44 kV feeder of the Hydro-One distribution network. Increase in PV power output causes voltage to rise in steady state. On the other hand, when an unsymmetrical fault such as single-line-to-ground (SLG) or line-to-line-ground (L-L-G) fault occurs, a temporary over voltage (TOV) occurs in one phase or two phases until the fault is cleared. Connection of more number of PV plants aggravates both the steady state over voltage and TOV, especially during low load conditions, causing them to go beyond acceptable limits. It is therefore required to regulate both the steady state overvoltage and TOV, in order to connect more PV solar systems in the grid.

For the study system depicted in Figure 6-2, only one of the three PV systems is equipped with the smart PV inverter. Other PV systems operate as conventional PV systems generating only active power. The smart inverter control operates in two modes: i) Partial STATCOM mode, and ii) Full STATCOM mode.

During daytime, the smart PV control operates as a conventional PV system i.e in Full PV mode. If voltage control or power factor correction is required together with real power generation, Partial STATCOM mode is activated. In this mode the controller uses the capacity of the inverter remaining after real power generation (which is unhindered) for controlling the steady state voltage at PCC or for correcting the power factor. The Full STATCOM mode is activated when a TOV occurs. In this mode, the solar panels are disconnected from the VSI and the entire inverter capacity is utilized to absorb reactive power in order to reduce the phase voltage. After the TOV is mitigated, the solar panels are reconnected to the VSI and control mode is switched to Partial STATCOM mode.

Figure 6-8 shows the flowchart of the smart PV inverter control to define the operation mode. During daytime, the voltages in three phases are measured. If any phase voltage exceeds the TOV limit while the voltages in other phase/phases reduce substantially, the output of TOV Detector unit is trigged “ON”, and the Full STATCOM mode is activated. The controller keeps absorbing reactive power to reduce TOV until the phase voltages reach an acceptable value. After the fault is cleared all the phase voltages will rise up to their normal values. The controller recognizes that TOV is mitigated, and therefore reconnects the solar panel and changes the control mode to Partial STATCOM mode for voltage control. During nighttime, the PV solar system operates in Full STATCOM mode to control either the steady state voltage or the TOV. In this mode the voltage is controlled to the specified value with the required amount of reactive power exchange. For mitigating TOV, the entire inverter capacity is used for reactive power absorption. In other words, the smart PV inverter control autonomously determines its operation mode and prioritizes between active power generation and reactive power exchange based on the system requirements, nature of transient/disturbance, time of the day and remaining inverter capacity.

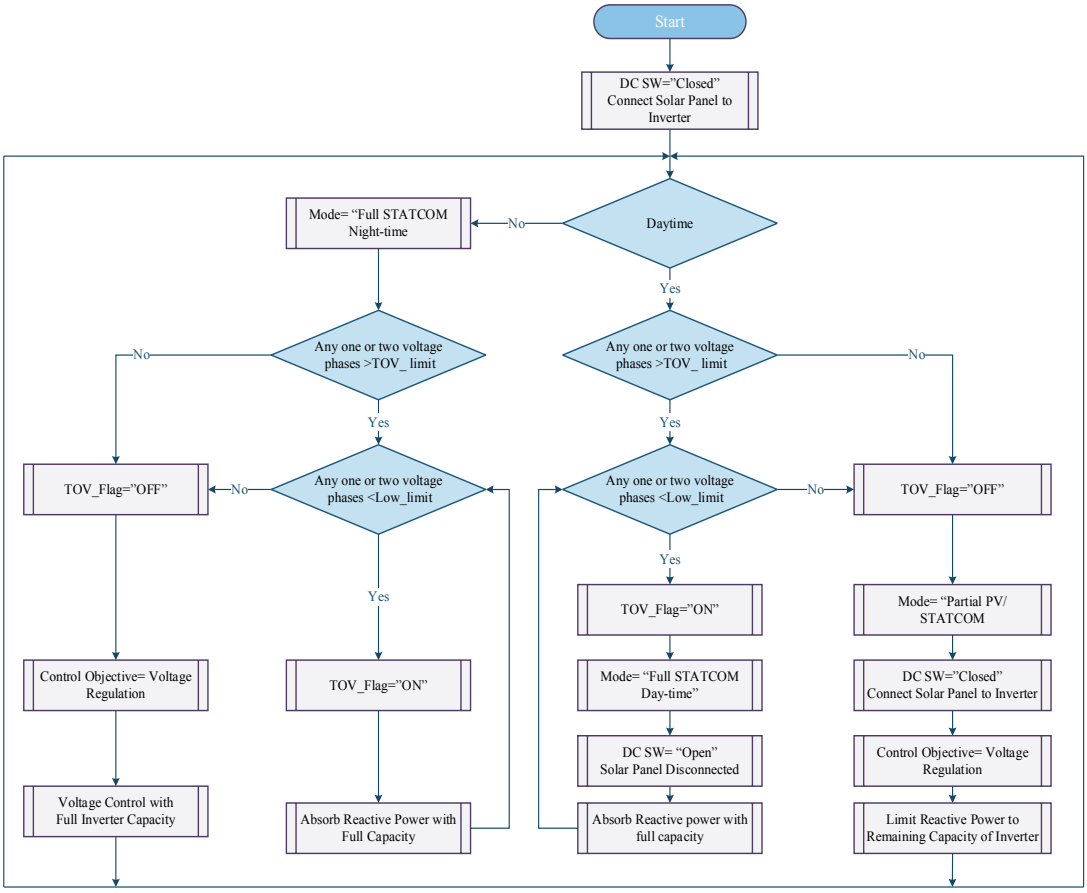

Figure 6-8: Flowchart of the smart PV inverter operating mode

6.4.5 PCC Voltage Control

In voltage control mode, the AC voltage controller defines the reactive current reference for current controller, whereas in TOV reduction mode the reference value for reactive current controller is a constant. As discussed in Sec. 2.5.6.1, the uncompensated AC voltage loop is described as:

$$G_{ac}(s) = G_{iq}(s) \times \left(-L_g \omega_0\right) = \frac{-L_g \omega_0}{1 + \sigma_{i,q} s} \tag{6.42}$$

where L_g is the grid inductance which represents line inductance plus the short circuit inductance. ω_0 is the nominal frequency and $\sigma_{i,q}$ is time constant for the reactive current controller. By considering (2.89), the structure of PCC voltage control loop is shown in Figure 6-9.

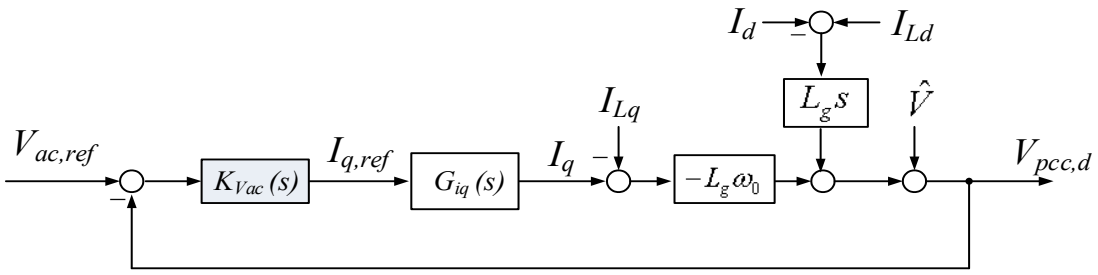

Figure 6-9: Block diagram of PCC voltage control loop

It is noted that the PCC voltage control loop requires a smaller bandwidth than reactive current control loop. The controller is chosen as,

$$K_{ac}(s) = \frac{k_{gain,ac}}{s} \tag{6.43}$$

Since the closed-loop transfer function includes a pole at right side of the coordinates due to negative gain, it is the necessary to choose a negative gain for the controller. By applying the controller, the compensated transfer function is written as:

$$H_{ac}(s) = K_{ac}(s) \times G_{ac}(s) = \frac{-k_{gain,ac} L_g \omega_0}{s(1+\sigma_{i,q} s)} \tag{6.44}$$

In (6.44), $\omega_0 = 2\pi f_0 = 120\pi$, $L_g = 36\,\text{mH}$ and $\sigma_{i,q} = 1\,\text{ms}$. By choosing $k_{gain,ac} = -6$, bandwidth of the closed-loop transfer function would be $\omega_{c,AC} = 81$ rad/s which is about 12 times smaller than bandwidth of reactive current control loop. Figure 6-10 depicts the Bode diagram of the compensated AC voltage loop.

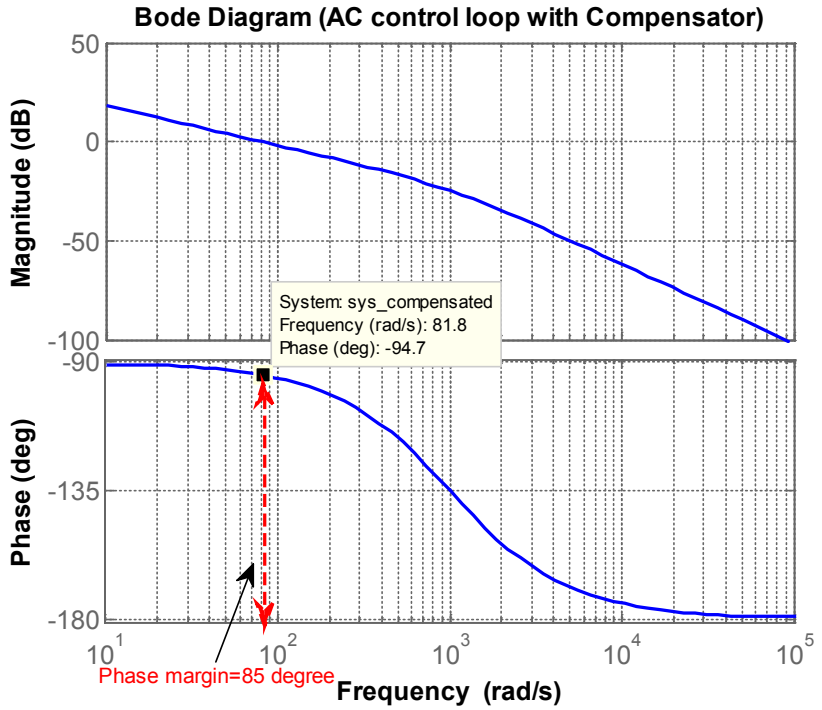

Figure 6-10: Bode diagram of the compensated AC voltage control loop

6.4.6 TOV Detection Block

The TOV Detection block triggers the TOV flag when a temporary overvoltage occurs. When TOV flag is "ON", the controller converts PV system to Full STATCOM mode of operation by changing the DC voltage to the open circuit voltage level of the solar panel and absorbing reactive power with full inverter capacity. The controller virtually disconnects the solar panel by keeping the DC side voltage at open circuit voltage level of solar panel. When the fault is cleared and PCC voltage has reached acceptable values, the TOV flag is triggered "OFF" and the smart PV controller transforms to Partial STATCOM mode with voltage control.

Figure 6-11 depicts the structure of the TOV Detection block. This block includes three different sections, Voltage Rise Detection (VRD), Voltage Fall Detection (VFD) and Fault Detection (FD) units. Each unit uses rms blocks to obtain the rms value of each phase and then converts it to its per-unit value. The Voltage Rise Detection unit compares the each phase per-unit voltage with its hysteresis bands. If one or two of the phase voltages exceed

high band of the hysteresis then the output of VRD unit will be “1” otherwise the output is “0”. Based on Hydro One network requirements, the low and high bands of the hysteresis block for VRD unit are chosen 1.20 pu and 1.25 pu respectively.

The VFD unit detects the fall in voltage. The output of VFD is triggered to “1” if one or two phase voltages pass the lower band of the hysteresis. The low and high bands of VFD unit are 0.8 pu and 0.85 pu respectively. When the output of both VRD and VFD blocks are “1” the TOV Detection block recognizes the TOV event and triggers the output to “1”.

In other words, the TOV event is detected when one or two phase voltages are larger than 1.25 pu and other phase/phases are below 0.8 pu. After the fault is cleared all phase voltages will be above a certain value which is chosen as 0.85 pu. Hence, FD unit triggers the TOV flag to become “0” when the fault is cleared. The hysteresis limits for different units are as below:

$$\begin{cases} \text{VRD unit} \rightarrow H_1 = 1.20\,\text{pu}\ ,\ H_2 = 1.25\,\text{pu} \\ \text{VFD unit} \rightarrow L_1 = 0.80\,\text{pu}\ ,\ L_2 = 0.85\,\text{pu} \\ \text{FD unit} \rightarrow L_3 = 0.50\,\text{pu}\ ,\ L_4 = 0.55\,\text{pu} \end{cases} \tag{6.45}$$

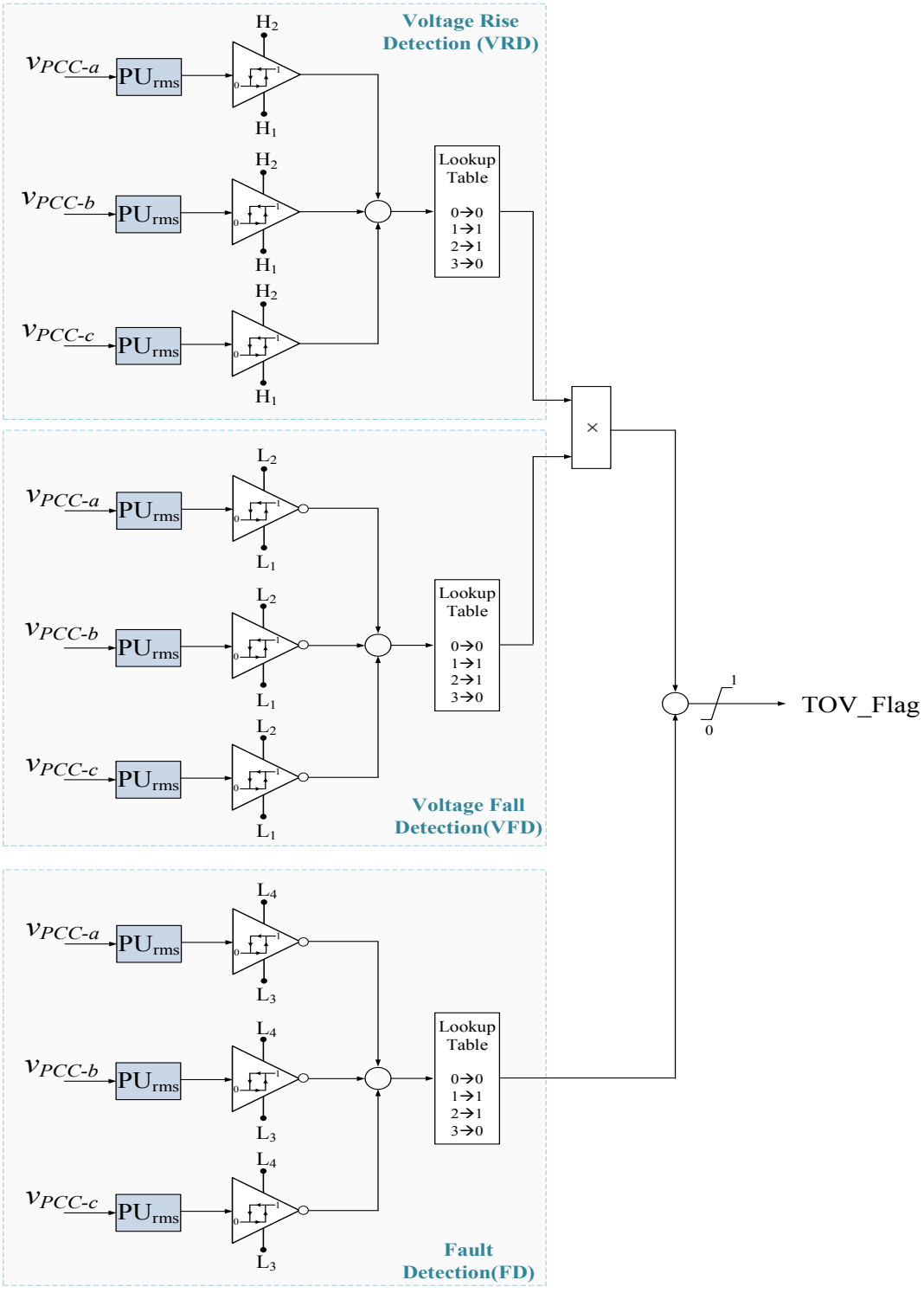

Figure 6-11: Structure of TOV Detection block

6.5 Simulation Results

The performance of the smart PV inverter while fulfilling two control objectives, voltage control and TOV reduction, are presented in this section. The PSCAD/EMTDC software is used for the simulation of the study system shown in Figure 6-2. First, the operation of a conventional PV system during its connection and during occurrence of a fault, is investigated. Then, the performance of a separate physical STATCOM for voltage control and TOV control is illustrated. Finally, the performance of smart PV inverter controller with the two control objectives is presented during steady-state and fault scenarios. In all these studies, a light (small) load is defined as 6 MW active power load and 2 Mvar reactive power load, whereas a heavy (large) load is considered to be 27 MW and 9 Mvar. The simulation model of the study system and modeling of smart PV inverter controller in PSCAD/EMTDC software are shown in Appendices D. 6 and D. 7, respectively.

6.5.1 Conventional PV System without Smart Inverter Control

In this study, the 10 MW PV solar system, which is connected at the bus where two 10 MW solar farms are already connected, does not have a smart PV inverter control. It operates as a conventional PV solar system with real power generation only.

6.5.1.1 Small Load Condition

Figure 6-12 demonstrates the PCC voltages in three phases and their per-unit rms values when PV systems generate their rated power output during small load conditions. Before connection of PV systems, the PCC voltage is about 1.04 pu which is in the acceptable range of Hydro One requirements. However, after the connection of the PV systems, the voltage rises up to 1.10 pu and causes an unacceptable steady-state overvoltage. Further, at $t= 0.54$ sec a single line-to-ground (SLG) fault occurs on phase "A". Subsequently, voltage of phase "A" falls to zero whereas rest of two phases reach 1.35 pu during fault. The temporary overvoltage (TOV) during SLG fault is beyond the Hydro One specified limit of 1.25 pu. Therefore, there is a necessity to control both the steady-state overvoltage and the temporary overvoltage.

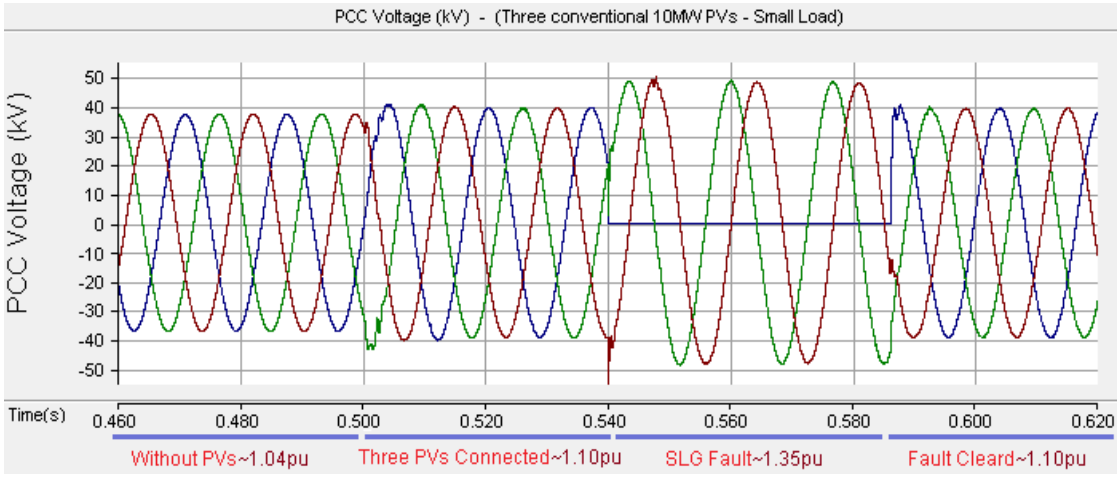

(a)

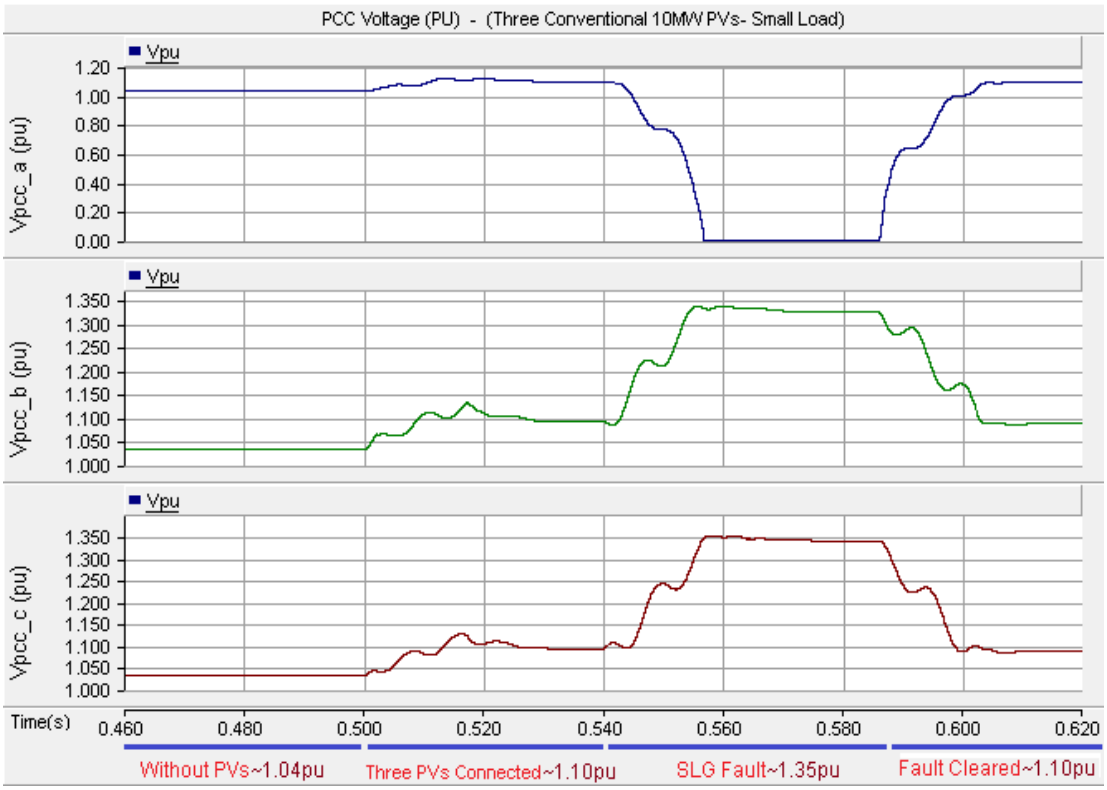

(b)

Figure 6-12: Performance of three conventional PV systems during small load and SLG Fault

a) **Instantaneous three phases PCC voltage**
b) **PCC phase voltages in P.U. *rms***

6.5.1.2 Large Load Condition

The three phase PCC voltages and their per-unit rms values are shown in Figure 6-13. It reveals that the steady-state voltage is 1.01 pu whereas the TOV is 1.23 pu during SLG fault, both of which are within Hydro One specified limits. This demonstrates that there is no need for either voltage regulation or TOV reduction during heavy loading condition.

6.5.2 Conventional PV Systems with a Physical STATCOM

One of the devices to prevent the steady-state and temporary overvoltage problems is STATCOM. As shown in Figure 6-2, the voltage can be controlled by installing a STATCOM at the same bus as PV systems. Hydro One has decided to employ a STATCOM to overcome the steady-state overvoltage to increase PV connectivity. This STATCOM however does not mitigate TOV. Hence, in this study, two different control objectives are considered for the STATCOM. First, the performance of STATCOM with symmetrical voltage controller alone is assessed during steady-state overvoltage and TOV conditions. Subsequently, the performance of STATCOM is considered with both voltage control and the proposed TOV controller is demonstrated.

6.5.2.1 STATCOM with Voltage Control

Figure 6-14 demonstrates the three phase instantaneous PCC voltages and their per-unit *rms* values when a STATCOM with voltage control is applied to the study system in presence of small amount of load. At *t=0.5* sec, three PV systems are connected to the grid which elevates the PCC voltage to 1.10 pu, which is unacceptable. At *t=0.54* sec, the STATCOM with symmetrical voltage control is connected to the PCC. The STATCOM effectively reduces the voltage from 1.10 pu to 1.02 pu which is within acceptable range. At *t=0.58* sec, an SLG fault occurs on Phase "A" until *t=0.63* sec. It is seen from Figure 6-14 (a) and (b) that the STATCOM with symmetrical voltage control operates incorrectly and in fact increases the TOV instead of reducing it. The symmetrical STATCOM control perceives that the PCC voltage is reduced and endeavors to enhance the voltage, thereby increasing the TOV. This illustrates that conventional symmetrical voltage control of STATCOM is not the appropriate control of STATCOM during TOV scenarios.

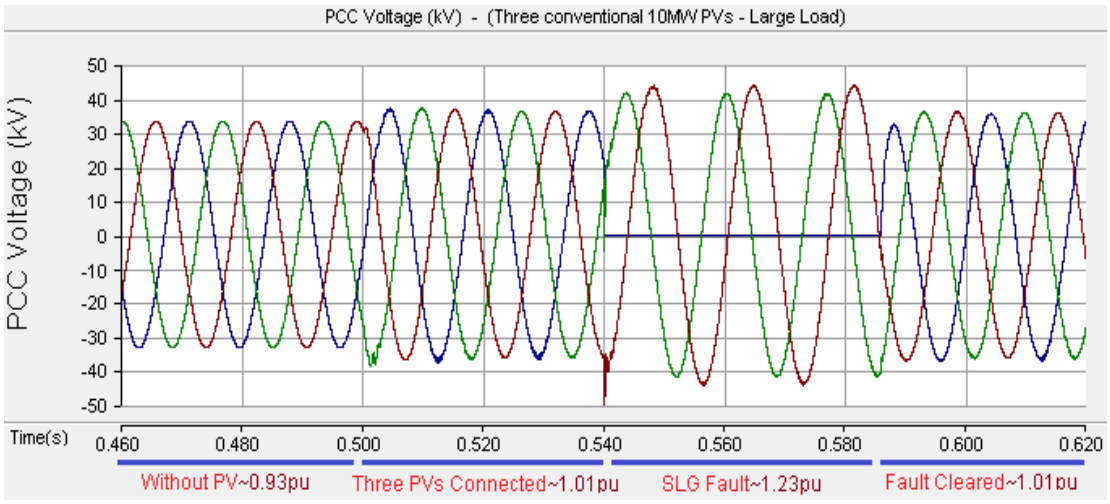

(a)

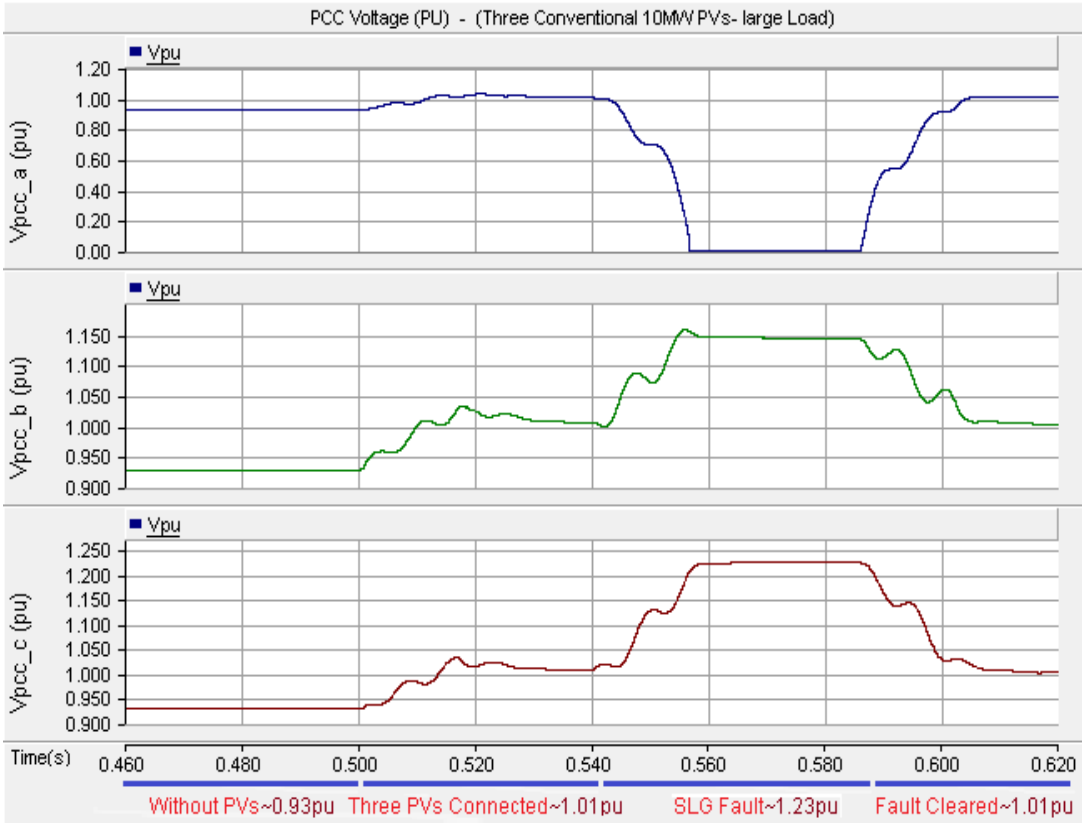

(b)

Figure 6-13: Performance of three conventional PV systems during large load and SLG Fault

a) **Instantaneous three phase PCC voltages**
b) **PCC phase voltages in P.U. *rms***

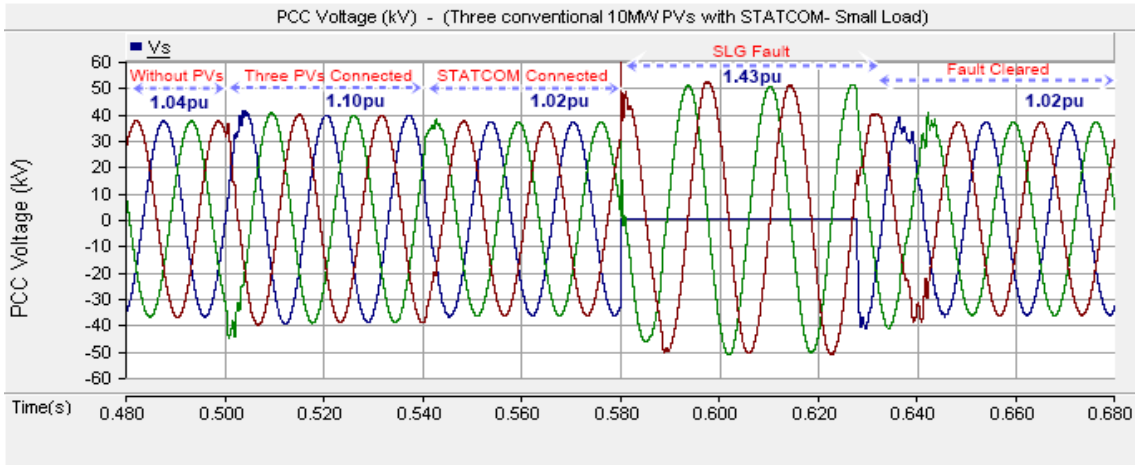

(a)

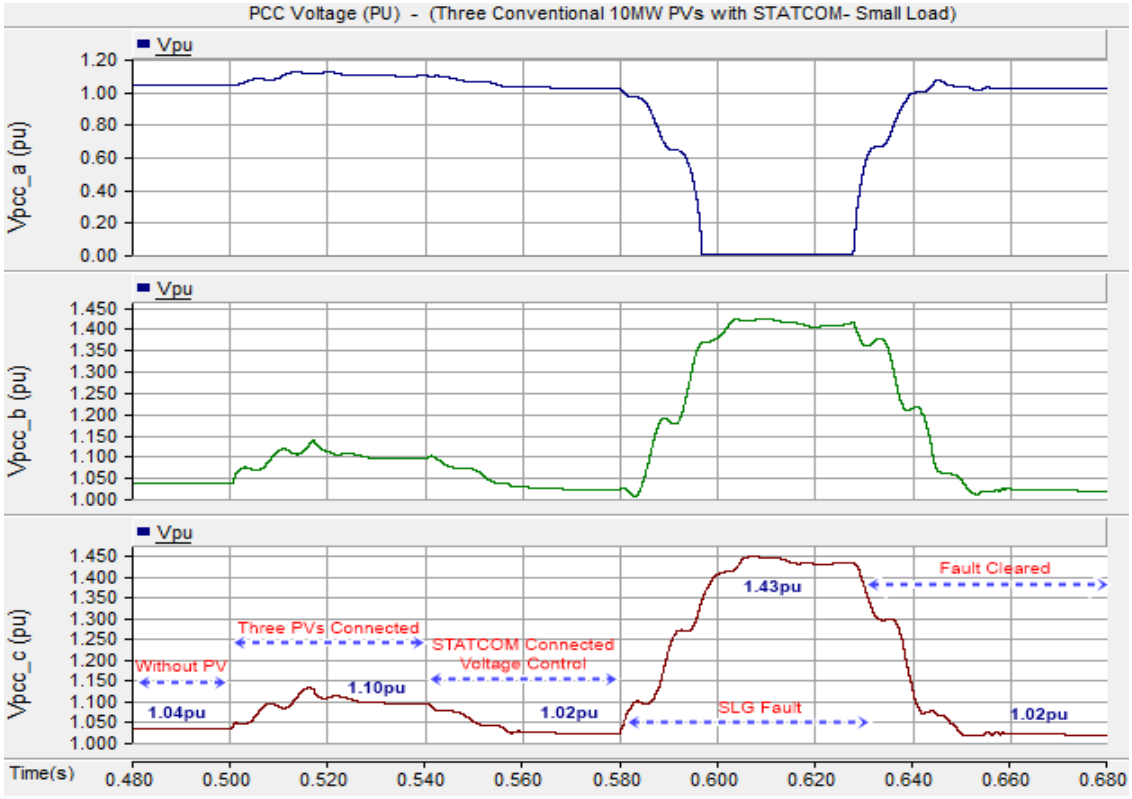

(b)

Figure 6-14: Performance of STATCOM with symmetrical voltage control, together with three- conventional PV systems during small load and SLG Fault

a) Instantaneous three phase PCC voltages
b) PCC voltage changes in P.U. rms

6.5.2.2 STATCOM with Voltage and TOV Control

In this study, the STATCOM control is modified with TOV reduction control to keep the TOV in acceptable range during fault while controlling the voltage in steady-state. Figure 6-15 demonstrates the three phase instantaneous PCC voltages and the per-unit *rms* voltage when a STATCOM with combined voltage control and proposed TOV control is applied to the study system with small load. When the three PV systems are connected the STATCOM controller regulates the PCC voltage from 1.10 pu to an acceptable value of 1.02 pu. When a SLG fault occurs at $t=0.58$ sec, the STATCOM controller switches from voltage control mode to TOV reduction control to decrease the temporary overvoltage. It should be noted that as all three PV systems are connected to the grid and generate active power during fault, for TOV reduction it is necessary to choose a STATCOM with larger capacity in comparison to the STATCOM for voltage control. In other words, both the size and cost of STATCOM will be increased for this objective.

6.5.3 Performance of a PV system with Smart PV Inverter and Two Conventional PV systems

In this section, instead of using an external STATCOM, the incoming third PV system is utilized with the proposed smart PV inverter controller, while the other two PV systems operate as conventional PV systems. The proposed smart inverter controller regulates the PCC voltage in steady-state with the remaining capacity of the inverter and also converts the PV system to Full STATCOM mode during a temporary overvoltage event. Two different faults, single line-to-ground (SLG) fault and line-to-line-ground (LLG) fault, are considered as the test conditions for assessment of the proposed controller performance.

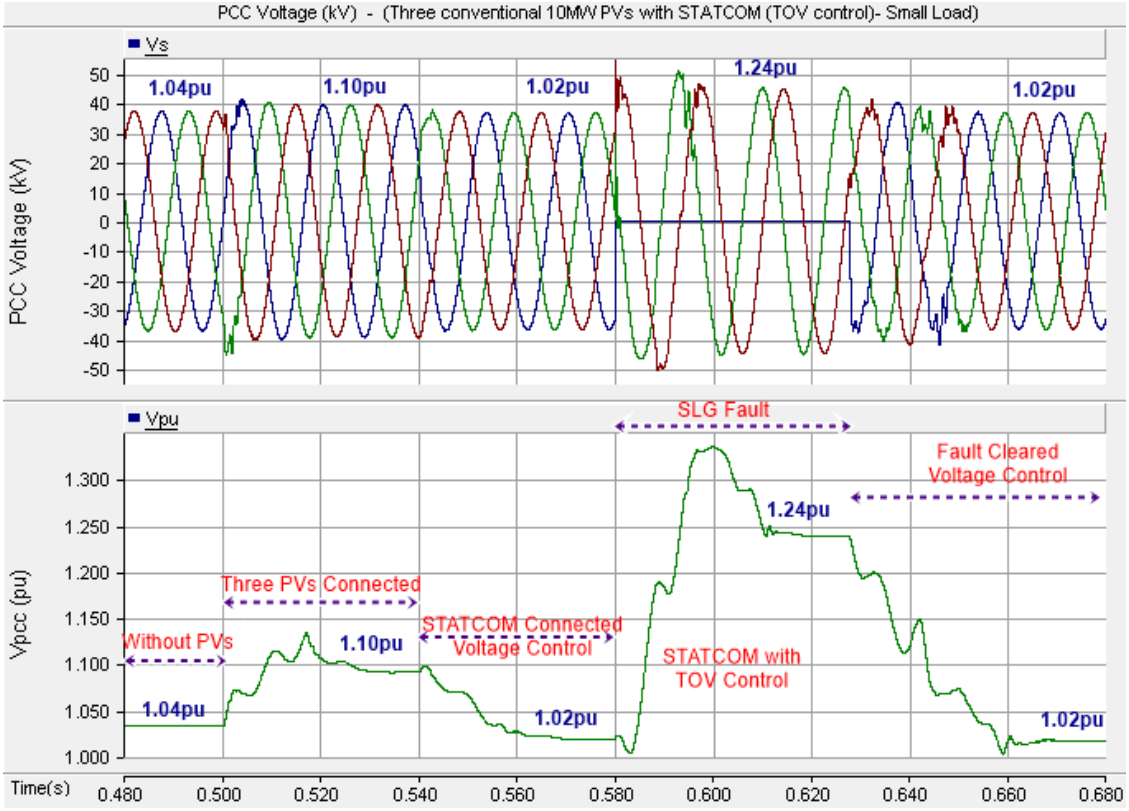

Figure 6-15: Performance of STATCOM with combined voltage and TOV controllers, together with three conventional PV systems, during small load and SLG Fault

6.5.3.1 SLG Fault

Figure 6-16 (a) and (b) illustrate the three phase instantaneous and per unit *rms* PCC voltage, respectively. At *t=0.5* sec, the three conventional systems are connected to the grid. Due to active power generation of PV systems, the PCC voltage increases from 1.04 pu to 1.10 pu which is unacceptable. The Partial STATCOM mode of the smart inverter for voltage control is enabled at *t=0.54* sec. This controller mode reduces the voltage to an acceptable range in less than one cycle utilizing the remaining capacity of the inverter. At *t=0.58* sec, the SLG fault causes the voltage of phase "A" falls to zero, whereas the other phase voltages experience a TOV. The proposed TOV detection unit detects this TOV event and triggers the TOV flag. Hence, the smart inverter autonomously switches from Partial STATCOM mode for voltage control to Full STATCOM mode for TOV reduction. In this situation, the controller changes the DC link voltage of the inverter to a value equal

to the open circuit voltage of the solar panels. It subsequently absorbs reactive power with full capacity of the inverter to reduce the voltages of phase “B” and phase “C”. By comparing Figure 6-16 and Figure 6-12, it is revealed that the PCC voltage is reduced from 1.35 pu to 1.23 pu which is below the TOV limit of Hydro One requirements. At *t=0.63* sec, the fault is cleared and the controller returns to Partial STATCOM mode for voltage control while generating active power.

Figure 6-17 depicts the AC voltage and DC link voltages of each PV system. The AC voltage signal represents the per-unit value of v_d in control plant. At *t=0.54* sec, when the smart inverter Partial STATCOM mode is activated, the controller decreases the PCC voltage to its reference value (1 pu). During fault, the Full STATCOM operating mode of the smart PV inverter is invoked and the above voltage control is deactivated. Only reactive power is absorbed to reduce the TOV in the healthy phases.

While the three PV systems are connected to the grid, the controller regulates the DC link voltage of each PV system to its reference value (925 V) within one cycle. It is emphasized that the DC voltage controller of smart PV inverter controller is made faster than the DC controller of conventional PV systems. This is achieved by choosing different cut-off frequency of the different DC voltage controllers. The reason of choosing a faster controller for smart PV inverter is because the smart controller requires full capacity of the inverter, and the DC voltage controller of smart PV should immediately regulate the DC voltage to a value equal to the open circuit voltage of solar panels. Although the DC voltage controller of the smart PV inverter is faster, the controller of the conventional PV systems needs to have more stability margin to maintain their stability during fault.

Figure 6-17 illustrates that the controller regulates the DC link voltage V_{dc1} to 1.02 kV very fast to virtually disconnect the solar panels, whereas the DC voltages of other PV systems change only slightly.

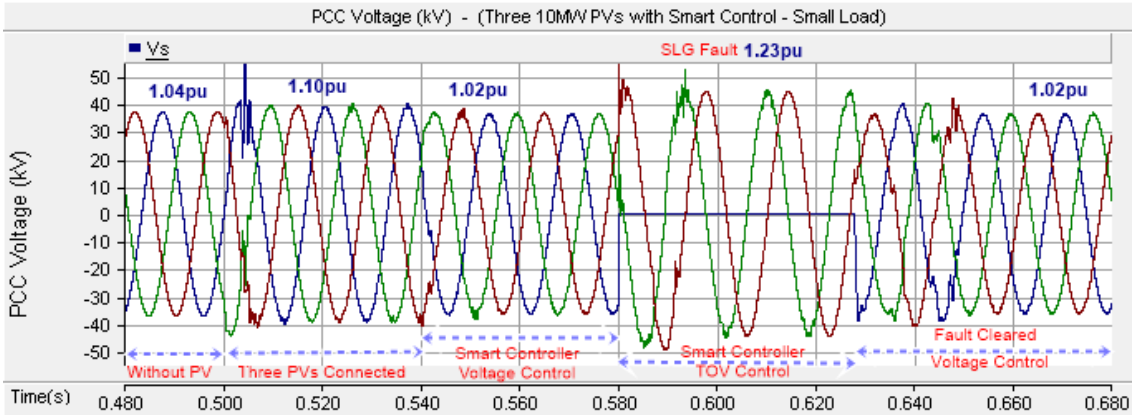

(a)

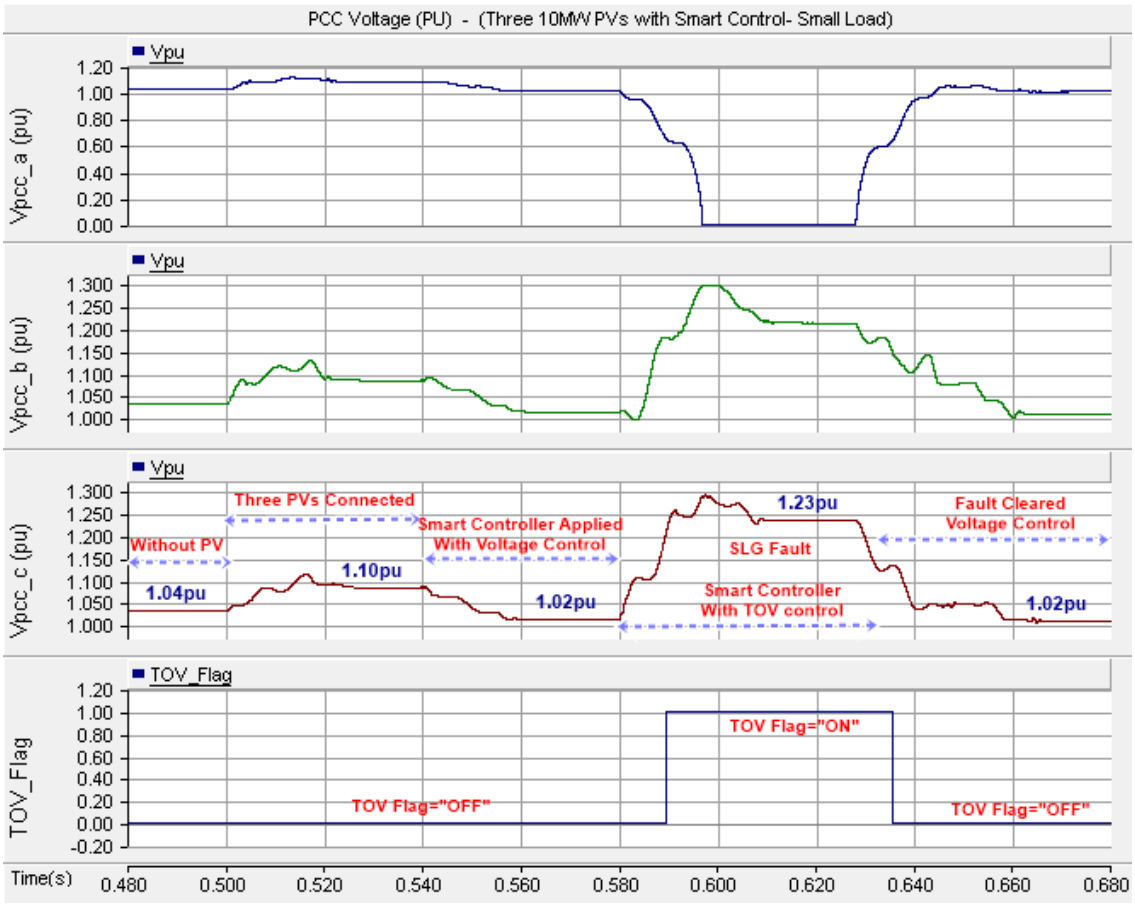

(b)

Figure 6-16: Performance of one PV system with proposed smart inverter control, together with two conventional PV systems, during small load and SLG fault

a) Instantaneous three phase PCC voltages b)PCC phase voltages in P.U. *rms*

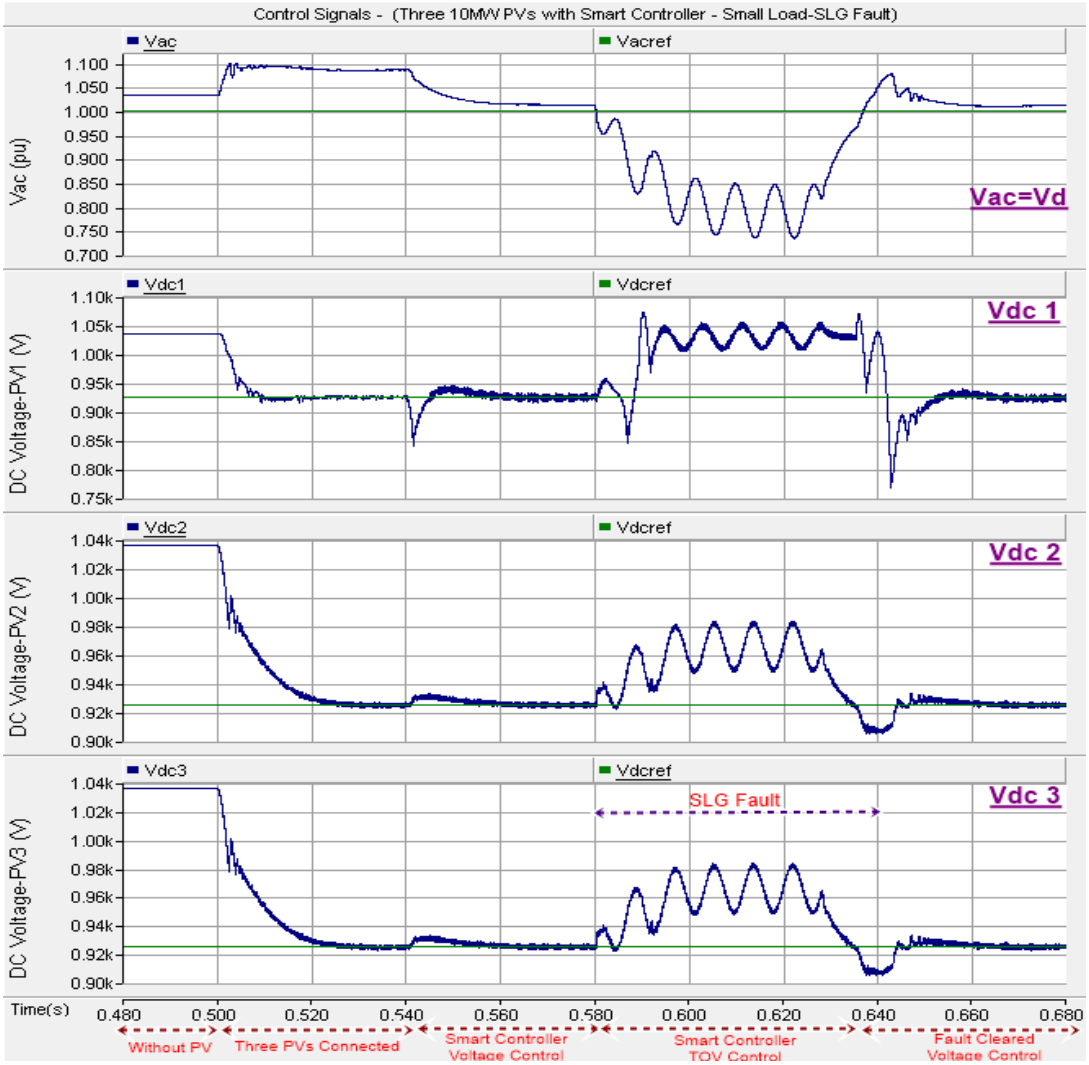

Figure 6-17: AC voltage and DC voltages signals for the smart PV inverter controller and conventional PV systems during a SLG fault

6.5.3.2 LLG Fault

The performance of the proposed smart inverter controller during a LLG fault is demonstrated in Figure 6-18. As in the previous SLG fault, the smart PV inverter controls the PCC voltage to its reference value during steady-state. As shown in Figure 6-18 (a) and (b), at *t=0.58* sec the voltages of two phases, phase "A" and phase "B", fall to zero due to LLG fault. This causes a TOV in the voltage of phase "C". The TOV detection unit triggers the TOV flag and the controller changes its mode from Partial STATCOM mode for voltage control to Full STATCOM mode for TOV reduction. This smart inverter control effectively reduces the TOV in the healthy phase to an acceptable value of 1.22 pu.

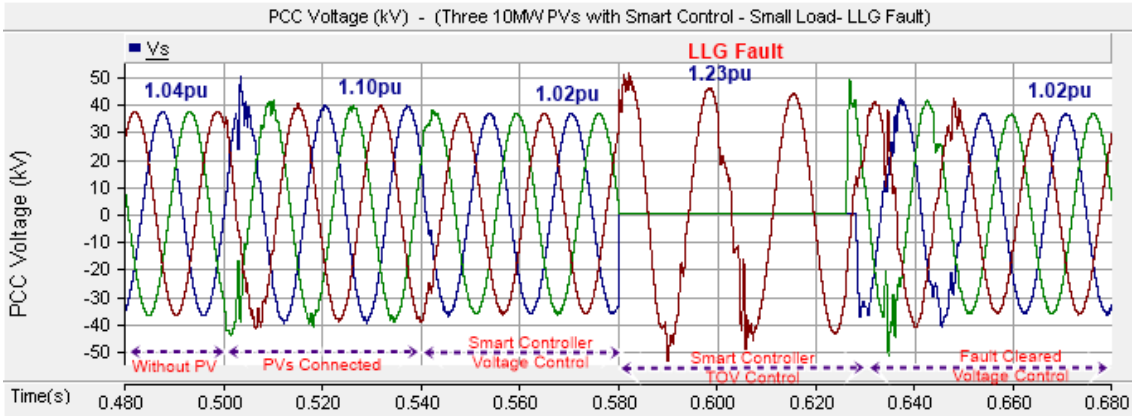

(a)

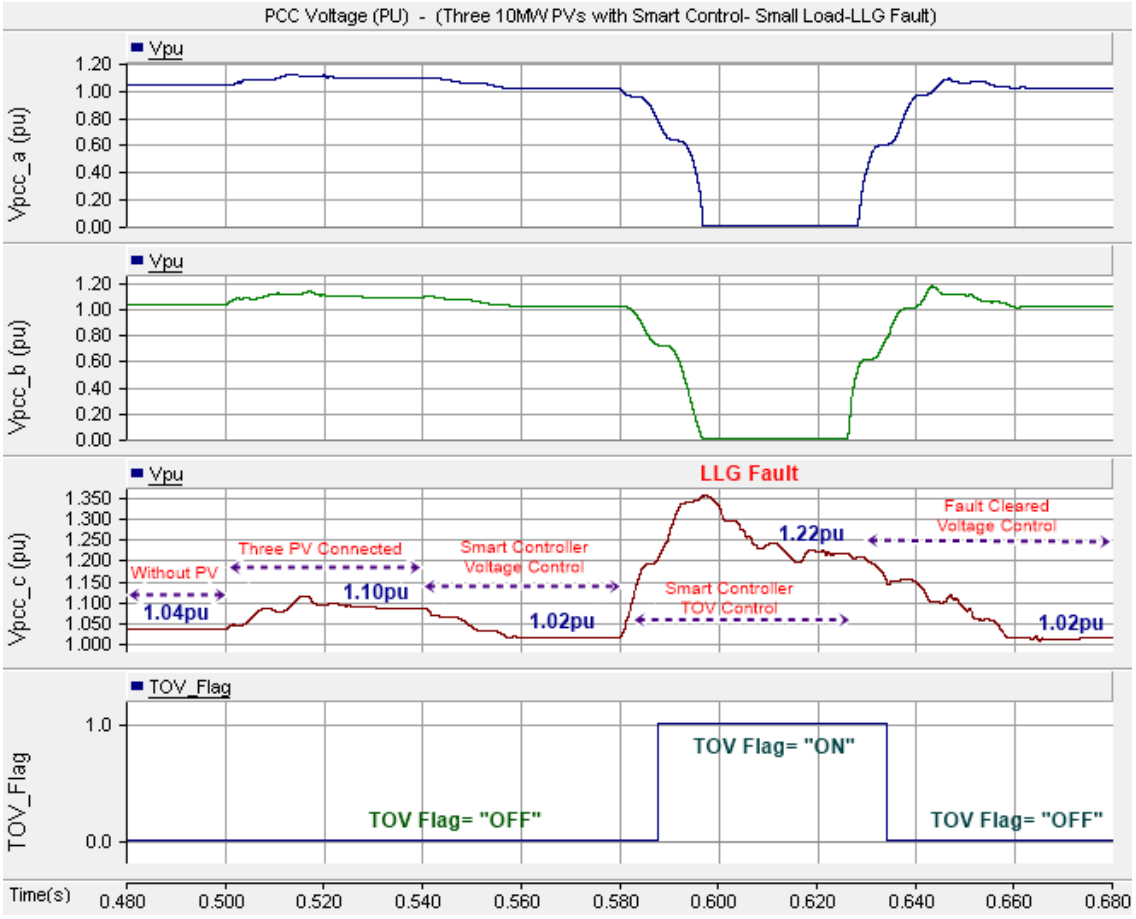

(b)

Figure 6-18: Performance of one PV system with proposed smart inverter control, together with two conventional PV systems, during small load and LLG fault

a) Instantaneous three phase PCC voltages b)PCC phase voltages in P.U. *rms*

6.6 Conclusion

This chapter presents an innovative smart PV inverter control for controlling the steady state voltages and restricting the TOVs resulting from unsymmetrical faults to within acceptable values. A 44 kV realistic distribution feeder of the Hydro One is chosen as the study system. This system has two 10 MW PV solar farms already installed. Connection of a third 10 MW PV solar system created problems of steady state overvoltage and TOV. To alleviate these issues, Hydro One installed a physical STATCOM at the PCC of the three PV solar farms.

PSCAD Simulation studies are presented to illustrate the exact problem of steady state overvoltage and TOV with the connection of the third 10 MW PV solar system. It is shown that conventional symmetrical voltage control of STATCOM fails to curtail the TOV. This has indeed been the problem with the actually STATCOM installed in Hydro One system, which failed to limit the TOV.

The proposed patent-pending smart inverter control is implemented on the third incoming 10 MW PV solar farm. It is shown that this novel control in Partial STATCOM mode regulates the steady state over voltage to the desired reference value within one and half cycle. Further, this smart inverter control in Full STATCOM mode successfully reduces the TOV caused during both single line to ground (SLG) fault and line to line to ground (LLG) fault to within acceptable values within one cycle.

This proposed novel smart inverter control can therefore potentially eliminate the need for the physical STATCOM already installed in the Hydro One distribution system, thereby saving an enormous expense for Hydro One.

CHAPTER 7

7 CONCLUSIONS AND FUTURE WORK

PV solar systems employ inverters to transform dc power from solar panels into real ac power for injecting into the power transmission and distribution grids. Inverters that perform multiple functions in addition to real power production are known as “smart inverters”.

This thesis presents a novel patent-pending [43, 44, 52] control of PV inverter as a dynamic reactive power compensator – STATCOM. This “smart PV inverter” control enables a PV solar inverter to operate in three modes – i) Full PV mode, ii) Partial STATCOM mode, and iii) Full STATCOM mode, depending upon system needs. The above novel control is developed and demonstrated for the objectives of a) symmetrical voltage regulation, b) temporary overvoltage (TOV) reduction, c) power factor correction, and d) reactive power control.

In Full PV mode the inverter performs only real power production based on solar radiation. In Partial STATCOM mode, the inverter utilizes the capacity of the inverter remaining after real power production for voltage control, power factor correction and reactive power control. The real power production is not affected at all in this mode. The Full STATCOM mode is invoked in emergency scenarios, such as faults, or severe voltage fluctuations. In this mode, the real power production is shut down temporarily (typically for a few seconds) and the entire inverter capacity is utilized for voltage regulation or TOV curtailment for providing critical support to the power system.

This thesis presents a comprehensive design of the proposed smart inverter controller with all its associated system components. The performance of the smart inverter is simulated on the industry grade electromagnetic transients software EMTDC/PSCAD. It is further validated through Real Time Digital Simulation (RTDS) and Control Hardware in the Loop (CHIL) simulation. Finally the successful performance of the smart inverter controller is demonstrated on a 10 kW inverter in the laboratory on a simulated feeder of Bluewater Power, Sarnia, where this smart inverter is proposed to be installed.

The smart PV inverter control is further shown to enhance the connectivity of PV solar farms in a realistic 44 kV Hydro One distribution feeder. It is demonstrated that if such a novel control is implemented on a 10 MW PV solar farm, the need for the actually installed STATCOM for voltage regulation and TOV control can be either minimized or altogether eliminated, bringing a significant savings for the utility.

The summary of main conclusions of this thesis as well as proposed future studies are described below.

7.1 Modeling of Distribution System with Smart PV Inverter

In chapter 2, the operating principles of the smart PV inverter are presented for both Partial and Full STATCOM modes, for the two control objectives of voltage control and power factor correction. The design of the novel smart inverter control in d-q reference frame is described. The general design procedure of each system component is illustrated. The controller parameters are determined utilizing classic control design principles. The different inverter components and controller parameters are subsequently designed for a 10kVA smart PV inverter system to be implemented in the distribution network of the Bluewater Power, Sarnia.

7.2 Software Simulation of Smart PV Inverter

In chapter 3, a system model of a realistic feeder of Bluewater Inc. network is developed in PSCAD/EMTDC software. A 10 kVA PV system is connected to the grid in presence of different loads. The controller of the conventional PV system is replaced by a smart inverter controller to operate in Partial STATCOM mode and Full STATCOM mode depending upon the system requirements. The control objectives for partial STATCOM operation mode are power factor correction, voltage regulation and reactive power control. However, control objective for full STATCOM operation mode is voltage control alone. The software simulation studies are utilized to demonstrate the controller performance for both modes of operation for achieving the two control objectives. In partial STATCOM mode, the controller implements the grid power factor at unity by providing required reactive power of the load. The smart inverter controller performance is further evaluated

for voltage control in both capacitive and inductive regions. During voltage control, the active power output of PV system is changed to demonstrate the successful decoupling of the active and reactive power controllers. A sudden connection of a large load causes the smart inverter to transition to the full STATCOM operation mode. In this mode, the solar panels are disconnected from the inverter and voltage is controlled utilizing the full capacity of the inverter. The smart inverter controller is shown to regulate the PCC voltage in both capacitive and inductive regions, in one cycle, which is the standard response of a commercial STATCOM.

7.3 Real Time Digital Simulation (RTDS) and Hardware-In-Loop Simulation of Smart PV Inverter

In chapter 4, the control-hardware-in-loop (CHIL) study of the proposed novel inverter control is presented. The CHIL studies are typically performed for the evaluation of the real time operation of the controller, and are considered to be industry standard before the deployment of the controllers in field. The designed smart PV inverter controller for the study system is implemented on a dSPACE board. The entire study system including Bluewater Power network equivalent, passive loads and PV solar system are modeled in the Real Time Digital Simulator (RTDS). The controller inside the dSPACE board receives the required signals from RTDS and generates the PWM pulses for the inverter switches inside RTDS after processing the control algorithm. The CHIL studies presented in this chapter verify the effectiveness of the proposed novel smart PV inverter controller in real-time for both steady-state and transient conditions. The EMPTDC/PSCAD software studies of the smart inverter controller performance presented in Chapter 3 correlate well with the CHIL results in this chapter and are thus validated.

7.4 Lab Validation of Smart PV Inverter Performance

Chapter 5 presents the implementation of the entire 10 kW study system in the Power Systems Lab of Western University. A PV Solar Simulator which mimics an actual solar array is used to generate DC power based on irradiance and temperature profiles. A voltage source inverter based on a two-level three-phase IGBT module is connected to the PV Simulator. The smart PV inverter controller is implemented on the dSPACE board. The

controller sends the switching pulses to the actual inverter based on the control objectives. An LC filter and an interface transformer are connected after the inverter to remove the harmonics as well as to provide isolation from the grid. Laboratory tests are performed for validating of the controller performance in both partial and full STATCOM modes of operation. The operation modes, control objectives and reference value of the DC link voltage are set through a designed graphic user interface (GUI) in ControlDesk software. Also, the real-time value of the PCC voltage, inverter current, load current and DC link voltage are monitored in the GUI.

It is successfully demonstrated in the Partial STATCOM mode, that the controller uses the remaining capacity of the inverter to control PCC voltage and correct the power factor as per the provided reference values. To evaluate the controller performance in Full STATCOM operation mode, two tests are performed by applying inductive and capacitive loads suddenly to provide transient voltage drop and voltage rise, respectively. In this full STATCOM operation mode, the controller induces the PV Simulator to operate in a region which is close to open source voltage of solar panel. This condition is similar to disconnection of the solar panels. Hence, the entire capacity of the inverter is available for the controller to regulate the PCC voltage to the desired values. The experimental results of this chapter confirm the successful operation of the designed smart inverter controller in the Full STATCOM mode in transient system conditions. Moreover the response time of the smart PV inverter in Full STATCOM mode is similar to that of commercial STATCOMs.

7.5 Temporary Overvoltage Reduction and PV Connectivity Enhancement with Smart PV Inverter

This chapter presents an innovative patent-pending smart PV inverter control for controlling the steady state voltages and restricting the TOVs resulting from unsymmetrical faults to within acceptable values. A 44 kV realistic distribution feeder of the Hydro One is chosen as the study system. This system has two 10 MW PV solar farms already installed. Connection of a third 10 MW PV solar system created problems of steady state overvoltage and TOV. To alleviate these issues, Hydro One installed a physical STATCOM at the PCC of the three PV solar farms.

At first, PSCAD Simulation studies are presented to illustrate the exact problem of steady state overvoltage and TOV with the connection of the third 10 MW PV solar system. It is shown that conventional symmetrical voltage control of STATCOM fails to curtail the TOV. This has indeed been the problem with the actually STATCOM installed in Hydro One system, which failed to limit the TOV. The proposed smart inverter control is implemented on the third incoming 10 MW PV solar farm. It is shown that this novel control in Partial STATCOM mode regulates the steady state over voltage to the desired reference value within one and half cycle. Further, this smart inverter control in Full STATCOM mode successfully reduces the TOV caused during both single line to ground (SLG) fault and line to line to ground (LLG) fault to within acceptable values, within one cycle. This proposed novel smart inverter control can therefore potentially eliminate the need for the physical STATCOM already installed in the Hydro One distribution system, thereby saving an enormous expense for Hydro One.

7.6 Contributions

- A novel patent-pending smart PV inverter control in both Partial STATCOM and Full STATCOM mode is presented. The smart inverter is theoretically modeled, and its performance successfully demonstrated through:
    - Industry grade electromagnetic transients simulations software EMTDC/PSCAD
    - Real Time Digital Simulator (RTDS),
    - Control Hardware in Loop simulations, and,
    - 10 kW PV inverter connected to a PV solar simulator with 10 kW resistive/inductive/capacitive loads in the Laboratory.

Development of such a novel patent-pending smart PV inverter control and comprehensive demonstration of the effectiveness of this smart inverter controller through various procedures employed in actual commercial development of inverter controls, has been done for the first time.

- The effectiveness of the smart PV system control in reducing temporary over-voltages in distribution feeders, is illustrated. It is demonstrated that implementation of such smart PV inverter controls in PV solar farms can potentially increase the connectivity of PV solar farms in distribution feeders by minimizing or completely obviating the need of physical expensive STATCOMs used for the same purpose.

  Such a novel control of PV inverters can be of great help to utilities to minimize investments in expensive STATCOMs for accomplishing the same tasks as actual STATCOMs

7.7 Publications

The following journal and conference papers have been published (or submitted), as a result of this thesis:

7.7.1 Refereed Journals

[1] Rajiv K. Varma and Ehsan Siavashi, "Novel Smart PV Inverter for Voltage Regulation and Reactive Power Control Part 1: Modeling and Software Simulation", *IEEE Transactions on Smart Grid.*

[2] Rajiv K. Varma and Ehsan Siavashi, "Novel Smart PV Inverter for Voltage Regulation and Reactive Power Control Part 2: Hardware In Loop Simulation and Experimental Validation", *IEEE Transactions on Smart Grid.*

[3] Rajiv K. Varma, Ehsan Siavashi, Andrew Yan, Lianxian Tang, "Novel Smart PV Inverter Control as STATCOM (PV-STATCOM) for Increasing PV Hosting Capacity of Distribution Feeders", *IEEE Transactions on Smart Grid.*

7.7.2 Refereed Conference papers

[1] Rajiv K. Varma, Shah Arifur Rahman, Ehsan Siavashi, and Mahendra A.C., "Nighttime Applications of PV Solar Farms", *Proc. 2014 Solar Power International Conference*, Las Vegas, USA, Oct. 2014

[2] Rajiv K. Varma, Ehsan M. Siavashi, Byomakesh Das, and Vinay Sharma, "Real Time Digital Simulation of PV Solar System as STATCOM (PV-STATCOM) for Voltage Regulation and Power Factor Correction", *Proc. IEEE Electric Power and Energy Conference* - 2012, Oct. 2012, London, Canada

[3] Rajiv K. Varma, Ehsan Siavashi, Byomakesh Das, Vinay Sharma "Novel application of a PV Solar Plant as STATCOM during Night and Day in a Distribution Utility Network – Part 2", Panel Session on "FACTS/Power Electronics Installations", *Proc. 2012 IEEE T&D Conference*, Orlando, USA, May 2012.

7.8 Future Work

Further research and development work may be performed on the smart PV inverters as follows:

- Field implementation and testing of smart PV inverter in the network of Bluewater Power Corporation
- Coordination control of multiple smart PV inverters at the same bus or neighboring buses in a distribution feeder
- Addition of more smart inverter functions with the main controller such as active filter, unbalanced voltage control, anti-islanding and auxiliary damping control
- Temporary overvoltage detection method to trigger the controller faster
- Implementation of MPPT algorithm to control DC link voltage faster

REFERENCES

[1] International Energy Agency, "Snapshot of Global PV 1992-2013," 2014.

[2] European Photovoltaic Industry Association. (2014). *Global market outlook for photovoltaics 2014–2018*.

[3] http://fit.powerauthority.on.ca/. (Jan 2014). *FIT Price Schedule*.

[4] R. Singh and R. Banerjee, "Estimation of roof-top photovoltaic potential using satellite imagery and GIS," in *Photovoltaic Specialists Conference (PVSC), 2013 IEEE 39th*, 2013, pp. 2343-2347.

[5] F. Katiraei, Agu, x, and J. R. ero, "Solar PV Integration Challenges," *Power and Energy Magazine, IEEE,* vol. 9, pp. 62-71, 2011.

[6] Thomas Ackermann, Göran Andersson, and Lennart Söder, "Distributed generation: a definition," *Electric power systems research,* vol. 57, pp. 195-204, 2001.

[7] G. A. Hamoud and L. Lee, "Criticality Assessment of Distribution Feeder Sections," *Power Systems, IEEE Transactions on,* vol. 27, pp. 298-304, 2012.

[8] B. Kroposki, P. K. Sen, and K. Malmedal, "Selection of Distribution Feeders for Implementing Distributed Generation and Renewable Energy Applications," *Industry Applications, IEEE Transactions on,* vol. 49, pp. 2825-2834, 2013.

[9] Guido Pepermans, Johan Driesen, Dries Haeseldonckx, Ronnie Belmans, and William D'haeseleer, "Distributed generation: definition, benefits and issues," *Energy policy,* vol. 33, pp. 787-798, 2005.

[10] R. K. Varma, G. Sanderson, and K. Walsh, "Global PV incentive policies and recommendations for utilities," in *Electrical and Computer Engineering (CCECE), 2011 24th Canadian Conference on*, 2011, pp. 001158-001163.

[11] H Lee Willis, *Distributed power generation: planning and evaluation*: CRC Press, 2000.

[12] Digambar M Tagare, "Distributed Generation (DG) and Distributed Resources (DR)," *Electric Power Generation: The Changing Dimensions,* pp. 275-299.

[13] R. K. Varma, V. Khadkikar, and R. Seethapathy, "Nighttime Application of PV Solar Farm as STATCOM to Regulate Grid Voltage," *Energy Conversion, IEEE Transactions on,* vol. 24, pp. 983-985, 2009.

[14] M Oprisan and S Pneumaticos, "Potential for electricity generation from emerging renewable sources in Canada," in *EIC Climate Change Technology, 2006 IEEE*, 2006, pp. 1-10.

[15] C. L. Masters, "Voltage rise: the big issue when connecting embedded generation to long 11 kV overhead lines," *Power Engineering Journal,* vol. 16, pp. 5-12, 2002.

[16] M. A. Mahmud, H. R. Pota, and M. J. Hossain, "Dynamic Stability of Three-Phase Grid-Connected Photovoltaic System Using Zero Dynamic Design Approach," *Photovoltaics, IEEE Journal of,* vol. 2, pp. 564-571, 2012.

[17] M. G. Molina, E. C. dos Santos, and M. Pacas, "Improved power conditioning system for grid integration of photovoltaic solar energy conversion systems," in *Transmission and Distribution Conference and Exposition: Latin America (T&D-LA), 2010 IEEE/PES*, 2010, pp. 163-170.

[18] S. Rahman, "Going green - the growth of renewable energy," *Power and Energy Magazine, IEEE,* vol. 99, pp. 16-18, 2003.

[19] Aldo Canova, Luca Giaccone, Filippo Spertino, and Michele Tartaglia, "Electrical impact of photovoltaic plant in distributed network," *Industry Applications, IEEE Transactions on,* vol. 45, pp. 341-347, 2009.

[20] SJ Steffel, PR Caroselli, AM Dinkel, JQ Liu, RN Sackey, and NR Vadhar, "Integrating solar generation on the electric distribution grid," *Smart Grid, IEEE Transactions on,* vol. 3, pp. 878-886, 2012.

[21] Rupesh G Wandhare and Vivek Agarwal, "Reactive Power Capacity Enhancement of a PV-Grid System to Increase PV Penetration Level in Smart Grid Scenario," 2014.

[22] T. S. Basso and R. DeBlasio, "IEEE 1547 series of standards: interconnection issues," *Power Electronics, IEEE Transactions on,* vol. 19, pp. 1159-1162, 2004.

[23] IEC Standard, "61727,“Characteristic of the utility interface for photovoltaic (PV) systems,”" IEC, Tech. Rep2002.

[24] "IEEE Recommended Practice for Utility Interface of Photovoltaic (PV) Systems," *IEEE Std 929-2000,* p. i, 2000.

[25] "IEEE Application Guide for IEEE Std 1547(TM), IEEE Standard for Interconnecting Distributed Resources with Electric Power Systems," *IEEE Std 1547.2-2008,* pp. 1-217, 2009.

[26] Tang Lianxiang, A. Yan, L. Marti, and J. Fuerth, "Hydro one distribution voltage performance design criteria and power distance test in enabling distributed generation," in *Transmission and Distribution Conference and Exposition (T&D), 2012 IEEE PES*, 2012, pp. 1-8.

[27] S. Deshmukh, B. Natarajan, and A. Pahwa, "Voltage/VAR Control in Distribution Networks via Reactive Power Injection Through Distributed Generators," *Smart Grid, IEEE Transactions on,* vol. 3, pp. 1226-1234, 2012.

[28] Narain G Hingorani and Laszlo Gyugyi, *Understanding facts*: IEEE press, 2000.

[29] R Mohan Mathur and Rajiv K Varma, *Thyristor-based FACTS controllers for electrical transmission systems*: John Wiley & Sons, 2002.

[30] Frede Blaabjerg, Remus Teodorescu, Marco Liserre, and Adrian V Timbus, "Overview of control and grid synchronization for distributed power generation systems," *Industrial Electronics, IEEE Transactions on,* vol. 53, pp. 1398-1409, 2006.

[31] C Schauder, M Gernhardt, E Stacey, T Lemak, L Gyugyi, TW Cease*, et al.*, "TVA STATCOM project: Design, installation, and commissioning," *CIGRE paper,* pp. 14-106, 1996.

[32] Y. L. Tan, "Analysis of line compensation by shunt-connected FACTS controllers: a comparison between SVC and STATCOM," *Power Engineering Review, IEEE,* vol. 19, pp. 57-58, 1999.

[33] Amirnaser Yazdani and Reza Iravani, *Voltage-sourced converters in power systems: modeling, control, and applications*: John Wiley & Sons, 2010.

[34] M. Molinas, J. A. Suul, and T. Undeland, "Low Voltage Ride Through of Wind Farms With Cage Generators: STATCOM Versus SVC," *Power Electronics, IEEE Transactions on,* vol. 23, pp. 1104-1117, 2008.

[35] Zheng Ce and M. Kezunovic, "Distribution system voltage stability analysis with wind farms integration," in *North American Power Symposium (NAPS)*, 2010, pp. 1-6.

[36] M Chamana and BH Chowdhury, "Impact of smart inverter control with PV systems on voltage regulators in active distribution networks," in *High-capacity Optical Networks and Emerging/Enabling Technologies (HONET), 2014 11th Annual*, 2014, pp. 115-119.

[37] Matthew J Reno, Robert J Broderick, and Santiago Grijalva, "Smart Inverter Capabilities for Mitigating Over-Voltage on Distribution Systems with High Penetrations of PV," *strategies,* vol. 7, p. 9, 2013.

[38] J. Langston, K. Schoder, M. Steurer, O. Faruque, J. Hauer, F. Bogdan*, et al.*, "Power hardware-in-the-loop testing of a 500 kW photovoltaic array inverter," in *IECON 2012 - 38th Annual Conference on IEEE Industrial Electronics Society*, 2012, pp. 4797-4802.

[39] B. Mather and R. Neal, "Integrating high penetrations of PV into Southern California: Year 2 project update," in *Photovoltaic Specialists Conference (PVSC), 2012 38th IEEE*, 2012, pp. 000737-000741.

[40] B. A. Mather, M. A. Kromer, and L. Casey, "Advanced photovoltaic inverter functionality verification using 500kw power hardware-in-loop (PHIL) complete system laboratory testing," in *Innovative Smart Grid Technologies (ISGT), 2013 IEEE PES*, 2013, pp. 1-6.

[41] Converters Inverters, "Controllers and interconnection system equipment for use with distributed energy resources," *UL Std,* vol. 1741, 2005.

[42] JW Smith, W Sunderman, R Dugan, and Brian Seal, "Smart inverter volt/var control functions for high penetration of PV on distribution systems," in *Power Systems Conference and Exposition (PSCE), 2011 IEEE/PES*, 2011, pp. 1-6.

[43] Rajiv K. Varma, "Multivariable Modulator Controller for Power Generation Facility," United States Provisional Patent Application Serial No.: 61/912,969, 2013.

[44] Rajiv Kumar Varma, Vinod Khadkikar, and Shah Arifur Rahman, "Utilization of distributed generator inverters as statcom," PCT Patent application PCT/CA2010/001419, 2010.

[45] R. A. Walling and K. Clark, "Grid support functions implemented in utility-scale PV systems," in *Transmission and Distribution Conference and Exposition, 2010 IEEE PES*, 2010, pp. 1-5.

[46] Leo F Casey, Colin Schauder, James Cleary, and Michael Ropp, "Advanced inverters facilitate high penetration of renewable generation on medium voltage feeders-impact and benefits for the utility," in *IEEE conference on innovative technologies for an efficient and reliable electricity supply*, 2010, pp. 86-93.

[47] R Dugan, W Sunderman, and B Seal, "Advanced inverter controls for distributed resources," 2013.

[48] California Energy Commission. (2014, Recommendations for Utility Communications with Distributed Energy Resources (DER) Systems with Smart Inverters. Available: http://www.cpuc.ca.gov/NR/rdonlyres/899E4077-36AE-4946-8515-E68EA95C0B32/0/SIWGPhase2CommunicationsRecommendationsv2_Updated10222014.pdf

[49] California Energy Commission. (2013, Candidate DER Capabilities: Recommendations for Updating Technical Requirements in Rule 21. Available: http://www.cpuc.ca.gov/NR/rdonlyres/0643355A-A378-4C1E-B471-0D0AF21E895E/0/CandidateDERCapabilitiesRecommendationsforUpdatingTechnicalRequirementsinRule21.pdf

[50] A Beekmann, J Marques, E Quitmann, and S Wachtel, "Wind energy converters with FACTS Capabilities for optimized integration of wind power into transmission and distribution systems," in *Integration of Wide-Scale Renewable Resources Into the Power Delivery System, 2009 CIGRE/IEEE PES Joint Symposium*, 2009, pp. 1-1.

[51] N. W. Miller and K. Clark, "Advanced controls enable wind plants to provide ancillary services," in *Power and Energy Society General Meeting, 2010 IEEE*, 2010, pp. 1-6.

[52] Rajiv K Varma and Vinod Khadkikar, "Utilization of solar farm inverter as STATCOM," *US Provisional Patent application filed,* vol. 15, 2009.

[53] Rajiv K Varma, Shah Arifur Rahman, and Ravi Seethapathy, "Novel Control of Grid Connected Photovoltaic (PV) Solar Farm for Improving Transient Stability and Transmission Limits Both During Night and Day," in *Proc. 2010 World Energy Conference, Montreal, Canada*, pp. 1-6.

[54] Rajiv K Varma, SA Rahman, AC Mahendra, R Seethapathy, and T Vanderheide, "Novel nighttime application of PV solar farms as STATCOM (PV-STATCOM)," in *Power and Energy Society General Meeting, 2012 IEEE*, 2012, pp. 1-8.

[55] G. C. Pyo, H. W. Kang, and S. I. Moon, "A new operation method for grid-connected PV system considering voltage regulation in distribution system," in *Power and Energy Society*

General Meeting - Conversion and Delivery of Electrical Energy in the 21st Century, 2008 IEEE, 2008, pp. 1-7.

[56] Fabio L Albuquerque, Adélio J Moraes, Geraldo C Guimarães, Sérgio MR Sanhueza, and Alexandre R Vaz, "Photovoltaic solar system connected to the electric power grid operating as active power generator and reactive power compensator," *Solar Energy,* vol. 84, pp. 1310-1317, 2010.

[57] D. T. Rizy, Xu Yan, Li Huijuan, Li Fangxing, and P. Irminger, "Volt/Var control using inverter-based distributed energy resources," in *Power and Energy Society General Meeting, 2011 IEEE*, 2011, pp. 1-8.

[58] A. Maknouninejad, N. Kutkut, I. Batarseh, and Qu Zhihua, "Analysis and control of PV inverters operating in VAR mode at night," in *Innovative Smart Grid Technologies (ISGT), 2011 IEEE PES*, 2011, pp. 1-5.

[59] A. Moawwad, V. Khadkikar, and J. L. Kirtley, "Interline photovoltaic (I-PV) power plants for voltage unbalance compensation," in *IECON 2012 - 38th Annual Conference on IEEE Industrial Electronics Society*, 2012, pp. 5330-5334.

[60] H. Patel and V. Agarwal, "PV Based Distributed Generation with Compensation Feature Under Unbalanced and Non-linear Load Conditions for a 3-ϕ, 4 Wire System," in *Industrial Technology, 2006. ICIT 2006. IEEE International Conference on*, 2006, pp. 322-327.

[61] H Patel and V Agarwal, "PV based distributed generation with compensation feature under unbalanced and non-linear load conditions for a 3-ϕ, 4 wire system," in *Industrial Technology, 2006. ICIT 2006. IEEE International Conference on*, 2006, pp. 322-327.

[62] R. K. Varma, S. A. Rahman, and T. Vanderheide, "New Control of PV Solar Farm as STATCOM (PV-STATCOM) for Increasing Grid Power Transmission Limits During Night and Day," *Power Delivery, IEEE Transactions on,* vol. 30, pp. 755-763, 2015.

[63] Nak-gueon Sung, Jae-deuk Lee, Bong-tae Kim, Minwon Park, and In-Keun Yu, "Novel concept of a PV power generation system adding the function of shunt active filter," in *Transmission and Distribution Conference and Exhibition 2002: Asia Pacific. IEEE/PES*, 2002, pp. 1658-1663.

[64] Huajun Yu, Junmin Pan, and An Xiang, "A multi-function grid-connected PV system with reactive power compensation for the grid," *Solar energy,* vol. 79, pp. 101-106, 2005.

[65] Minwon Park and In-Keun Yu, "A novel real-time simulation technique of photovoltaic generation systems using RTDS," *Energy Conversion, IEEE Transactions on,* vol. 19, pp. 164-169, 2004.

[66] Dae-Jin Park, Young-Ju Kim, Mohd Hasan Ali, Minwon Park, and In-Keun Yu, "A novel real time simulation method for grid-connected wind generator system by using RTDS," in *Electrical Machines and Systems, 2007. ICEMS. International Conference on*, 2007, pp. 1936-1941.

[67] Ju-Han Lee, Tae-Hun Kim, Gyeong-Hun Kim, Serim Heo, Minwon Park, and In-Keun Yu, "RTDS-based modeling of a 100 MW class wind farm applied to an integrated power control system," in *2012 IEEE Vehicle Power and Propulsion Conference*.

[68] Junbiao Han, J Prigmore, Zhenyuan Wang, and S Khushalani-Solanki, "Modeling and coordinated controller design of a microgrid system in RTDS," in *Power and Energy Society General Meeting (PES), 2013 IEEE*, 2013, pp. 1-5.

[69] Adnan Sattar, Ahmed Al-Durra, and SM Muyeen, "Real time implementation of STATCOM to analyze transient and dynamic characteristics of wind farm," in *IECON 2011-37th Annual Conference on IEEE Industrial Electronics Society*, 2011, pp. 3742-3747.

[70] Xu Baoliang, He Jinghan, and Wang Xiaojun, "Study of improving the voltage stability of wind farm by utilizing STATCOM based on RTDS," in *Innovative Smart Grid Technologies-Asia (ISGT Asia), 2012 IEEE*, 2012, pp. 1-6.

[71] Yunwen Guo, Jianshe Zhang, Yun Hu, Weiqiang Han, Kaijian Ou, Greg Jackson*, et al.*, "Analysis on the effects of STATCOM on CSG based on RTDS," in *Innovative Smart Grid Technologies Europe (ISGT EUROPE), 2013 4th IEEE/PES*, 2013, pp. 1-5.

[72] FS Al-Ismail, MA Hassan, and MA Abido, "RTDS Implementation of STATCOM-Based Power System Stabilizers," *Electrical and Computer Engineering, Canadian Journal of,* vol. 37, pp. 48-56, 2014.

[73] Hyo-Ryong Seo, Gyeong-Hun Kim, Seong-Jae Jang, Sang-Yong Kim, Sangsoo Park, Minwon Park*, et al.*, "Harmonics and reactive power compensation method by grid-connected Photovoltaic generation system," in *Electrical Machines and Systems, 2009. ICEMS 2009. International Conference on*, 2009, pp. 1-5.

[74] Lawrence J Borle, Michael S Dymond, and Chemmangot V Nayar, "Development and testing of a 20-kW grid interactive photovoltaic power conditioning system in Western Australia," *Industry Applications, IEEE Transactions on,* vol. 33, pp. 502-508, 1997.

[75] E. Muljadi, M. Singh, R. Bravo, and V. Gevorgian, "Dynamic Model Validation of PV Inverters under Short-Circuit Conditions," in *Green Technologies Conference, 2013 IEEE*, 2013, pp. 98-104.

[76] "IEEE Standard for Interconnecting Distributed Resources with Electric Power Systems - Amendment 1," *IEEE Std 1547a-2014 (Amendment to IEEE Std 1547-2003),* pp. 1-16, 2014.

[77] NEMA ANSI, "C84. 1," *Electric Power Systems and Equipment-Voltage Ratings (60 hertz)*.

[78] A. I. Jones, B. E. Smith, and D. J. Ward, "Considerations for higher voltage distribution," *Power Delivery, IEEE Transactions on,* vol. 7, pp. 782-788, 1992.

[79] S. Yanabu, E. Zaima, and T. Hasegawa, "Historical review of high voltage switchgear developments in the 20th century for power transmission and distribution system in Japan," *Power Delivery, IEEE Transactions on,* vol. 21, pp. 659-664, 2006.

[80] Turan Gonen, *Electrical Power Transmission System Engineering: Analysis and Design*: CRC Press, 2014.

[81] J Duncan Glover, Mulukutla Sarma, and Thomas Overbye, *Power System Analysis & Design, SI Version*: Cengage Learning, 2011.

[82] John J Grainger and William D Stevenson, *Power system analysis* vol. 621: McGraw-Hill New York, 1994.

[83] James H Harlow, *Electric power transformer engineering*: CRC press, 2007.

[84] Hadi Saadat, "Power System Analysis,(2nd)," ed: McGraw-Hill Higher Education, 2009.

[85] Leonard L Grigsby, *The electric power engineering handbook*: CRC Press, 2001.

[86] Prabha Kundur, Neal J Balu, and Mark G Lauby, *Power system stability and control* vol. 7: McGraw-hill New York, 1994.

[87] Libo Wu, Zhengming Zhao, and Jianzheng Liu, "A Single-Stage Three-Phase Grid-Connected Photovoltaic System With Modified MPPT Method and Reactive Power Compensation," *Energy Conversion, IEEE Transactions on,* vol. 22, pp. 881-886, 2007.

[88] Kyung-Hoon Yoon, Donghwan Kim, and Kyung Shick Yoon, "National Survey Report of PV Power Applications in Korea 2006," *International Energy Agency Photovoltaic Power Systems Program,* 2002.

[89] "IEEE Recommended Criteria for Terrestrial Photovoltaic Power Systems," *ANSI/IEEE Std 928-1986,* p. 0_1, 1986.

[90] Widalys De Soto, SA Klein, and WA Beckman, "Improvement and validation of a model for photovoltaic array performance," *Solar energy,* vol. 80, pp. 78-88, 2006.

[91] Seul-Ki Kim, Jin-Hong Jeon, Chang-Hee Cho, Eung-Sang Kim, and Jong-Bo Ahn, "Modeling and simulation of a grid-connected PV generation system for electromagnetic transient analysis," *Solar Energy,* vol. 83, pp. 664-678, 2009.

[92] Mohammad AbdulHadi, Abdulrahman M Al-Ibrahim, and Gurvinder S Virk, "Neuro-fuzzy-based solar cell model," *Energy Conversion, IEEE Transactions on,* vol. 19, pp. 619-624, 2004.

[93] MA De Blas, JL Torres, E Prieto, and A Garcıa, "Selecting a suitable model for characterizing photovoltaic devices," *Renewable Energy,* vol. 25, pp. 371-380, 2002.

[94] David L King, Jay A Kratochvil, and William Earl Boyson, *Photovoltaic array performance model*: United States. Department of Energy, 2004.

[95] Marcelo Gradella Villalva and Jonas Rafael Gazoli, "Comprehensive approach to modeling and simulation of photovoltaic arrays," *Power Electronics, IEEE Transactions on,* vol. 24, pp. 1198-1208, 2009.

[96] C Carrero, J Amador, and S Arnaltes, "A single procedure for helping PV designers to select silicon PV modules and evaluate the loss resistances," *Renewable Energy,* vol. 32, pp. 2579-2589, 2007.

[97] A. Kavimandan and S. P. Das, "Control and protection strategy for a three-phase single-stage boost type grid-connected current source inverter for PV applications," in *Industrial Technology (ICIT), 2013 IEEE International Conference on*, 2013, pp. 1722-1727.

[98] P. P. Dash and M. Kazerani, "Dynamic Modeling and Performance Analysis of a Grid-Connected Current-Source Inverter-Based Photovoltaic System," *Sustainable Energy, IEEE Transactions on,* vol. 2, pp. 443-450, 2011.

[99] Amirnaser Yazdani, Anna Rita Di Fazio, Hamidreza Ghoddami, Mario Russo, Mehrdad Kazerani, Juri Jatskevich*, et al.*, "Modeling guidelines and a benchmark for power system simulation studies of three-phase single-stage photovoltaic systems," *Power Delivery, IEEE Transactions on,* vol. 26, pp. 1247-1264, 2011.

[100] A. Yazdani and P. P. Dash, "A Control Methodology and Characterization of Dynamics for a Photovoltaic (PV) System Interfaced With a Distribution Network," *Power Delivery, IEEE Transactions on,* vol. 24, pp. 1538-1551, 2009.

[101] Bo Yang, Wuhua Li, Yi Zhao, and Xiangning He, "Design and analysis of a grid-connected photovoltaic power system," *Power Electronics, IEEE Transactions on,* vol. 25, pp. 992-1000, 2010.

[102] N. N. V. S. Babu and B. G. Fernandes, "Cascaded Two-Level Inverter-Based Multilevel STATCOM for High-Power Applications," *Power Delivery, IEEE Transactions on,* vol. 29, pp. 993-1001, 2014.

[103] B. Eskandari, M. T. Bina, and M. A. Golkar, "New concept on sinusoidal modulation for three-phase DC/AC converters: analysis and experiments," *Power Electronics, IET,* vol. 7, pp. 357-365, 2014.

[104] A. K. Gupta and A. M. Khambadkone, "A Space Vector PWM Scheme for Multilevel Inverters Based on Two-Level Space Vector PWM," *Industrial Electronics, IEEE Transactions on,* vol. 53, pp. 1631-1639, 2006.

[105] M. F. Kangarlu and E. Babaei, "A Generalized Cascaded Multilevel Inverter Using Series Connection of Submultilevel Inverters," *Power Electronics, IEEE Transactions on,* vol. 28, pp. 625-636, 2013.

[106] E. A. Mahrous, N. A. Rahim, and W. P. Hew, "Three-phase three-level voltage source inverter with low switching frequency based on the two-level inverter topology," *Electric Power Applications, IET,* vol. 1, pp. 637-641, 2007.

[107] H. P. Mohammadi and M. T. Bina, "A Transformerless Medium-Voltage STATCOM Topology Based on Extended Modular Multilevel Converters," *Power Electronics, IEEE Transactions on,* vol. 26, pp. 1534-1545, 2011.

[108] V. T. Somasekhar and K. Gopakumar, "Three-level inverter configuration cascading two two-level inverters," *Electric Power Applications, IEE Proceedings -,* vol. 150, pp. 245-254, 2003.

[109] Heinz Willi Van Der Broeck, H-C Skudelny, and Georg Viktor Stanke, "Analysis and realization of a pulsewidth modulator based on voltage space vectors," *Industry Applications, IEEE Transactions on,* vol. 24, pp. 142-150, 1988.

[110] Ned Mohan and Tore M Undeland, *Power electronics: converters, applications, and design*: John Wiley & Sons, 2007.

[111] A. M. Trzynadlowski, "An overview of modern PWM techniques for three-phase, voltage-controlled, voltage-source inverters," in *Industrial Electronics, 1996. ISIE '96., Proceedings of the IEEE International Symposium on*, 1996, pp. 25-39 vol.1.

[112] Yu Zhenyu, A. Mohammed, and I. Panahi, "A review of three PWM techniques," in *American Control Conference, 1997. Proceedings of the 1997*, 1997, pp. 257-261 vol.1.

[113] J. Segundo-Ramirez and A. Medina, "Modeling of FACTS Devices Based on SPWM VSCs," *Power Delivery, IEEE Transactions on,* vol. 24, pp. 1815-1823, 2009.

[114] S. Anand, B. G. Fernandes, and K. Chatterjee, "DC Voltage Controller for Asymmetric-Twin-Converter-Topology-Based High-Power STATCOM," *Industrial Electronics, IEEE Transactions on,* vol. 60, pp. 11-19, 2013.

[115] T. Atalik, M. Deniz, E. Koc, C. O. Gercek, B. Gultekin, M. Ermis*, et al.*, "Multi-DSP and -FPGA-Based Fully Digital Control System for Cascaded Multilevel Converters Used in FACTS Applications," *Industrial Informatics, IEEE Transactions on,* vol. 8, pp. 511-527, 2012.

[116] J. Chivite-Zabalza, P. Izurza-Moreno, D. Madariaga, G. Calvo, Rodri, x*, et al.*, "Voltage Balancing control in 3-Level Neutral-Point Clamped Inverters Using Triangular Carrier PWM Modulation for FACTS Applications," *Power Electronics, IEEE Transactions on,* vol. 28, pp. 4473-4484, 2013.

[117] B. Gultekin and M. Ermis, "Cascaded Multilevel Converter-Based Transmission STATCOM: System Design Methodology and Development of a 12 kV ±12 MVAr Power Stage," *Power Electronics, IEEE Transactions on,* vol. 28, pp. 4930-4950, 2013.

[118] Shu Zeliang, Ding Na, Chen Jie, Zhu Haifeng, and He Xiaoqiong, "Multilevel SVPWM With DC-Link Capacitor Voltage Balancing Control for Diode-Clamped Multilevel Converter Based STATCOM," *Industrial Electronics, IEEE Transactions on,* vol. 60, pp. 1884-1896, 2013.

[119] Walter A Hill and Suresh C Kapoor, "Effect of two-level PWM sources on plant power system harmonics," in *Industry Applications Conference, 1998. Thirty-Third IAS Annual Meeting. The 1998 IEEE*, 1998, pp. 1300-1306.

[120] A Reznik, MG Simões, A Al-Durra, and SM Muyeen, "LCL filter design and performance analysis for small wind turbine systems," in *Power Electronics and Machines in Wind Applications (PEMWA), 2012 IEEE*, 2012, pp. 1-7.

[121] AA Rockhill, Marco Liserre, Remus Teodorescu, and Pedro Rodriguez, "Grid-filter design for a multimegawatt medium-voltage voltage-source inverter," *Industrial Electronics, IEEE Transactions on,* vol. 58, pp. 1205-1217, 2011.

[122] S. A. Khajehoddin, M. Karimi-Ghartemani, P. K. Jain, and A. Bakhshai, "A Control Design Approach for Three-Phase Grid-Connected Renewable Energy Resources," *Sustainable Energy, IEEE Transactions on,* vol. 2, pp. 423-432, 2011.

[123] S. V. Araujo, A. Engler, B. Sahan, and F. Antunes, "LCL filter design for grid-connected NPC inverters in offshore wind turbines," in *Power Electronics, 2007. ICPE '07. 7th Internatonal Conference on*, 2007, pp. 1133-1138.

[124] Marco Liserre, Frede Blaabjerg, and Steffan Hansen, "Design and control of an LCL-filter-based three-phase active rectifier," *Industry Applications, IEEE Transactions on,* vol. 41, pp. 1281-1291, 2005.

[125] Emre Kantar, S Usluer, and Ahmet M Hava, "Design and performance analysis of a grid connected PWM-VSI system," in *Electrical and Electronics Engineering (ELECO), 2013 8th International Conference on*, 2013, pp. 157-161.

[126] S. G. Parker, B. P. McGrath, and D. G. Holmes, "Regions of Active Damping Control for LCL Filters," *Industry Applications, IEEE Transactions on,* vol. 50, pp. 424-432, 2014.

[127] M Simoes, A Reznik, Ahmed Al Durra, and SM Muyeen, "LCL Filter Design and Performance Analysis for Grid Interconnected Systems," 2012.

[128] "IEEE Recommended Practice for Grounding of Industrial and Commercial Power Systems," *IEEE Std 142-2007 (Revision of IEEE Std 142-1991),* pp. 1-225, 2007.

[129] Moon Won Sik, Hur Jae-Sun, and Kim Jae-Chul, "A Protection of interconnection transformer for DG in Korea distribution power system," in *Power and Energy Society General Meeting, 2012 IEEE*, 2012, pp. 1-5.

[130] S. Bifaretti, A. Lidozzi, L. Solero, and F. Crescimbini, "Anti-Islanding Detector Based on a Robust PLL," *Industry Applications, IEEE Transactions on,* vol. 51, pp. 398-405, 2015.

[131] S. K. Chung, "Phase-locked loop for grid-connected three-phase power conversion systems," *Electric Power Applications, IEE Proceedings -,* vol. 147, pp. 213-219, 2000.

[132] Lee Kyoung-Jun, Lee Jong-Pil, Shin Dongsul, Yoo Dong-Wook, and Kim Hee-Je, "A Novel Grid Synchronization PLL Method Based on Adaptive Low-Pass Notch Filter for Grid-Connected PCS," *Industrial Electronics, IEEE Transactions on,* vol. 61, pp. 292-301, 2014.

[133] F. A. Ramirez and M. A. Arjona, "Development of a Grid-Connected Wind Generation System With a Modified PLL Structure," *Sustainable Energy, IEEE Transactions on,* vol. 3, pp. 474-481, 2012.

[134] Chung Se-Kyo, "A phase tracking system for three phase utility interface inverters," *Power Electronics, IEEE Transactions on,* vol. 15, pp. 431-438, 2000.

[135] Remus Teodorescu and Frede Blaabjerg, "Flexible control of small wind turbines with grid failure detection operating in stand-alone and grid-connected mode," *Power Electronics, IEEE Transactions on,* vol. 19, pp. 1323-1332, 2004.

[136] Prajna Paramita Dash and Amirnaser Yazdani, "A Mathematical Model and Performance Evaluation for a Single-Stage Grid-Connected Photovoltaic (PV) System," *International Journal of Emerging Electric Power Systems,* vol. 9, 2008.

[137] Kim Sam-Young and Park Seung-Yub, "Compensation of Dead-Time Effects Based on Adaptive Harmonic Filtering in the Vector-Controlled AC Motor Drives," *Industrial Electronics, IEEE Transactions on,* vol. 54, pp. 1768-1777, 2007.

[138] N. Urasaki, T. Senjyu, K. Uezato, and T. Funabashi, "An adaptive dead-time compensation strategy for voltage source inverter fed motor drives," *Power Electronics, IEEE Transactions on,* vol. 20, pp. 1150-1160, 2005.

[139] Werner Leonhard, *Control of electrical drives*: Springer, 2001.

[140] Ganesh K Venayagamoorthy, "Comparison of power system simulation studies on different platforms-RSCAD, PSCAD/EMTDC, and SIMULINK SimPowerSystems," in *International Conference on Power Systems, Operation and Planning*, 2005.

[141] PSCAD. (2015). Available: https://hvdc.ca/pscad/

[142] RTDS Hardware Manual, "Rev. 2," *RTDS Technologies, Winnipeg, MB,* pp. 13.1-13.19, 2012.

[143] OPAL-RT. Available: http://www.opal-rt.com/

[144] Pinaki Mitra, K Vinothkumar, and Lidong Zhang, "Dynamic performance study of a HVDC grid using real-time digital simulator," in *Complexity in Engineering (COMPENG), 2012*, 2012, pp. 1-6.

[145] PR Bishop, ZQ Bo, XF Shen, L Denning, and M O'Keeffe, "Implementation of dynamic distance relay scheme evaluation testing. Guidelines using analogue and real time digital simulators," 2001.

[146] Jin-Hong Jeon, Jong-Yul Kim, Hak-Man Kim, Seul-Ki Kim, Changhee Cho, Jang-Mok Kim*, et al.*, "Development of hardware in-the-loop simulation system for testing operation and control functions of microgrid," *Power Electronics, IEEE Transactions on,* vol. 25, pp. 2919-2929, 2010.

[147] M Steurer, S Woodruff, T Baldwin, H Boenig, F Bogdan, T Fikse*, et al.*, "Hardware-in-the-loop investigation of rotor heating in a 5 MW HTS propulsion motor," *Applied Superconductivity, IEEE Transactions on,* vol. 17, pp. 1595-1598, 2007.

[148] MESH Steurer, "PEBB based high-power hardware-in-loop simulation facility for electric power systems," in *Power Engineering Society General Meeting, 2006. IEEE*, 2006, p. 3 pp.

[149] F. S. Al-Ismail, M. A. Hassan, and M. A. Abido, "RTDS Implementation of STATCOM-Based Power System Stabilizers," *Electrical and Computer Engineering, Canadian Journal of,* vol. 37, pp. 48-56, 2014.

[150] R. Kuffel, J. Giesbrecht, T. Maguire, R. P. Wierckx, P. A. Forsyth, and P. G. McLaren, "A fully digital real-time simulator for protective relay testing," in *Developments in Power System Protection, Sixth International Conference on (Conf. Publ. No. 434)*, 1997, pp. 147-150.

[151] Baek Seung-Mook and Park Jung-Wook, "Nonlinear Parameter Optimization of FACTS Controller via Real-Time Digital Simulator," *Industry Applications, IEEE Transactions on,* vol. 49, pp. 2271-2278, 2013.

[152] "dSPACE Catalog 2014," ed: dSPACE Inc., pp. 314-318.

[153] Sigifredo Gonzalez, Scott Kuszmaul, Don Deuel, and Roberto Lucca, "PV array simulator development and validation," in *Photovoltaic Specialists Conference (PVSC), 2010 35th IEEE*, 2010, pp. 002849-002852.

[154] Broshure Elgar TerraSAS, "Programmable Solar Array Simulator," in *AMETEK Programmable Power Co*, ed.

[155] Lihua Chen and Fang Zheng Peng, "Dead-time elimination for voltage source inverters," *Power Electronics, IEEE Transactions on,* vol. 23, pp. 574-580, 2008.

[156] Eric R Motto and John F Donlon, "IGBT Modules Optimized for Three Level Inverters," in *Energy Conversion Congress and Exposition IECCE*, pp. 2194-2199.

[157] POWEREX. Three Phase IGBT Assembly. Available: http://www.pwrx.com/pwrx/docs/pp100t060.pdf

[158] Crydom. Three-Phase Solid-State Relay. Available: http://www.crydom.com/en/Products/Catalog/5_3tp.pdf

[159] FAIRCHILD Semiconductor. Schmitt Trigger Output Optocoupler. Available: https://www.fairchildsemi.com/datasheets/H1/H11N1M.pdf

[160] Sarah J Brown and Ian H Rowlands, "Nodal pricing in Ontario, Canada: Implications for solar PV electricity," *Renewable Energy,* vol. 34, pp. 170-178, 2009.

[161] Adonis Yatchew and Andy Baziliauskas, "Ontario feed-in-tariff programs," *Energy Policy,* vol. 39, pp. 3885-3893, 2011.

[162] Hydro One Inc. (2013). *Distributed Generation Technical Interconnection Requirements-Interconnections at Voltages 50kV and Below (Rev. 3 ed.)*. Available: http://www.hydroone.com/Generators/Pages/TechnicalRequirements.aspx

[163] Solar One. (2015). Available: http://solar-one.ca

[164] BP Solar. (2015). Available: http://www.bp.com

[165] Hammond Manufacturing Ltd. (2015). Available: http://www.hammondmfg.com/

APPENDIX A

A. 1 Parameters of a Realistic System similar to Bluewater Power Network

AC Source Voltage (L-L)	$V_{g,L-L} = 208V$
AC Source Thevenin Impedance	$R_g = 0.001\Omega$, $L_g = 0.0012\,\text{mH}$
System Parameters	$X_g / R_g = 3$

A. 2 Typical Solar panel Parameters [163, 164]

Open Circuit Voltage	V_{OC} = 21.7 V
Short Circuit Current	I_{SC} = 3.35 A
Voltage at Maximum Power	V_{MPP} = 17.4 V
Current at Maximum Power	I_{MPP}= 3.05 A
PV Modules in Series	N_S= 23
PV Modules in Parallel	N_P = 8

A. 3 PV Inverter Parameters [157]

IGBT ON State Resistance	R_{ON} = 0.001 Ω
IGBT Off State Resistance	R_{OFF} = 1e5 Ω
IGBT Forward Voltage Drop	V_D = 0 V
Snubber Resistance	$R_{Snubber}$= 1000 Ω
Snubber Capacitance	$C_{Snubber}$= 0.002 μF
DC link Capacitor	C_{DC} = 18000 μF
DC link Voltage	V_{DC} = 400V DC
Switch rating	V_{rating} = 600 V, I_{rating} = 100 A

A. 4 PV Transformer Parameters [165]

Transformer Configuration	Delta (Inverter Side)/Wye (Grid Side)
Nominal Power of Transformer	$S= 10\ kVA$
Winding Voltages	$V_p = V_s = 208V$ (L-L)
Base Frequency	$f = 60\,\text{Hz}$
Leakage Reactance	$L_t = 0.05\,\text{pu}$

APPENDIX B

B. 1 Structure of Control Hardware-In-Loop

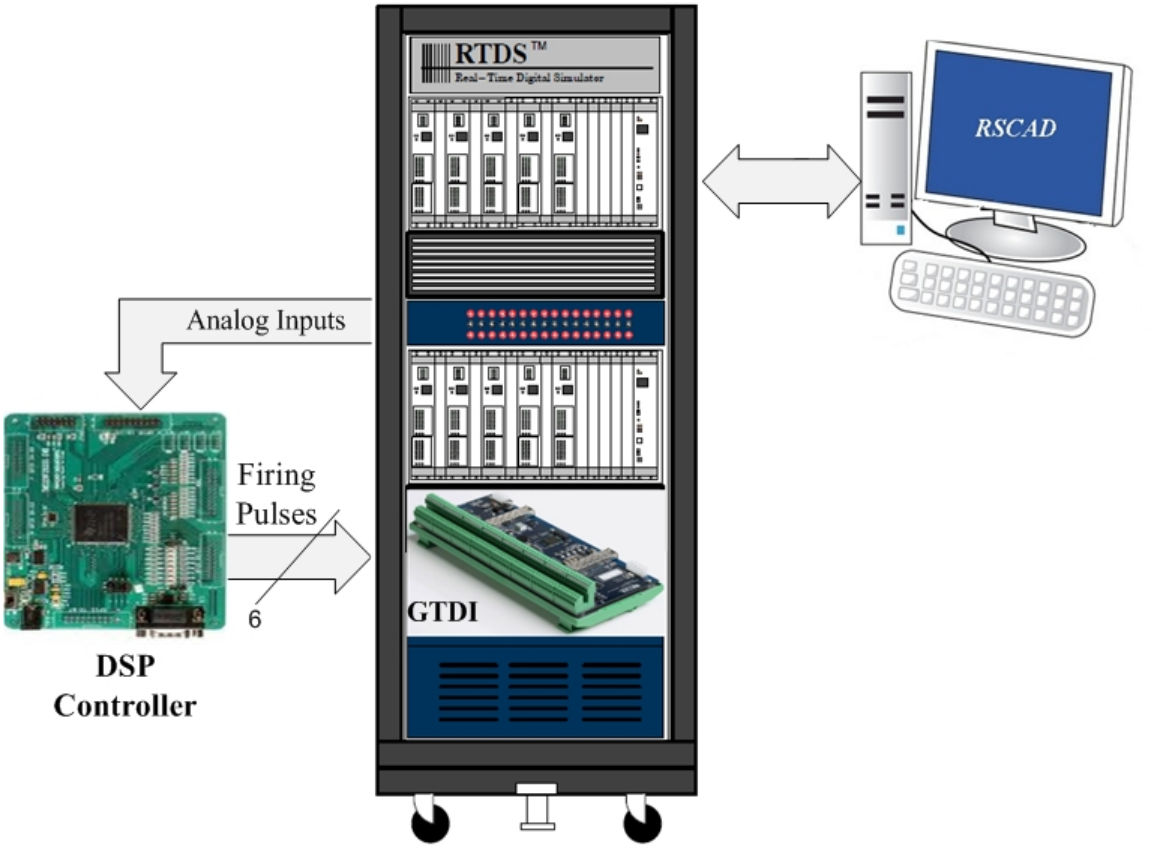

B. 2 Simplified Model of Controller in MATLAB/Simulink

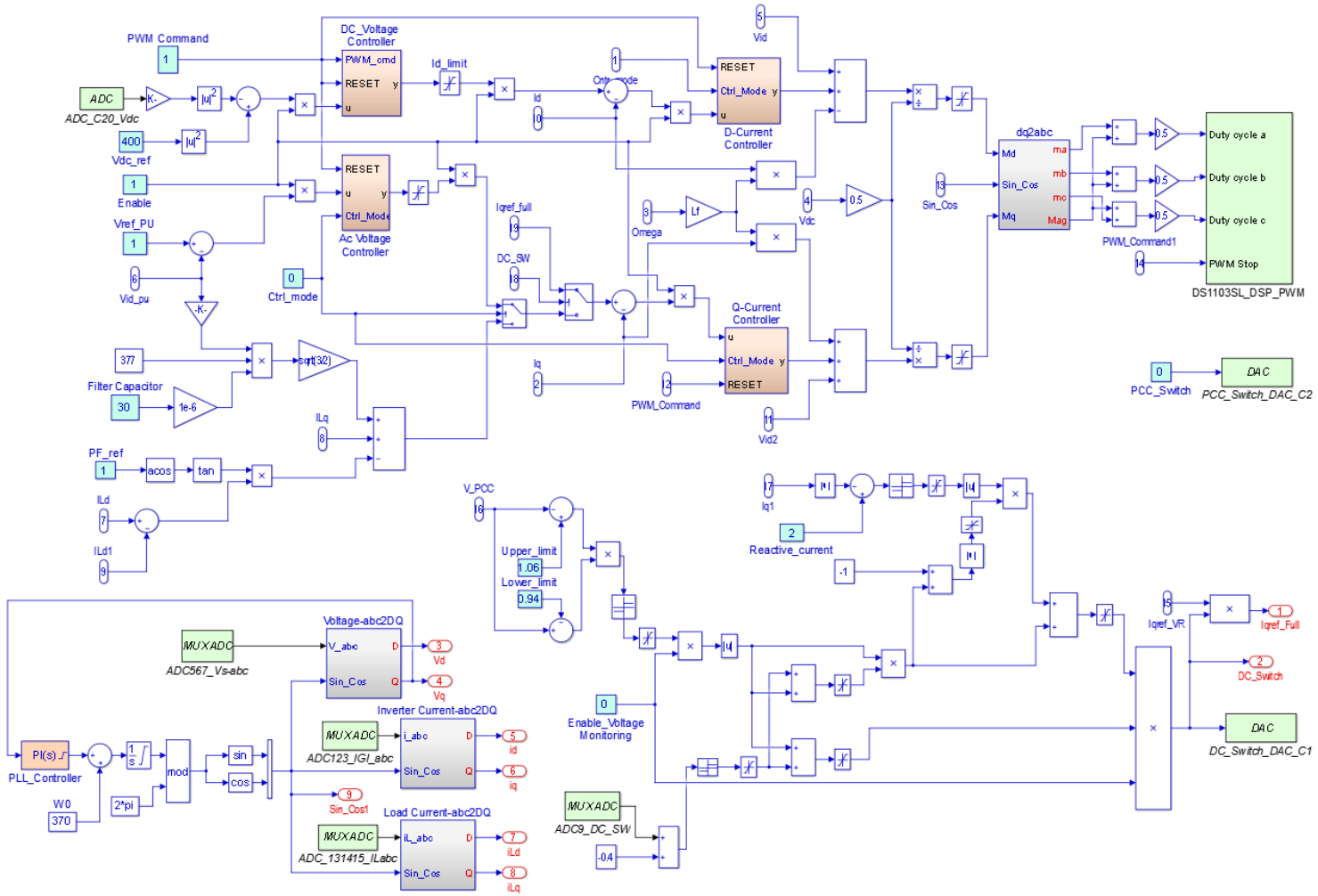

B. 3 Designed GUI in RSCAD-Runtime

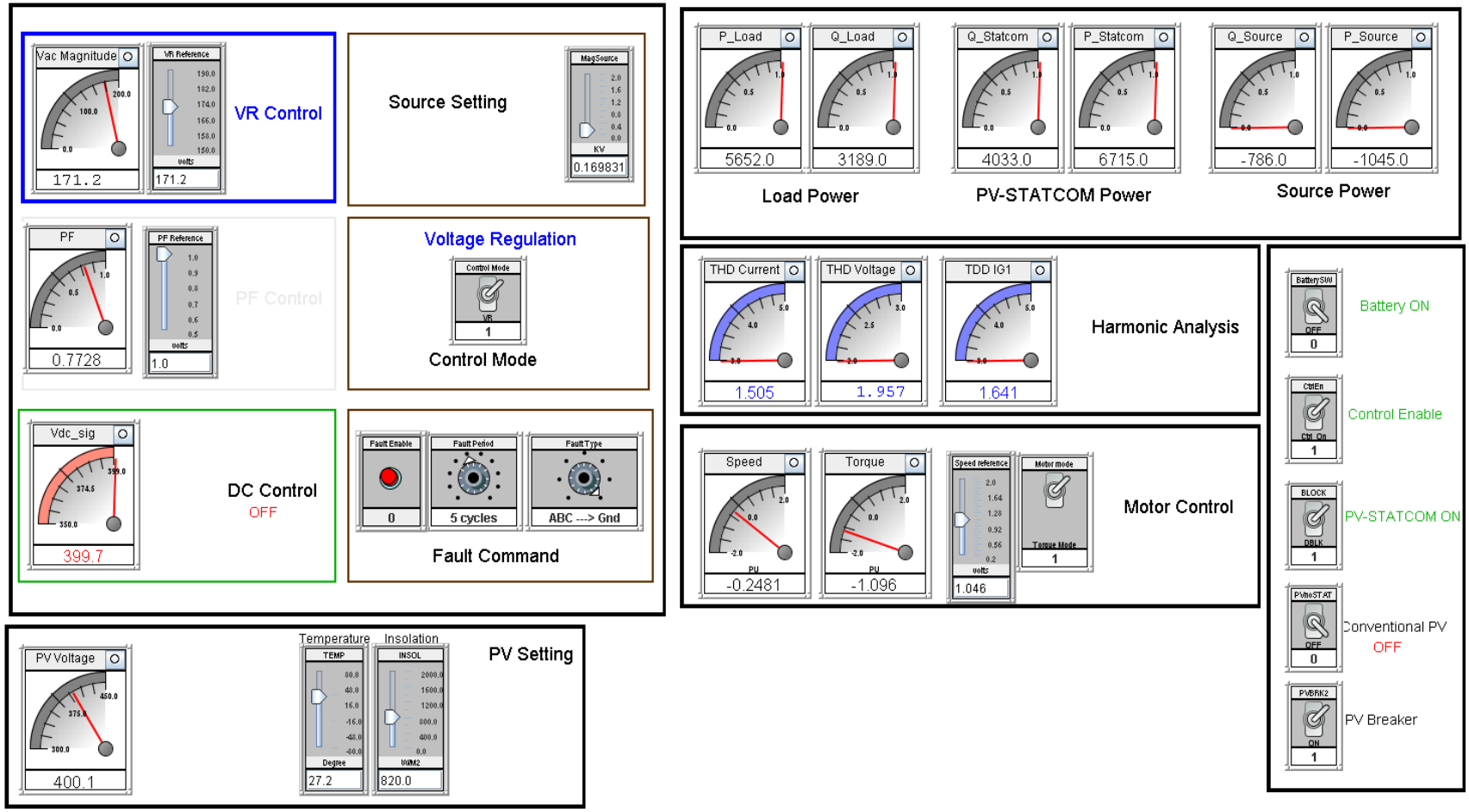

B. 4 Designed GUI in ControlDesk

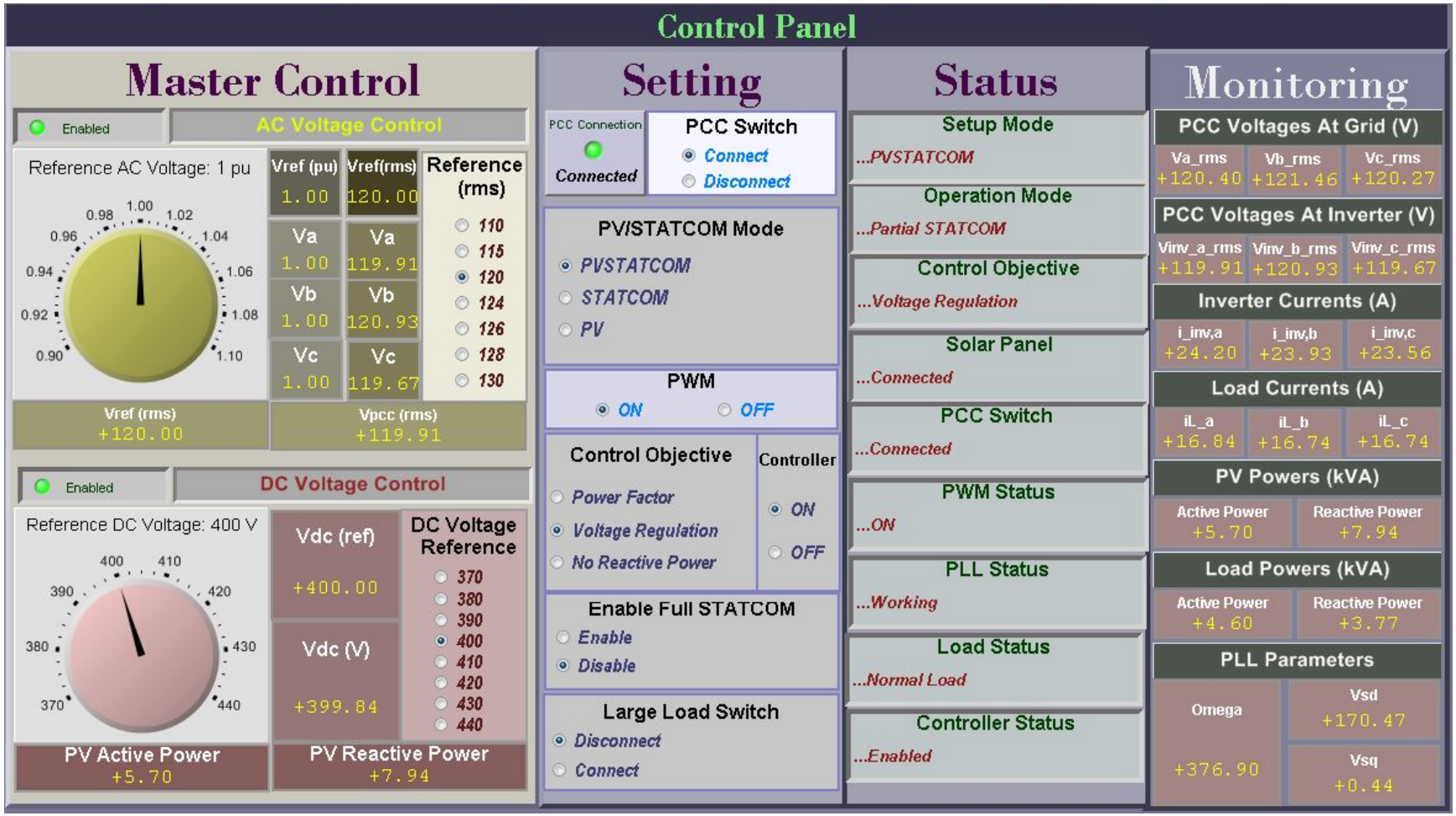

B. 5 Hardware-In-Loop Setup

APPENDIX C

C. 1 PV Simulator

C. 2 Three Phase IGBT Module

APPENDIX D

D. 1 Parameters of a Realistic System similar to Hydro One Power Network (confidential)

Nominal Voltage	$V_{grid} = 44\,kV$
Approximate Distance from Station to PCC	Line 1=35 km

D. 2 Typical Solar Panel Parameters [163, 164]

Each PV Size	$P_{PV} = 10\,MW$
Number of PV Units	N=3
Total output of DG facility	$P_{PV,total} = 30\,MW$
Rated Frequency	$f = 60\,Hz$
Rated Voltage of the PV unit	$V_{PV} = 360\,V$
PV Modules in Series (Each 10MW PV)	N_S= 20
PV Modules in Parallel(Each 10MW PV)	N_P =2120
Open Circuit Voltage	V_{OC} = 51.8 V
Short Circuit Current	I_{SC} = 5.84 A
Voltage at Maximum Power	V_{MPP} = 43 V
Current at Maximum Power	I_{MPP}= 5.48 A

D. 3 Typical PV Inverter Parameters [157]

IGBT ON State Resistance	R_{ON} = 0.0001 Ω
IGBT Off State Resistance	R_{OFF} = 1e6 Ω
IGBT Forward Voltage Drop	V_D = 0 V
Snubber Resistance	$R_{Snubber}$= 1000 Ω
Snubber Capacitance	$C_{Snubber}$= 0.002 μF
DC link Capacitor	C_{DC} = 150 mF
DC link Voltage	V_{DC} = 925 V(dc)

D. 4 DG Interface Transformer Parameters

Rating	$S_{DG,transformer} = 30\,\text{MVA}$
Number of Interface Transformer Units	$n_{DG,transformer} = 1$
Winding Connection and Voltage	Delta (44 kV)/Star-Grounded (27.6 kV)

D. 5 PV Intermediate Transformer Parameters

Rating	$S_{PV,transformer} = 10\,\text{MVA}$
Number of Interface Transformer Units	$n_{PV,transformer} = 3$
Winding Connection and Voltage	Delta (27.6 kV)/Star (360 V)

D. 6 Modeling of Study System in PSCAD/EMTDC Software

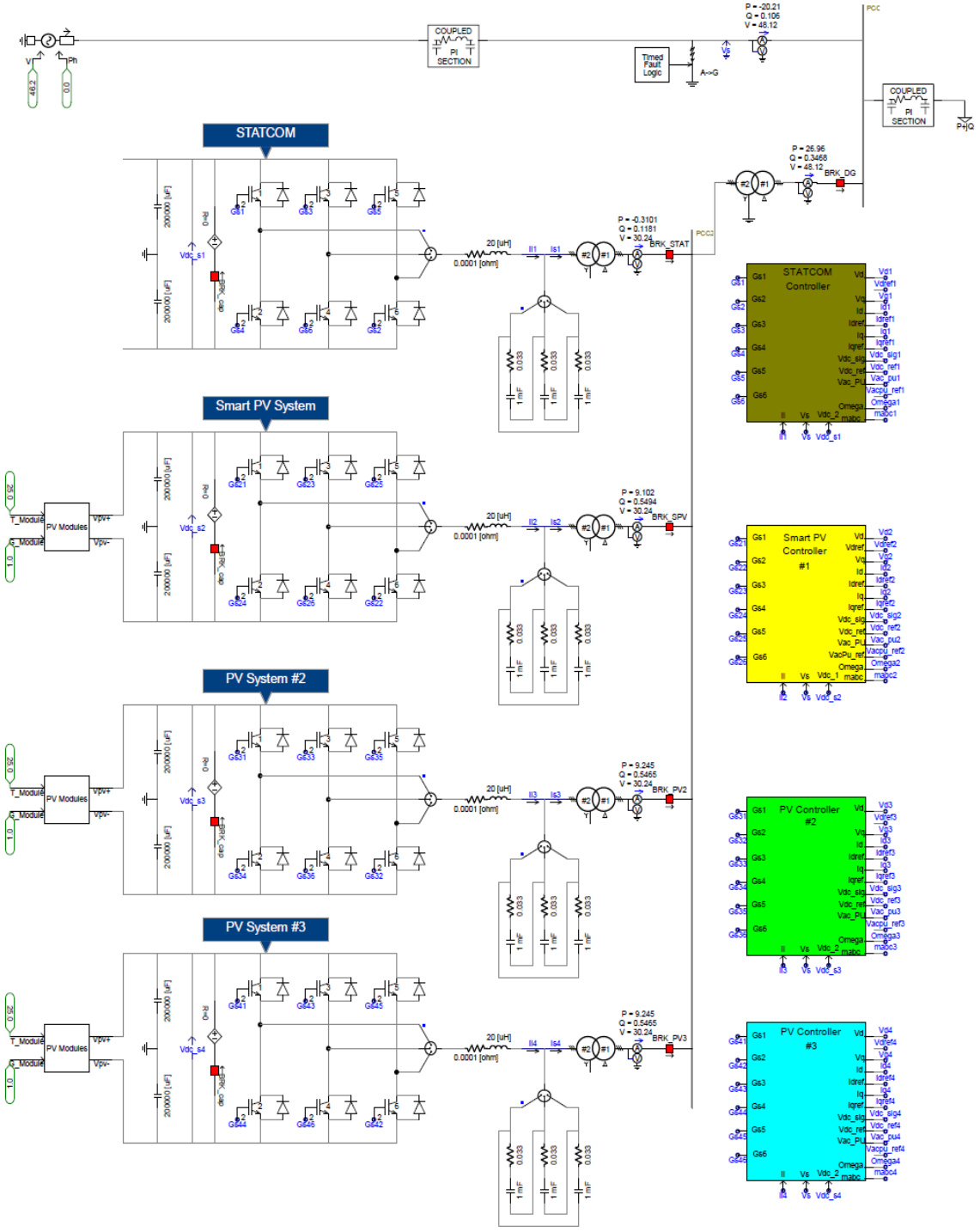

D. 7 Modeling of Smart PV Inverter Control in PSCAD/EMTDC Software

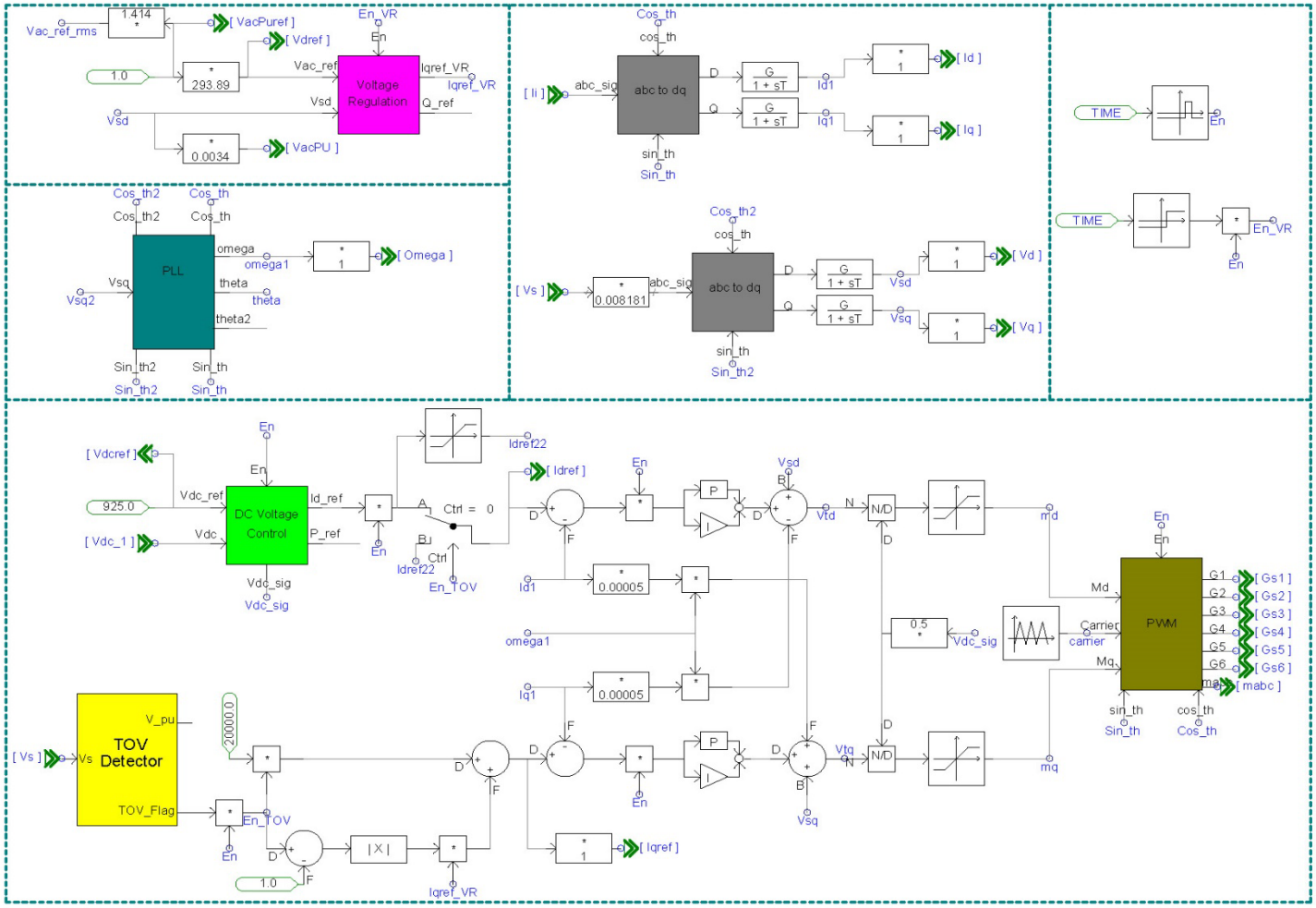

CURRICULUM VITAE

Name: Ehsan Mohammadi Siavashi

Post-secondary Education and Degrees:

K. N. Toosi University of Technology
Tehran, Tehran, Iran
2002-2007 B.Sc. in Electrical Engineering

The University of Tehran
Tehran, Tehran, Iran
2007-2010 M.Sc. in Electrical Engineering

The University of Western Ontario
London, Ontario, Canada
2010-2015 Ph.D. in Electrical Engineering (In progress)

Honours and Awards:

Hydro One Power Systems Award, 2015

Western Graduate Research Scholarship (WGRS-ECE), 2010

Related Work Experience

Teaching Assistant
The University of Western Ontario
Lab Instructor, "ELECTRIC POWER SYSTEMS Lab"
2011-2014

Teaching Assistant
Waterloo University
"FACTS Devices and controller", Graduate course
Fall 2014

Publications:

1 Varma, Rajiv. K; **Siavashi, Ehsan. M.**; Das, Byomakesh; Sharma, Vinay; "*Novel application of a PV Solar Plant as STATCOM (PV-STATCOM) during Night and Day in a Distribution Utility Network: Part 2",* IEEE PES Transmission & Distribution Conference & Exposition, Orlando, Florida, USA, 7-10 May 2012, Pages: 1-8.

2 Varma, Rajiv. K; **Siavashi, Ehsan. M.**; et al.; "*Real Time Digital Simulation of PV solar system as STATCOM (PV-STATCOM) for Voltage Regulation and Power Factor Correction",* Proc. of IEEE EPEC Electrical Power & Energy Conference, London, Ontario, Canada, 10-12 October 2012, pp 157-163.

3 Rajiv K. Varma, Shah Arifur Rahman, **Ehsan M. Siavashi**, and Mahendra A.C., "*Nighttime Applications of PV Solar Farms*", Proc. 2014 Solar Power International Conference, Las Vegas, USA, Oct. 2014.

4 **Siavashi, Ehsan. M.**; Rouhani, Alireza; Moslemi, Ramin; "*Detection of Voltage Sag Using Unscented Kalman Smoother",* IEEE Proc. Environment and Electrical Engineering (EEEIC 2010), 9th International Conference, Prague, Czech, 2010, Pages: 128 – 131.

5 **Siavashi, E.M**.; Baradar, M.R.; Afsharnia, S.; Bina, M.T.; "*Novel Method for Fault Section Identification",* IEEE Proc. Power Electronics and Intelligent Transportation System (PEITS), 2009 2nd International Conference, Shenzhen, China, 19-20 Dec 2009, Pages: 179 – 184.

6 **Siavashi, E.M**.; Afsharnia, S.; Bina, M.T.; Zadeh, M.K.; Baradar, M.R.;" *Frequency Estimation of Distorted Signals in Power Systems Using Particle Extended Kalman Filter",* IEEE Proc. Power Electronics and Intelligent Transportation System (PEITS), 2009 2nd International Conference, Shenzhen, China, 19-20 Dec 2009, Pages: 174 – 178.

7 Farahabadi, P.M.; **Siavashi, E.M.**; Hassani, Y.; Zadeh, M.K.;" *A novel method for tracking the resonance frequency of the series RLC loads using extended Kalman filter",* IEEE Proc. Industrial Electronics and Applications (ICIEA 2009) 4th IEEE Conference, Xi'an, China, 25-27 May 2009, Pages: 831 – 836.

8 M. Isapour Chehardeh; M. K. Zadeh; H. Lesani and **Siavashi, E.M**; "*An Optimal Control Strategy to Alleviate Sub-synchronous Resonance in VSC-HVDC Systems,",* IEEE Proc. Power Electronics and Intelligent Transportation System (PEITS), 2009 2nd International Conference, Shenzhen, China, 19-20 Dec 2009, Pages: 250 – 255.